ARTIFICIAL ANTERIOR CRUCIATE LIGAMENT RECONSTRUCTION



IN PARTIAL FULLFILMENT OF THE REQUIREMENTS FOR THE DEGREE OF

DOCTOR OF PHILOSOPHY

BY

MONA ALINEJAD

St. Edmund Hall



Hilary Term 2014

Abstract

Artificial Anterior Cruciate Ligament Reconstruction

Mona Alinejad — Doctor of Philosophy
St Edmund Hall — Hillary Term 2014

Conventional anterior cruciate ligament (ACL) reconstruction grafts have not been able to replicate the mechanical behaviour of the native ACL, reproduce normal knee mechanics and kinematics, or prevent degenerative disease progression of the knee. The aim of this thesis was to investigate a novel ACL design to more closely mimic the normal mechanical behaviour of the ACL, reconstruct the isometric ACL fibre and potentially reproduce the normal kinematics and mechanics of the knee. The designed artificial ACL reconstruction (ACLR) system could be used as a stand-alone device or in conjunction with a total knee replacement (TKR).

The nominated design option for the ACLR system consisted of a connecting cord made of ultra-high molecular weight polyethylene (UHMWPE) fibres and an elastic system made of cobalt-chrome-molybdenum (CoCrMo) alloy with similar load-elongation characteristics to the native ACL. The design requirements were defined based on the mechanical properties of the native ACL, size constraints from the bony geometry and TKR components, and the location of the isometric fibres of the native ACL.

The *in vitro* mechanical tests performed in this project on the designed cord showed a 2-3 times greater ultimate tensile load compared to the ACL in young human cadavers. The decreasing creep modulus of the UHMWPE cord under fatigue loading in simulated body conditions (3118 MPa at 6.5×10^6 cycle) indicated nominal creep and stabilised mechanical properties by the 3000^{th} loading cycle.

To replicate the non-linear stiffness of the ACL with ~38 N mm^{-1} toe and ~100 N mm^{-1} linear regions, the artificial ACLR device consisted of a femoral spring (~60 N mm^{-1}) in series with a tibial spring (~100 N mm^{-1}) and a connecting cord (~2000 N mm^{-1}). Two helical springs in series were used for the stand-alone ACLR, whereas a helical spring in series with a spiral spring was designed for the ACLR-TKR. As both the helical and spiral springs had a constant stiffness, stop mechanisms were added to the springs to create a non-linear stiffness and control the maximum safe deformation limit of each spring.

To understand the mechanical behaviour of the reconstructed isometric fibre of the ACL, passive and loaded motions were simulated in 18 sets of segmented MRI models of healthy human knees. Constant load and elongation was observed throughout flexion during the passive movements, whereas maximal load and elongation in the reconstructed ACL was identified at 50 ^{o} of flexion during loaded motion. An ACL attachment placement sensitivity study, conducted in this project to assess the effect of surgical implantation error on the behaviour of the reconstructed ACL, revealed that misplacement of the femoral attachment would significantly influence the load-elongation of the reconstructed ACL.

Finite element (FE) models of the designed ACLR devices enabled their behaviour under simulated axial loading, squatting and the Lachman test to be assessed. Both ACLR devices successfully reproduced stiffness of the native ACL with a multi-linear stiffness curve, however, elongation greater than 3.1 mm could not be achieved.

It can be concluded that the designed artificial ACLR devices were able to mimic the mechanical behaviour of the ACL provided it was positioned at the isometric attachment points; potentially enabling achievement of more natural kinematics and mechanics of the reconstructed knee. However, ACL placement was shown to have a significant impact on the behaviour of the reconstructed ACL, therefore, placement error may over-constrain the joint. For this reason, a more forgiving design with a lower stiffness and a larger deformation limit would be advised.

Acknowledgement

There are many people without whom completing this thesis would not have been possible.

First of all, I would like to thank Prof. David Murray for his guidance, support and valuable clinical input. I am delighted that I had the privilege to be one of his students.
Dr Elise Pegg was not only a knowledgeable supervisor, but also a very patient and caring friend. I would like to thanks her for her endless support and encouragement, for making time for me whenever I needed her help. She was just amazing.

Prof. John O'Connor has been a great source of inspiration; his passion for life and biomechanics is admirable. I express my gratitude for his wise words.

I am truly indebted to my manager Russell Lloyd for believing in me, helping me start and continue my DPhil and offering his unlimited support throughout the course of my studies.
I am grateful to Mr Chris Dodd, Mr John Goodfellow, Gemma O'Connor, Paul Kistle, Barbara and Laurence Marks and Stephanie Miot for their valuable support.

During the last four years, I made many good friends who made my time in Oxford more pleasant. I would like to thank Samira, Zuzana, Neil, Mo, Anneke, Anna, Monica, Catriona, Jen, Russ, Isaiah, Kelly, Saint, Rao, Michael, Sherry and Sara.

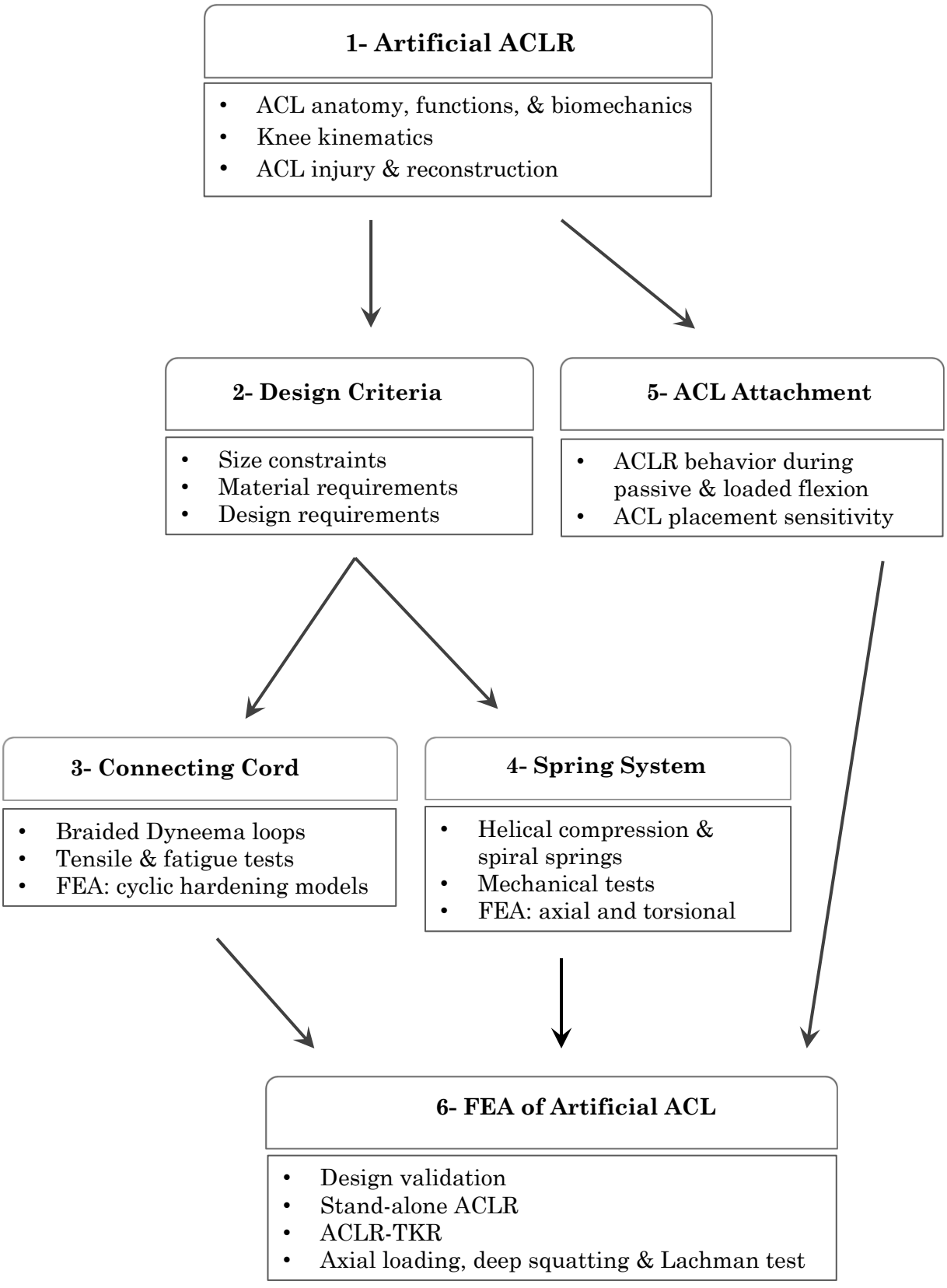
Biomet UK Healthcare Ltd., Botnar research centre, St. Edmund Hall, Linacre, Team viewer, Dropbox, Fandogh, ABAQUS, Mimics, Skype, Facebook, Jamie's, Summertown, Esporta, Frenchay Road and Elizabeth Jennings Way were inseparable parts of my experience in Oxford.

I would like to thank my dearest Reza for being my rock, for standing by my side during the most difficult period of my life, for being understanding, for inspiring me with his fascinating childhood stories, for teaching me statistics and more importantly giving me the best reason to finish.

I am grateful to my lovely parents and my brothers Nima, Milad and Meyad for their unconditional love and support. I could not have made it through this without them. I would like to dedicate this thesis to my beloved brother Milad who I have painfully lost. He will remain in my memory and heart forever.

This project was performed in collaboration with Biomet UK Healthcare Ltd. (Swindon, UK).

Thesis Outline



Contents

Chapter 1: Introduction 1

1.1 Introduction 1
1.2 Anatomy of the ACL 1
1.3 Knee Kinematics 5
1.4 Function & Biomechanics 9
1.5 Mechanical Properties 12
1.6 ACL Injury 18
1.7 ACL Reconstruction 19
1.8 Conclusions 26
1.9 Project Aims & Summary 26

Chapter 2: Design Criteria 29

2.1 Introduction 30
2.2 Material Requirements 30
2.3 Design Requirements 35
2.4 Size Constraints 36
2.4.1 Introduction 36
2.4.2 Methodology 38
2.4.3 Results 42
2.4.4 Discussion 45
2.5 Design Options 47
2.5.1 Overall Structure 47
2.5.2 Material Selection 49
2.5.3 Design Selection 55
2.6 Artificial ACLR 62
2.7 Artificial ACLR-TKR 62
2.8 Conclusion 63

Chapter 3: Connecting Cord 65

3.1 Introduction 66
3.2 Mechanical Tests 66
3.2.1 Methodology 66

3.2.2 Results 72
3.3 Finite Element Hardening Models 81
3.3.1 Methodology 81
3.3.2 Results 89
3.4 Discussion 92
3.5 Conclusion 97
Chapter 4: Spring System 98
4.1 Introduction 99
4.2 Methodology 100
4.2.1 Helical Spring 100
4.2.2 Spiral Spring 104
4.2.3 Parametric & Probabilistic 108
4.2.4 Statistical Analysis 114
4.3 Results 115
4.3.1 Mechanical Test 115
4.3.2 Parametric & Probabilistic 121
4.4 Discussion 126
4.5 Optimised Spring Designs 130
4.6 Conclusions 133
Chapter 5: ACL Attachments 134
5.1 Introduction 135
5.2 Conventional Arthroscopic Methods 135
5.2.1 Femoral Attachment 135
5.2.2 Tibial Attachment 139
5.3 Reconstructed ACL 140
5.3.1 Methodology 141
5.3.2 Results 149
5.4 Discussion 156
5.5 Conclusion 161
Chapter 6: FE Modelling of the Artificial ACL 162
6.1 Introduction 163

6.2 Methodology 164
6.2.1 Component Positioning 165
6.2.2 Properties 167
6.2.3 Interactions 168
6.2.4 Boundary Conditions 169
6.3 Results 172
6.3.1 Axial Loading 172
6.3.2 Squatting 175
6.3.3 Lachman Test 180
6.4 Discussion 181
6.4.1 Axial Loading 181
6.4.2 Squatting 182
6.4.3 Lachman Test 184
6.5 Conclusion 186
Chapter 7: Conclusions & Future Work 187
7.1 Conclusions 188
7.2 Future work 192
7.2.1 Design Modification 192
7.2.2 Knee Model 194
7.2.3 Mechanical Tests 195
7.2.4 Kinematic Study 195
Bibliography 196
Appendices 220

List of Figures

Figure 1.1: Schematic diagram of the knee showing the four main ligaments. Adapted from Tandeter and Shvartzman, 1999 [9]. 2

Figure 1.2: Microstructure of tendons and ligaments. Adapted from Kastelic *et al.*, 1978 [14]. 3

Figure 1.3: The sagittal view of the lateral femoral condyle illustrating; (a) the AMB and PLB parallel in extension, (b) the AM and PL bundles are twisted and bent at 90 degrees of flexion. Adapted from Kopf *et al.,* 2009 [18]. 4

Figure 1.4: Mean length change of the ACL fibres during passive flexion. Adapted from Robinson *et al.*, 2009 [19]. Ant = anterior, Cent = central, Post = posterior. 4

Figure 1.5: The patella tendon angle (α) subtended by the long axis of the tibia and the line of the patella tendon at (a) full extension and (b) 90 ° of flexion. 7

Figure 1.6: Patellar tendon angle versus flexion angle during active extension against gravity for normal knees, Oxford UKR after 1 and 10 years, and knees with TKR. Adapted from Price *et al.*, 2004 [39]. Standard deviation bars were removed for clarity. 8

Figure 1.7: ACL force versus quadriceps force at different flexion angles calculated using a mathematical model which assumes incompressible cartilage. Adapted from Huss *et al.*, 2000 [67]. 10

Figure 1.8: Schematic diagram of the sagittal tibiofemoral and patellofemoral joints at (a) 0 °, (b) 70 ° and (c) 140 ° of flexion. Two red lines represent the cruciate ligaments (A = ACL, P = PCL) and the dashed lines represent the tendons (Q = Quadriceps, PT = Patella Tendon, G = Gastrocnemius, H = Hamstring). The instantaneous centre of the model (I) moves relative to each bone and the tibiofemoral contact point (C) moves posteriorly during flexion. Adapted from Collins and O'Connor, 1991 [25]. 11

Figure 1.9: Typical load-elongation curve of the FATC from a young donor tested along the anatomical axis of the ACL. Adapted from Woo *et al.,* 1991 [80]. 13

Figure 1.10: ACL force during level walking. The gait cycle includes heel strike (HS), contralateral toe-off (CTO), contralateral heel strike (CHS), and toe-off (TO). Adapted from Shelburne *et al.*, 2004 [89]. 15

Figure 1.11: (a) *In vivo* weight-bearing elongation of the ACL and (b) *In vitro* force-elongation of the ACL at different flexion angles. Adapted from Hosseini *et al*., 2011 [88]. 16
Figure 2.1: Different femoral and tibial tunnel insertion sites for a single bundle ACL graft (a) high AM-PL, (b) AM-AM, and (c) centre-centre methods. Adapted from Tsukada *et al*., 2008 [149]. 37
Figure 2.2: Femoral tunnel angle in (a) the coronal plane and (b) the sagittal plane (inclination angle) while the knee is at full extension. Adapted from Illingworth *et al*., 2011 [148]. 38
Figure 2.3: Segmented MRI images of a human knee using Mimics software. 39
Figure 2.4: The length of the femoral tunnel on a 3D model of the knee. 40
Figure 2.5: Location of the centre of the AMB footprint relative to the most medial and the most posterior part of the tibial plateau. Black and blue circles represent the footprints of the AMB and PLB, respectively. 41
Figure 2.6: The attachment height (H) of the isometric ACL fibre relative to the transverse plane pasing through the centre of the medial tibial plateau. 41
Figure 2.7: The thickness of the tibial cortical bone at 28 mm and 48 mm below the lateral tibial plateau measured from a segmented tibial model. 42
Figure 2.8: Size constraints for an ACLR device in a medium size (71 mm) Vanguard primary tibial tray. 44
Figure 2.9: One of the early design concepts proposed for the artificial ACLR system consisting of a spring system and a cord-Patent GB2454251. 49
Figure 2.10: Strength based on the weight versus strength based on the volume of different fibres. Adapted from van Dingenen, 2001[169]. 51
Figure 2.11: Stress-strain curves of a number of high performance fibres. Adapted from van Dingenen., 2001 [169]. 52
Figure 2.12: Scanning Electron Microscopy (SEM) pictures of (a) 442 dtex Dyneema yarn made of multiple fibres, and (b) a fibre made of a number of filaments. Pictures were taken in John Radcliffe hospital (Oxford, UK) by Prof. David Ferguson in July 2013. 56
Figure 2.13: Structure of the braided Dyneema loop (42240 dtex). Each strand of the loop had a diameter of approximately 2 mm. 57

Figure 2.14: Available space for the tibial elastic system between medial and lateral tibial compartments. 63

Figure 3.1: Grips used for the tensile testing of the Dyneema samples (a) Instron CP103684 used to test the Dyneema yarns, (b) Sternum pins (diameter = 11mm) used to test the braided loops. 69

Figure 3.2: (a) Electromechanical test machine used to test the UHMWPE loop. (b) Fatigue test set up in a tank filled with saline, 2 pins were used to hold the loop sample and a heater was used to heat the saline up to 32 ° C ± 2 ° C. 71

Figure 3.3: Comparison of the mean and standard deviation (SD) of the UTS and strain of Dyneema yarns tested under four different test conditions (** $p < 0.01$). 73

Figure 3.4: Nominal stress-strain graph of five Dyneema yarns (442 dtex) tested under simulated body conditions. The solid line and the shaded area represent mean value and the standard deviation. 74

Figure 3.5: Mean and standard deviation of the UTS and the ultimate strain of the Dyneema loops tested at four different test conditions. (** $p < 0.01$), (*** $p < 0.001$). 75

Figure 3.6: Nominal stress-strain graph of braided loops (30480 dtex) tested under simulated body conditions. The solid line represents the mean values and the shaded area represents the standard deviation. 75

Figure 3.7: 40 mm Dyneema loops tested to failure under tensile load. Failure of the fibre occurred mainly at the spliced region of the loop. 76

Figure 3.8: Stress-strain curves of three groups of loop specimens tested at 150, 300 and 900 mm min^{-1} displacement rates. The solid lines represent the mean values and the shaded area represents the standard deviation. 77

Figure 3.9: Mean and standard deviation of (a) the UTS and (b) the stiffness of the Dyneema loops tested at 3 different strain rates. (* $p < 0.05$) and (** $p < 0.01$). 78

Figure 3.10: True stress-strain curve corresponding to the selected loading cycles of the fatigue tested Dyneema loop. 79

Figure 3.11: Hysteresis curves of the Dyneema loop subjected to a cyclic fatigue test. Sample exhibits plastic shake-down after 1 million (M) cycles. 79

Figure 3.12: Change in elastic modulus of the Dyneema loop with increasing loading cycles. . 80
Figure 3.13: Change in the stiffness of the UHMWPE loop with increasing number of loading cycles. 80
Figure 3.14: Change in creep modulus of the UHMWPE loop with increasing loading cycles. . 81
Figure 3.15: Amplitude of one loading cycle used in the FE hardening models of the Dyneema loop. 83
Figure 3.16: Schematic diagram of different hardening models. (a) Isotropic hardening: uniform expansion of the initial yield surface (black ellipse) with plastic strain. (b) Kinematic hardening: translation of the yield surface with plastic strain. (c) Non-linear isotropic-kinematic (combined) hardening: expansion and translation of yield surface with plastic strain. Adapted from Broggiato *et al.*, 2008 [191]. 84
Figure 3.17: Simulation of the fatigue test set up with a 3D loop and two pins, the left pin was fully constrained and the right pin was axially loaded 88
Figure 3.18: Comparison of the isotropic hardening model results and experimental data from Section 3.2.1.3 for the first 3 loading cycles. 89
Figure 3.19: Comparison of the linear kinematic hardening model results with experimental data from Section 3.2.1.3 for the first 3 loading cycles. 90
Figure 3.20: Comparison of the non-linear isotropic/kinematic (NLIK) hardening model results with the experimental data from Section 3.2.1.3 for the first 10 cycles. 91
Figure 3.21: Comparison of the non-linear isotropic/kinematic hardening (NLIK) model prediction of the Dyneema loop model with experimental data from Section 3.2.1.3 for the first five loading cycles. 92
Figure 4.1: Design options for (a) stand-alone ACLR and (b) ACLR for TKR. 99
Figure 4.2: Compression testing of a metal helical spring between test fixtures. 'F' represents the direction of compressive force applied on the spring. 101
Figure 4.3: Mesh convergence study on the helical compression spring. 103
Figure 4.4: Location of the spiral spring in the tibial tray used for TKR. 104

Figure 4.5: (a) Schematic diagram of the torsional test rig, (b) and (C) Torsional test rig used to test the spiral springs. A= Rotational disc, B = Spring fixture, C = Spiral spring, D = Rigid block, E = Metal cord. 106

Figure 4.6: Mesh convergence study on the spiral spring. 107

Figure 4.7: (a), (b) Side and front views of the spiral spring models tested under different loading conditions; tangential load was applied to the spring's head and the centre of the spring was fully constrained, c) rotational displacement applied to the centre of the spring and the movement of the head was restricted by a rigid bar. 108

Figure 4.8: (a) Schematic diagram of a helical compression spring with (b) a rectangular wire. '*b*' is the width and '*t*' is the thickness of the wire ($b > t$). 109

Figure 4.9: Examples of the helical compression spring models used in the parametric study. Model 1 is the control model, model 5 had an increased number of loops, model 9 had an increased thickness of wire, model 13 had an increased height of wire, and model 17 had an increased pitch angle compared to the control model. 110

Figure 4.10: (a) Schematic diagram of a flat spiral spring and (b) its cross section; '*b*' is the width and '*t*' is the thickness of the rectangular wire ($b > t$). 112

Figure 4.11: Some of the spiral models with different geometrical dimensions used for the parametric study. 113

Figure 4.12: Linear load - displacement results of the mechanically tested helical springs. .. 115

Figure 4.13: von Mises stress (MPa) in spring 'F' (Table 4.7) under 60 N compressive load. Mesh size 0.7 mm was used. 116

Figure 4.14: Schematic diagram of the torsional test set up showing the actuator force (F_A), spring load (F_s), distance between the metal cord and the centre of the torsional disc (r_A), and the distance between the spring's head and the centre of the disc (r_s). 117

Figure 4.15: Load-elongation results of the spiral springs tested under simulated axial (tangential) load. 118

Figure 4.16: Comparison of the mechanical results of the spiral spring with 1.7 mm thickness to those found from the FEA simulated torsional test. 119

Figure 4.17: Comparison of the mechanical test results of the spiral spring with a thickness of 2.2 mm with those found from the simulated torsional test in FE. 119
Figure 4.18: Deformed and failed spiral springs after the torsional test. 120
Figure 4.19: von Mises stress (MPa) in spiral spring (1.7 mm) (a) axial loading of 500 N and (b) simulated torsional test, where the centre was rotated by 2 radians. 120
Figure 4.20: Graphical representation of the effect of different geometrical factors on the stiffness of the helical springs. 121
Figure 4.21: von Mises stress (MPa) distribution in the control spiral spring model (Model 1) with 1 and 1.5 loops under 80 N load. 123
Figure 4.22: Graphical representation of the effect of different geometrical factors on the stiffness of the spiral springs. 124
Figure 4.23: Results of the probabilistic analysis investigating the effect of varying of thickness (2 mm), initial radius (6 mm) and width (4 mm) of the spiral springs within the manufacturing tolerance of ± 0.1 mm on the spring's stiffness. Red lines show the median stiffness. 126
Figure 4.24: Schematic diagram of the multilinear stiffness values required to reproduce the non-linear stiffness of the native ACL [88] with an artificial ACL consisting of a femoral spring (F), tibial spring (T) and cord (C). 131
Figure 4.25: Dimensions of the final designs of the (a) femoral helical spring (61 N mm^{-1}) and (b) tibial helical spring (102 N mm^{-1}) for ACLR device. (c) Tibial spiral spring for ACLR-TKR. 132
Figure 5.1: Schematic illustration of the o'clock method. AMB is inserted at 11:00 and PLB is inserted at 9:30 o'clock. Adapted from Giron *et al.*, 2006 [213]. 136
Figure 5.2: (a) Schematic illustration of the Takahashi method: The location of the centres of the AMB and PLB are expressed as their distances to the deep border of the articular surface. (b) Mochizuki method: Distances between the centre of the AMB and PLB to the deep and shallow borders of the articular surface are measured. Adapted from Tsukada *et al.*, 2008 [149]. 137

Figure 5.3: (a) Schematic diagram of the Watanabe's method: The centres of AM and PL bundles are found relative to the position of the reference points O, A, and I. (b) Quadrant method: 't' is the sagittal diameter of the femoral condyle along Blumensaat's line, and 'h' is the height of the intercondylar notch. Adapted from Tsukada *et al.*, 2008 [149] and Colombet et al., 2006; [218].....138

Figure 5.4: Locations of the centers of the AMB and PLB on the tibial plateau relative to the anterior and medial edges. Adapted from Tsukada *et al.*, 2008 [149]. 140

Figure 5.5: One of the MRI scans used in the current study showing a sagittal view of the knee. (a) 'd' is the distance between FFC (flexion facet centre) of the femoral condyle and the most posterior point of the tibial cortex. (b) Locations of the isometric ACL fibre attachment points on the femur (most proximal and anterior) and tibia (most anterior). 142

Figure 5.6: Antero-posterior (AP) translation of the centres of the medial and lateral femoral condyles during passive tibio-femoral knee motion found from the open MRI study. Adapted from Johal *et al.*, 2005 [225]. 142

Figure 5.7: Antero-posterior (AP) translation of the centres of the medial and lateral femoral condyles during weight bearing tibio-femoral knee motion found from the open MRI study. Adapted from Johal *et al.*, 2005 [225]. 143

Figure 5.8: Schematic illustation of the measured twist angle (θ) of the long axis of the ACL connecting the femoral attachment centre (F) to the tibial attachment centre (T). Adapted from Zavatsky and O'Connor., 1994 [136]. 145

Figure 5.9: Femoral attachment points considered in this study. F0 is isometric fibre attachment point, F1, F2, F3 and F4 are located 5 mm anterior, posterior, superior and inferior to the F0, respectively. 147

Figure 5.10: Tibial attachment points considered in this study. T0 is the isometric fibre attachment. T1, T2, T3, and T4 are located 5 mm anterior, posterior, medial and lateral to the T0, respectively. 147

Figure 5.11: Mean strain in the reconstructed ACL predicted by the knee model for eighteen knee geometries during passive flexion and squatting. Error bars represent the standard deviation. 150

Figure 5.12: Mean load in the reconstructed ACL predicted by the knee model for eighteen knee geometries during passive flexion and squating. Error bars represent the standard deviation. 150
Figure 5.13: Mean and standard deviation of the reconstructed ACL twist angle predicted by the knee model for eighteen knee geometries during passive flexion and squatting. 151
Figure 5.14: Effect of different femoral placements on the load of the reconstructed ACL during passive knee flexion. Positive and negative values imply the ACL is loaded or slack, respectively. 152
Figure 5.15: Effect of different femoral placements on the strain of the reconstructed ACL during passive knee flexion. Positive and negative values imply the ACL is loaded or slack, respectively. 152
Figure 5.16: Effect of different femoral placements on the twist angle of the reconstructed ACL during passive knee flexion. 153
Figure 5.17: Effect of different femoral placements on the load of the reconstructed ACL during squatting. Positive and negative values imply the ACL is loaded or slack, respectively. 155
Figure 5.18: Effect of different femoral placements on the strain of the reconstructed ACL during squatting. Positive and negative values imply the ACL is loaded or slack, respectively. 155
Figure 5.19: Effect of different femoral placements on the twist angle of the reconstructed ACL during squatting. 156
Figure 5.20: The ACL twist angle at different knee flexion angles (KFA) found in the current MRI study compared to a study by Jordan *et al.* [135]. 159
Figure 6.1: Illustration of the component positioning for (a) the artificial ACLR and (b) the ACLR-TKR models used in the axial loading study. 166
Figure 6.2: Illustration of the component positioning for (a) the artificial ACLR and (b) the ACLR-TKR models used in the FE simulations of squatting and the Lachman test. 167
Figure 6.3: von Mises stress (MPa) in the artificial ACLR system after 5 mm axial deformation. 172

Figure 6.4: Comparision of the load-elongation results of the artificial ACLR device made of the two helical springs to those of the native ACL [88]. 173
Figure 6.5: von Mises stress (MPa) within the artificial ACLR-TKR device after 5 mm axial defomation. 174
Figure 6.6: Comparision of the load-elongation results of the artificial ACLR-TKR device made of a helical and a spiral spring to the mechanical beaviour of the native ACL [88]. 174
Figure 6.7: Deformation of the stand-alone ACLR device including the helical femoral and tibial springs and Dyneema cord during squatting. 175
Figure 6.8: Load in the artificial ACLR device during squatting. 176
Figure 6.9: Maximum stress of 1625 MPa in the artificial ACLR device during squatting occurred in the cord where it was articulating with the tibial head. 176
Figure 6.10: Stress (MPa) in the artificial ACLR device at 120 º of KFA when the knee is squatting from 0 º to 120 º of KFA. 177
Figure 6.11: Deformation of the femoral helical spring, tibial spiral spring and Dyneema cord during squatting. 178
Figure 6.12: Load in the ACLR-TKR device during squatting. 178
Figure 6.13: Stress (MPa) in the artificial ACLR-TKR device during squatting from 0 º to 120 º of flexion. 179
Figure 6.14: Illustration of maximum stress (MPa) in (a) the spiral spring at 20 º of KFA and (b) in the Dyneema cord at 120 º of KFA. 179
Figure 6.15: Load in the artificial ACLR and ACLR-TKR devices during the Lachman test. 180
Figure 6.16: Results of the simulated Lachman test on the artificial ACLR devices compared to the result of the same test on the native ACL in cadaver knees (n=20) [233]. Dashed lines indicate the range of normal laxity. 185
Figure 7.1: A potential stop mechanism design for the helical compression spring. 193
Figure 7.2: (a) The artificial ACLR device comprised of femoral and tibial helical springs and (b) ACLR-TKR device comprised of a helical femoral spring and a tibial spiral spring. The TKR components and the spring containers are removed for clarity. 194

Figure A.0.1: Schematic diagram of an open coil helical spring, '*M*' is the bending moment and '*T*' is the twisting moment [204]. 220

Figure A.2: (a) Schematic diagram of a flat spiral spring and (b) its cross section. Where 'b' = width of the rectangular wire (b > t), 't' = thickness of wire, 'h'=gap between coils, and 'δ'=h+t. 222

Figure A.3: Schematic diagram of the KT-1000 arthrometer positioned on a human knee. ... 225

Figure A.4: Results of the anterior tibial draw test on a cadaver knee specimen after different ACL treatments perfomed at 30 °, 60 ° and 90 °. 226

Figure A.5: Significant difference in the measured anterior tibial translation at 30 ° of flexion for the different ACL treatments compared to the healthy control group. 226

List of Tables

Table 1.1: Some of the *in vivo* and *in vitro* techniques used to measure the ACL load. BW = Body weight. 17

Table 1.2: Some of the popular synthetic ACL grafts and details of their design, mechanical properties, advantages and disadvantages. 24

Table 2.1: Desired mechanical characteristics of the artificial ACLR system. 33

Table 2.2: Dimensions of the available space in different sizes of Vanguard tibial tray for an ACLR device. 44

Table 2.3: The average AP and ML dimensions of 18 tibial models at 8 mm, 28 mm and 48 mm below the centre of the lateral tibial plateau. SD = standard deviation. 45

Table 2.4: The mechanical and physical properties of Dyneema fibres [169]. 53

Table 2.5: Mechanical properties of some common alloys used in surgical implants 55

Table 2.6: Considered spring options for the elastic system of the artificial ACL (ideas from a brainstorm with the Strategic Simulation and Analysis (SSA) consultation team). 59

Table 3.1: Mechanical properties of Dyneema yarns tested under four different environmental conditions. SD = standard deviation. 74

Table 3.2: Mechanical properties of Dyneema loops tested under four different environmental conditions. SD = standard deviation. 76

Table 3.3: Mechanical test results for Dyneema loops loaded at different displacement rates. 77

Table 3.4: Mechanical properties of the Dyneema loop sample subjected to cyclic fatigue test. 81

Table 3.5: Yield stress and plastic strain of the first half cycle of the fatigue tested Dyneema loop (Section 3.2.2.3) was inputted into the FE isotropic hardening model. 85

Table 3.6: Material parameters used in the linear kinematic model 86

Table 3.7: Material parameters used in the cyclic hardening section of the non-linear isotropic/kinematic hardening model 87

Table 4.1: List of the helical compression springs tested, with their dimensions: inner diameter (ID), outer diameter (OD), and length. 102

Table 4.2: Material properties of Co-Cr-Mo alloy used in the FE models of the helical springs 103

Table 4.3: Dimensions of the spiral spring prototypes designed for the artificial ACL (see Figure 4.10). 105

Table 4.4: Helical spring models with variable dimensional parameters within the size constraints of artificial ACL were used in the parametric study. 111

Table 4.5: Length, inner diameter (ID) and outer diameter (OD) of some of the designed helical springs for the artificial ACL within the defined size constraints. 111

Table 4.6: List of the designed spiral models for the parametric study. Each model was made in 1 and 1.5 loops. 113

Table 4.7: Comparison of the FEA and mechanical test results on the helical compression springs. 116

Table 4.8: Results of the FEA and mechanical test on spiral springs. 118

Table 4.9: The helical spring stiffness reported by the spring manufacturer compared to that obtained from the FEA. 122

Table 4.10: Results of the FEA of the spiral models with different dimensions. 125

Table 4.11: Stiffness of the simple and advanced designs of spiral spring obtained from parametric calculation and FEA using axial and torsional loads. 125

Table 4.12: Results of the FEA on final designs of femoral and tibial springs. 133

Table 5.1: The coordinates of the femoral and tibial attachment points. 148

Table 5.2: The significance of the femoral and tibial placement on the load, strain, and twist angle of the reconstructed ACL during passive motion. *: $p<0.05$, ** $p<0.01$, ***$p<0.001$ 153

Table 5.3: The significance of the femoral and tibial placement on the load, strain, and twist angle of the reconstructed ACL during squatting. *: $p<0.05$, ** $p<0.01$, ***$p<0.001$ 156

Table 6.1: Coordinates of the isometric ACL femoral and tibial attachment points of a 3D knee model used to position the springs in the FE models. 166

Table 6.2: Material properties of the Dyneema cord used in the FEA model. 'E' represents the elastic modulus in MPa, 'v' the Poisson's ratio and 'G' the shear modulus in MPa, in the x (1), y (2), and z (3) directions. 168

Table 6.3: Translations (in mm) and rotations (in radians) of the femoral attachment point relative to the fixed tibial attachment point during squatting. 170

Table 6.4: Translations (in mm) and rotations (in radians) of the femur relative to the tibia used to simulate the Lachman test at 20 º of flexion. 171

Table A.1: Results of the anterior tibial draw test on a cadaveric specimen using the KT-1000 knee arthrometer. 226

Table A.2: Combinations of different tunnel placements on the femur and tibia. 227

Table A.3: The overall change in the load, strain, extension and twist angle of the reconstructed ACL with variable ACL placements during passive flexion. 228

Chapter 1: Introduction

1.1 Introduction

This thesis begins by presenting a review of the anatomy, function and biomechanics of the native ACL within the human knee joint. The importance of reconstructing the ACL is highlighted, and the problems associated with ACL injury and different reconstruction techniques to treat an injured ACL are discussed. Finally the main goals of the project are defined.

1.2 Anatomy of the ACL

A ligament is a band of fibrous connective tissue that connects one bone to another [1]. Ligaments and tendons have similar tissue structures; both consist of fibroblasts surrounded by collagen fibrils and proteoglycans. Tendon attaches muscle to bone and transfers muscle force to generate or resist skeletal movements, whereas, a ligament connects bone to bone and limits and guides the movements of the bones relative to each other [1,2]. The knee joint is stabilised by four main ligaments: the Medial Collateral Ligament (MCL), the Lateral Collateral Ligament (LCL), the Anterior Cruciate Ligament (ACL) and the Posterior Cruciate Ligament (PCL) (Figure 1.1) [3]. The ACL originates from the medial aspect of the lateral femoral condyle and runs an oblique path through the intercondylar fossa distal and anteromedial to its insertion on the medial tibial eminence [4,5]. The ACL is enveloped by a fold of the synovial membrane; therefore, it is considered intra-articular as well as extra-synovial [2,6]. The ACL has a poor intrinsic healing ability, and this is attributed to the

low number of the fibroblasts and their low level of mitotic activity, in addition to the lack of blood vessels within and around the ACL [2,7,8].

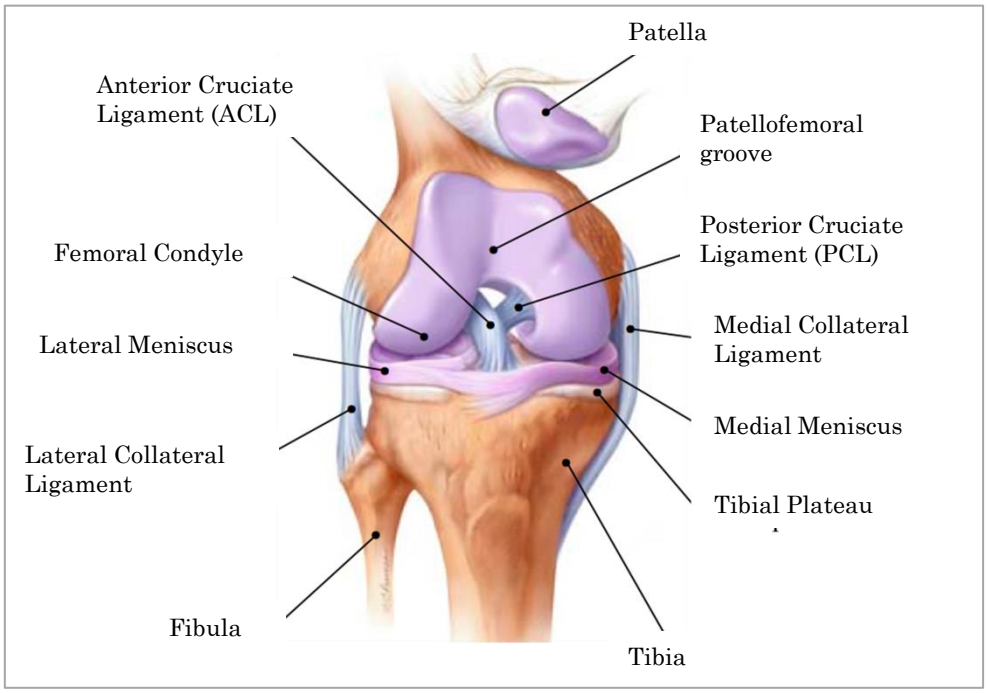


Figure 1.1: Schematic diagram of the knee showing the four main ligaments. Adapted from Tandeter and Shvartzman, 1999 [9].

The extra cellular matrix of the ligaments consists of fibroblasts, fibrils, fibril bundles and fascicles arranged parallel to the axis of the tissue and in the direction of the anatomical forces (Figure 1.2) [10]**.** About 70 % of a ligament's total weight is composed of water. Type I collagen is the major constituent of the ACL's dry weight and is primarily responsible for the ligament's tensile strength [1].

The average mediolateral width of the ACL varies between 7 - 12 mm with a mean value of 10 mm [1]. The average intra-articular length of the ACL is 32 mm, varying between 22 - 41 mm [1,11,12]. The ACL fans out towards its bony insertion sites on the femur and tibia; therefore, its narrowest diameter is

located at its centre with an average area of 36 mm^2 in females and 49 mm^2 in males [13].

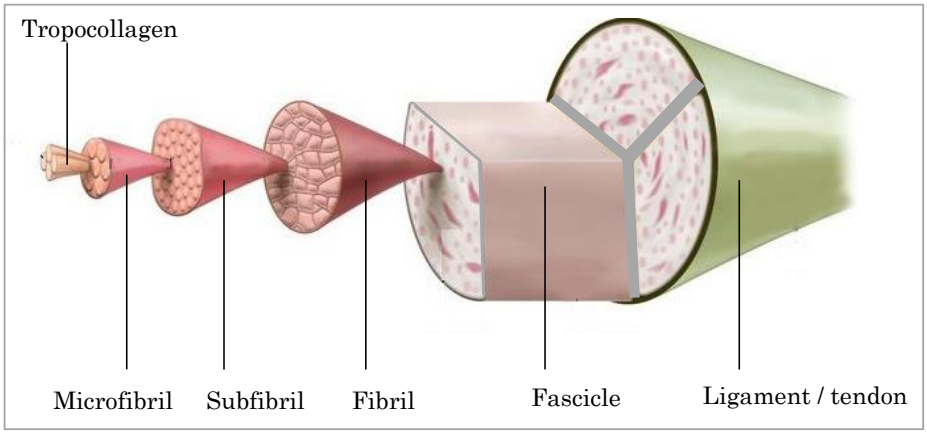


Figure 1.2: Microstructure of tendons and ligaments. Adapted from Kastelic *et al.*, 1978 [14].

It is claimed that the ACL can be distinguished into two functional bundles named according to their tibial insertion sites; the antero-medial bundle (AMB) and the postero-lateral bundle (PLB) (Figure 1.3) [12,15]. Due to the orientation of the ACL attachments on the femur relative to the tibia, the fibres of the ACL are parallel in full extension, however, as the knee flexes, they bend and twist around each other and display different tension-elongation patterns [6,16–18].

The most anterior fibre of the ACL remains more or less isometric during the range of passive flexion, whereas the posterior fibre slacken as the knee flexes (Figure 1.4) [19–22]. Sagittal plane magnetic resonance imaging (MRI) studies have reported an average length and width of 36.9 ± 2.8 mm and 5.1 ± 0.7 mm for the AMB [23]. The length and width of the PLB had an average value of 20.5

± 2.4 mm and 4.4 ± 0.8 mm, respectively. In the coronal plane the AMB and PLB had average width of 4.2 ± 0.8 mm and 3.7 ± 0.8 mm correspondingly [23].

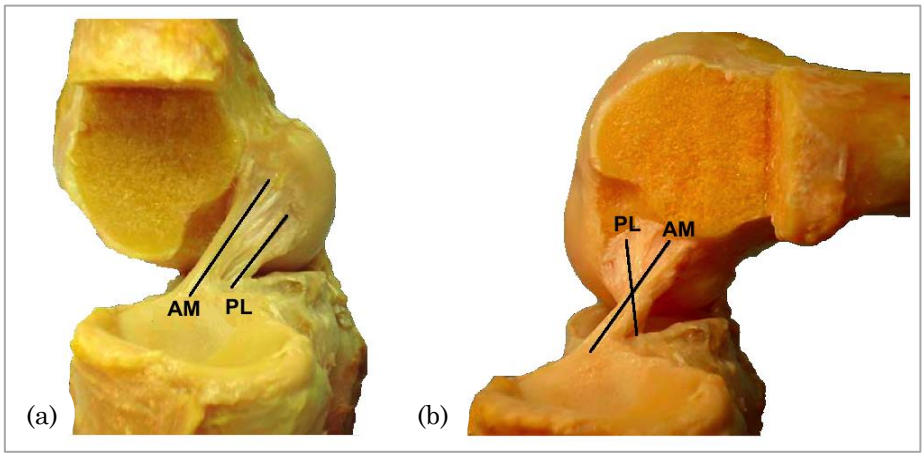


Figure 1.3: The sagittal view of the lateral femoral condyle illustrating; (a) the AMB and PLB parallel in extension, (b) the AM and PL bundles are twisted and bent at 90 degrees of flexion. Adapted from Kopf *et al.*, 2009 [18].

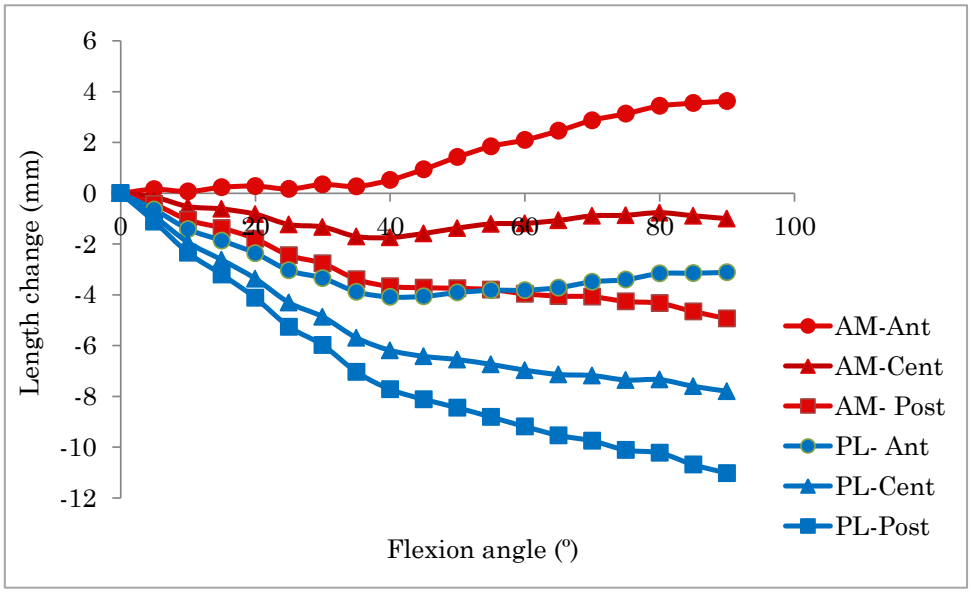


Figure 1.4: Mean length change of the ACL fibres during passive flexion. Adapted from Robinson *et al.*, 2009 [19]. Ant = anterior, Cent = central, Post = posterior.

1.3 Knee Kinematics

The kinematics of the knee are described by the motions of femur, tibia and patella relative to each other in two interdependent articulating joints; tibio-femoral and patello-femoral. The human knee joint has six degrees of freedom (6 DOF) including three rotations (internal-external rotation, abduction-adduction, and flexion-extension) and three translations (anterior-posterior, medial-lateral, and proximal-distal) which are mainly supressed by the knee ligaments. The knee's maximum range of motion occurs in the sagittal plane ranging from approximately -5 ^{o} of hyperextension to 150 ^{o} of flexion [24]. Femoral posterior translation occurs as a result of both rolling and sliding motions during knee flexion [25]; this phenomenon is believed to be beneficial in increasing flexion range by avoiding impingement between the posterior tibia and femur and also increasing the lever arm of the extensor mechanism to help extending the flexed knee [26]. The femur also translates slightly medial-lateral, relative to the tibia, as the knee flexes [27]. The tibia rotates externally relative to the femur during the terminal degrees of the knee extension; this motion is called the 'terminal screw home mechanism' and it is guided by the cruciate ligaments [28,29]. The lateral femoral condyle movement on the tibia is greater than the medial side, leading to rotation in the coronal plane and pivoting about the medial condyle. This phenomenon is referred to medial pivot movement. The cruciate and collateral ligaments ensure the controlled movement of the tibio-femoral joint.

Damage to the ACL can alter the knee mobility, stability, permit excessive laxity and abnormal kinematics of the knee [30–32]. Patients with chronic tears of the ACL have been observed to have a decreased flexion moment of the knee between 0 º and 40 º of flexion [33]. The flexion moment is balanced by the quadriceps muscles; therefore, a decreased flexion moment indicates a decreased quadriceps muscle moment. This reaction is called quadriceps-avoidance gait that has been observed in 75 % patients with a deficient ACL [34]. The quadriceps-avoidance gait is effective at preventing anterior tibial subluxation in low-level activities such as walking. In higher level activities such as running and jumping, increased contraction of the hamstring prevents excessive anterior tibial translation [33,34]. Therefore a modified gait could compensate for kinematic alterations associated with the ACL deficiency [30,34,35]. However, the change in rotational position may cause changes in tibio-femoral contact which could consequently lead to degenerative changes in the meniscus and the articular cartilage following ACL injury [36] .

The patella tendon angle (PTA) has been used as an indicator of knee kinematics particularly in the sagittal plane [37,38]. The PTA is the angle between the patella tendon and the long axis of the tibia (Figure 1.5). The sagittal knee kinematics can be described by the relationship between the PTA and the knee flexion angle (KFA) that depends on both the tibio-femoral and patello-femoral joints. The PTA and the KFA can be measured on sagittal fluoroscopic images. In the normal knee, the PTA is approximately 20 ° in the extended knee, however, as the knee flexes, the PTA diminishes in a linear

fashion and becomes zero at approximately 80° of flexion. The PTA decreases further to approximately -10 ° at 120 ° of flexion [39].

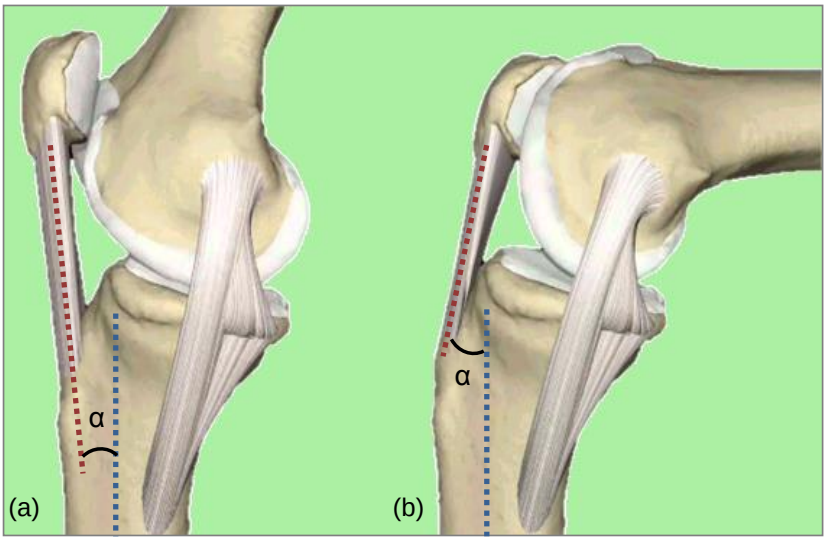


Figure 1.5: The patella tendon angle (α) subtended by the long axis of the tibia and the line of the patella tendon at (a) full extension and (b) 90 º of flexion.

The kinematics of ACL deficient arthritic knees treated with ACL reconstruction and medial Oxford Unicompartmental Knee Replacement (UKR) (Biomet Ltd, UK) has been reported to be similar to the kinematics of the normal knee (Figure 1.6) [38]. ACL deficiency is a contraindication for Oxford UKR as it is associated with high incidence of early tibial loosening [40]. Oxford UKR with an intact ACL has achieved good long-term clinical outcome and survival rates in excess of 90 % after 10 to 15 years [41,42].

In vitro and *in vivo* kinematic studies following total knee replacement (TKR) have revealed abnormal sagittal plane knee kinematics [37,43–46]. Although some of early designs of TKR systems allowed the retention of both cruciate ligaments, in the majority of conventional TKR systems either both cruciate ligaments are dissected or only the PCL is retained. Cloutier *et al.* [47] reported

good anteroposterior (AP) stability and 95 % survival rate after 10 years in 104 TKR cases with both cruciate ligaments retained. It has been argued that in patients who require a TKR, the ACL is commonly degenerated, non-functional, or that ACL retention complicates the operative procedure by preventing anterior subluxation of the tibia for surgical exposure and also a tibial component with a central stem cannot be used [47].

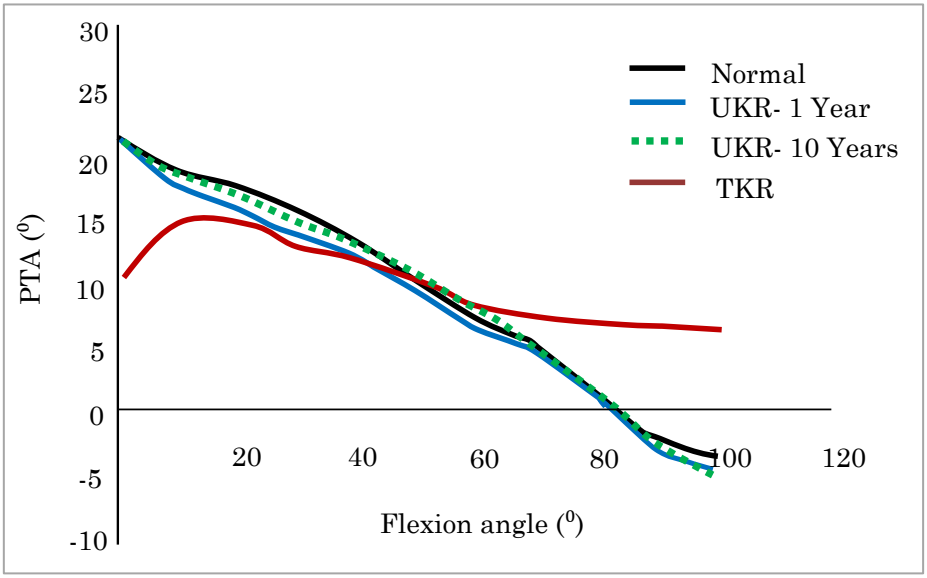


Figure 1.6: Patellar tendon angle versus flexion angle during active extension against gravity for normal knees, Oxford UKR after 1 and 10 years, and knees with TKR. Adapted from Price *et al.*, 2004 [39]. Standard deviation bars were removed for clarity.

Some TKR designs have been developed to attempt to resolve the instability of the joint in the absence of the cruciate ligaments. A cam-post mechanism is often used to provide posterior stability for PCL-deficient knees; however, studies have shown although cam-post mechanisms aid stability, they do not reproduce normal knee kinematics [46,48]. Despite substantial advances in primary TKR including the good long-term survival rate of TKR (over 95 % at 10 years [49]), a number of studies suggest that approximately 30 % patients are

dissatisfied due to pain [50,51] and functional impairment [52–54], which may be partially related to abnormal knee kinematics and mechanics.

It can be concluded that there is a need to preserve or reconstruct the ACL in TKR in order to restore the normal kinematics of the knee.

1.4 Function & Biomechanics

Knee ligaments have a number of distinct mechanical functions: they limit, control and guide the motions of the bones relative to one another; stretch and transmit tensile force to resist movements outside their defined limits; and work in partnership with muscles and articulating surfaces to transmit the loads across the joint [21].

The ACL has two complementary roles; the proprioceptive and the mechanical [55]. The proprioceptive role of the ACL is due to the existence of a small number of mechanoreceptors in the neurovascular system of the ligament that mainly react to stretch, inflammation, and pain [33,56] which enables awareness of joint movement and position [57]. As well as the sensory role of the ACL, proprioception is also thought to initiate reflex muscular contractions [33]. The ACL deficient (ACLD) knee has been associated with neuromuscular alterations such as a decrease in muscle reflexes, reduction in muscle stiffness, quadriceps force deficiencies and changes in gait [33,58].

Mechanically the ACL is primarily a passive restraining element to anterior tibial translation relative to the femur, but also acts as a restraining element to the internal/external and abduction/ adduction rotations [59–62]. The AMB of

the ACL has been shown to be more important in flexion and PLB contributes more to the stability in full extension [12]. The ACL also resists hyperextension and medial displacement of the tibia.

The ACL is anisotropic, and exhibits viscoelastic behaviour such as stress relaxation, hysteresis, and strain-rate dependence[7]. The parallel fibre structure of the ACL and the interaction between the collagen fibres, water and proteoglycans, is the reason for its viscoelasticity and anisotropy [17,63]. It has been shown that the ACL becomes stiffer at higher strain rates [63,64]. This enables the ACL to minimise the strain it experiences under impact loading, preventing damage to the ACL and other structures in and around the knee [65,66].

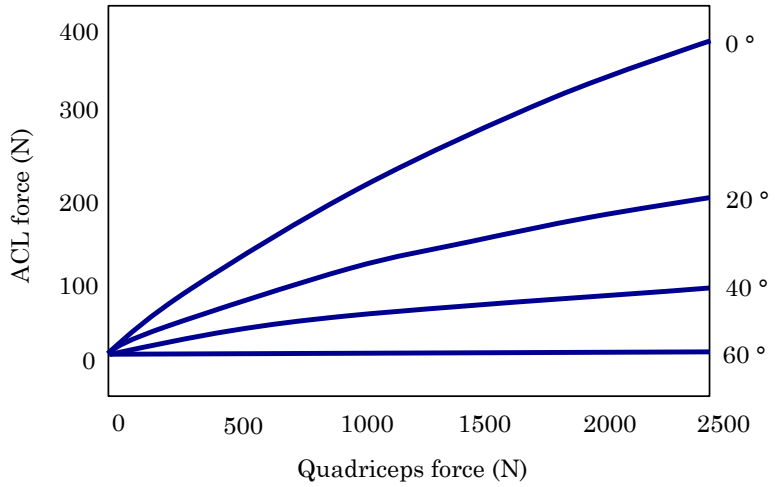


Figure 1.7: ACL force versus quadriceps force at different flexion angles calculated using a mathematical model which assumes incompressible cartilage. Adapted from Huss *et al.*, 2000 [67].

The load experienced by the ACL increases non-linearly with increasing quadriceps muscle force (Figure 1.7) [67–69]. This behaviour is the result of the

interaction between the quadriceps muscle force and patella tendon angle at different knee flexion angles (Figure 1.8).

As the patellar tendon becomes more vertical, the forward component of its force that loads the ACL is reduced. As a result, anterior fibres of the ACL become mainly responsible for resisting anterior tibial laxity at most knee flexion angles. Eventually, the hamstring tendon force pulls the tibia backwards relative to the femur at higher flexion angles and the PCL is loaded [70]. The relationship between the ACL, muscle force and PTA have been demonstrated using a number of 2-dimensional (2D) [25,69,71,72] and 3-dimensional (3D) knee models [20,73,74].

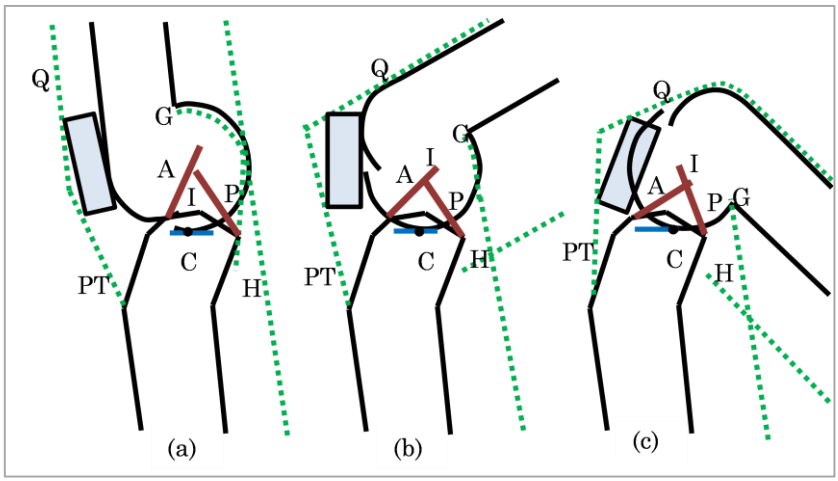


Figure 1.8: Schematic diagram of the sagittal tibiofemoral and patellofemoral joints at (a) 0 °, (b) 70 ° and (c) 140 ° of flexion. Two red lines represent the cruciate ligaments (A = ACL, P = PCL) and the dashed lines represent the tendons (Q = Quadriceps, PT = Patella Tendon, G = Gastrocnemius, H = Hamstring). The instantaneous centre of the model (I) moves relative to each bone and the tibiofemoral contact point (C) moves posteriorly during flexion. Adapted from Collins and O'Connor, 1991 [25].

The tensile behaviour of the ACL is highly dependent on the flexion angle of the knee. The ACL is maximally loaded from 0° to 30° of flexion under

quadriceps muscle contraction [35,75]. In an unloaded joint, most of the ACL fibres are just tight in full extension and the stiffness is highest; however, as the knee flexes the fibres slacken and the stiffness diminishes up to 90 º of flexion [67,76]. The interplay between decreasing ACL load and decreasing ACL stiffness results in maximal ligament elongation at about 15 º to 30 º of flexion [67,77,78]. The ACL stiffness increases with increasing load, this is because more fibres are recruited, and the effective cross-sectional area increases. The result is the non-linear relationship between ligament elongation and quadriceps muscle force [67,72].

1.5 Mechanical Properties

Ligaments transfer load from bone to bone along their longitudinal direction. Different studies have investigated the load-elongation characteristics of the dissected cadaveric Femur-ACL-Tibia-Complex (FATC) using uniaxial tensile loading [79–83]. Mechanical tests of the FATC demonstrate three different loading phases: 1) the toe region, 2) the linear region and 3) the yield or failure region [64,84]. The toe region is thought to be a result of straightening the crimp pattern in the collagen fibres; this occurs in the first 2-4 % of the strain [80]. In the linear region, the fibrils are elongated and the numbers of fibrils that become load bearing are increased [63]. Figure 1.9 demonstrates a typical load-elongation curve of the FATC in a young cadaver under tensile load. Woo *et al.* [80] reported that the structural properties of the human ACL deteriorate with increasing age.

The tensile strength of the ACL in younger patients was found to be 2-3 times greater than those for the middle, and older groups. The mean stiffness of the FATCs in young (22-35 years), middle (40-50) age and old patients (60-97) were found to be 242 ± 28 N mm^{-1}, 220 ± 24 N mm^{-1} and 180 ± 25 N mm^{-1}, respectively [80]. The stiffness of the ACL found from loading the FATCs along the ligament axis was higher than the *in vivo* stiffness of the ACL; this is because all of the fibres are recruited at once under axial load, whereas, *in vivo* the ratio of slack to strained fibres varies depending on the knee flexion angle and the muscle load.

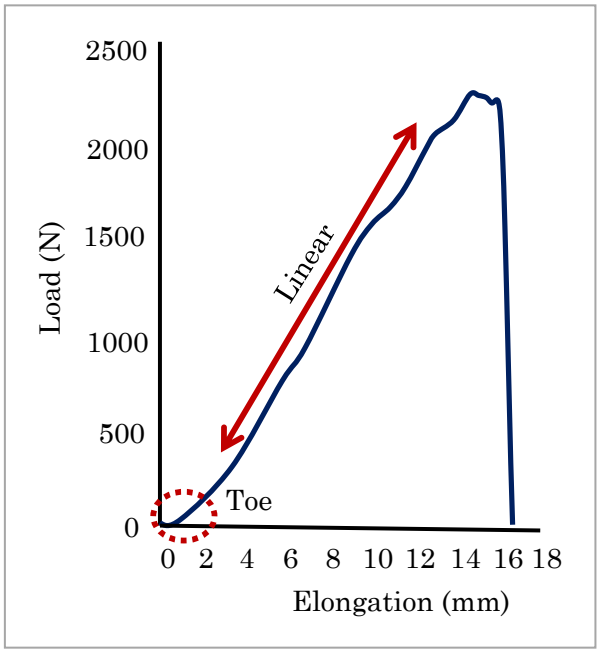


Figure 1.9: Typical load-elongation curve of the FATC from a young donor tested along the anatomical axis of the ACL. Adapted from Woo *et al.,* 1991 [80].

Different techniques have been used to find the mechanical properties of the ACL *in vivo*; these methods include both direct contact measurements and non-contact measurements. Table 1.1 summarises some of these methods and the limitations associated with each technique.

Contact methods involve connecting a force or strain measuring device, such as a buckle or implantable transducer, directly to the ligament or to the ligament insertion site. Results from direct contact studies indicate the force experienced by the ACL during a Lachman test is only slightly less than the force applied to the tibia [85,86] (Table 1.1). However, direct contact studies can only be performed with the patient unconscious, so do not account for muscle action.

Non-contact methods described in the literature include using gait analysis combined with mathematical modelling [87] and fluoroscopic videos analysed in conjunction with *in vitro* data [88]. Results from non-contact methods estimate the forces in the ACL range from 156 N to 303 N [88–91]; however, these studies examine different patient activities so are difficult to compare. A number of *in vitro* tests have been developed for more accurate quantification of the motion and loading in the knee joint. One of these methods was a mathematical model of the cruciate ligaments, the femur and the tibia in the sagittal plane called the 'four-bar linkage' model [21,68,92–94]. This model was based on the studies of the cadaveric specimens and 2D radiographs. Huss *et al.* [67] used a four-bar linkage model with extensible arrays of ligaments and deformable cartilage to simulate the ACL responses under isometric quadriceps contraction. The authors reported that the ACL force was maximum in full extension and zero at 60 º of flexion. The PCL was loaded at higher flexion angles. A peak ACL load of 360 N was calculated under a maximum quadriceps force of 2500 N in a model with incompressible cartilage. Shelburne *et al.* [89] used a musculoskeletal model of the lower limb to find the force on the ACL during

different phases of walking. A maximum ACL load of 303 N was calculated at the contralateral toe off point of the gait cycle (Figure 1.10) [95].

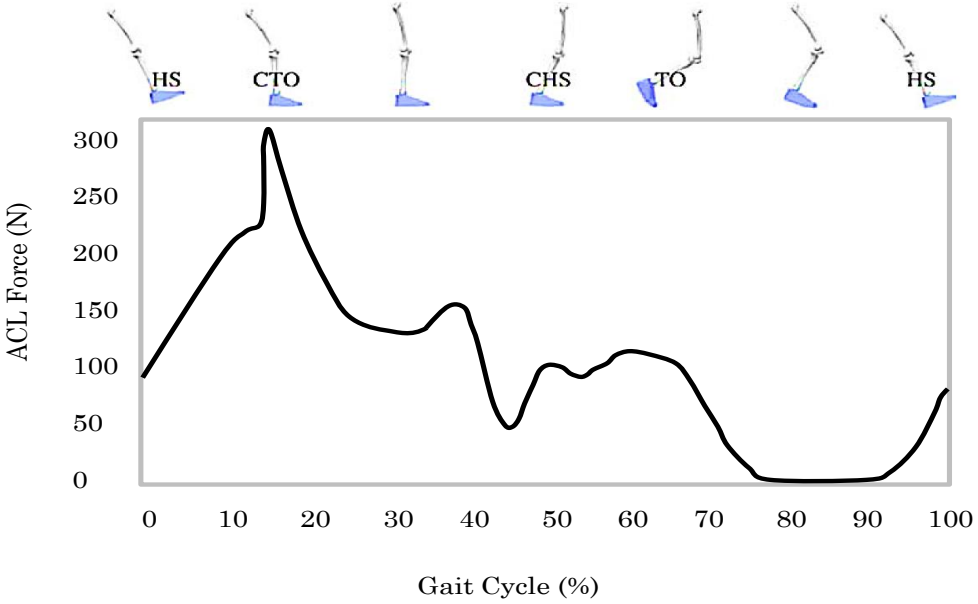


Figure 1.10: ACL force during level walking. The gait cycle includes heel strike (HS), contralateral toe-off (CTO), contralateral heel strike (CHS), and toe-off (TO). Adapted from Shelburne *et al.*, 2004 [89].

A robotic technique has been developed to estimate the force of the ACL in a non-invasive, non-contact manner reproducing the motion pattern of the knee joint[75,96–98]. This robotic system recorded the resulting motions of the ACL intact (ACLI) cadaveric knee in response to applied load and then reproduced precisely the same motions after the ACL was sacrificed. Hence force changes between a knee with an intact and deficient ACL were quantified [98]. Hosseini *et al.* [88] estimated *in vivo* ACL forces at different flexion angles using a non-contact method which combined *in vivo* video fluoroscopy and robotic test results from cadaveric knees. Results showed peak ACL force at a flexion angle of 15 °, but peak ACL elongation at 30 °, highlighting the influence of fibre recruitment (Figure 1.11).

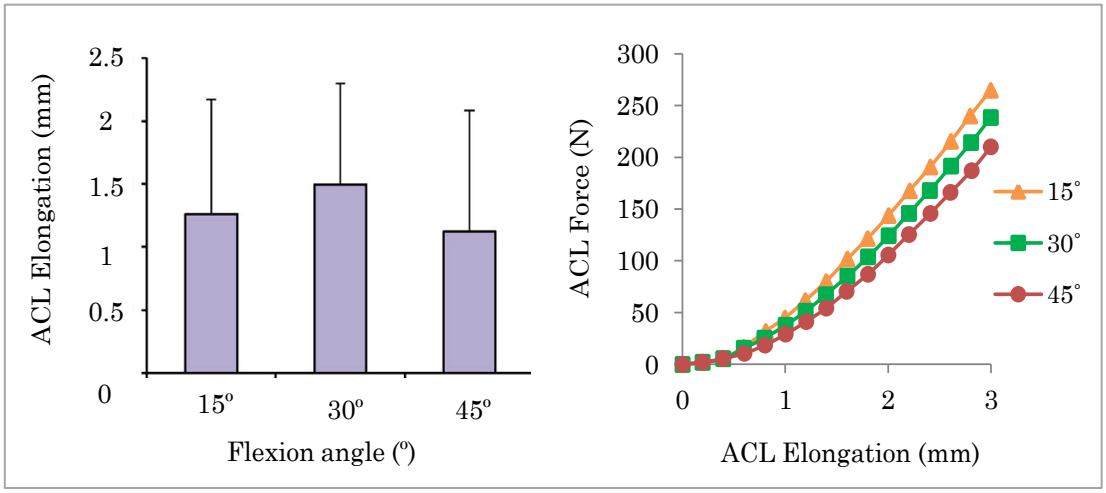


Figure 1.11: (a) *In vivo* weight-bearing elongation of the ACL and (b) *In vitro* force-elongation of the ACL at different flexion angles. Adapted from Hosseini *et al.*, 2011 [88].

Table 1.1: Some of the *in vivo* and *in vitro* techniques used to measure the ACL load. BW = Body weight.

Technique		Experimental Summary	Limitations	Max. ACL Load (N)	Flexion Angle	Ref.
In vivo tests Contact	Intra-operative	Using force or strain transducer (e.g. buckle or implantable devices)	• Invasive procedure • Can only test passive motion • Pre-shortening ligament fibres • Tissue impingement issues • Only tests local behavior of the tissue • Difficulties in calibration	307 N (under 356 N tibial force)	30 º	[85]
				140 N (under 150 N tibial force)	30 º	[86]
In vivo tests Non-Contact	Gait analysis	Data from gait analysis results during normal walking inputted into a musculoskeletal model of the lower limb	• Simplified internal mechanics by grouping synergistic muscles. • Assumption of equilibrium when calculating ligament loading. • The effect of velocity and internal forces were neglected.	156 N (level walking)	-	[90]
				303 N (early stance)	10 º	[89]
	Video Fluoroscopy with Cadaveric Test Results	Combined video fluoroscopy data with *in vitro* cadaveric test results to estimate the *in vivo* ACL elongation	• Difficulties in obtaining healthy young cadaver specimens • ACL elongation measured only at 3 flexion angles (15 º, 30 º and 45 º)	242 N (under full BW)	15 º	[88]
In vitro tests Non-Contact	2D mathematical model	Using 4 bar linkage model to simulate AP translation or isometric quadriceps contraction	• Simplified 2D model, omitted collateral ligaments and menisci. • Assumes the ACL was made of an isotropic, homogeneous material	396 N	0 º	[91]
				1.3-1.7 BW	-	[99]
				360 N (under 2500 N quadriceps force)	0 º	[67]
	Robotic Cadaveric Mechanical Test	Used a robotic manipulator combined with a force-moment sensor and a control system.	• Simple loading condition applied externally in cadaver knees. • Can only test passive motion	119 N (under 134 N tibial force)	15 º	[75,98,100]

1.6 ACL Injury

The ACL is the most injured ligament of the knee [66,101]. The incidence of ACL injury has been estimated to be 2 in 1000 in the normal population [102]. The risk of ACL injury in female athletes is 4 to 6 times higher than their male counterparts playing at the same sport level [103]. Injuries of the ACL can lead to instability, which may be associated with tears and degenerative changes to the surrounding tissues as well as increased laxity of other knee ligaments and unsatisfactory knee function [104,105].

ACL injuries can be classified into contact and non-contact injuries. A non-contact injury occurs in the absence of body contact (e.g. player to player), whereas the contact injury happens due to a direct blow to the knee. The majority of the non-contact ACL injuries happen during acceleration or deceleration motions with excessive quadriceps contraction and reduced hamstrings contraction at, or close, to extension combined with tibial rotation [106]. Around 70 % of ACL injuries are non-contacting and 30 % of injuries occur due to contact [106]. The mechanisms of ACL injury are commonly described as: internal rotation of the tibia relative to the femur (majority of injuries), abduction together with external rotation which is commonly seen in skiing, hyperextension, and flexion with posterior traction [17].

Some of the common symptoms in patients with an injured ACL are buckling, pain, swelling, giving-way, or twisting of the knee [101]. Some of the common examination methods used to assess the AP laxity in patients with injured

ACL are the Lachman test, the anterior drawer test and the pivot-shift test. The Lachman test is performed at approximately 20 º of the knee flexion and the tibia is translated anteriorly while femur is held fixed. The amount of anterior laxity of the tibia and the condition of the end point (e.g. firm, loose or spongy) are noted [28]. In the anterior drawer test, the knee is flexed to 90 º and the tibia is pulled anteriorly as the foot is in a neutral position [107]. The pivot-shift test is used to test anterolateral stability. The tibia is internally rotated and a valgus force is applied to the knee as the joint is flexed from full extension to 30 º of flexion. The KT1000 knee arthrometer (MED Metric, San Diego, CA) can also be used to quantify the anterior tibial translation on patients in supine position [108]. The calibrated device is secured against the tibia with two straps. The patella support is fixed with one hand and the anterior tibial load is applied with another hand by pulling the force sensor handle. Anterior tibial translation in millimeters can be read from the dial indicator.

1.7 ACL Reconstruction

Due to the poor intrinsic healing ability of the ACL, different surgical procedures have been developed to reconstruct a torn ACL in young active patients [7]. Reconstruction aims to restore the normal kinematics and stability to prevent future degenerative changes [1,18]. A surgical graft is used to replace a ruptured ACL and to restore the ACL function after injury. The torn ligament is removed from the knee and the graft is implanted arthroscopically.

The factors that can affect the outcome of ACL reconstruction are; patient selection, graft selection, operative procedure, graft positioning, graft fixation, treatment of related injuries and post-operative rehabilitation [109]. During ACL reconstruction, the surgeon attempts to attach the graft to the isometric attachment sites on the bones, which is a way to avoid excessive graft forces during movement of the knee. The isometric fibre attachments of the ACL are a couple of points where their distance between the femur and tibia remains constant during passive flexion-extension [110]. The concept of isometricity applies only during passive-unloaded movement of the joint [71].

There are a variety of treatment options for the damaged ACL; primary repair with or without augmentation devices, reconstruction using autograft, allograft or synthetic graft [111,112]. Autografts are biological tissues transplanted from the patient's own body. The most common autografts are bone-patellar tendon-bone (BPTB) and hamstring tendon (semitendinosus and/or gracilis) [112]. Autografts have reduce risk of tissue rejection and good mechanical properties such as high ultimate tensile strength (UTS) and low strain [113]. Hamstring tendon autografts are associated with less anterior knee pain and better knee extension, whereas patella tendon autograft is claimed to provide better stability [114]. Some of the complications following ACL reconstruction using autograft are donor site morbidity, patello-femoral pain, patellar fracture, muscle weakness and nerve injury [111,112].

Allografts are biological grafts transplanted from another human. The most common allografts are patellar tendon, Achilles' tendon, and iliotibial

band/fascia lata. Allografts eliminate complications associated with the autograft donor site, however; the main disadvantages are limited resource, cost, delayed biological incorporation, risks of disease transfer and tissue rejection [111,112].

Synthetic grafts were mainly popular in 1980's because they offered the benefit of quick recovery and rapid rehabilitation without sacrificing the autogenous tissue [115]. Synthetic grafts were used either as a complete artificial ligament (e.g. Gore-Tex and Dacron ligaments) or to augment a biological graft substitute (e.g. Kennedy ligament). Ligament augmentation devices are most commonly made of polyester, polypropylene or polyethylene. These devices are designed to share the load with the biological grafts and protect them from deteriorating until revascularisation is complete and the integrated tissue is capable of withstanding loads [109].

Permanent or degradable tissue in-growth scaffolds (e.g. LARS and Leeds-Keio) were designed to promote soft tissue in-growth into the graft. Problems associated with these types of grafts include; variable tissue in-growth, immature degeneration of the graft, synovitis, and poor mechanical properties [112,116,117]. Despite the moderate success of synthetic graft reconstruction, long-term results have been poor, mainly due to wear, creep, fatigue and mechanical failure from 2-5 years after implantation [55,118,119]. Guidoin *et al.* [117] analysed 117 failed artificial ligaments harvested from young active patients and suggested that the primary cause of the failure, which was observed in almost all cases, was abrasion of the textile fibres as a result of yarn on yarn

and/or yarn on bone contact. Some other failure mechanisms were flexural and rotational fatigue of the fibres and loss of the integrity of the textile structure due to non-uniform tissue ingrowth [117]. The analysed grafts made of Ultra High Molecular Weight Polyethylene (UHMWPE) showed less rotational fatigue failure compared to other types of the grafts. In some areas, surface peeling and twisted fibres were observed, but overall there was little evidence of wear damage. For the more porous knitted and braided structures, the collagenous tissue penetrated to the centre of the device; whereas, for the devices made of UHMWPE, collagenous tissue colonised only the outer layers. No penetration of collagen tissue was found into the tightly braided structures. Collagen penetration into the textile structure caused the fibres to fray, swell and separate individually. This phenomenon subsequently contributed to increasing the level of abrasion against the bone [117] .

Table 1.2 summarises the advantages and disadvantages of some the most popular synthetic grafts. Out of the listed artificial ligaments, only Trevira and LARS ligaments are currently being used clinically.

One of the most important characteristics of the ACL to be reproduced is its stiffness; it has been reported that an inextensible ACL would transmit a force of 1000 N during activities such as normal walking under maximum quadriceps force [25], this high force would eventually lead to mechanical failure of either the artificial ACL or its fixation. The majority of the artificial ligaments used for ACL reconstruction have been made of a single cord with a high stiffness (Table 1.2). Ligament elasticity allows anteroposterior

translation of the tibia relative to the femur and would decrease the force the ligament would be required to resist. Therefore, it is important to reproduce elasticity or stiffness of the ACL in the designed artificial ligament.

None of the biological and artificial ACL reconstruction grafts replicate the normal mechanical behaviour of the ACL and do not prevent degenerative disease progression [120–123]. Approximately 50 % of patients with an ACLR, develop osteoarthritis within 6 years after surgery [124]. Some of the predictive factors for osteoarthritis after ACLR were found to be menisectomy, condylar damage, patella tendon grafting, quadriceps weakness, and low strength ratio of quadriceps to hamstring [124]. An ideal ACL reconstruction graft would have no morbidity associated with its procurement, be readily available for implantation, have strong fixation with sufficient inherent strength, provide favourable long-term results, replicate the normal mechanical behaviour of the ACL, and restore the natural kinematics and range of motion of the knee [109]. Such an ideal ACL reconstruction graft currently does not exist. As a result there is a need to design a novel artificial ACLR device with the mentioned requirements.

Table 1.2: Some of the popular synthetic ACL grafts and details of their design, mechanical properties, advantages and disadvantages.

Graft	Material	Structure	Mechanical properties	Advantages	Disadvantages	Ref.
ABC (Surgicraft Ltd., Redditch UK)	Carbon and polyester fibres	24 braided narrow ribbons with a zigzag pattern	UTS: 3130 N	Good short term outcome based on Lysholm score	Mechanical failure, abrasion of the ligament at the tibial tunnel exit	115
Gore-Tex (W.L.Gore, AR, USA)	PTFE	A single long fibre arranged into loops	UTS: 5300 N Stiffness: 322 N mm^{-1} Strain: 9 %	3 times stronger than native ACL	Mechanical failure due to flexural and rotational fatigue, inflammation, loosening, osteolysis	119,125
Dacron (Stryker, Meadox medicals, USA)	Polyester	Permanent graft of 4 tightly woven polyester strips wrapped in an 8 mm diameter sleeve of woven velour	UTS: 3631N Stiffness: 420 N mm^{-1} Strain: 18.7 %	Good short term result of Lachman, anterior drawer, and pivot shift tests	Mechanical failure, degenerative osteoarthritis	119,126
Kennedy-LAD (3M, MN, USA)	Polypropylene	Augmentation graft made of 8mm diameter ribbon	UTS: 1500 N Stiffness: 280 N mm^{-1}	Protects autografts from excessive stresses. Good short term results of anterior drawer and pivot shift tests	Poor implant-autograft interface, abrasion, inflammation, synovitis and effusions	127
Leeds-Keio (Neoligaments Ltd, Leeds, UK)	Polyester	Mesh like structure anchored to the femur and tibia with bone plugs	UTS: 2000 N Stiffness: 270 N mm^{-1}	Short term stability	Graft rupture, increased anterior laxity	112,128
Trevira (Telos, SARL, Marburg, Germany)	Polyester	Flat woven structure	UTS: 1866 N Stiffness: 68.3 N mm^{-1}	Reduced water absorption, short term AP stability	Mechanical failure, osteoarthritis	119

Table 1.2: Continued- Some of the popular synthetic ACL grafts and details of their design, mechanical properties, advantages and disadvantage.

Apex (DePuy, Leeds, UK)	PET	20,000 parallel filaments with 2 end loops	UTS: 5400 N	Long history of use in vascular/cardiac implants, high tensile strength, good tissue integration	Mechanical failure, bone impingements at the exit of tibial tunnel, long-term instability	[129]
LARS (Arc sur Tille, France)	PET	Parallel fibres twisted at 90 ° and bound together by a transverse knitted structure	UTS: 1500N, 2500 N, 3700N, 4700 N Strain: 9.8 %	Mimics natural ACL structure, high porosity for tissue ingrowth	Post-operative laxity No long-term follow-up studies yet	[130]
Richards PACL (TN, USA)	UHMWPE	A single rod with 6.35 mm diameter and 3 lengths of 30, 35, and 40 mm	UTS: 40 MPa Strain : 350 % Yield at 420 N	Good fatigue strength	Postoperative pain, instability, swelling	[131,132]
Raschel® (Cendis MeH dical, France)	UHMWPE	Knitted structure rolled into tubular shape	-	Good fatigue strength, low wear	Abrasion, twisted fibres	[117]
PHP (Cendis MeH dical, France)	UHMWPE	Double concentric tubular braids	-	Good fatigue strength, low wear	Synovitis, abrasion	[117]

1.8 Conclusions

This chapter provided a review of the literature about the structure, function and mechanical properties of the ACL. The importance of preserving or reconstructing the ACL in restoring normal kinematics and mechanics of the knee was highlighted. Different types of grafts that have been used to reconstruct an injured ACL and the problems associated with each graft type were discussed.

1.9 Project Aims & Summary

This project aims to design an ACLR system that can replicate the mechanical behaviour of the native ACL and reproduce the normal kinematics and mechanics of the knee. The ACLR devices are designed to be implanted in ACL deficient (ACLD) patients who require ACLR alone, or those who require an ACLR in conjunction with TKR (ACLR-TKR). The nominated design option for the artificial ACLR consists of a connecting cord and an elastic system with the aim of reproducing the non-linear mechanical properties of the native ACL.

First, the design criteria for an ACLR device such as suitable materials, design requirements, and size constraints must be determined. Different design options to be used for the ACLR alone, or for the ACLR-TKR device, are explored and the most suitable options are selected.

The design of the connecting cord component of the device is then assessed and optimised. A series of mechanical tests (e.g. tensile and fatigue) performed on

the connecting cord are described and the effect of simulated body conditions on the mechanical properties of the cord are investigated. Finally, finite element (FE) analysis is used to predict the cyclic behaviour of the designed cord.

The design of the elastic component of the device is then examined. Designs are assessed mechanically using FE analysis and validated with mechanical tests. Parametric FE analysis is used to evaluate the effect of dimensional factors on the stiffness of each design, and probabilistic FE analysis is performed to assess the influence of manufacturing tolerances on the stiffness of the springs. Based upon these results, the designs of mechanical springs for the ACLR devices which meet the defined design requirements are finalised.

The location of the ACL graft attachment sites on the femur and tibia are known to influence the success of ACL reconstruction. Eighteen computer-based geometrical models defined from segmentation of MRI taken in patients are used to predict the load, elongation, and twist, of the reconstructed ACL during passive and loaded knee flexion. Also, a sensitivity study is performed to investigate the impact of the ACL surgical placement errors on the behaviour of the reconstructed ACL.

To assess the feasibility of the chosen ACLR designs, a number of FE analyses are conducted on the designed ACL devices consisting of two mechanical springs and a connecting cord; axial loading, weight bearing flexion, and a Lachman test are simulated on both devices designed for ACLR alone and ACLR-TKR. The load-elongation behaviour of the designed ACLR system is

compared to those of the native ACL and the weaknesses of the designs are highlighted.

The last chapter gives a summary of what has been achieved in this project. The limitations of this work and also recommendations to overcome these limitations in future studies are discussed.

Chapter 2: Design Criteria

2.1 Introduction

The majority of the ACLR grafts designed to date have demonstrated mechanical failure post operatively and were unable to reproduce the mechanical behaviour of the native ACL and restore normal kinematics of the knee [117,119,133]. In order to design an artificial ACLR system that can reproduce the functions of the native ACL, it is important to define the design requirements.

This chapter aims to define the artificial ACLR design criteria, material and design requirements. The size constraints for implanting the ACL device in the femoral and tibial bony tunnels or in conjunction with the TKR implants are measured. Finally, a number of potential design options for the ACLR devices are explored and the most suitable options nominated based on the defined requirements.

2.2 Material Requirements

As it was discussed in Chapter 1, an ACLR device should reproduce normal stability and mobility of the knee joint, together with mechanical characteristics of the native ACL. Therefore, the material properties of this artificial ligament will be based on the mechanical properties of the native ACL, but must also meet all the criteria necessary for any implantable device to ensure durability and minimise adverse biological responses.

The material requirements for an artificial ACL such as stiffness, loading condition, strain, fatigue, corrosion, creep, wear, and biocompatibility are found from the literature and discussed below.

- **Stiffness**: The native ACL has a non-linear stiffness which would ideally be reproduced by the artificial ACLR system. In an unloaded joint, the stiffness of the ACL is highest at full extension and its stiffness decreases as the knee flexes. The interaction between decreasing ACL stiffness and ACL force leads to maximum ACL elongation at about 30 º of flexion [67,78,134]. At each flexion angle, the ACL stiffness increases with increasing load [67]. To prevent over-constraining the knee joint, the artificial ligament must provide adequate elongation; therefore, the ACL stiffness should be based upon the load-elongation behaviour of the ACL at 30 º of flexion. The stiffness of the linear region of the ACL load-elongation curve for middle-aged people at 30° of flexion up to 400 N load was found to be 117.7 ± 11.3 N mm^{-1} [88]. The stiffness of the ACL has been reported to be age and patient dependant [80]. Based on the measured stiffness of the FATCs in cadavers, the ratio between the stiffness of the ACL in young (242 N mm^{-1} for 22-35 years old), middle aged (220 N mm^{-1} for 40-50 years old), and elderly (180 N mm^{-1} for 60-97 years old) groups were found [80]. Using these ratios, the *in vivo* stiffness of the ACL for young and elderly groups can be estimated to be approximately 130 N mm^{-1} and 97 N mm^{-1}.

- **Loading**: In healthy young adults, the ultimate tensile load of the native ACL is approximately 2160 N [80]; therefore, the designed artificial ACL should be able to tolerate a similar or greater tensile load (Table 2.1).

  The ACL twists internally from full extension to 120 º of flexion by approximately 60 º - 100 º [135,136]. The twist of the ACL is caused by tibial rotation as well as the changing orientation of the femoral and tibial insertion areas relative to each other during flexion [136]. Also as the knee flexes from 0 º to 140 º, the ACL rotates 110 º about its femoral insertion point and 30 º towards the tibia [94]. Thus, it is certainly a requirement to consider these angular rotations when designing an artificial ACLR device. To minimise abrasion and bending fatigue of the linking component between the femoral and tibial attachment sites, two bearings with smooth surfaces should be used at the bony insertion points. The estimated mechanical characteristics of the artificial ACLR system are listed in Table 2.1.

- **Strain**: The *in vivo* elongation of the ACL at 30 ° flexion under full body weight has been reported to be 4.6 % ± 3.3 % [77], which equates to 1.5 ± 1.1 mm for the human ACL with an average length of 32 mm [6]. However, this assumes that the artificial ACL is inserted perfectly by the surgeon at the isometric points. Studies indicate malpositioning of the ACL can vary the strain on the ligament by more than 12.5 % [137] and will increase the risk of failure [138–140]. For this reason a target elongation of 3-5 mm was chosen (Table 2.1).

Table 2.1: Desired mechanical characteristics of the artificial ACLR system.

Stiffness (N mm^{-1})		Ultimate Load (N)	Elongation (mm)
Toe region	Linear region		
~30 - 40 [88]	~97 -117 [88]	2160 N or higher	3-5

- **Fatigue:** One of the major issues associated with orthopaedic implants is fatigue fracture. The fatigue limit is the stress value below which a material can theoretically withstand infinite loading cycles without failure. The ACL will be exposed to both tensile and bending-torsional fatigue; therefore the material(s) used in the cord must have sufficient tensile and bending fatigue strength. Based on the standards for surgical implants [141,142], survival to a minimum of 5×10^6 loading cycles under worst-case scenario load magnitudes is required to test knee implants for regulatory approval. Due to the time constraints and availability of the test equipment, a minimum of 6 million cycles was considered for initial testing the artificial ACL devices which is above the standard specification.
- **Corrosion:** The selected material(s) used in the artificial ACL should not degrade in response to the corrosive biological environment; these conditions may alter the mechanical properties, jeopardise the structural integrity of the device and also elicit adverse local or systematic biological reactions [143]. All materials used in the device must therefore have a proven long-term clinical record of corrosion and degradation resistance for orthopaedic implant applications. Galvanic corrosion is a type of corrosion that occurs due to the electrochemical potential difference between two

different metals if they are in contact. To avoid this, direct contact of multiple types of metals in the artificial ACLR system should be eliminated.

- **Creep:** Due to the long-term implantation of the device, the selected material(s) used for the artificial ACL should have a high resistance to creep. This can be achieved by selecting creep resistant materials, and minimised by over-engineering the implant's modulus. The device may be able to accommodate some creep. Considering the average intra-articular length of the ACL (32 mm) [1] and the stiffness of the linear region of the ACL (Table 2.1), a total 3-6 % creep would cause 1-2 mm permanent deformation of the system, which may be acceptable based upon the defined acceptable elongation criteria.
- **Wear:** The long-term durability and performance of a prosthesis can be detrimentally affected by wear and the resultant wear particles; inducing mechanical failure, component loosening and/or osteolysis of the surrounding bone [144]. Based on the classic Archard wear law, the volume of the produced wear debris is related to the wear coefficient, normal load, and sliding distance, and inversely proportional to the hardness of the softest contacting surface [145]. Therefore some of the factors affecting the wear rate of the artificial ACL would be the combination of materials used, the surface roughness, size, shape, and loading condition for any articulating surfaces [146].
- **Biocompatibility**: Any device required to be permanently implanted in the human body must be biocompatible. The selected material(s) should have the capability to perform its intended function within the human knee

without eliciting any undesirable local or systemic effects on the host tissue. Ideally the material(s) used should have a good clinical history for load-bearing orthopaedic applications.

2.3 Design Requirements

The design requirements for an artificial ACLR device that will be implanted in the human body are listed below.

- **Sterilisation**: It must be possible to sterilise the prosthesis using standard methods, without substantial degradation or alteration of the mechanical properties of the device. Sterilisation falls into three main categories; high temperature or pressure (e.g. steam autoclave), chemical (e.g. ETO gas) and radiation (e.g. gamma).

- **Surgical implantation**: The designed artificial ACL should be easy to surgically implant. The assembly or disassembly of different components of the ligament system should be hassle-free and quick for an average surgeon. It should be possible to implant the device using the standard surgical exposure for the ACL reconstruction or total knee replacement.

- **Manufacturing**: It should be possible to manufacture the artificial ligament to within ± 0.1 mm tolerances (based on the Biomet UK healthcare implant manufacturing standards). The basic processes involved in the manufacturing of orthopaedic implants are; manufacturing of the alloys, polymers, or other raw materials; casting, forging, or textile processes; machining, and finishing; packaging; and sterilisation. None of

these manufacturing processes should affect the desired mechanical properties of the artificial implant. The selected material(s) used should have properties that permit fabrication in the optimum design configurations while being cost-effective. Food and Drug Administration (FDA) approval or CE marking should be obtained before implanting the device into patients in the USA or Europe, respectively.

- **Fit and fixation:** The ACLR device needs to be securely fitted into the bone or the TKR implant(s) through either chemical bonding (e.g. bone cement-PMMA), biological fixation (e.g. bony ingrowth or press fit), or mechanical fixation. Also, connections between different parts of the artificial ligament (e.g. cord and elastic system) should be strong to prevent breakage of the system. Interfaces can also be prone to increased wear; therefore any sharp corners should be avoided, and any potential articulating surfaces should be minimised.

2.4 Size Constraints

2.4.1 Introduction

The designed artificial ACL must fit within the knee joint; it must be possible to connect the ACL to the femur and the tibia without causing any impingement with neighbouring tissues such as the PCL and the intercondylar notch.

As the artificial ACL might be implanted with or without a TKR, both the shape of the femoral and tibial bones and the TKR components need to be

considered for differently sized patients. Currently, single or double bundle surgical grafts are being used to reconstruct the ACL. As can be seen in Figure 2.1, different attachment locations for connecting the single bundle graft on the femur to the tibia are being chosen by different surgeons such as; high AMB to PLB (so-called vertical graft), AMB to AMB, and centre to centre [147]. In the vertical ACL graft, the tibial tunnel is positioned in the posterior region of the ACL tibial footprint, whereas the femoral tunnel is high in the notch, out of the native ACL attachment area. It is claimed that the vertical graft does not reproduce normal rotational stability of the joint [147]. The inclination angle and tunnel angle of the ACL have been reported to be 49.9 ^{0} ± 2.8 ^{0} and 39.3 ^{o} ± 4.2 ^{0} respectively (Figure 2.2) [148]. Inaccurate femoral tunnel positioning is a common cause of failure in ACL reconstruction [138,139].

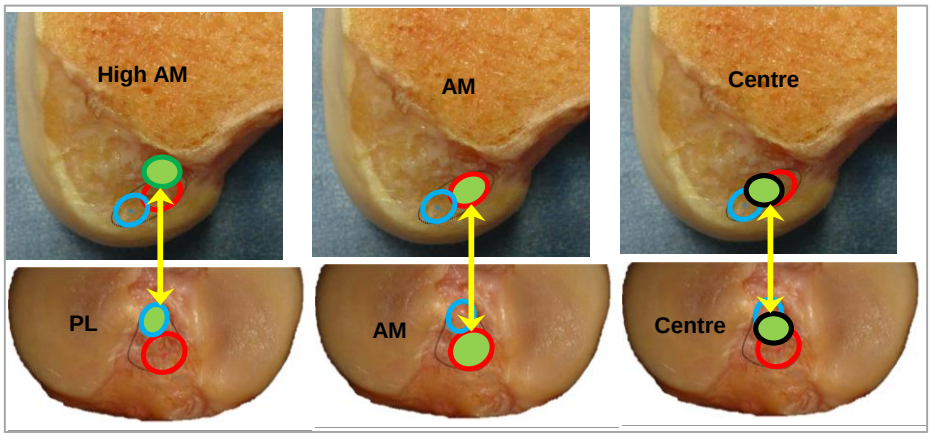


Figure 2.1: Different femoral and tibial tunnel insertion sites for a single bundle ACL graft (a) high AM-PL, (b) AM-AM, and (c) centre-centre methods. Adapted from Tsukada *et al.*, 2008 [149].

In the double bundle reconstruction technique, the centres of the AMB and PLB on the femur are connected to the centres of the AMB and PLB on the tibia, respectively. It has been reported that a single bundle ACL graft can

restore all displacement and rotational knee stabilities during pivot shift test to the ACL intact knee level [150]. Therefore, considering the complexity and time consumption of the double bundle reconstruction procedure, the single bundle reconstruction was nominated for the artificial ACL system.

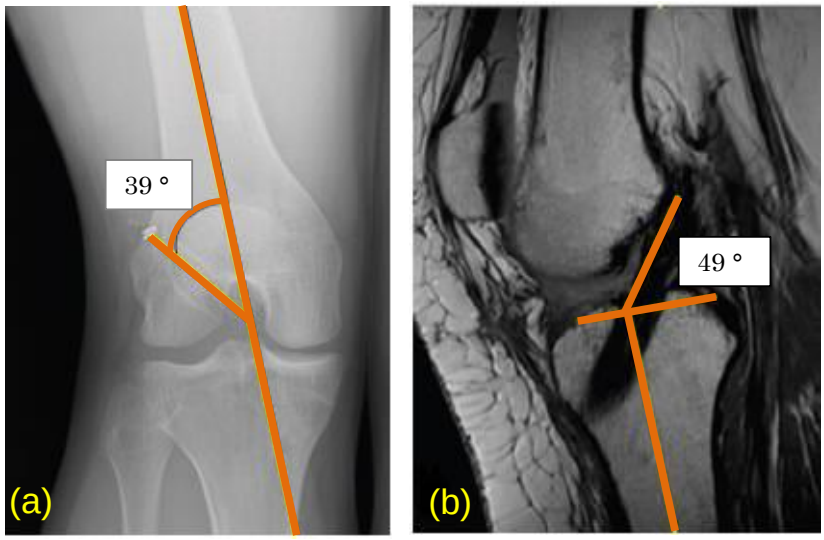


Figure 2.2: Femoral tunnel angle in (a) the coronal plane and (b) the sagittal plane (inclination angle) while the knee is at full extension. Adapted from Illingworth *et al.*, 2011 [148].

2.4.2 Methodology

2.4.2.1 MRI Segmentation

Eighteen sets of high resolution MRI scans (3 Tesla) of patients with healthy cruciate ligaments which had been taken at the Nuffield Orthopaedic Centre (Oxford, UK) were used. The patient cohort consisted of nine females with an average age of 49 (31-63) years and nine males with an average age of 60 (45-71) years; all the scans were of right knees. These patients were diagnosed with either meniscal tear or patello femoral osteoarthritis. Three-dimensional geometrical models of the distal femur, proximal tibia, ACL, and PCL were

created by segmenting the MRI images using Mimics software (version 14.12, Materialise, Leuven, Belgium) (Figure 2.3).

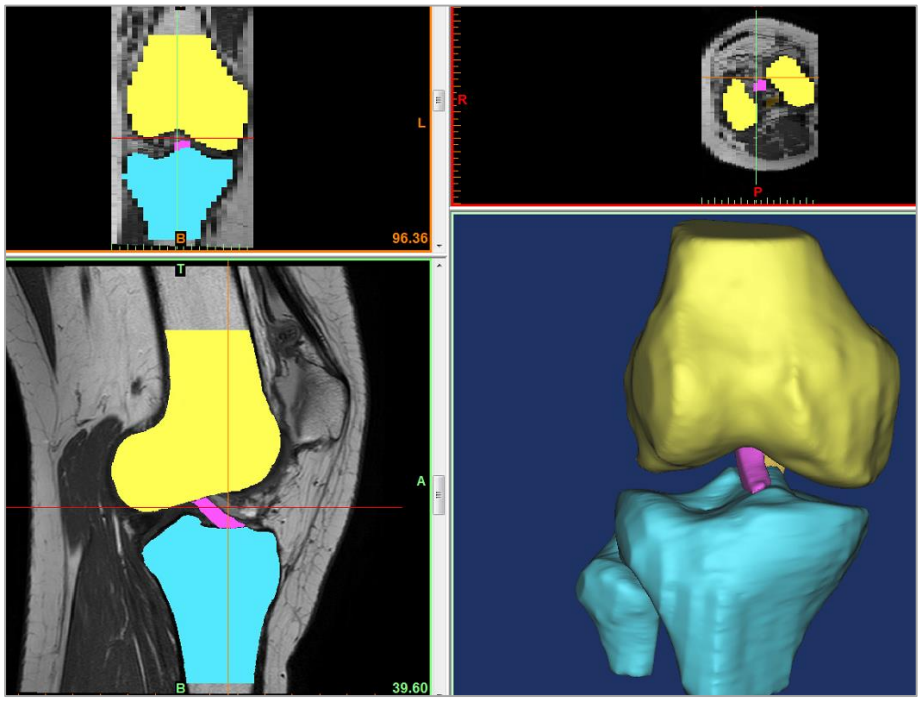


Figure 2.3: Segmented MRI images of a human knee using Mimics software.

When determining the size constraints for the artificial ACL within the segmented knee geometries, it was assumed that the device was implanted at the attachment locations of the isometric fibre of the native ACL

2.4.2.2 Femoral Measurements

The depth of the femoral tunnel was measured in 18 sets of 3D femoral models at the isometric ACL fibre attachment point. The femoral isometic fibre attachment point has been reported to be located on the most anterior and proximal point of the ACL [20] (Figure 2.4).

The femoral isometric fibre attachment point was projected on the lateral surface of the distal femur so that the connecting line between these points had appromately a 40 ° angle in the coronal plane relative to the femoral mechanical axis (Figure 2.2 (a)).

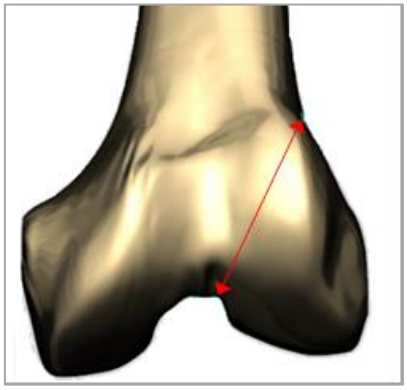


Figure 2.4: The length of the femoral tunnel on a 3D model of the knee.

2.4.2.3 Tibial Measurements

The position of the centre of the AMB was measured in 18 sets of 3D tibial models. The distance between the centre of the AMB to the most medial and the most posterior points of the tibial plateau were measured in terms of percentages of the overall mediolateral width and anteroposterior length of the tibial plateau. This was done by fitting a rectangle in the transverse plane around the tibial plateau (Figure 2.5). The location of the centre of the AMB was measured in this section instead of the isometric fibre attachment point in order to enable direct comparison of the results to other published studies.

The height of the isometric ACL fibre attachment on the tibia relative to the transverse plane passing through the centre of the medial tibial plateau was measured in 18 tibial models (Figure 2.6).

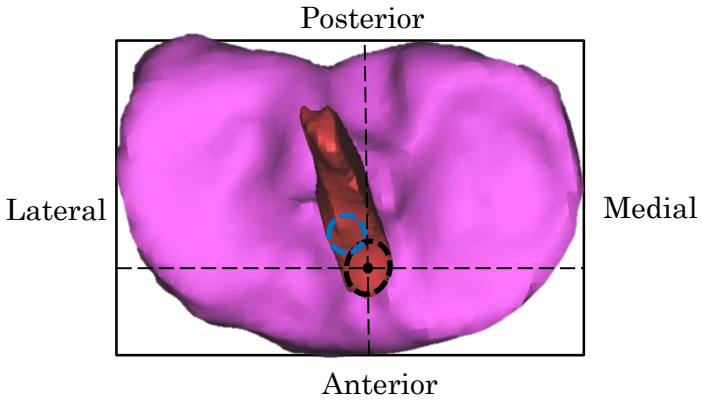


Figure 2.5: Location of the centre of the AMB footprint relative to the most medial and the most posterior part of the tibial plateau. Black and blue circles represent the footprints of the AMB and PLB, respectively.

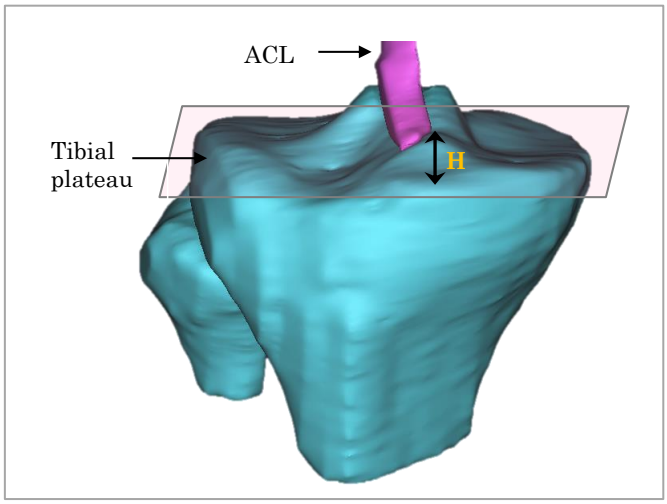


Figure 2.6: The attachment height (H) of the isometric ACL fibre relative to the transverse plane pasing through the centre of the medial tibial plateau.

The available space for the elastic system of the ACLR device located on top of the Vanguard TKR tibial tray (Biomet Inc., Warsaw, USA) was measured in a medium size tibial tray (71 mm). Size of the Vanguard tibial tray indicates the overall width of the component. The dimensions of this gap were then calculated for the entire size range of the Vanguard tibial trays using the ratio between different implants. The available space for the elastic system of the

ACLR device located under the Vanguard TKR tibial tray was found by measuring the anteroposterior (AP) and mediolateral (ML) width of the cancellous bone at different heights of the tibia along the longitudinal tibial axis. The AP and ML width of the tibia at 8 mm, 28 mm, and 48 mm below the lateral tibial plateau were measured in 18 segmented MRI models of the human tibia. A Computed Tomography (CT) scan of a fresh frozen cadaveric tibia of a 60 years old Caucasian male [151] was used to estimate the thickness of the cortical bone at 28 mm and 48 mm lower than the lateral tibial plateau (Figure 2.7). The available space in the tibia was calculated by reducing the thickness of the cortical bone from the AP and ML tibial measurements.

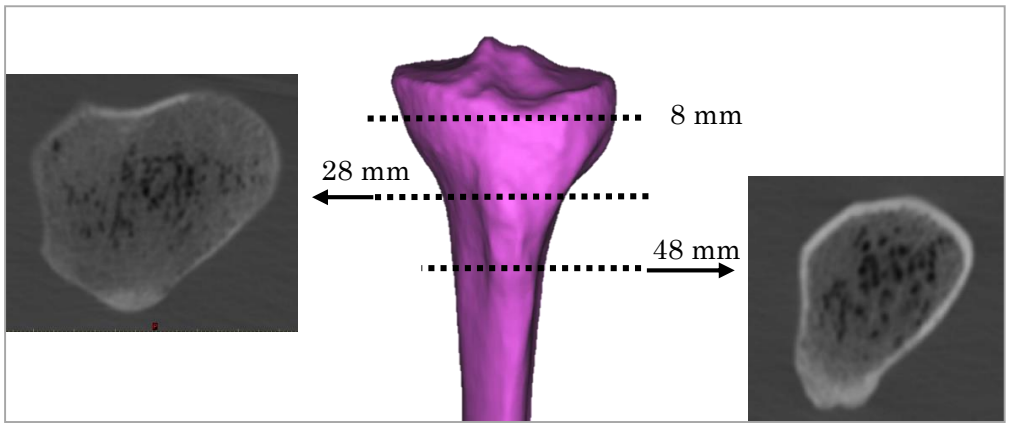


Figure 2.7: The thickness of the tibial cortical bone at 28 mm and 48 mm below the lateral tibial plateau measured from a segmented tibial model.

2.4.3 Results

2.4.3.1 Femoral

The average length of the femoral tunnel measured in 18 femoral models was found to be 39.16 mm ± 2.99 mm.

2.4.3.2 Tibial

The centre of the AMB on the tibial plateau was located 35.98 % ± 2.16 % from the anterior edge of the tibial plateau and at 48.61 % ± 2.11 % from the medial edge of the tibial plateau. The tibial models analysed in this study had an average mediolateral width of 75.55 mm ± 6.22 mm and anteroposterior length of 51.70 mm ± 3.58 mm.

Results of the measurements of the tibial isometric fibre attachment height relative to transverse plane passing through the centre of the medial tibial plateau showed an average height of 5.27 mm ± 1.19 mm. This height is necessary to position the elastic systems in both the ACLR and ACLR-TKR devices in the isometric position on the tibial side.

The size constraints for an artificial ACL in the tibial tray of the Vanguard TKR system (Biomet, Warsaw, USA) were measured. The Vanguard TKR system was used in this study because it was the primary TKR system of Biomet Ltd and it has been associated with good clinical outcome (97% survivorship at 7 years), improved function and pain relief [152,153].

The dimensions of the available space for the ACLR device on top of a medium size Vanguard TKR tibial tray (71 mm) are shown in Figure 2.8. Dimension 'A' indicates the anteroposterior length of the ACLR space that varies in different size Vanguard tibial trays (Table 2.2). Dimension 'B' is the mediolateral width of the ACLR space positioned between the medial and lateral meniscal bearings that is constant for all sizes of Vanguard tibial tray. Dimension 'C' is the vertical height of the isometric ACL fibre attachment relative to the centre

of the medial meniscal bearing measured earlier in 18 tibial models. The size of the Vanguard tibial tray indicates the mediolateral width of the tibia plateau in a patient.

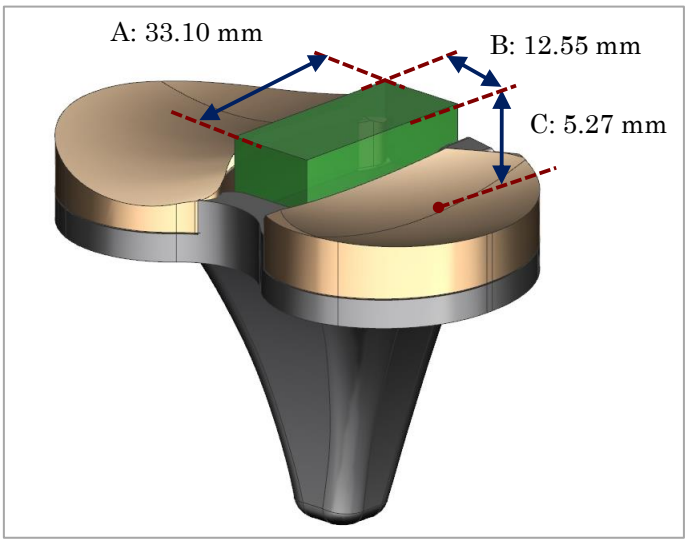


Figure 2.8: Size constraints for an ACLR device in a medium size (71 mm) Vanguard primary tibial tray.

Table 2.2: Dimensions of the available space in different sizes of Vanguard tibial tray for an ACLR device.

Dimensions	Tibial size (mm)								
	59	63	67	71	75	79	83	87	91
A	26.62	28.78	30.05	33.10	34.37	37.41	38.68	41.73	43.00
B	12.55								
C	5.27								

The AP and ML width of the tibial at different heights are shown in Table 2.3. The average thickness of the cortical bone measured from a CT scan of the cadaveric tibia used in this study was 1.84 ± 0.47 mm at 28 mm depth and

2.78 ± 0.36 at 48 mm depth. 2.5 ± 0.1 mm and 4.13 ± 0.66 mm cortical thickness was measured at about 14 % and 38 % of the mid tibial shaft.

Table 2.3: The average AP and ML dimensions of 18 tibial models at 8 mm, 28 mm and 48 mm below the centre of the lateral tibial plateau. SD = standard deviation.

	Tibial level	Width (mm)		ACLR-TKR space (mm)
		Mean	SD	
AP	8 mm	51.78	3.60	51.78
	28 mm	40.98	3.55	37.30
	48 mm	32.48	4.87	26.92
ML	8 mm	75.80	6.02	75.80
	28 mm	58.70	7.32	55.02
	48 mm	36.24	4.67	30.68

2.4.4 Discussion

Usually an 8 - 12 mm diameter femoral drill [154,155] is used to create tunnels for implanting a conventional single bundle ACL reconstruction graft. The average depth of the femoral tunnel measured in 18 sets of 3D knee models was 39 mm. Therefore, the allocated femoral tunnel for the stand-alone ACLR device should have a maximum diameter of 12 mm and an average length of 39 mm. The femoral tunnel length measurements match well with the literature, which reports a typical tunnel length of 30-40 mm for implanting single bundle ACL reconstruction grafts [154,155].

A 11-12 mm drill [156,157] is commonly used to create tibial tunnels for implanting a single bundle ACL reconstruction graft. The depth of the tibial tunnel created to fix the conventional ACLR grafts is 50 mm[158]. Therefore, the

allocated tibial tunnel for the stand-alone ACLR device should have a maximum diameter of 12 mm and an average length of 50 mm.

The centre of the AMB on the tibial plateau was located 35.98 % ± 2.16 % from the anterior edge of the tibial plateau and at 48.61 % ± 2.11 % from the medial edge of the tibial plateau. Tsukada *et al.* [149] reported that the centre of the tibial AMB in 36 cadaveric knees was situated at 37.6 % ± 3.6 % from the anterior edge in the sagittal plane, and at 46.5 % ± 3.2 % from the medial edge in the coronal plane. Visually detecting the centre of the AMB on the MRI images was one of the limitations of this study. The most isometric fibre of the ACL located on the most anterior area of the AMB [20,21] can be found by considering the centre of the AMB as well as it's diameter. Cohen and co-workers measured the sagittal and coronal length and width of the AMB in 50 MRI images. These authors reported sagittal length, sagittal width and coronal width of 36.9 ± 2.8 mm, 5.1 ± 0.7 mm and 4.2 ± 0.8 mm respectively [23].

The ACL attachment is located between the medial and lateral tibial plateau. It is stretched out from the area between the tibial spines towards the anterior region of the tibia [159]. The average height of the isometric ACL attachment point relative to the centre of the tibial plateau was found to be 5.27 mm ± 1.19 mm in 18 knee models. This height is important for positioning the tibial elastic system and preventing the impingement of the elastic system on the femoral intercondylar notch.

The average thickness of the cortical bone in Caucasians at 14 % and 38 % of the mid-tibial shaft has been reported to be 1.9 ± 0.4 mm and 4.6 ± 0.7 mm

respectively [160], which was close to the average thickness of the cortical bone measured in this study. Based upon the positioning of the AMB on a tibia of anterior-posterior width of 52 mm [161,162], and the cortical thickness measurements; a tibial tunnel in the ACLR-TKR could be drilled to a depth of 48 mm without perforating the tibial cortex. Normally surgeons make a 6-8 mm tibial resection by referencing from the centre of the lateral tibial plateau when performing a Vanguard TKR [163]. It is therefore important that the ACLR device sits in the correct AMB position at the un-resected depth to not adversely affect the knee kinematics. The available space above the tibial TKR component is limited due to the nearby bearings and the closeness of the intercondylar notch; as a result the space is rectangular with a width of only 13 mm. The distance between the medial and lateral tibial spines where the native ACL is located has been reported to be 12.9 ± 1.6 mm [159] which is similar to the defined width of the elastic system on the TKR tibial tray. The available space surrounding the tibial stem decreases with increasing depth. For these reasons, any components implanted on the tibial side must have an approximately rectangular profile and cannot extend too deep.

2.5 Design Options

2.5.1 Overall Structure

The simplest design to reconstruct the injured ACL is a cord connecting the femur to the tibia; however, using standard polymers the construct would have a high stiffness and small elongation similar to the majority of synthetic ACL

grafts used in 1980's which had a poor clinical outcome (Table 1.2). The force-elongation characteristics of the native ACL shows that it behaves like a hardening spring, with relatively little resistance to the initial load. In order to reproduce this mechanical response, three options were identified:

1. Create a single polymeric cord with material properties that match the natural ACL
2. Create a series of metal springs with stops to produce a multi-linear response to load
3. Create a combination of metal springs and a non-linear polymeric cord to create a multi-linear response with a smoother transition between each linear region.

The problem with design option 1 is that using a single cord for the artificial ACL may creep or permanently deform over time under *in vivo* cyclic loads and also it will provide insufficient elongation. Permanent deformation of the artificial ACL would alter its mechanical behaviour potentially reducing the stability of the knee joint. It would also be difficult to design a cord with a reproducible non-linear stiffness; this would require a complex structure.

The disadvantage of design option 2 is that the attachments between each metal elastic system may experience excessive stress and fatigue. In addition, the structures may also restrain the movements of the knee and the artificial ACL due to the low bending modulus and low elongation at failure of the metal springs.

Design option 3 was selected for the artificial ACL because the polymeric cord has a high bending modulus that eases the movements of the artificial ACL

within the knee joint, and transmit the forces between the elastic components. In addition, the elastic springs can provide the required mechanical properties and elongation of the artificial ACL. An early version of this design was patented in 2007 (Patent number: GB2454251) (Figure 2.9).

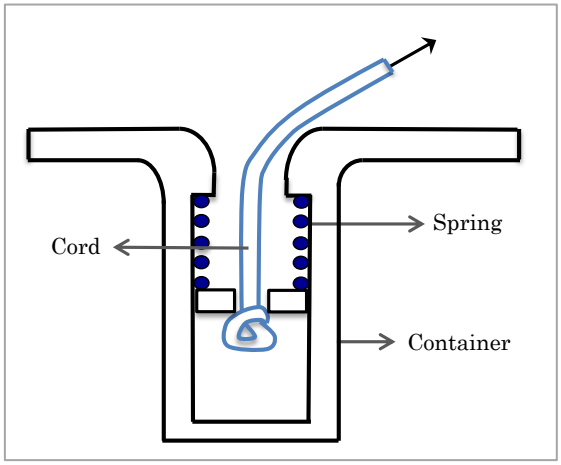


Figure 2.9: One of the early design concepts proposed for the artificial ACLR system consisting of a spring system and a cord-Patent GB2454251.

2.5.2 Material Selection

2.5.2.1 Connecting cord

The connecting cord could be produced from a polymeric textile, or alternatively a metallic alloy. As the desired stiffness of the artificial ACL is provided by the elastic system, the cord should be designed to provide stiffness greater than that of the elastic system in order to avoid significant reduction of the overall stiffness. A metallic cord would be significantly stiffer than a polymeric one but the consequences of impingement, wear or fracture would be

worse [164]. The stiffness of a polymeric cord can be improved by increasing the linear density or by adding more fibres to the textile construct.

Creep is a potential issue, particularly with polymeric cords [165]. The risk of creep can be reduced by using artificial cross linking processes with gamma irradiation, or through modification of the formation of the material. Some of the common materials used previously for synthetic ACL grafts were Carbon fibre, polyester, PTFE (Polytetrafluoroethylene), polyethylene, and PET (polyethylene terephthalate) (Table 1.2). One of the main disadvantages of these materials was their poor mechanical behaviour due to creep, fatigue, wear and rupture [117,119]. Also Carbon fibre had a high stiffness (230×10^9 N mm^{-1}) and its wear particles caused biological reactions [119].

High modulus of elasticity, tensile strength, and flexibility are important characteristics of the fibres that should be used in the artificial ACL. Highly crystalline UHMWPE fibre (Dyneema Purity® fibres, DSM, Netherlands) has been reported to have the highest strength based on its weight and volume when compared to other potential materials (Figure 2.10); as the volume of the cord is relatively small this is an important factor.

UHMWPE has been used as one of the bearing surfaces of hip and knee replacements since mid-1960's because of its biocompatibility, chemical inertness, impact resistance, abrasion resistance, and low coefficient of friction [166,167]. The preferred sterilisation method for Dyneema is ethylene oxide (EtO) gas which does not affect the mechanical strength of UHMWPE compared to other sterilisation methods (e.g. steam and gamma irradiation) [168]. Dyneema

has been used clinically in several orthopaedic devices: the XO Button (ConMed Linvatec, Largo, USA) and Ziploop (Biomet Ltd, Warsaw, USA) are used for fixation of an ACL replacement; the Maxbraid suture (Arthrotek, Biomet Inc, Warsaw, USA) is used for soft tissue repair, and the HiFi™ Suture (ConMed Linvatec, Largo, USA) is used for rotator cuff repair.

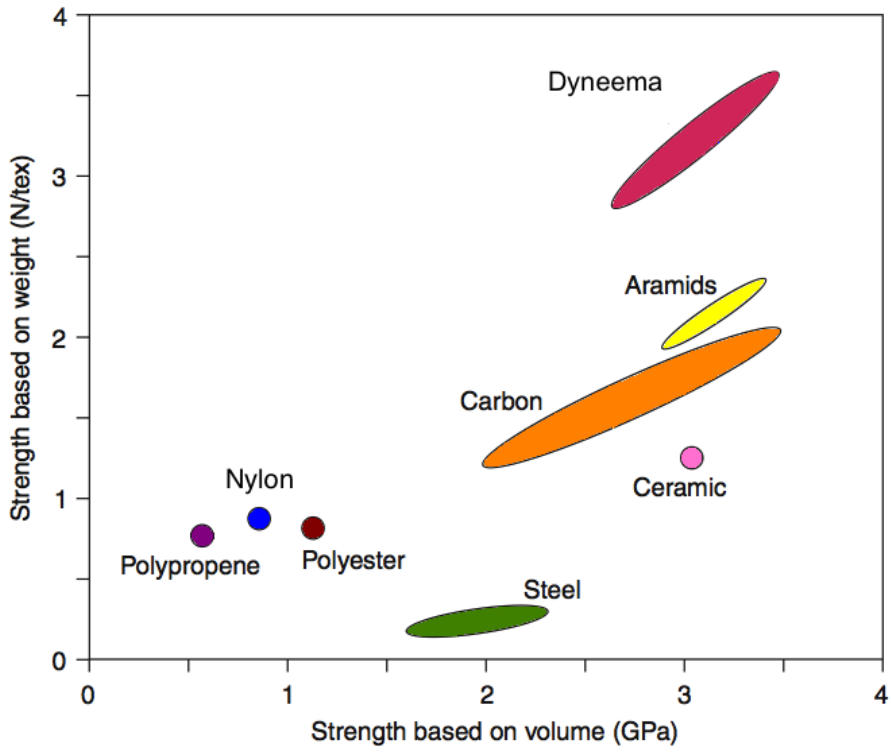


Figure 2.10: Strength based on the weight versus strength based on the volume of different fibres. Adapted from van Dingenen, 2001[169].

Decitex (dtex) is a unit which represents the density of filaments within a fibre, or the fibre linear density, where 1 dtex is equal to 1 gram per 10,000 metres. Fibre tenacity, or specific strength, is described in textile units of $Ndtex^{-1}$, or in the engineering unit of GPa. Textile units relate the strength to the weight of the fibre, whilst engineering units refer to the cross-section and the volume of a fibre. The specific strength of Dyneema fibres is greater than

that of Carbon fibre as well as other fibre materials, and it has a low elongation at break [169] (Figure 2.11)

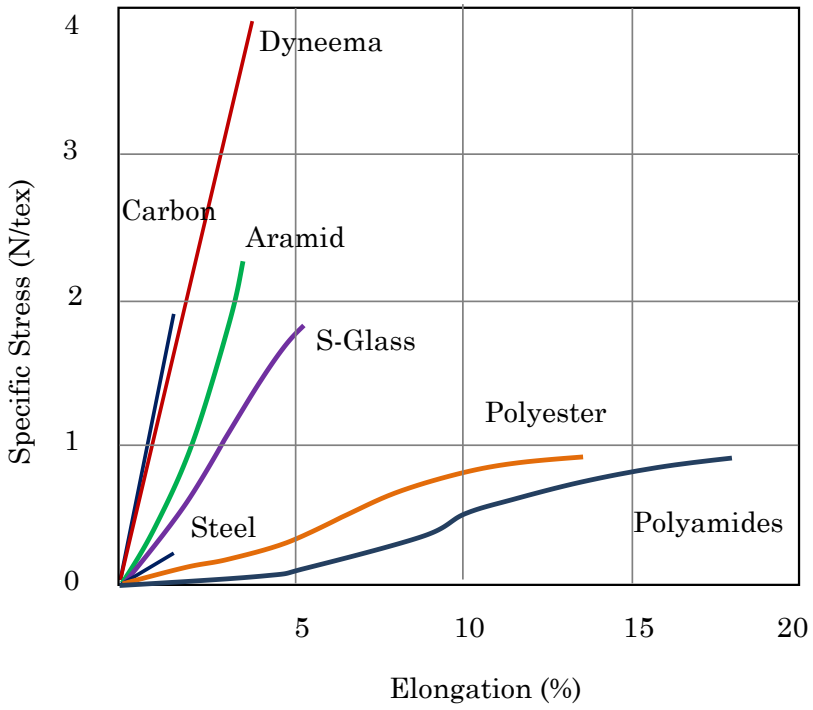


Figure 2.11: Stress-strain curves of a number of high performance fibres. Adapted from van Dingenen., 2001 [169].

Despite the high elastic modulus of Dyneema fibres, they have high flexibility and good tensile and bending fatigue properties [169]. Because of the high crystallinity and low porosity of Dyneema fibres, water is not readily absorbed and so it does not swell [169]. Table 2.4 summarises some of the mechanical and physical properties of UHMWPE (Dyneema) fibres. For all of the reasons outlined above, Dyneema was chosen as the most appropriate material to use for the connecting cord.

Table 2.4: The mechanical and physical properties of Dyneema fibres [169].

Melting point	144-155 ° C
Axial tensile strength	3 GPa
Axial tensile modulus	100 GPa
Transverse tensile strength	0.03 GPa
Transverse tensile modulus	3 GPa

2.5.2.2 Spring System

As the elastic portion of the artificial ligament system is mainly responsible for providing elastic elongation and the desired non-linear stiffness of the native ACL, a spring-like system should be designed. The selected material should have high elastic modulus, high yield strength, fabricability, corrosion resistance, high toughness; metals were therefore thought to be the best option.

The metallic alloys used in the orthopaedic industry can be divided into 3 major groups; CoCrMo alloys, titanium alloys, and stainless steel alloys. A number of biocompatible materials that are currently being used in orthopaedic devices were considered for the spring system (Table 2.5).

- **Titanium**: This alloy has a high tensile strength, high corrosion and fatigue resistance, good machinability, is light-weight, and has a lower modulus than CoCrMo alloy. Titanium-6Aluminium-4Vanadium (Ti-6Al-4V) alloy has been widely used in dental and orthopaedic implants. Titanium however, has a relatively poor wear resistance [170].

- **Stainless steel**: Surgical grade 316L stainless steel (18Cr-14Ni-2.5Mo) has been used in surgical implants due to its high elastic modulus, high corrosion resistance in a biological environment, and its comparatively low cost and particularly high ultimate strength. Although stainless steel is very ductile and easily machined, its fatigue strength is lower than other implant alloys.

- **Cobalt Chromium Molybdenum:** CoCrMo contains 60 % Cobalt, 28 % Chromium and 6 % Molybdenum [171] and has been widely used in the manufacture of orthopaedic implants, particularly joint replacements, due to its high strength, good fatigue and corrosion resistance, high elastic modulus, biocompatibility, and wear resistance [144,167]. The high Carbon content (0.05-0.35 %) [164,171] of this alloy results in the formation of carbides in the microstructure of the material that aids resistance to corrosion and wear. CoCrMo alloys used for orthopaedic applications are mainly manufactured from either cast or wrought material.

CoCrMo alloy (BioDur CCM+) was selected for making the elastic spring system of the artificial ACL design as it has high tensile strength and good fatigue and corrosion resistance. Unlike some other surgical alloys, it contains no nickel, so does not cause any sensitivity problems for Nickel sensitive patients. The yield strength of this alloy is 930 MPa, therefore, to ensure no plastic deformation, stress should be less than 930 MPa. The fatigue stress limit of CoCrMo alloy in air is above 500 MPa; however, this value is highly dependent on the manufacturing process and manufacturing post-processing

[144,167,172]. Therefore, in order to ensure a good fatigue life under body conditions, the expected stress within the artificial ACL design should be no more than 465 MPa, which is approximately less than half of the yield strength of CoCrMo alloy.

Table 2.5: Mechanical properties of some common alloys used in surgical implants

Alloy		UTS (MPa)	Elongation at break (%)	Yield strength (MPa)	Fatigue strength (MPa) at 10^7 cycles	Elastic Modulus (GPa)
Titanium	Ti-6Al-4V (ASTM F136), [173,174]	860-1220	10-16	795-1130	620-725 [144]	114
Stainless Steel	316 LVM (ASTM F138)	490-1350	12-40	190-690	310-448 [144]	188
Co-Cr alloys	Cast Co-Cr Mo (ASTM F75)- min	655	8	450	310 [144]	210
	(BioDur™ CCM+®), [175]	1035-1310	25	585-930	400 [144]	241
	Wrought- forged Co-Cr-Mo (ASTM F1537, ASTM F799)	897-1172	12-20	517-827	496-896 [144]	210
	Co-Ni-Cr-Mo (MP35N) ASTM 562, [176177]	1000-2068	8-20	655-1999	689-793 [144]	235

2.5.3 Design Selection

2.5.3.1 Connecting Cord

Each Dyneema yarn is made of multiple filaments (Figure 2.12); therefore, the diameter of the yarn is determined by the diameter, the number of filaments and how closely the filaments are packed together. Each yarn of Dyneema UG with 440 dtex consists of 800 filaments; each filament has a diameter of

approximately 8.5 µm. Multiple yarns can combine into a construct through different textile process such as braiding (Figure 2.13), knitting, and weaving. The mechanical properties of the UHMWPE connecting cord can be tailored by altering the number of yarns, the grade of the fibre, and its textile architecture.

In order to ease the connection between the cord and the elastic system, obtain more uniform tensile strength along the cord (e.g. to avoid making knots to close the cord), and also to have a variety of loops with different lengths for different size patients; a number of closed loops of braided Dyneema cord were made by Cortland Ltd. (NY, USA) using a novel manufacturing technique to splice the end fibres of the braid through each other. Due to confidentiality, the splicing technique cannot be discussed in more detail.

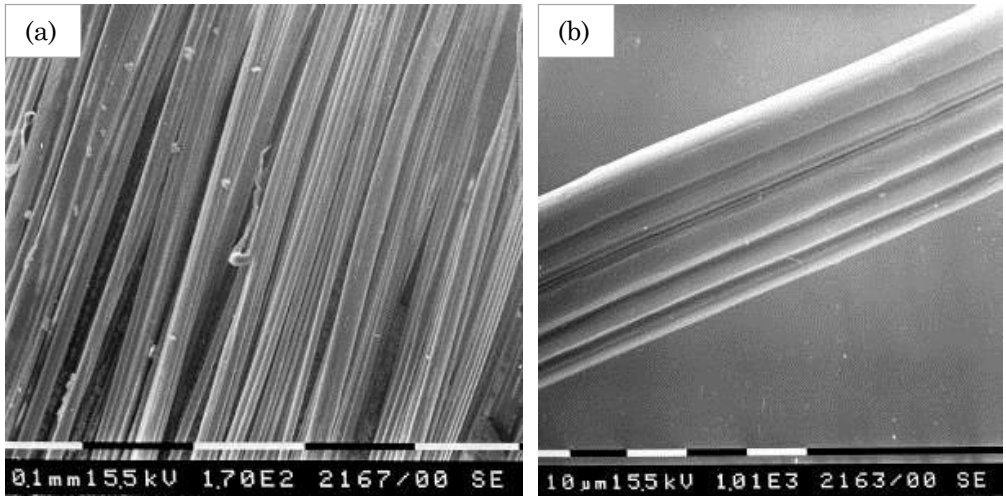


Figure 2.12: Scanning Electron Microscopy (SEM) pictures of (a) 442 dtex Dyneema yarn made of multiple fibres, and (b) a fibre made of a number of filaments. Pictures were taken in John Radcliffe hospital (Oxford, UK) by Prof. David Ferguson in July 2013.

To ensure the artificial ACL design can tolerate up to 2160 N tensile load (Table 2.1), the diameter of the braided cord could be varied to suit the mechanical requirements. The length of the loop should be sufficient to connect the attachment points on the femur to the tibia in differently sized patients.



Figure 2.13: Structure of the braided Dyneema loop (42240 dtex). Each strand of the loop had a diameter of approximately 2 mm.

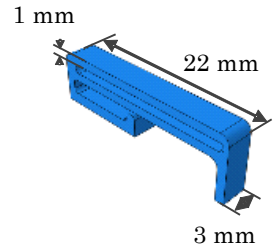
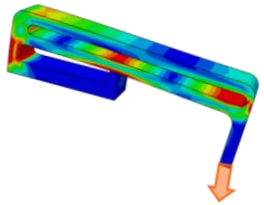
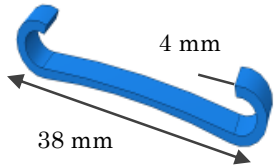
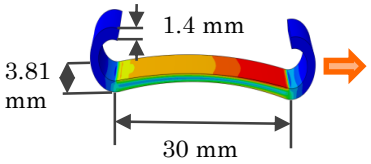
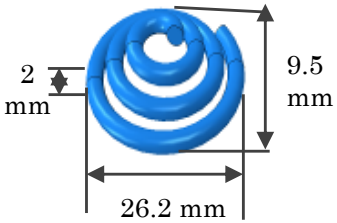
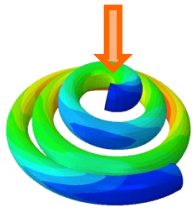
2.5.3.2 Spring System

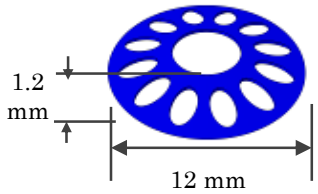
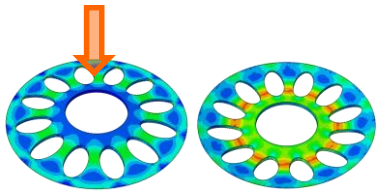
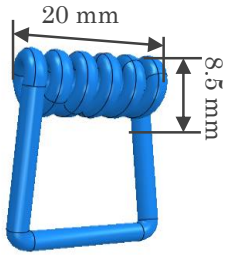
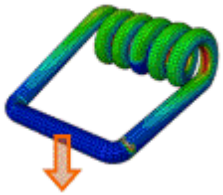
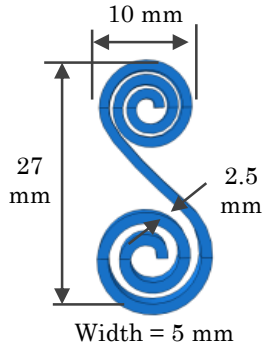
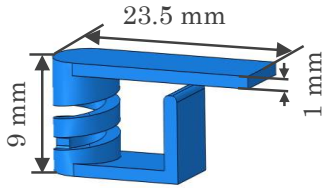
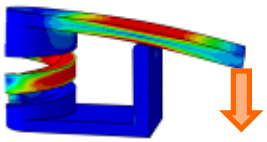
The desired non-linearity discussed in Section 1.5 could be achieved either by designing a single elastic component with a non-linear stiffness, or by combining two, or more, linear elastic components in series. The designed artificial ACL should reproduce the stiffness of the toe region (~38 N mm^{-1}) as well as the linear region (~100 N mm^{-1}) of the load-elongation curve of the native ACL.

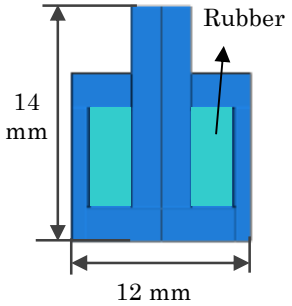
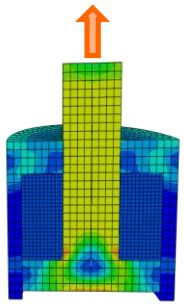
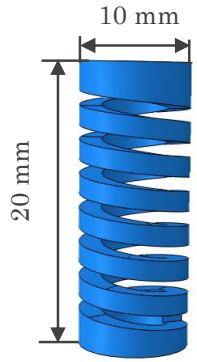
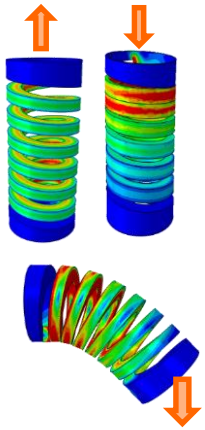
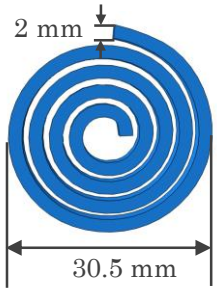
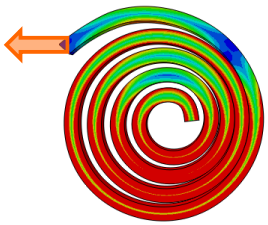
Various different spring designs were considered and tested in this project (Table 2.6). A number of potential elastic systems were assessed by Strategic Simulation and Analysis (SSA, Charlbury, UK), a consultation FE analysis (FEA) team. Out of all of the considered elastic systems, helical and spiral springs showed the most desirable load-elongation characteristics, the most

suitable stiffness and strength, the least risk of wear and fatigue and the most suitable shape for implantation. For these reasons, the helical and spiral spring designs were selected to investigate further and optimise for use in the artificial ACLR.

Table 2.6: Considered spring options for the elastic system of the artificial ACL (ideas from a brainstorm with the Strategic Simulation and Analysis (SSA) consultation team).

Elastic system		FEA-Deformation under load	Notes	Disadvantages
Cantilever beam			• Bi-linear stiffness due to contacting region	• Sudden transition between bi-linear stiffness • Contacting area would be likely to wear and fatigue • Zones with high stress concentration • Max load <100N
			• Nonlinear stiffness (but small difference between initial and final stiffness)	• Small deflection (<2mm) • A longer beam is required to get the desired elongation
Conical			• Similar nonlinear stiffness to the native ACL	• Difficulties in accommodating the spring into the joint along the natural loading directions • Problem of space constraint • Max load <150N

Washer			• Non-linear stiffness	• Low deflection • Load-elongation behavior did not match those of natural ACL • Problem of space constraint
Torsion			• Torsional spring	• Linear stiffness • Max load is <100 N
Other concepts			• Machined spring with variable wall thickness • Non-linear stiffness	• Problem of space constraint • A bigger device is required to achieve the desired elongation
			• Bi-linear stiffness if contact	• Contact between the bar and one end can cause excessive stress concentration, fatigue and wear • Max load <100 N

			• Non-linear stiffness	• Creep of the rubber material • Small deformation
Helical (coil)			• Extension spring: linear stiffness • Compression spring: Non-linear stiffness if the coils come into contact • Bending spring: Non-linear stiffness if coils come into contact	• Contact between coils can cause fatigue and wear • Low stiffness • Maximum load is <100N
Flat spiral			• Non-linear stiffness if coils come into contact. • Adequate deformation and strength • Stiffness differs depending on the loading direction	• Contact between coils can cause fatigue and wear

2.6 Artificial ACLR

Size constraints should be always considered when designing different components of an artificial ligament. The elastic system for the artificial ACL, designed to work without a TKR, could be implanted into either the tibia and/or the femur. The end part(s) of the elastic system(s) must connect with the Dyneema cord while minimising the risk of wear and fatigue failure. Also the complexity of surgical implantation should be avoided by introducing a design that can be easily implanted in the knee. As was found in Section 2.4, the space available for the elastic system in a medium sized patient was a 12 mm outer diameter (OD) and a 50 mm length in the tibia, and a 12 mm OD with a maximum 39 mm length in the femur

From the elastic systems listed in Table 2.6, the helical spring was selected for the artificial ACL reconstruction because it can be easily fitted in the available space in the tibial and femoral tunnels within a metal cylindrical pot. The available space on the tibia and femur should be sufficient to include both the elastic system and its packaging.

2.7 Artificial ACLR-TKR

When reconstructing the ACL in conjunction with a TKR system, the shape and size of the knee implant should be taken into the account. For this work, the design will be optimised for the Vanguard TKR design (Biomet UK Healthcare Ltd., Swindon, UK). The elastic system of the artificial ACL could be implanted into the tibial component, in the femoral bone, or to the femoral

implant. The approximate 13 mm wide available space between the medial and lateral tibial compartments, where the tibial stem is located, can be used for implanting an elastic system (Figure 2.14).

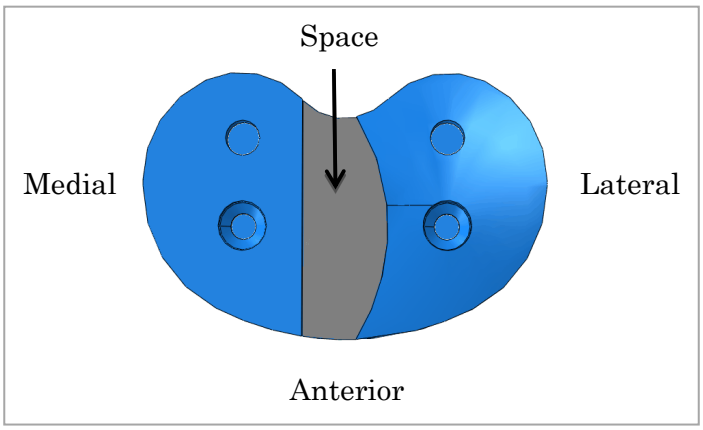


Figure 2.14: Available space for the tibial elastic system between medial and lateral tibial compartments.

Flat spiral springs were selected for the ACLR device in the TKR because of their superior mechanical behaviour and ease of their housing into the stem of the tibial tray. There would be insufficient depth available to house a helical spring in the correct anterior position. It would not be possible to implant the flat spiral spring into an ACL deficient knee which was not to undergo total knee replacement due to the difficulties in accommodating the spring into the tibia.

2.8 Conclusion

In this chapter, the criteria for designing an artificial ACLR system were defined and the necessary material and design requirements were described. The theory that the functional artificial ACL should replicate the non-linear

stiffness of the native ACL was discussed. The size constraints for a stand-alone ACLR device and an artificial ACLR device for TKR were determined.

The nominated design option for an ACLR device consisted of a connecting cord and an elastic system. Dyneema (UHMWPE fibre) and CoCrMo alloy were selected to be used for the connecting cord and elastic system, respectively. It was decided that the connecting cord would be made of a closed loop of braided Dyneema yarns.

Out of a number of different mechanical springs that were considered, helical compression springs and spiral springs represented the best mechanical properties within the defined size constraints. Therefore, only the feasibilities of using two helical compression springs in series for the stand-alone ACLR and a helical compression spring in series with a spiral spring for the ACLR-TKR were described in this thesis.

Chapter 3: Connecting Cord

3.1 Introduction

The chosen design option for the artificial ACLR system consists of a connecting cord and an elastic system. As the artificial ACL is implanted in the human body, it is important to investigate the effects of environmental conditions on the mechanical properties of the Dyneema (UHMWPE fibre) cord. Experimental studies on UHMWPE have indicated that its material properties vary when it is exposed to cyclic loading as a result of changes in its morphology and structure [178–180]. As the artificial ACL will be cyclically loaded when *in vivo*, it is important to be able to predict this material response to ensure it is not detrimental to the function of the device.

This chapter aims to investigate the effect of *in vivo* conditions such as humidity, body temperature, varying strain rate and cyclic loading on the mechanical properties of the connecting cord. The experimental data derived from the fatigue test was inputted into a material hardening model particular to Dyneema, which when combined with finite element analysis techniques, were used for design optimisation and validation of the connecting cord of the artificial ACL.

3.2 Mechanical Tests

3.2.1 Methodology

3.2.1.1 Humidity and Temperature Sensitivity

The effect of humidity and temperature on Dyneema Purity® (DSM-Netherland) yarns (442 dtex) and loops (between 28160 and 30480 dtex) was studied. Samples with 200 mm length were tensile tested in this experiment according to ASTM D885 [181] and ASTM D2256 [182].

Dry and wet samples were tested at room temperature (RT = 21 ° C) and body temperature (BT = 37 ° C). To summarise, the samples tested were as follows:

- Dry samples at room temperature (n=5)
- Dry samples at body temperature (n=5)
- Wet samples at body temperature (n=5)
- Wet samples at room temperature (n=5)

When considering the effect of humidity, preconditioning times to soak the specimens were based on standard protocols used in hip simulator testing. According to ASTM F2025–06 (2012), five weeks is required to soak an UHMWPE specimen (maximum thickness 10 mm) in the test lubricants (saline or bovine serum) [183]. For Dyneema yarns and loops with diameters of 0.242 mm (yarn) and 1.93 - 2.011 mm (loop), a comparative soaking time of 169 hours was calculated. However, as the samples were made of multiple fibres with gaps through which the saline could penetrate thus reducing the thickness and increasing the contact area, the preconditioning time was reduced to 100 hrs.

Specimens were preconditioned in a bobbin filled with saline (0.85 %) and were placed in an oven (Heraeus, UT6120, Germany) at 37 ° C for 100 hours.

Instron clamps (CP103684, Instron, MA, USA) were used to test the yarns (Figure 3.1). The contact area of these clamps was large and prevented slippage of the yarn samples. The clamping pressure was between 6-7 bars, high enough to prevent slippage and low enough to prevent breakage within 5 mm of the faces.

Loop samples were fixed to an electromechanical test machine (Instron, MA, USA) using Sternum pins (Figure 3.1). A pre-tension (in Newton) of 0.2 % of the specimen's linear density (in dtex) was applied at a speed of 50 mm min^{-1} to remove any slack from the specimen.

The yarn and loop samples were then tested at displacement rates of 100 mm min^{-1} and 150 mm min^{-1} respectively. Force and elongation data were recorded until specimen failure. A climate chamber (Weiss Enet, ETE 220LN2, Germany) was used for testing the samples at body temperature.

The modulus of the loops was found from the slope of the stress-strain curves between 50 N and 400 N. The cross-sectional area used to calculate the nominal stress was found by dividing the linear density of the samples (dtex= 1 gram/10 Km) by the density of the Dyneema material (960 kg m^{-3}).

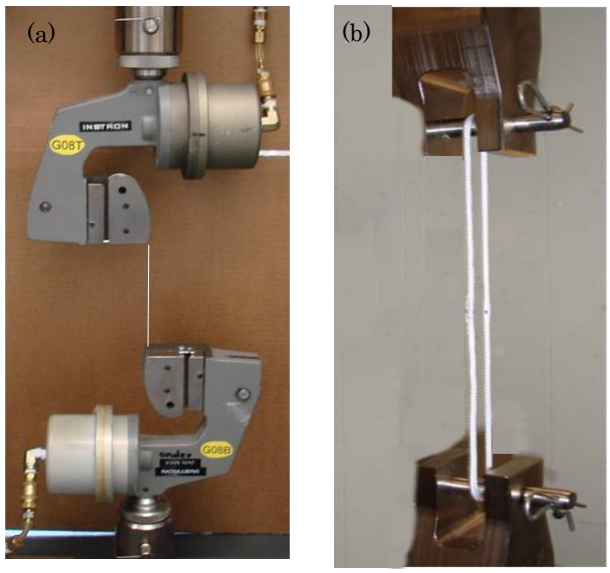


Figure 3.1: Grips used for the tensile testing of the Dyneema samples (a) Instron CP103684 used to test the Dyneema yarns, (b) Sternum pins (diameter = 11mm) used to test the braided loops.

3.2.1.2 Strain Rate Effects

Shelburne and co-workers [89] reported ACL loading during normal gait (Section 1.5). The duration of the gait cycle period during normal walking for a middle-aged adult is roughly 1 second [184]. Therefore, the loading speed of the ACL from heel strike (80 N) to its maximum value (303 N) at 15 % of the gait cycle (20 ° -30 ° KFA) [185] (Figure 1.11) was found to be approximately 1500 N s^{-1}. Using the estimated *in vivo* stiffness of the ACL at 30 ° of flexion in middle-aged humans (117 N mm^{-1}) [88], the extension rate can be calculated by dividing the loading rate (N s^{-1}) by stiffness (N mm^{-1}). The calculated displacement rate was roughly 760 mm min^{-1}. Based upon this, three displacement rates of 150, 300 and 900 mm min^{-1} were selected to investigate the effect of strain rate on the mechanical properties of Dyneema loops.

Braided Dyneema loops were preconditioned in saline (0.85 %) at body temperature (37 °C) for 193 hours. Samples had a length of 40 mm and linear density of 21120 dtex. An electromechanical test machine (Lloyd-EZ50, Lloyd Instruments, Sussex, UK), was used to apply an elongation to failure. Samples were displaced at 3 different rates; 150 mm min^{-1} (n = 5), 300 mm min^{-1} (n = 5) and 900 mm min^{-1} (n = 4). These displacement rates were equal to 5.56 % s^{-1}, 11.11 % s^{-1} and 33.33 % s^{-1} strain rates, respectively. The stress-strain curves were analysed in the same manner as described in Section 3.2.1.1.

3.2.1.3 Fatigue Properties

A load-controlled cyclic fatigue test was performed on one Dyneema Purity® loop (Cortland, NY, USA) with a linear density of 21120 dtex and a gauge length of 45 mm. The sample was preconditioned under simulated body conditions as described in Section 3.2.1.1.

The sample was pre-loaded over one loading cycle (40-400 N) prior to commencing the test to remove slack from the braided structure of the loop and align the fibres along the loading direction. It was then subjected to sinusoidal loading between 40 and 400 N at a frequency of 1 Hz using an electromechanical test machine (Electroforce 3330, Bose Inc., Minnesota, USA). Time, load and displacement were recorded up to 6.47 million cycles. The loop was wrapped around 2 horizontal pins with diameter of 7.78 mm (Figure 3.2). The true stress, true strain and plastic strain for each loading cycle were calculated using Equations 3-1, 3-2 and 3-3 [186].

$$\varepsilon_{true} = \ln(1 + \varepsilon_{nom})$$ Equation 3-1

$$\sigma_{true} = \sigma_{nom}(1 + \varepsilon_{nom})$$ Equation 3-2

$$\varepsilon_{pl} = \varepsilon_{true} - (\frac{\sigma_{true}}{E})$$ Equation 3-3

3.2.1.4 Creep Modulus

The creep modulus was calculated for each loading cycle of the fatigue test described in Section 3.2.1.3 by finding the ratio of the applied stress to the plastic strain; this was then analysed as a function of time.

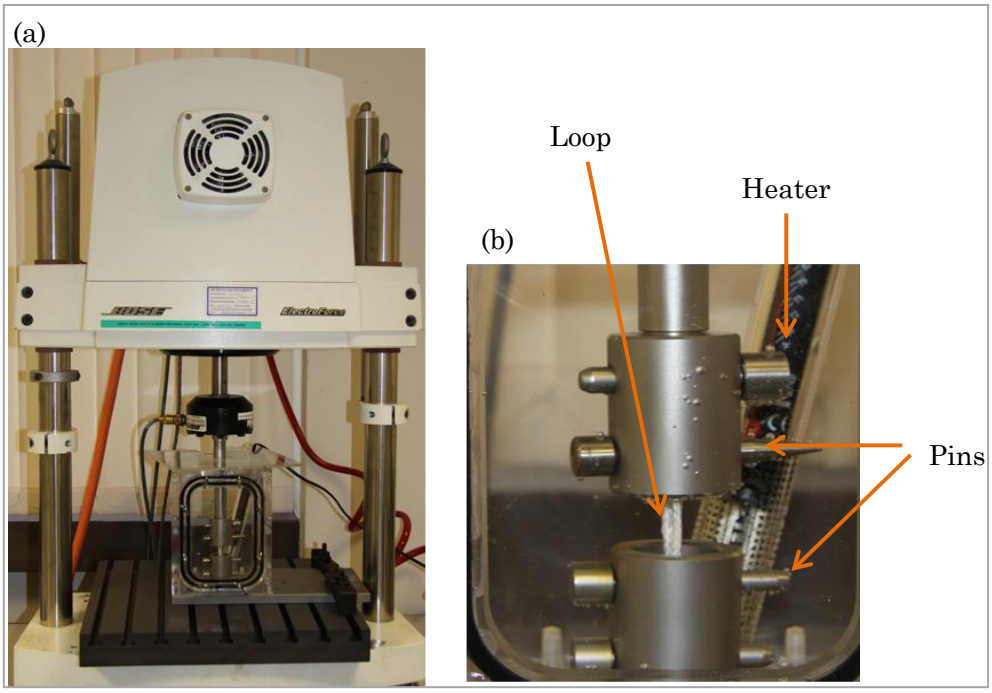


Figure 3.2: (a) Electromechanical test machine used to test the UHMWPE loop. (b) Fatigue test set up in a tank filled with saline, 2 pins were used to hold the loop sample and a heater was used to heat the saline up to 32 ° C ± 2 ° C.

3.2.1.5 Statistical Analysis

Results were expressed as mean ± standard deviation (SD). Two-way and three-way analyses of variance (ANOVA) were used to assess the results of the tests on Dyneema yarns and loops, respectively. As dry Dyneema loops tested at room temperature had a lower linear density (28160 dtex) compared to the other three groups of samples (30480 dtex), the effect of linear density in addition to humidity and temperature was considered. The null hypothesis assumed that humidity, temperature and the linear density had no effect on the UTS and strain.

The results of the strain rate experiment were analysed using a one-way ANOVA test. The mean variance of the UTS of specimens at different strain rates was compared.

These analyses were followed by Bonferroni post-hoc tests to compare all pairs of groups listed in Section 3.2.1.1. A 95 % confidence level was selected to define significance for all statistical tests. GraphPad Prism® (version 5.2, CA, USA) was used to perform all the statistical analyses.

3.2.2 Results

3.2.2.1 Humidity and Temperature Sensitivity

Results of the tensile tests on Dyneema yarns showed that neither humidity ($p = 0.52$) nor temperature ($p= 0.23$) had a significant effect on the UTS; however, increasing humidity significantly ($p < 0.007$) increased the failure strain of the yarns (Figure 3.3). The mean UTS and strain of the samples tested under

simulated body conditions were 3.6 ± 0.37 GPa and 3.98 % ± 0.5 %, respectively (Table 3.1). Figure 3.4 illustrates the nominal stress-strain results of Dyneema yarns tested at simulated body condition.

Results of the statistical analysis on the Dyneema loops, investigating the effect of fibre linear density, humidity and temperature on the UTS and ultimate strain of the samples, showed that only humidity had a significant (p <0.01) effect on the UTS of the loops; the preconditioned samples had lower UTS than those samples that were not preconditioned (Figure 3.5). It was observed that the linear density of the material had a significant (p <0.001) impact on the strain of the Dyneema loops; the tested samples with lower linear density had a significantly larger strain.

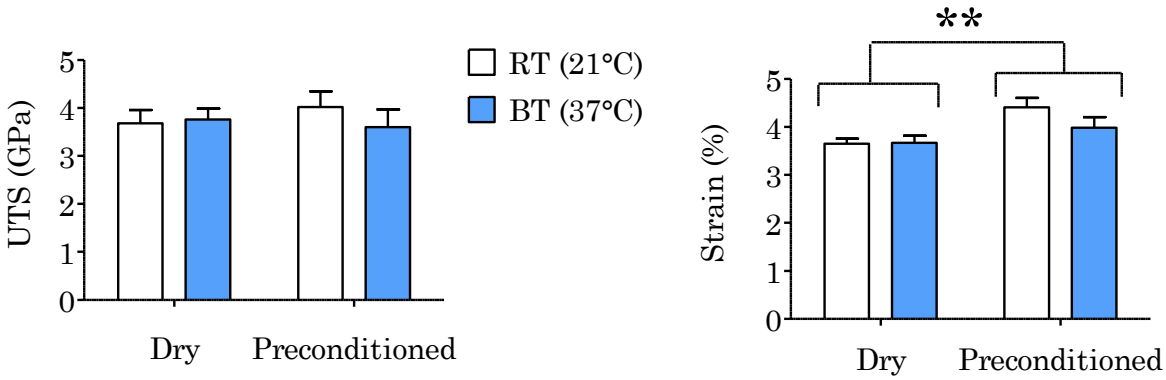


Figure 3.3: Comparison of the mean and standard deviation (SD) of the UTS and strain of Dyneema yarns tested under four different test conditions (** p < 0.01).

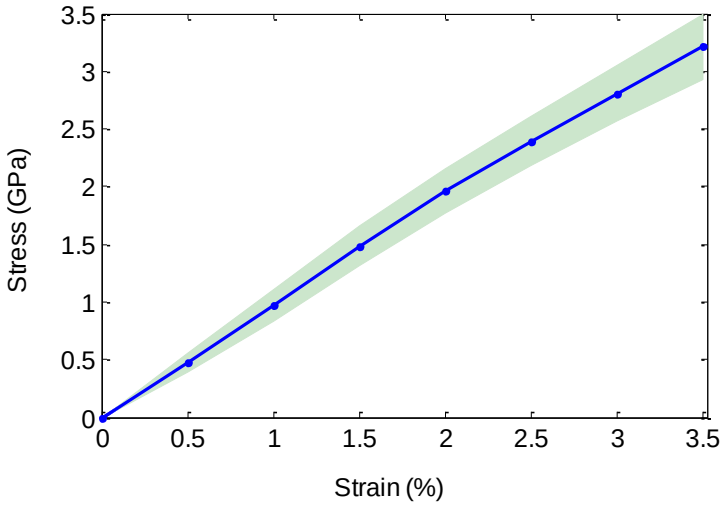


Figure 3.4: Nominal stress-strain graph of five Dyneema yarns (442 dtex) tested under simulated body conditions. The solid line and the shaded area represent mean value and the standard deviation.

Table 3.1: Mechanical properties of Dyneema yarns tested under four different environmental conditions. SD = standard deviation.

Condition		Force (kN)		UTS (GPa)		Ultimate Strain (%)		Elastic modulus (GPa)		Stiffness (N mm^{-1})	
		Mean	SD	Mean	SD	Mean	SD	Mean	SD	Mean	SD
Dry	21 °C	0.17	0.01	3.68	0.28	3.65	0.23	96.57	1.38	22.34	0.25
Dry	37 °C	0.17	0.01	3.76	0.23	3.67	0.33	91.20	2.90	20.88	0.66
Wet	21 °C	0.18	0.02	4.02	0.33	4.41	0.43	94.70	2.04	21.68	0.47
Wet	37 °C	0.17	0.02	3.60	0.37	3.98	0.50	86.42	3.69	19.80	0.85

The effects of humidity (p =0.052) and temperature (p=0.097) on the ultimate strain of the Dyneema loops were not significant. The mean UTS and ultimate strain of the loops tested under simulated body conditions were 1.78 ± 0.08 GPa and 6.42 % ± 0.11 % respectively. Failure of the loops mostly occurred at the area of the loop where the ends of the braided cord were connected to each other via splicing (Figure 3.7).

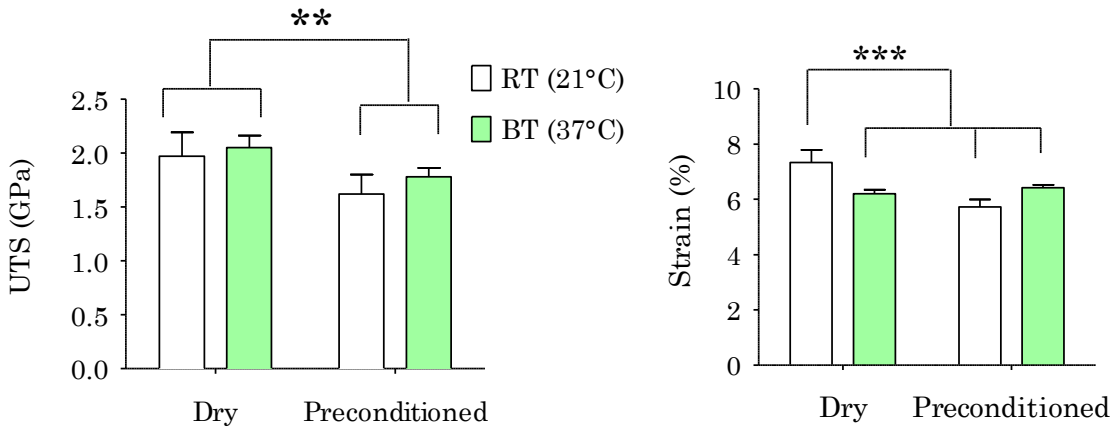


Figure 3.5: Mean and standard deviation of the UTS and the ultimate strain of the Dyneema loops tested at four different test conditions. (** $p < 0.01$), (*** $p < 0.001$).

The stress-strain curve of the tensile tested Dyneema loops under simulated body conditions is shown in Figure 3.6.

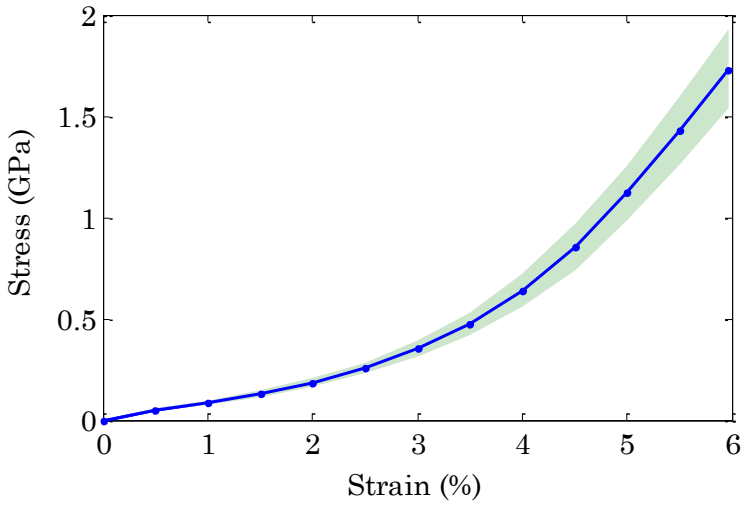


Figure 3.6: Nominal stress-strain graph of braided loops (30480 dtex) tested under simulated body conditions. The solid line represents the mean values and the shaded area represents the standard deviation.



Figure 3.7: 40 mm Dyneema loops tested to failure under tensile load. Failure of the fibre occurred mainly at the spliced region of the loop.

Table 3.2: Mechanical properties of Dyneema loops tested under four different environmental conditions. SD = standard deviation.

Condition		Force (kN)		UTS (GPa)		Strain (%)		Elastic modulus (GPa)		Stiffness (N mm^{-1})	
		Mean	SD	Mean	SD	Mean	SD	Mean	SD	Mean	SD
Dry	21ºC	5.76	0.65	1.97	0.22	7.33	0.46	6.63	0.20	97.97	3.51
Dry	37ºC	6.50	0.34	2.05	0.11	6.20	0.15	7.91	0.45	115.87	5.14
Wet	21ºC	5.16	0.59	1.62	0.18	5.73	0.26	7.57	0.44	112.57	6.59
Wet	37ºC	5.65	0.27	1.78	0.08	6.42	0.11	7.46	0.32	109.79	5.12

3.2.2.2 Strain Rate Effects

The stress–strain curves obtained at the three strain rates presented similar trends for all the specimens (Figure 3.8, Table 3.3). Comparison of the UTS between the three groups of samples showed that the mean UTS of the samples tested at 900 mm min^{-1} were significantly smaller than those tested at 150 mm min^{-1} ($p < 0.01$). No significant difference was seen between the UTS of the other groups (Figure 3.9a).

It was observed that the stiffness of the samples tested at 150 mm min^{-1} were significantly lower than the specimens tested at 300 mm min^{-1} (p <0.05) and those tested at 900 mm min^{-1} (p<0.001) (Figure 3.9b).

Table 3.3: Mechanical test results for Dyneema loops loaded at different displacement rates.

Rate (mm min^{-1})	Force (kN)		UTS (GPa)		Strain (%)		E (GPa)		Stiffness (N/mm)	
	Mean	SD	Mean	SD	Mean	SD	Mean	SD	Mean	SD
150	5.51	0.66	1.25	0.15	0.19	0.01	2.00	0.15	219.57	16.37
300	4.72	0.20	1.07	0.05	0.18	0.03	2.68	0.19	272.00	33.69
900	4.27	0.48	0.97	0.11	0.18	0.02	2.57	0.12	282.45	13.15

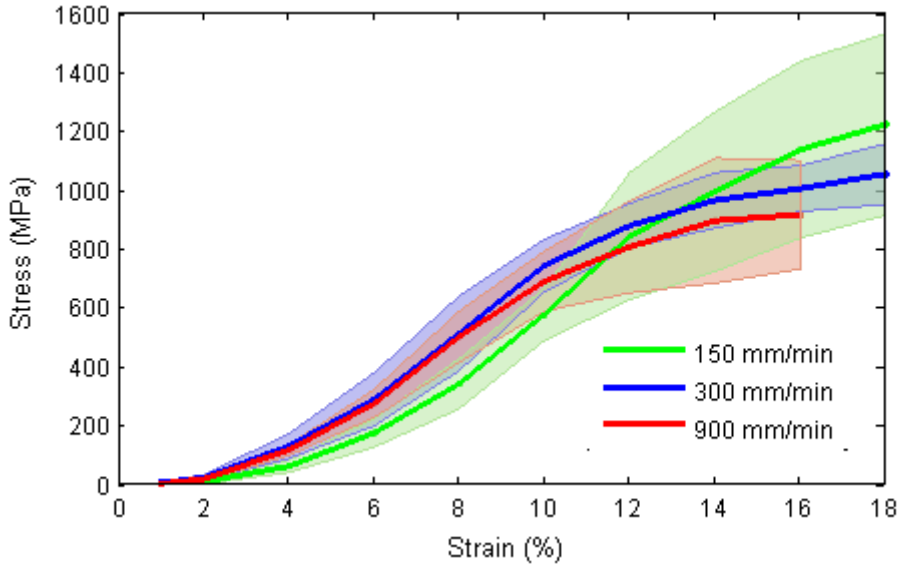


Figure 3.8: Stress-strain curves of three groups of loop specimens tested at 150, 300 and 900 mm min^{-1} displacement rates. The solid lines represent the mean values and the shaded area represents the standard deviation.

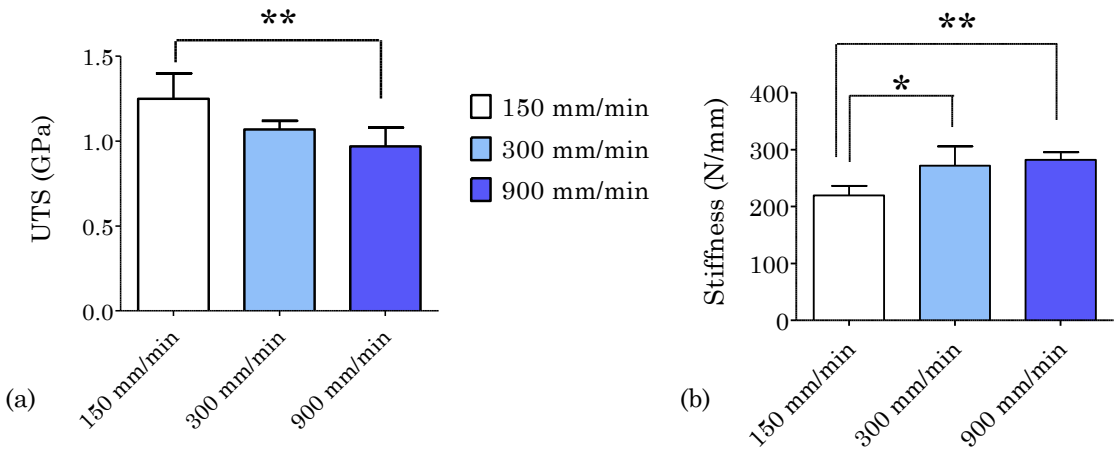


Figure 3.9: Mean and standard deviation of (a) the UTS and (b) the stiffness of the Dyneema loops tested at 3 different strain rates. (* $p < 0.05$) and (** $p < 0.01$).

3.2.2.3 Fatigue Properties

The true stress-strain curves for the fatigue test demonstrated that the hysteresis loop within each cycle, reduced with increasing cycle number (Figure 3.10). Figure 3.11 shows that approximately after 1 million cycles, the accumulative plastic strain of the sample becomes zero and it exhibits plastic shake-down. The plastic strain of the Dyneema loop was found to be very small (Table 3.4).

The modulus of elasticity of the tested sample was calculated from the linear slope of the stress-strain curves corresponding to the stress between 20 to 80 MPa (Figure 3.12). A coefficient of determination (R^2) with minimum value of 0.99 was used to find the best linear fit to the curve (Table 3.4). The elastic modulus of the Dyneema at 1000^{th} cycle reached its steady state value of about 20000 MPa.

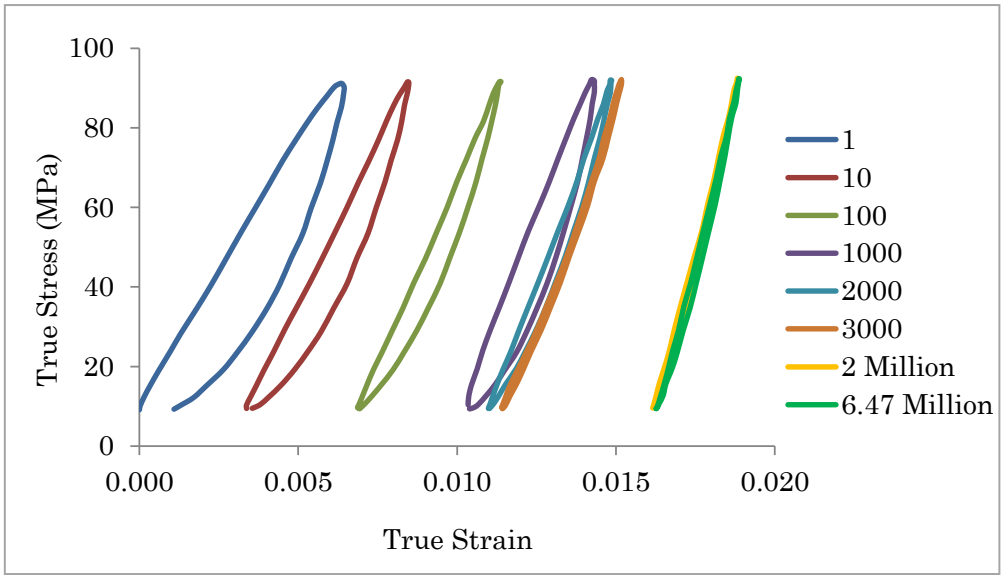


Figure 3.10: True stress-strain curve corresponding to the selected loading cycles of the fatigue tested Dyneema loop.

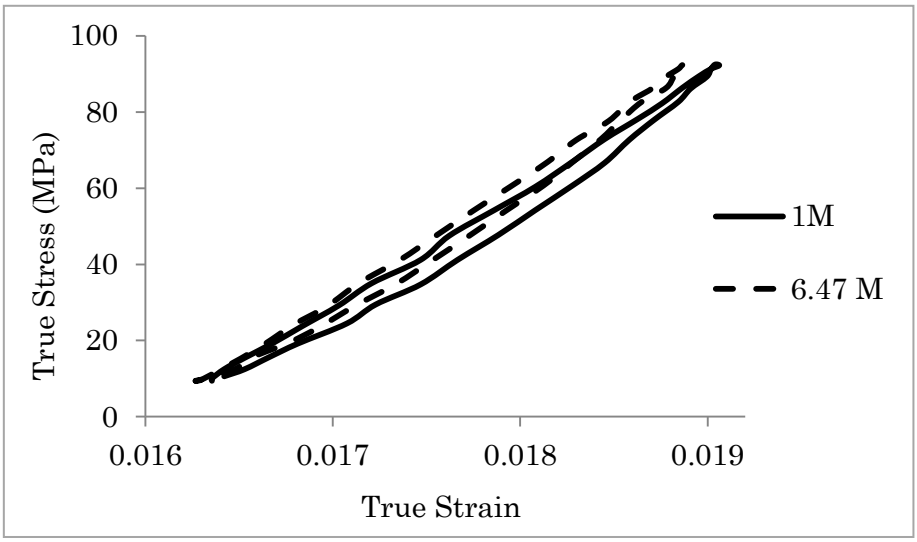


Figure 3.11: Hysteresis curves of the Dyneema loop subjected to a cyclic fatigue test. Sample exhibits plastic shake-down after 1 million (M) cycles.

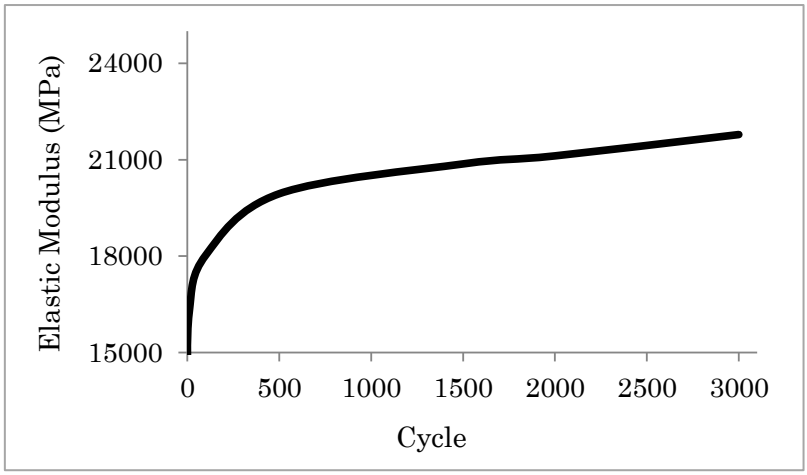


Figure 3.12: Change in elastic modulus of the Dyneema loop with increasing loading cycles.

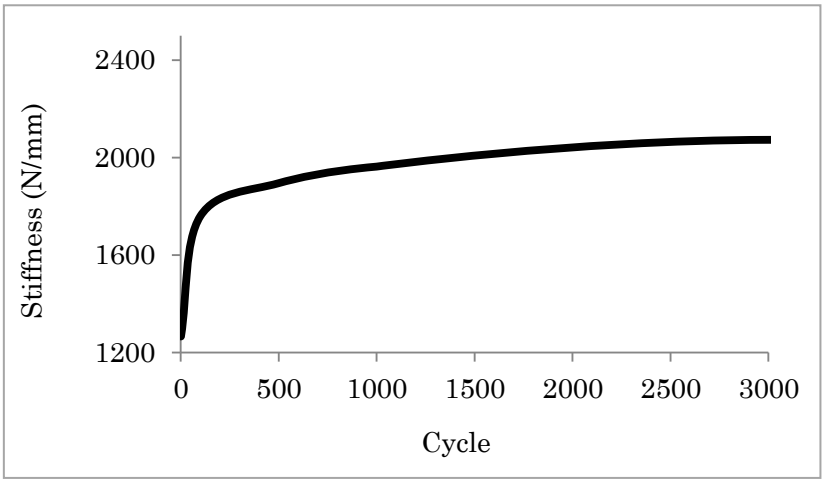


Figure 3.13: Change in the stiffness of the UHMWPE loop with increasing number of loading cycles.

3.2.2.4 Creep Modulus

The creep modulus and creep rate of the tested Dyneema loop reduced significantly with time (Figure 3.14). Table 3.4 summarises the material properties of the tested sample at different loading cycles.

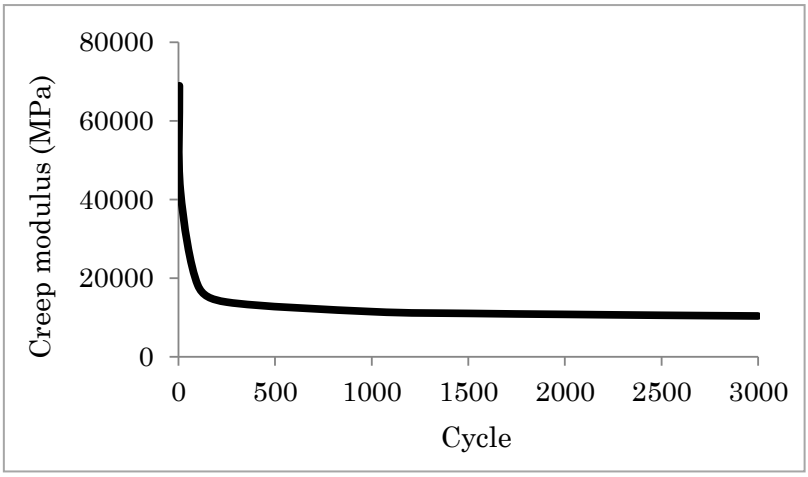


Figure 3.14: Change in creep modulus of the UHMWPE loop with increasing loading cycles.

Table 3.4: Mechanical properties of the Dyneema loop sample subjected to cyclic fatigue test.

Cycle number	Peak stress (MPa)	Plastic strain	Modulus of elasticity (MPa)	Stiffness (N mm^{-1})	Creep modulus (MPa)	Creep rate (hr^{-1})
1	91.125	0.002	13337	1292	-	-
3000	92.137	0.011	21781	2080	10478	0.0106
6470006	94.339	0.033	32642	3019	3118	0.00002

3.3 Finite Element Hardening Models

3.3.1 Methodology

To simulate the change in the mechanical behaviour of UHMWPE loop in the presence of cyclic loading, different plasticity models have been developed. A material model is required to predict the viscoelastic behaviour of the UHMWPE, in particular its sensitivity to time-dependent behaviour such as creep and stress relaxation. However, the combination of viscous effects and

yielding under high strain levels results is a very complex phenomenon and an adequate model has not been developed comprehensively for polymers, particularly when subjected to cyclic loading [178]. The cyclic behaviour of UHMWPE is similar in many ways to the cyclic behaviour of metals; it flows under high constant stress, it kinematically hardens, and it can demonstrate ratcheting and plastic shake-down [187]. Therefore, material models designed originally for metallic parts have been used to represent the behaviour of UHMWPE [178]. Ratcheting refers to the accumulative deformation of a material that is subjected to cyclic loading [188]. After some progressive deformation, if the material reaches a steady state, plastic shake-down occurs with no more accumulation of plastic strain.

In this study, the results of the fatigue test on the Dyneema loop, described in Section 3.2.2.3, are input into different FE hardening models to predict the cyclic behaviour of the loop that will be used as a part of the artificial ACLR system.

3.3.1.1 Boundary Conditions of the Model

UHMWPE has been modelled using various material models throughout the literature; of the standard material models, three are most commonly used; (1) the isotropic hardening model, (2) the linear kinematic hardening model, and (3) the non-linear kinematic hardening model.

In order to investigate which plasticity model best represented the cyclic behaviour of UHMWPE loops, a loading-unloading uniaxial cyclic test was

simulated using ABAQUS finite element analysis software (version 6.11, Simulia, RI, USA).

The model consisted of a single element (T2D3) with circular cross section (A': 4.4 mm^2) and a length (45 mm) equal to UHMWPE loop's gauge length. The cross sectional area of the element was defined to be equal to the cross sectional area of two strands of the loop combined.

Cyclic loading was simulated by applying an alternating tensile load on one end of the FE element with amplitude equal to the experimentally employed sinusoidal loading (Figure 3.15). The end of the FE element which was subjected to cyclic load was allowed to move in the direction of loading, whereas the other end was fully constrained.

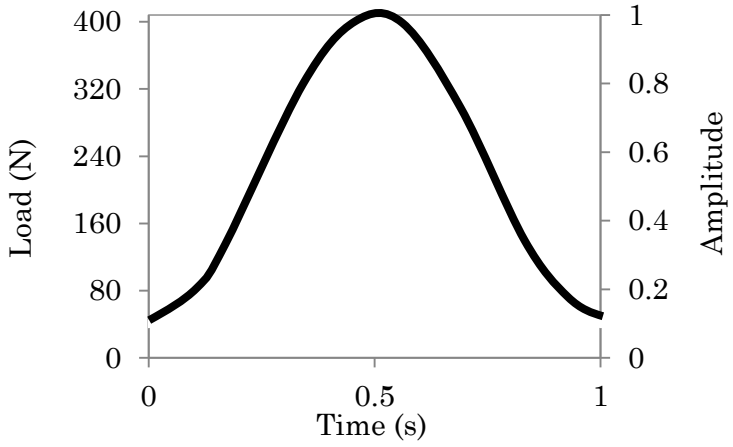


Figure 3.15: Amplitude of one loading cycle used in the FE hardening models of the Dyneema loop.

3.3.1.2 Isotropic Hardening Model

Isotropic hardening theory is based on the assumption that the size of the yield surface changes uniformly in all directions independent of the strain rate

(Figure 3.16a) [178,189,190]. Table 3.5 shows the material properties of the isotropic hardening model that were defined in the ABAQUS simulation using yield stress (σ^0) as a function of plastic strain (ε_p) calculated from Equation 3-1 and Equation 3-3 based on the results of the fatigue test on Dyneema loop (Section 3.2.2.3). These data represent a monotonic curve that is constant for all loading cycles.

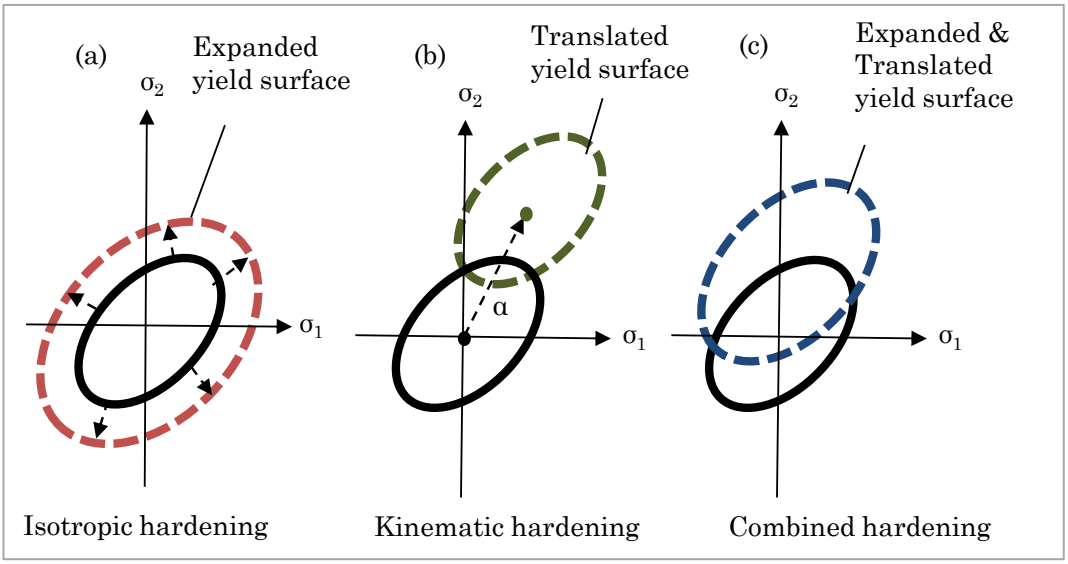


Figure 3.16: Schematic diagram of different hardening models. (a) Isotropic hardening: uniform expansion of the initial yield surface (black ellipse) with plastic strain. (b) Kinematic hardening: translation of the yield surface with plastic strain. (c) Non-linear isotropic-kinematic (combined) hardening: expansion and translation of yield surface with plastic strain. Adapted from Broggiato *et al.*, 2008 [191].

3.3.1.3 Linear Kinematic Hardening Model

The linear kinematic hardening model uses a constant hardening modulus which represents translation of the centre of the yield surface in stress space, while the shape, size and orientation of the elastic region remain unchanged (Figure 3.16b) [178].

Table 3.5: Yield stress and plastic strain of the first half cycle of the fatigue tested Dyneema loop (Section 3.2.2.3) was inputted into the FE isotropic hardening model.

Yield stress (σ^0)	Plastic strain (ε_p)
18.85	0
23.84	0.0003
28.40	0.0005
34.49	0.0008
53.67	0.0016
71.62	0.0024
81.50	0.0029
88.11	0.0034
91.12	0.0037

The Ziegler hardening law which describes the translation of the yield surface in stress space through backstress (α) or shift-stress (Figure 3.16b) was used for the linear-kinematic hardening model (Equation 3-4) [178].

$$\dot{\alpha} = C\frac{1}{\sigma^0}(\sigma - \alpha)\dot{\bar{\varepsilon}}^{pl} \qquad \text{Equation 3-4}$$

where 'C' is the kinematic hardening modulus, σ^0 is the equivalent stress that defines the size of the yield surface and is assumed to remain constant, $\sigma^0 = \sigma|_0$, where $\sigma|_0$ is the equivalent stress defining the size of the yield stress at zero plastic strain; σ is the peak yield stress at plastic strain ε^{Pl}, α is the backstress and $\dot{\bar{\varepsilon}}^{pl}$ is the equivalent plastic strain rate. Table 3.6 shows the linear Kinematic hardening modulus (C) calculated from Equation 3-5. The elastic modulus used in the linear kinematic hardening model was derived from the linear slope of the unloading part of the first hysteresis cycle [178] (Figure 3.10).

These parameters for the linear kinematic material model were input into the ABAQUS simulation.

$$C = \frac{\sigma - \sigma^0}{\varepsilon^{Pl}} \qquad \text{Equation 3-5}$$

Table 3.6: Material parameters used in the linear kinematic model

E (MPa)	σ	σ^0	ε^{pl}	C	Gamma (γ)
34476	91.12	18.85	0.00367	19689	0

3.3.1.4 Non-linear isotropic Kinematic Hardening Model

The non-linear isotropic kinematic (NLIK) hardening model allows the yield surface to expand or contract as well as translating in the stress space (Figure 3.16c). The NLIK hardening law is as described in Equation 3-6 [178,190]:

$$\dot{\alpha} = C\frac{1}{\sigma^0}(\sigma - \alpha)\dot{\bar{\varepsilon}}^{pl} - \gamma\alpha\dot{\bar{\varepsilon}}^{pl} \qquad \text{Equation 3-6}$$

where 'C' is the initial kinematic hardening modulus and 'γ' is a material parameter that defines the rate at which the kinematic hardening modulus decreases with increasing plastic strain. o^0 is the equivalent stress that defines the size of the yield surface and $\dot{\bar{\varepsilon}}^{pl}$ is the equivalent plastic strain rate.

Due to the two unknown material variables detailed in Equation 3-6, 'C' and 'γ', it is not possible to determine these parameters deterministically. A fitting procedure was used to calibrate these parameters based upon the yield surface size and the corresponding equivalent plastic strain; the calibration was performed using in-built ABAQUS functions. The yield stress surface size (σ_i^0)

was found from the stress length of the linear unloading part of the cyclic stress-strain curves measured in Section 3.2.1.3 (Figure 3.10). The value of initial equivalent plastic strain ($\bar{\varepsilon}^{pl}$) was calculated from Equation 3-7.

$$\bar{\varepsilon}^{pl} = \frac{1}{2}(4i - 3)\Delta\varepsilon^{pl} \qquad \text{Equation 3-7}$$

where $\Delta\varepsilon$ is the strain range, 'i' is the cycle number and $\Delta\varepsilon^{pl}$ is the plastic strain range calculated from Equation 3-8:

$$\Delta\varepsilon^{pl} \approx \Delta\varepsilon - \frac{\sigma_1^t}{E} \qquad \text{Equation 3-8}$$

where σ_1^t the peak stress of the first cycle and E is the elastic modulus. Table 3.7 shows the yield stress surface (σ_i^0) and equivalent plastic strain (ε_i^{-pl}) data calculated from the results of the experimental test (Figure 3.10) described in Section 3.2.1.3.

Table 3.7: Material parameters used in the cyclic hardening section of the non-linear isotropic/kinematic hardening model

Cycle (i)	σ_i^0	ε_i^{-pl}
250	18.8	0
1000	16.54	2.75
1500	11.21	3.79
2000	8.83	4.96
2500	8.69	5.86
3000	6.15	6.77

The values of kinematic hardening (C) and gamma (γ) found from the ABAQUS calibration were 22359 MPa and 49.15 respectively

3.3.1.5 3D Model Validation

In order to validate the non-linear isotropic/kinematic model, a 3D loop geometry with similar test set up to that detailed in Section 3.2.1.3 was modelled. The cross-sectional area of the loop was 4.4 mm^2 and the distance between the centres of two rigid pins (of pin diameter 4 mm) was 45 mm, similar to the gauge length of the tested specimen (Figure 3.17). These pins represented the pins used in the fatigue test set up to load the loop (Figure 3.2b). The pins were modelled as analytical rigid surfaces; the cord was meshed with quadratic tetrahedral elements (C3D10) with an average mesh size of 0.7 mm. The centre of one pin was fully constrained, whereas the other pin was allowed to move in the loading direction along the long axis of the loop.



Figure 3.17: Simulation of the fatigue test set up with a 3D loop and two pins, the left pin was fully constrained and the right pin was axially loaded

The loading of the pin was performed in the same manner as detailed in Section 3.2.1.3. Nominal strain was calculated by dividing the pin movement along the loading direction by the length of the loop. The model was subjected to 250 loading cycles and the behaviour of the model between the centres of the pins was studied.

3.3.2 Results

3.3.2.1 Isotropic Hardening Model

The isotropic hardening model gave an accurate prediction of the first half cycle (Figure 3.18), but the residual strain upon the first unloading cycle was over-estimated (0.0037 compared with 0.0011). The shape of the unloading curve from the finite element model was linear, whereas the experimental results had a non-linear unloading curve, which gave rise to the over-estimated strain. Cyclic hardening and creep could not be accurately modelled using the isotropic hardening model because it is independent of the cycle number.

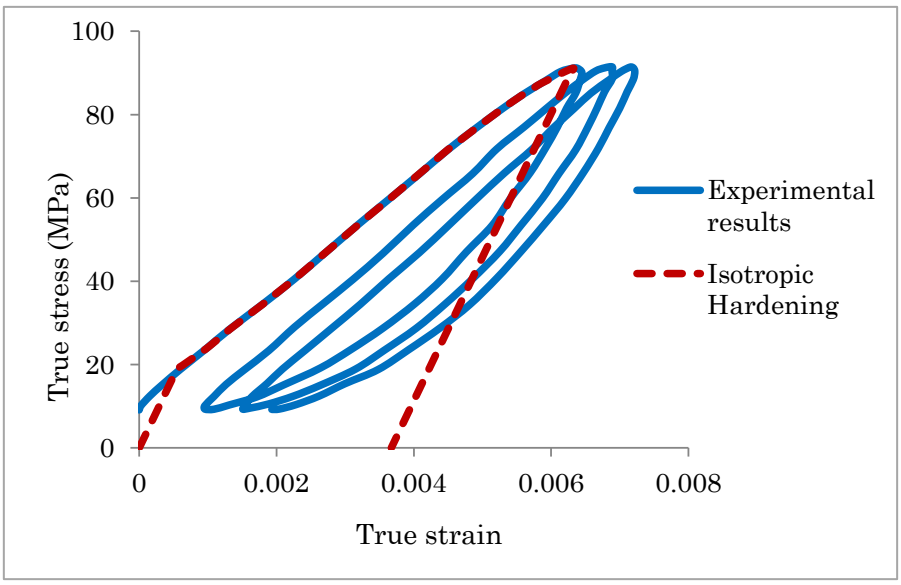


Figure 3.18: Comparison of the isotropic hardening model results and experimental data from Section 3.2.1.3 for the first 3 loading cycles.

3.3.2.2 Linear Kinematic Hardening Model

By implementing the linear kinematic hardening rule, residual strain upon unloading for the first cycle was 0.0017, which still did not correspond well with the experimental value of 0.0011 (Figure 3.19). The linear kinematic model gave a reasonable prediction of cyclic behaviour for the first half cycle; however, the peak strain remained the same after cycling and the shape of the hysteresis did not change. The resulting hysteresis curve had a multi-linear shape, but still did not reproduce the non-linear behaviour observed experimentally.

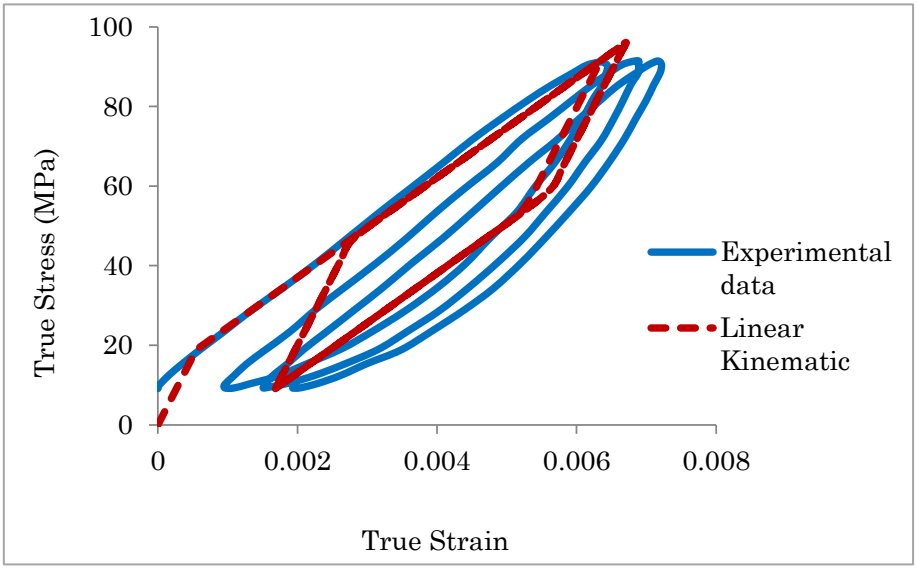


Figure 3.19: Comparison of the linear kinematic hardening model results with experimental data from Section 3.2.1.3 for the first 3 loading cycles.

3.3.2.3 Non-linear Kinematic Hardening Model

The growth rate of peak strain observed experimentally was 102.46 % (from 0.0064 to 0.0129) over 250 cycles, whereas the FE model exhibited a 2188.31 % increase in the strain (from 0.006 to 0.142) over 250 cycles. Although the

model was relatively accurate over the first 5 cycles (Figure 3.20); as observed with the other models, the residual strain upon unloading was higher than found experimentally. In addition, the model did not accurately represent the shape of the stress-strain cycle observed experimentally.

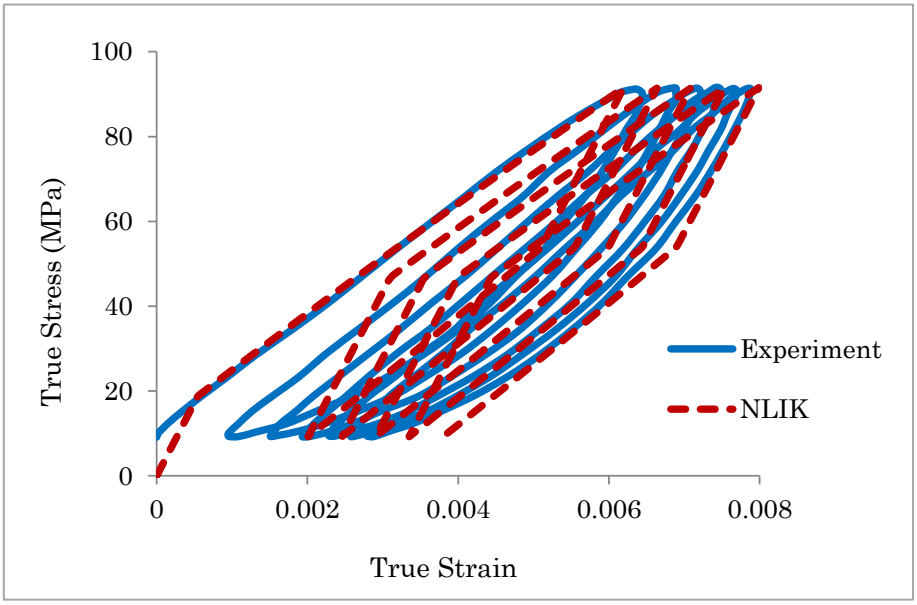


Figure 3.20: Comparison of the non-linear isotropic/kinematic (NLIK) hardening model results with the experimental data from Section 3.2.1.3 for the first 10 cycles.

3.3.2.4 3D Model Validation

The shape of hysteresis stress-strain cycles was improved when using the non-linear isotropic material model with the 3D loop geometry; indicating the geometrical dimensions of the tested specimen may have influenced the parameters (Figure 3.21). The growth rate of the peak strain for the finite element model was 1817.46 % (from 0.0066 to 0.1271) over 250 cycles which was closer to the 102.46 % increase observed experimentally than predicted by the other models; but was still significantly different.

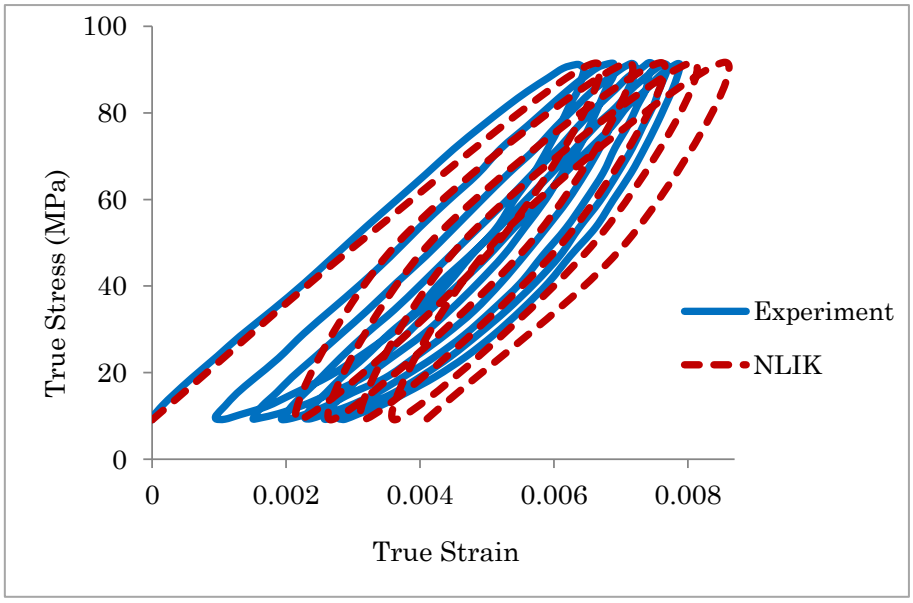


Figure 3.21: Comparison of the non-linear isotropic/kinematic hardening (NLIK) model prediction of the Dyneema loop model with experimental data from Section 3.2.1.3 for the first five loading cycles.

3.4 Discussion

UHMWPE fibre (Dyneema) was identified as one of the potential materials to be used in the connecting cord of the artificial ACL. In order to evaluate the mechanical behaviour, a series of tensile tests were carried out in different environmental conditions. Temperature did not affect the mechanical properties of the tested samples; however, humidity significantly reduced the UTS of Dyneema loops. There is evidence that fluid uptake can affect the mechanical properties of UHMWPE [192–194]. As fluid cannot be avoided *in-vivo,* the Dyneema cord should be over-engineered to minimise the effect of humidity on the tensile failure load. This can be achieved by increasing the linear density of the textile structure or using more loops in parallel.

The difference between the shapes of the stress-strain curves obtained from the tensile test on the Dyneema yarns and loops were due to the difference in their textile structures; yarns were made of multiple filaments that were approximately parallel to each other whereas the loop samples were made of braided yarns intertwined in an angle. Therefore, the higher slack in the braided loop construct caused a more non-linear stress-strain curve.

The ultimate tensile load of the loops tested at simulated body condition was 2-3 times higher than that of the ACL in young (22-35 years) adults measured by Woo *et al*,[80]. The UTS of the same loops was found to be 70 times higher than that of the native ACL in young human (16-25 years) reported by Noyes and Grood [79].

The elastic modulus and strength of the viscoelastic polymers has been reported to be higher at high strain rate or low temperatures [169]. An increased strain rate can cause UHMWPE to behave in a brittle manner instead of ductile [2]. Results of this study showed that higher strain rates significantly increased the elastic modulus of the Dyneema loops. The displacement rates used in this test were equivalent of 5.56 % s^{-1}, 11.11 % s^{-1} and 33.33 % s^{-1} strain rates. The native ACL has also been shown to demonstrate an increased modulus in response to higher strain rates. Pioletti and co-workers [195] reported that an increased strain rate mostly affects the initial part (toe region) of the stress-strain curve of the ACL-bone complex. The authors found approximately 3 times larger stress at 4% strain in the samples tested at 40 % s^{-1} compared to those tested at 0.1 % s^{-1}.

Russell and co-workers [196] investigated the effect of strain rate on the mechanical properties of Dyneema yarns. The authors reported that the failure strength and strain of the yarn was almost insensitive to strain rate within the range of 10^{-1} to 10^{3} s^{-1}, which is contrary to the findings of this study. However, although the loops are constructed from the yarns, it may be that the braided structure of the loops induces the strain dependent behaviour. Haunge *et al.* [197] studied the impact of strain rate (300 s^{-1} and 700 s^{-1}) on Dyneema fiber bundles and found that increasing strain rate decreased strain, supporting the concept that the Dyneema structure can influence strain dependence.

The UTS was significantly smaller in the group of samples tested at 900 mm min^{-1} compared to those tested at 150 mm min^{-1}. The sample failure occurred in the spliced end of the loops, which may indicate that the splicing method cannot produce a link equally strong as the Dyneema cord.

The fatigue behaviour of UHMWPE depends on its material purity, crystallinity, irradiation, oxidation, and geometry [131,167,198]. Therefore, some of these factors should be taken into account when comparing the results of the current study with those obtained in the literature. In particular, the UHMWPE specimens tested in this study were made of braided Dyneema fibres with spliced ends to form a complete loop. As the test was controlled by load and not displacement, specimens exhibited cyclic hardening behaviour as the peak stress increased over time; however, this increment was very small (0.8 % over 250 cycles). Most polymers tested under displacement controlled

cyclic loads display plastic softening [178,199]. Thermal effects also can cause a major softening effect on the polymer; however, the presence of saline solution in the test environment in this study would have minimised local temperature fluctuations. The hysteresis exhibited during loading reduced with increasing cycles, it is likely that this was as a result of alignment of the fibres in the direction of loading reducing laxity in the cord. This effect has been reported in other studies on UHMWPE [178,179,200] and was also visually inspected on the tested sample.

It was observed that the tested loop specimen continued to ratchet up to 1 million cycles, with the hysteresis curves moving continuously in the direction of increasing strain (Figure 3.10). After 1 million cycle, the specimen exhibited shake-down with no more accumulative plastic strain.

The ACL is exposed to cyclic load at a frequency of approximately 1.6 Hz during fast walking [2]. In this study, a frequency of 1 Hz was chosen to represent the normal level walking speed for an average adult (ISO 14243-1) [201]. In the study by Avanzini [178] which examined solid UHMWPE specimens, it was reported that the cyclic steady-state was reached after 250 cycles, when the stress changed no more than 1 % in 100 continuous cycles. However, in the current study, although the difference between peak stresses for every 100 continuous cycles remained smaller than 0.5 %, a true steady-state was not reached until 3000 cycles.

When designing an artificial ACL, it is important to minimise the creep [132] in order to obtain reproducible mechanical behaviour throughout the lifetime of

the device, because the elongation of the ligament has a direct influence on the joint's stability and kinematics. For this device, the Dyneema cord is considered to be the connecting link between the elastic systems, therefore it must have a high resistance to creep and plastic softening to ensure the elastic systems are loaded. The fatigue test results showed that the creep modulus reduced as the number of loading cycles increased, and the modulus stabilised by 3000 cycles; this indicates creep would only be a potential issue immediately after implantation, and this effect could be reduced by pre-loading the device.

Several material hardening models were considered to describe the behaviour of the Dyneema loops. All of the models, particularly the classical isotropic plasticity model, over-predicted the residual plastic strain upon unloading [202]. Material parameters found from the non-linear isotropic/kinematic hardening plasticity model were used to find a good prediction of the cyclic behaviour of the UHMWPE loop for the first few (<5) loading cycles. It can be concluded that the material parameters obtained from the constitutive modelling in this study can be used to predict the early cyclic behaviour of the UHMWPE cord in the artificial ACL system; however, accurately modelling the long-term cyclic behaviour of this UHMWPE cord would require further work. As the cyclic properties of the cord were shown to stabilise by 3000 cycles (which would be reached at a relatively early time point clinically) the cord will be modelled as being in the steady state condition in the later chapters of this thesis.

3.5 Conclusion

The first section of this chapter considered the effect of different environmental conditions such as humidity, body temperature and varying strain rate on the load-elongation behaviour of the Dyneema yarns and braided loops. As humidity significantly reduced the UTS of the braided Dyneema loops, it can be concluded that when designing and testing a Dyneema construct for human implantation, the effect of humidity should be considered. Increasing the linear density of Dyneema loops could significantly reduce the ultimate strain of the designed construct and increase the ultimate tensile load and accommodate for the effect of humidity.

The second section of this chapter described the development of a number of different FE material hardening models to predict the cyclic behaviour of the Dyneema loops. Material parameters found from the non-linear isotropic-kinematic hardening plasticity model in this study were shown to provide a good prediction of the early cyclic behaviour of the Dyneema loop; however, accurate long term prediction of the cyclic behaviour requires further work.

Chapter 4: Spring System

4.1 Introduction

Two different design options for the elastic part of the artificial ACL were outlined in Chapter 2. The first option was chosen for the artificial ACL as a stand-alone system, and consisted of two helical springs with a Dyneema cord connecting them together. The second option was chosen for the artificial ACL to be used in combination with TKR implants, and consisted of a tibial spiral spring and a femoral helical spring connected to each other via a Dyneema cord (Figure 4.1).

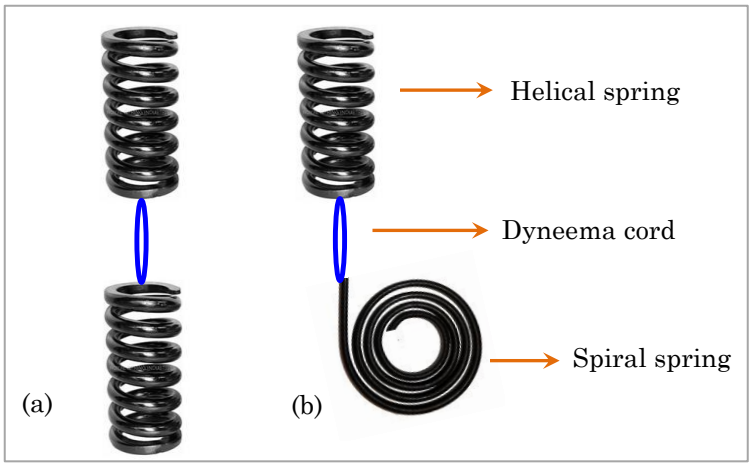


Figure 4.1: Design options for (a) stand-alone ACLR and (b) ACLR for TKR.

The purpose of this chapter was to study the selected elastic system in more detail by performing preliminary mechanical tests and FE analysis, and to optimise the spring designs so that they mimic the load-elongation behaviour of the native ACL (Section 2.2), while also fitting within the defined size constraints for medium size patients (Section 2.4). In this study, preliminary mechanical tests were performed on metal helical compression springs and

spiral springs with different stiffness parameters. FE models of the same springs were then created and the results of the FEA were validated against the mechanical tests. Parametric analyses were performed to evaluate the effects of changing the dimensional geometry of the springs on their stiffness. A probabilistic study was also performed with the aim of finding the effect of varying dimensional factors within the manufacturing tolerances on the stiffness of the spiral springs.

4.2 Methodology

4.2.1 Helical Spring

Helical springs are one of the most common types of springs and are made of elastic materials formed into the shape of a helix. Metal helical springs can be made by winding a wire around a cylinder or by machining the spring out of a solid bar. The spring wire can have a rectangular cross section. Helical springs can be tensile, compressive or torsional. Helical tensile springs are designed to resist tensile load and are usually attached to a hook or eyelet at each end. Helical compression springs resist compressive load and are most typically used in car suspension systems. Helical torsional springs are designed to resist twisting moment. Some of the advantages of helical springs are their ease of manufacturing, availability in a wide range, and reliability.

4.2.1.1 Mechanical Test

Four different machined CoCrMo alloy helical compression springs (Heli-Cal Ltd, California, US) were mechanically tested in this study (Table 4.1). An

electromechanical test machine (Lloyd EZ50) with a 500 N load cell was used to apply a compressive load on the springs.

As the springs of the artificial ACL will be within containers which restrict their loading to be only axial (Section 2.6), the helical springs were examined only under axial loading conditions. The maximum load applied to each spring was the safe loading suggested by the spring manufacturer (Table 4.7). Springs were positioned between two flat fixtures; the lower fixture was fully constrained, whereas the upper fixture applied a compressive load on the specimen through the actuator (Figure 4.2). Three samples of each type of spring were tested and each test was repeated three times.

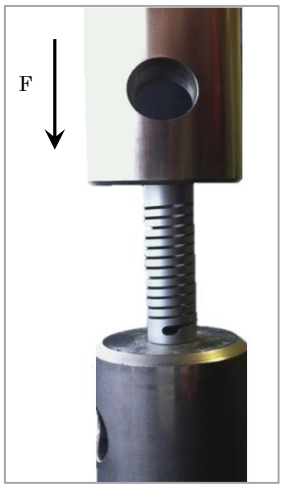


Figure 4.2: Compression testing of a metal helical spring between test fixtures. 'F' represents the direction of compressive force applied on the spring.

Table 4.1: List of the helical compression springs tested, with their dimensions: inner diameter (ID), outer diameter (OD), and length.

Spring	ID (mm)	OD (mm)	Length (mm)	Width (mm)	Thickness (mm)	Pitch angle (º)	Number of coils
A (20738)	5.79	8	35	1.11	0.97	4.9	10.5
B (20739)					1.1	5.5	11.5
C (20690)	6.35	10	40	1.83	1.5	5	11.5
D (20691)					1.8	5.2	11.5

4.2.1.2 Finite Element Analysis

ABAQUS software (version 6.11, Simulia, RI, USA) was used to simulate axial (tangential) loading of the FE models of the helical compression springs listed in Table 4.1. The CAD models of the helical springs were created by their spring manufacturer (Heli-Cal, California, US).

In order to select a suitable mesh size for the spring models, a mesh convergence study was performed using the ABAQUS meshing algorithm to create 3D quadratic tetrahedral elements (C3D10M). Mesh seed densities of 0.4, 0.5, 0.6, 0.7, 0.8, 0.9, 1, 1.5, 2 and 3 mm were applied on the spring model 1, and the maximum displacement and von Mises stress were recorded for each mesh refinement**.** The mesh was defined as converged when the difference from the previous point was less than 1 %. An element size of 0.7 mm was found to be the most suitable size that did not compromise the accuracy of the simulation, but minimised the computing time of the analysis (Figure 4.3).

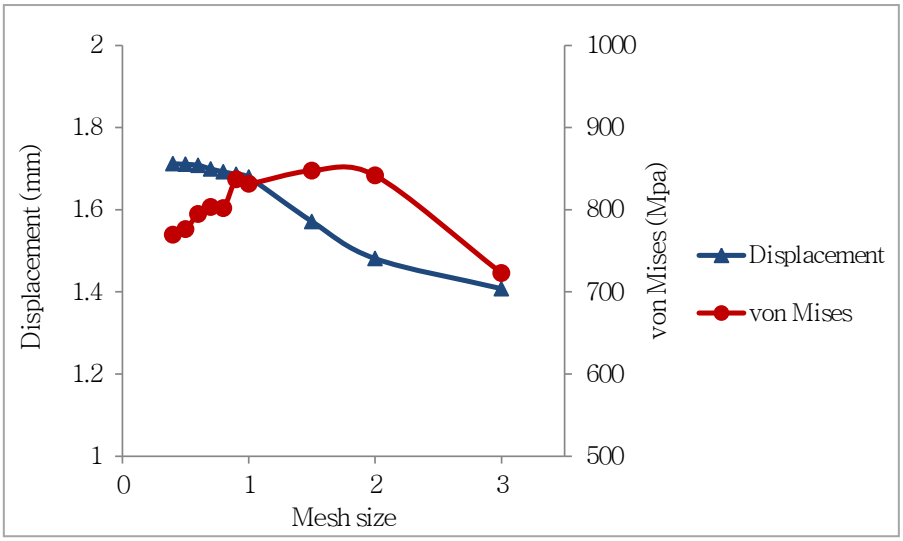


Figure 4.3: Mesh convergence study on the helical compression spring.

All of the helical compression spring models used in the mesh sensitivity test as well as the FE compression test (Table 4.4) and parametric study (Table 4.5), were fully constrained at one end and a compressive load was applied to the other end. The non-linear material properties of the CoCrMo alloy were assigned to the FE models based on the true stress-true strain data and elastic modulus reported in the literature [203] (Table 4.2). Plastic strain was calculated using Equation 3-3. Load and displacement along the long axis of the spring models were recorded so the results could be compared directly to the mechanical test results.

Table 4.2: Material properties of Co-Cr-Mo alloy used in the FE models of the helical springs

E (MPa)	Poisson's ratio	Yield stress (MPa)	Plastic Strain
241,317	0.3	722	0
		948	0.0027
		1316	0.0211

4.2.2 Spiral Spring

A spiral spring with a rectangular wire was developed with central and end attachments. The central attachment added strength to the spring and helped to house the spring in a small box-shaped cavity for implantation (Figure 4.4). The spiral spring was designed to be positioned in the tibial pocket so that the bollard head would be aligned at about 45 º towards the ACL's isometric fibre attachment point on the femur at full extension. The end attachment was used for connecting the Dyneema cord to the spring.

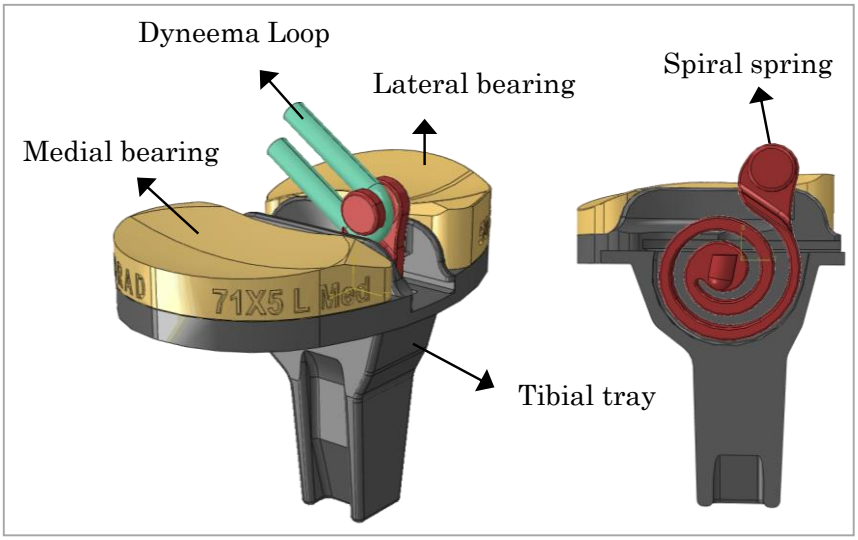


Figure 4.4: Location of the spiral spring in the tibial tray used for TKR.

4.2.2.1 Mechanical Test

Based on the defined size constraints for an artificial ACL in a Vanguard TKR tibial tray (Section 2.4), 2 spiral springs with a rectangular cross-section were designed. Six CoCrMo alloy spiral springs were designed and manufactured (Biomet UK Healthcare Ltd., Swindon, UK) for the artificial ACL system. Three springs had a thickness of 1.7 mm, and three had a thickness of 2.2 mm

(DD14023-1.7 and DD14023-2.2) (Table 4.3). The spiral springs were manufactured using a wire cutter. An endpin (bollard) was laser welded to the outer end of the spring to provide secure attachment for the Dyneema loop. The endpin was positioned horizontally to allow correct loading direction between the connecting cord and the spring. The central part of the spring where it would be fixed to the tibial tray was fully constrained.

As the flat spiral springs will not be constrained within a container, their performance under both axial (tangential) and rotational loading conditions must be considered. Due to the limited number of available spiral spring samples, it was decided to only conduct the torsional loading tests mechanically, as these best represented the expected loading during knee flexion. However, both axial and rotational loading was tested using FEA.

Table 4.3: Dimensions of the spiral spring prototypes designed for the artificial ACL (see Figure 4.10).

Spring	Wire thickness (*t*)- (mm)	Gap (*h*)- (mm)	Wire width (*b*)- (mm)	OD- (mm)	Number of coils
DD13864-1.7	1.7	2	5.25	20.25	1.5
DD13864-2.2	2.2	1.8		20.59	

A torsional test rig available in Biomet UK Healthcare Ltd was modified for this experiment (Figure 4.5). The test rig comprised a central disc connected to a metal cord. The metal cord was connected to an electromechanical test machine (Lloyd-EZ50, UK); vertical movement of the actuator pulled a metal cord (E) which caused the central disc to rotate. The centre of the spiral spring (C) was fitted in a fixture (B) and was positioned on the centre of the rotating

disc, whereas, the head of the spring rested on a metal block (D). As the centre of the spring rotated anti-clockwise, the head of the spring was compressed against the metal block resulting in the spring deformation. A displacement was applied by the actuator at a rate of 60 mm min^{-1}.

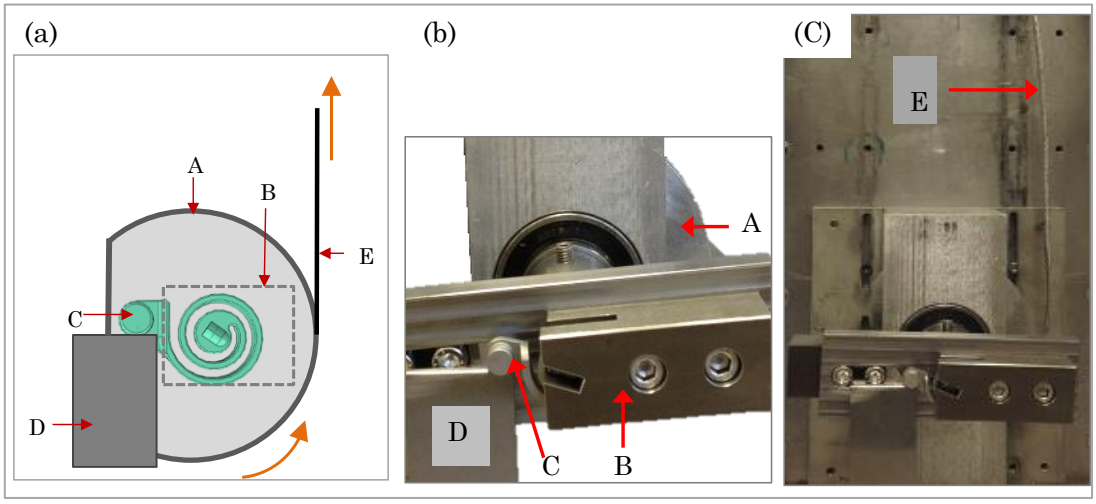


Figure 4.5: (a) Schematic diagram of the torsional test rig, (b) and (C) Torsional test rig used to test the spiral springs. A= Rotational disc, B = Spring fixture, C = Spiral spring, D = Rigid block, E = Metal cord.

4.2.2.2 Finite Element Analysis

Both the axial (tangential) and torsional loading of the flat spiral spring were simulated using ABAQUS software (version 6.11, Simulia, RI, USA). The spiral spring geometries were modelled using NX-UniGraphics (NX7.5, Siemens, NJ, USA) software. The geometries were then converted to a parasolid format for pre-processing, solving, and post-processing. The CoCrMo alloy material definition used was the same as detailed in Table 4.2. The springs were meshed with quadratic tetrahedral elements (C3D10M), of size of 0.7 mm. The mesh size was determined as a result of a mesh sensitivity test (Figure 4.6).

When simulating the axial (tangential) loading test, the central part of the spring was fully constrained in all degrees of freedom and an axial load of 500 N was applied to a point on the surface of the bollard head (Figure 4.7b). Load and displacement (U) of the loaded point were recorded and consequently the stiffness of the spring was calculated.

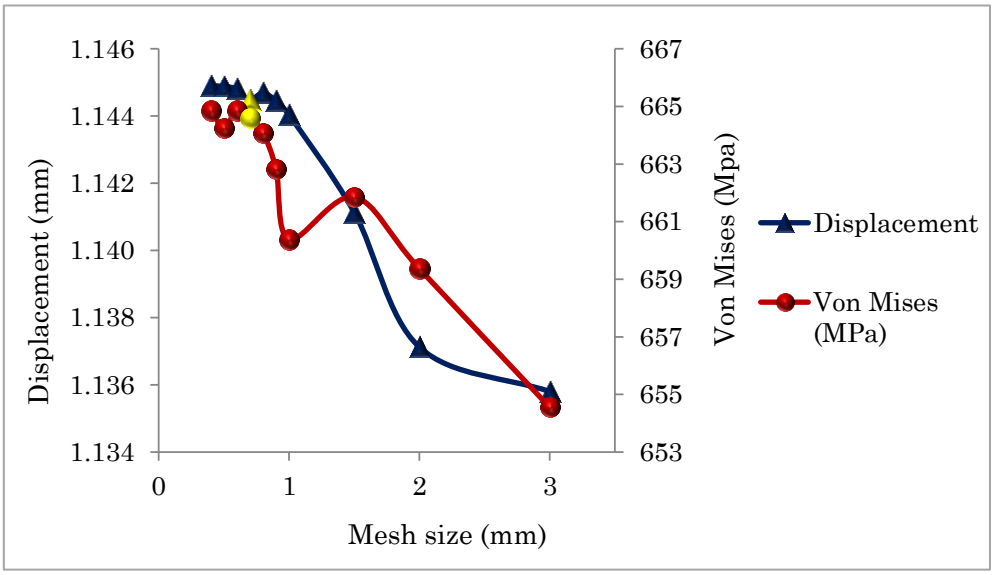


Figure 4.6: Mesh convergence study on the spiral spring.

In order to load the springs along their spiral path in the torsional test, the head of the spring was positioned against a rigid bar (3.5 mm OD) and a rotation of 2 radians (UR3) was applied to the central point of the spring (Figure 4.7c). The reaction force at the centre of the rigid bar corresponding to the rotation of the centre of the spiral was measured at each time step. To find the overall displacement of the springs, the rotational displacement of the spiral centre in radians was multipied by the radius of the spiral; the radius was 15.06 mm for the spiral spring with a thickness of 1.7 mm, and 17.96 mm for the spring with a thickness of 2.2 mm.

Models were solved non-linearly to accurately investigate the plastic deformation of the springs. Self contact (surface to surface) was defined between the spiral coils and also contact was defined between the spring and the rigid bar with a frictionless contact interaction property.

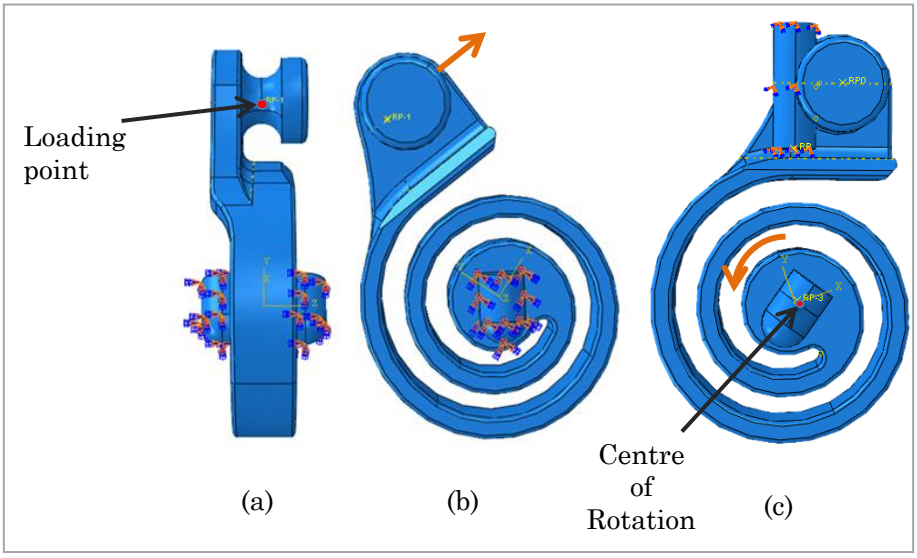


Figure 4.7: (a), (b) Side and front views of the spiral spring models tested under different loading conditions; tangential load was applied to the spring's head and the centre of the spring was fully constrained, c) rotational displacement applied to the centre of the spring and the movement of the head was restricted by a rigid bar.

4.2.3 Parametric & Probabilistic

4.2.3.1 Helical Spring

4.2.3.1.1 Parametric Study

When designing a mechanical system, it is important to characterise the effect of changing various dimensions on the outcome of the design, which in this case is the stiffness of spring. The aim of this study was to assess the sensitivity of the spring stiffness to changes in a number of geometrical

parameters, such as the number of coils (*n*), the thickness of wire (*b*), the height of wire (*t*), and the pitch angle (α). These parameters are used to calculate the stiffness of a simple helical spring (Figure 4.8 and Appendix 1). This was performed parametrically and the stiffness was assessed using the finite element method.

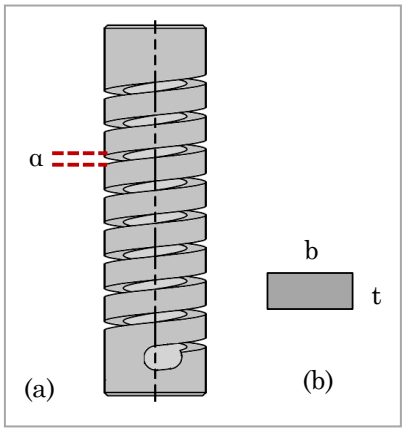


Figure 4.8: (a) Schematic diagram of a helical compression spring with (b) a rectangular wire. '*b*' is the width and '*t*' is the thickness of the wire ($b > t$).

Each design parameter was varied one at a time while keeping the others constant; interaction between the factors was not permitted. The internal diameter of the springs remained constant (5 mm), therefore, change in the external diameter resulted in changing the thickness (*t*) of the spring wire. The 3D computer-aided design (CAD) models of the helical springs were created by Heli-Cal Ltd. (California, USA) using predefined parameters listed in Table 4.4. ABAQUS was used to perform FEA on the spring models.

One of the limitations of the design was that the pitch angle could not be kept constant for models 6 to 17 due to the nature of the helical spring's design, shape and geometry (Table 4.4).

In addition to the analysis that was performed on the helical compression spring models listed in Table 4.4, further analyses were performed on a number of springs within the size constraints defined in Chapter 2. This analysis helped to validate the parametric study results and confirm the relationship between the geometrical factors (within the size constraints) and the stiffness of the helical compression springs. Table 4.5 shows the dimensions of the designed springs that were analysed in this study. Safe load limits suggested by the manufacturing company were applied to each model.

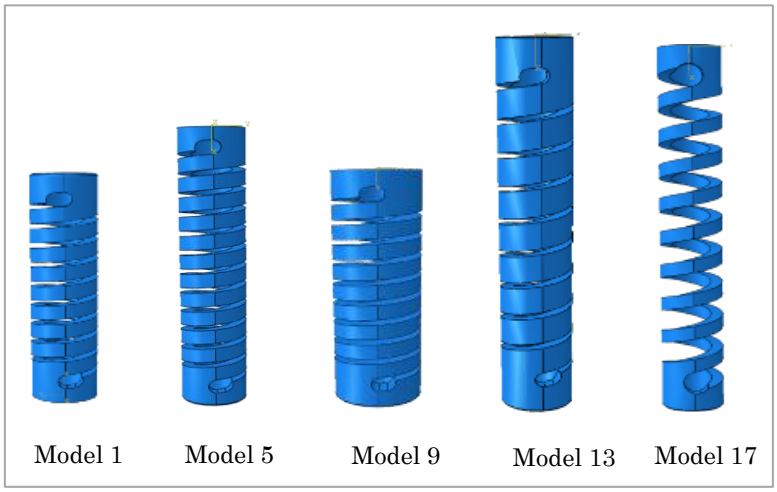


Figure 4.9: Examples of the helical compression spring models used in the parametric study. Model 1 is the control model, model 5 had an increased number of loops, model 9 had an increased thickness of wire, model 13 had an increased height of wire, and model 17 had an increased pitch angle compared to the control model.

Table 4.4: Helical spring models with variable dimensional parameters within the size constraints of artificial ACL were used in the parametric study.

Helical spring Model		Number of coils	Thickness (mm)	Height (mm)	Pitch angle (°)
1	Control group	8	1.5	2	6.3
2	Number of coils	7	1.5	2	6.3
3		9	1.5	2	6.3
4		10	1.5	2	6.3
5		11	1.5	2	6.3
6	Thickness (mm)	8	1	2	7.2
7		8	2	2	5.6
8		8	2.5	2	5
9		8	3	2	4.6
10	Height (mm)	8	1.5	1.5	5.2
11		8	1.5	2.5	7.4
12		8	1.5	3	8.6
13		8	1.5	3.5	9.7
14	Pitch angle (°)	8	1.5	2	5.7
15		8	1.5	2	8.1
16		8	1.5	2	10
17		8	1.5	2	11.9

Table 4.5: Length, inner diameter (ID) and outer diameter (OD) of some of the designed helical springs for the artificial ACL within the defined size constraints.

Spring	Length (mm)	ID (mm)	OD (mm)
A	35	5.79	8
B	35	5.79	8
C	40	6.35	10
D	40	6.35	10
E	35	5	8
F	30	5	8
G	35	5	8

4.2.3.2 Spiral Spring

4.2.3.2.1 Parametric Study

The effects of key dimensional factors on the stiffness of the spiral springs were investigated, and also the sensitivity of the spring's stiffness to varying geometrical factors within their manufacturing tolerances was assessed.

In order to model a simple spiral, its radius at each point was calculated by '$r_0 + \Delta\theta$'. Where 'r_0' is the initial radius of the spiral, 'Δ' = δ / 2π, 'δ' = $h + t$, 'h' is the gap between a complete coil, 't' is the thickness of the wire and 'θ' is the revolution angle (in radians) (Figure 4.10) (Appendix 2).

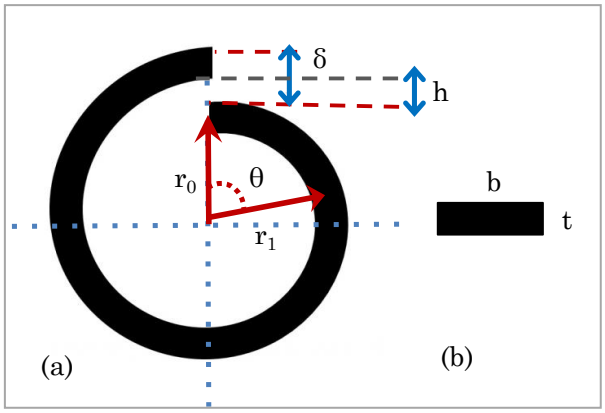


Figure 4.10: (a) Schematic diagram of a flat spiral spring and (b) its cross section; 'b' is the width and 't' is the thickness of the rectangular wire ($b > t$).

Each geometrical factor of thickness (t), width (b), initial radius (r_0), and gap between turns (h) was varied one at a time while keeping the other factors constant. Interaction between the parameters was not permitted.

For the analysis it was necessary to simplify the geometry of the flat spiral spring, Figure 4.11 illustrates some of the typical simplified spiral spring geometries used in this study. Table 4.6 summarises the parameters examined

for the parametric analysis of the spiral springs. The inner end of the spiral was fully constrained, whereas an 80 N force was applied to the outer end of the spiral.

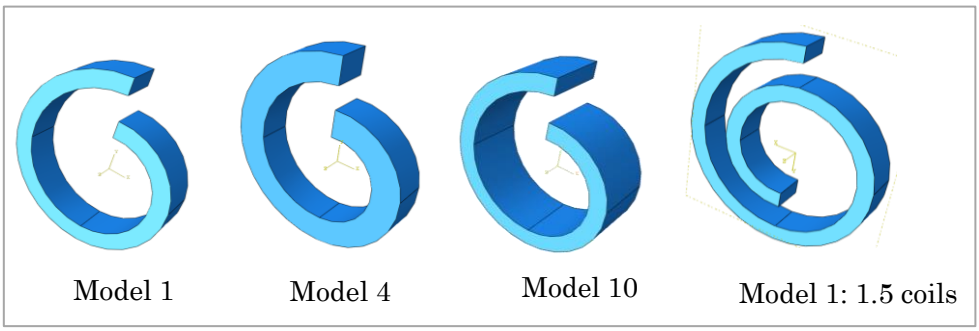


Figure 4.11: Some of the spiral models with different geometrical dimensions used for the parametric study.

Table 4.6: List of the designed spiral models for the parametric study. Each model was made in 1 and 1.5 loops.

Model		Thickness (t)	Initial radius (r_0)	Width (b)	Gap (h)
1	Control group	2	6	4	3
2	Thickness (t)	2.5	6	4	3
3		3	6	4	3
4		3.5	6	4	3
5	Initial rad (r_0)	2	7	4	3
6		2	8	4	3
7		2	9	4	3
8	Width (b)	2	6	5	3
9		2	6	6	3
10		2	6	7	3
11	Gap (h)	2	6	4	1.5
12		2	6	4	2
13		2	6	4	2.5

4.2.3.2.2 Probabilistic Study

Probabilistic analysis can be used in the engineering design process to find the impact of random variability, due to manufacturing, on the performance of the designed system. In this case, a probabilistic study was performed to find the effect of varying thickness, width and initial radius of the spirals spring, within the manufacturing tolerance, on the stiffness error of the designed springs. Assessment of the influence of manufacturing tolerances was particularly important for the spiral spring design because it was a custom component which would be manufactured in-house by Biomet UK Healthcare Ltd., whereas the helical springs could be bought as a certified product.

The selected input parameters (thickness, width and initial radius) were found from the results of the parametric study. The input parameters were defined by a Gaussian statistical distribution in terms of mean and standard deviation. The values of the input parameter were found using random Gaussian distribution sampling. The standard distribution selected for this analysis was the manufacturing tolerance of ± 0.1 mm for each of the geometrical parameter listed in Table 4.6. Random Gaussian sampling was used to select 20 random samples for each geometrical input parameter. In this manner, 60 spring models were generated for this study. Similar loading and boundary conditions to the previous section were applied to the models.

4.2.4 Statistical Analysis

Multiple regression analysis (Microsoft Excel 2010, WA, USA) with 95 % confidence interval was performed to determine the relationship between the

dependant variable (stiffness) and independent variables (geometrical parameters) of the helical and spiral springs

4.3 Results

4.3.1 Mechanical Test

4.3.1.1 Helical Spring

Figure 4.12 shows the constant (linear) stiffness of the mechanically tested helical springs. The difference between the stiffness obtained from the mechanical tests to those found from the FEA (Table 4.7) was found to be 3 ± 3.55 %. FEA showed that the von Mises stress for all of the tested springs was lower than the yield strength of Co-Cr-Mo alloy (930 MPa [175]). The stress in a compressed helical compression spring is shown in Figure 4.13.

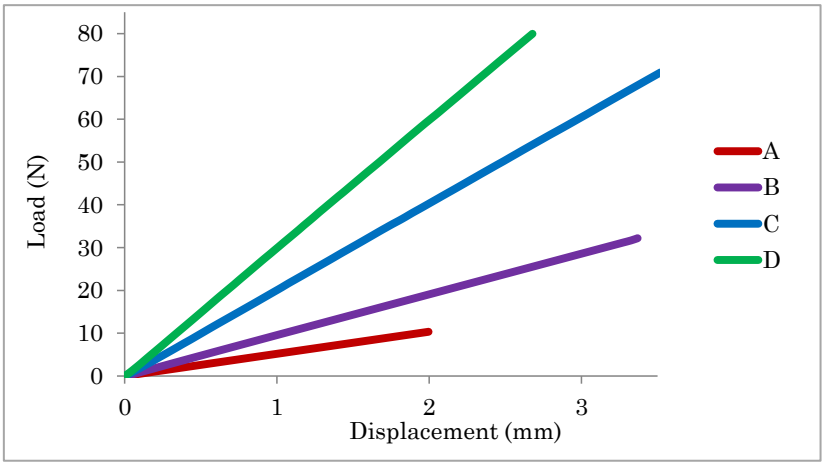


Figure 4.12: Linear load - displacement results of the mechanically tested helical springs.

Table 4.7: Comparison of the FEA and mechanical test results on the helical compression springs.

Spring	Mechanical	FEA	Difference
	Stiffness (N mm^{-1})	Stiffness (N mm^{-1})	(%)
A	5.14 ± 0.17	5.59	8.05
B	9.39 ± 0.19	9.66	2.80
C	20.27 ± 0.13	20.38	0.54
D	29.94 ± 0.37	30.10	0.53
E	-	46.24	-
F	-	61.98	-
G	-	72.58	-

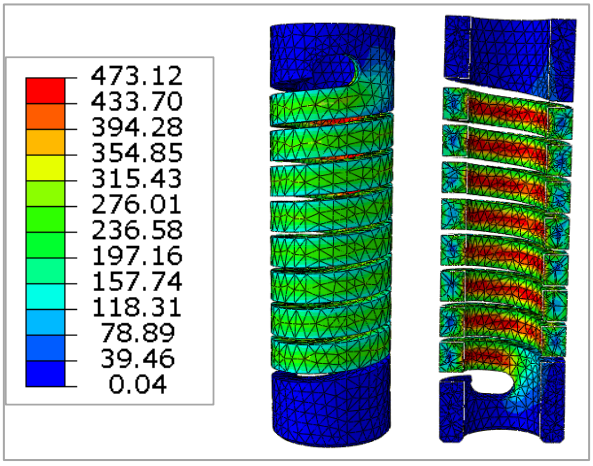


Figure 4.13: von Mises stress (MPa) in spring 'F' (Table 4.7) under 60 N compressive load. Mesh size 0.7 mm was used.

4.3.1.2 Spiral Spring

The recorded force and displacement of the actuator at each time step during the torsional mechanical test were calculated from the load and deformation of the spiral spring. The force on the head of the spring was calculated by using the following equation for the work done by torque:

$$F_s \times r_s \times \theta = F_A \times r_A \times \theta \quad \text{Equation 4-1}$$

$$F_s = F_A \times (\frac{r_A}{r_s}) \quad \text{Equation 4-2}$$

where 'F_s' is the force on the spring's head, 'F_A' is the force applied by the actuator, force 'r_s' is the distance between the metal cord to the central of the disk (51.4 mm), and 'r_A' is the distance between the spring head to the central of the disk (17.96 mm for the stiffer spring and 15.06 mm for the softer spring), and θ is the angle (in radians) (Figure 4.14).

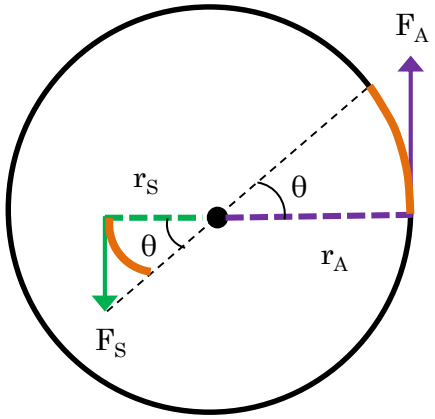


Figure 4.14: Schematic diagram of the torsional test set up showing the actuator force (F_A), spring load (F_s), distance between the metal cord and the centre of the torsional disc (r_A), and the distance between the spring's head and the centre of the disc (r_s).

The stiffness values of the spiral springs mechanically tested were smaller than those calculated by the FEA simulated torsional test (Table 4.8). Figure 4.15 shows the load-elongation results of the simulated axial (tangential) loading test using FEA.

Table 4.8: Results of the FEA and mechanical test on spiral springs.

Spring	Stiffness (N/mm)		
	FEA- Axial	FEA- Torsional	Mechanical-Torsional
DD13864-1.7	18.68	18.38	15.34 ± 2.29
DD13864-2.2	38.96	41.57	24.92 ± 7.45

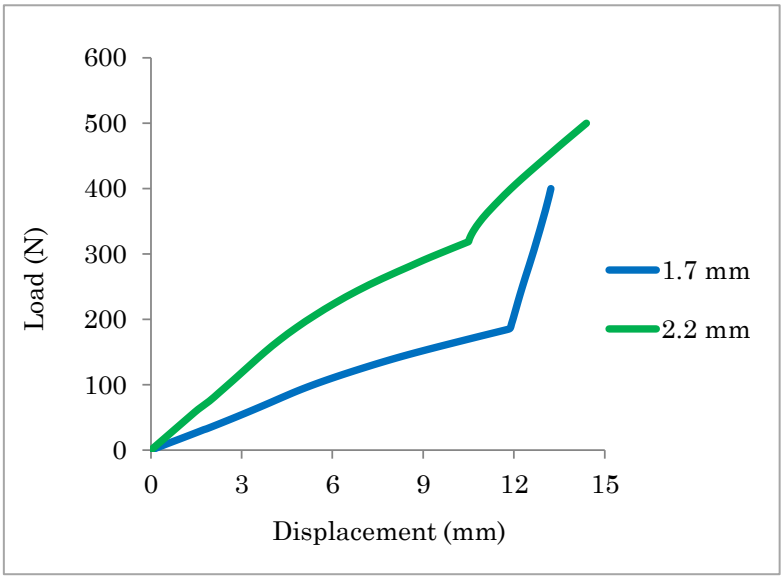


Figure 4.15: Load-elongation results of the spiral springs tested under simulated axial (tangential) load.

Slippage of the metal cord in the test rig at high loads was evident from the load-displacement results of the mechanically tested samples. This issue with the test set-up may have influenced the mechanical test data and increased the measured displacement (Figure 4.16 and Figure 4.17). The sudden increase of the load at higher displacements was because the head-pin started to break and was jammed against the rigid block (Figure 4.5).

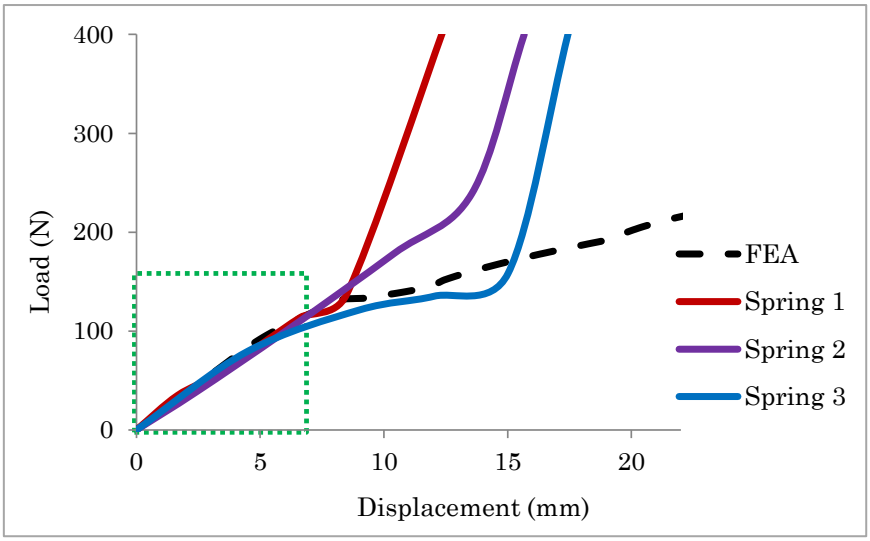


Figure 4.16: Comparison of the mechanical results of the spiral spring with 1.7 mm thickness to those found from the FEA simulated torsional test.

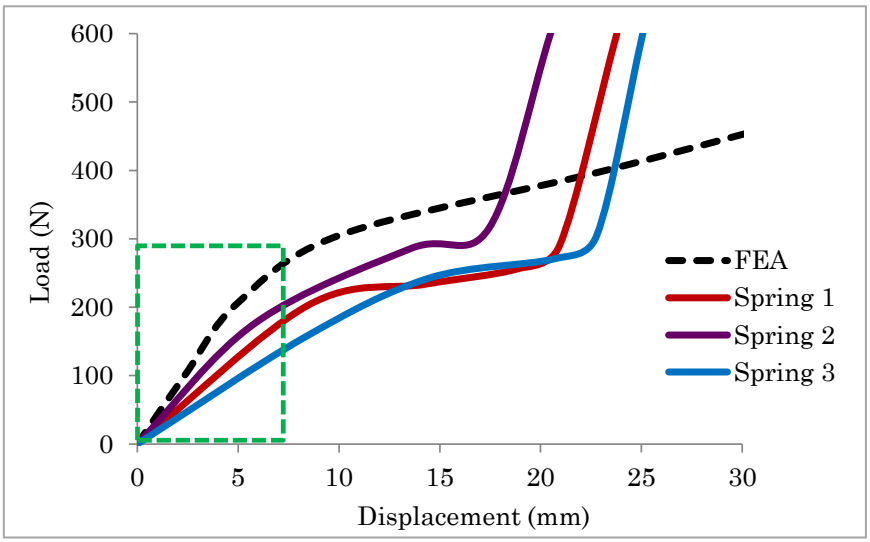


Figure 4.17: Comparison of the mechanical test results of the spiral spring with a thickness of 2.2 mm with those found from the simulated torsional test in FE.

50 % of the springs that were mechanically tested failed due to the breakage of their welded head-pins (Figure 4.18), whereas maximum stress in the FE models occurred in different areas than the head-pin. Stress distribution in FE models of the spiral spring subjected to axial and torsional forces are shown in

Figure 4.19. Maximum von Mises stress occurred close to the centre of the springs under 500 N axial forces, whereas in the springs subjected to torsional motion, the maximum stress was seen where the coils were in contact.



Figure 4.18: Deformed and failed spiral springs after the torsional test.

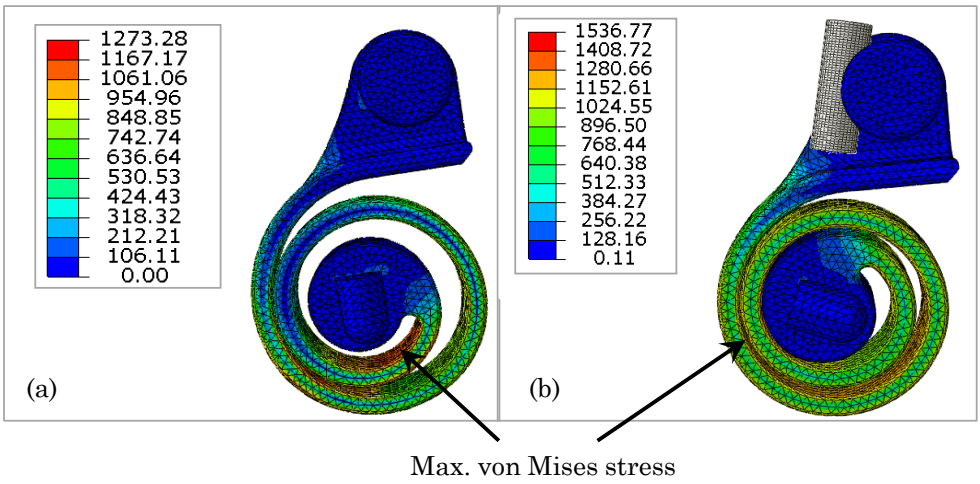


Figure 4.19: von Mises stress (MPa) in spiral spring (1.7 mm) (a) axial loading of 500 N and (b) simulated torsional test, where the centre was rotated by 2 radians.

The coils of the spiral springs with thickness of 1.7 mm and 2.2 mm tested in under the simulated tangential load came into contact under 188 N and 319 N respectively. The coils of the same spiral spring models tested under torsional

load, came into contact at 0.75 radians under 141 N (1.7 mm spring) and 305 N (2.2 mm spring) respectively.

4.3.2 Parametric & Probabilistic

4.3.2.1 Helical Spring

4.3.2.1.1 Parametric Study

The stiffness results of the helical spring models tested under compression load in this study are listed in Table 4.9. The effects of changing dimensional factors on the stiffness of the helical compression springs are shown in Figure 4.20. The average difference between the stiffness of the spring models obtained from FEA and those provided by the spring manufacturer was 1.74 % ± 1.22 %.

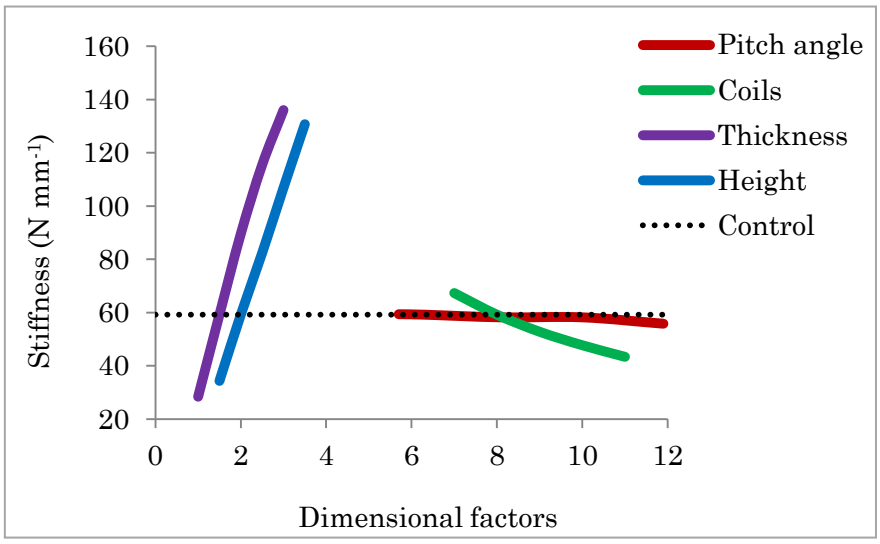


Figure 4.20: Graphical representation of the effect of different geometrical factors on the stiffness of the helical springs.

Table 4.9: The helical spring stiffness reported by the spring manufacturer compared to that obtained from the FEA.

Spring Model	Stiffness (N/mm)		Difference
	Manufacturer	FEA	(%)
1	58.6	59.19	1.00
2	67.1	67.32	0.32
3	52.1	52.79	1.31
4	46.8	47.72	1.93
5	42.6	43.38	1.79
6	28	28.39	1.38
7	87	89.55	2.85
8	111.7	115.45	3.25
9	130.5	136.02	4.06
10	34.2	34.33	0.37
11	83.1	82.37	0.89
12	109	106.84	2.02
13	134.6	130.72	2.97
14	58.6	59.37	1.29
15	58.4	58.20	0.35
16	58.1	58.20	0.17
17	57.8	55.81	3.57

The results of the multiple regression analysis showed that the pitch angle did not have a significant effect on the stiffness of the helical springs (t-test: p = 0.148). Therefore, the pitch angle as a variable was excluded from the input data. The results of the regression excluding the pitch angle showed the following relationship between helical spring's geometrical parameters and the stiffness (Y):

$$\text{Stiffness} = 54.2t + 48.1h - 5.5n - 75 \qquad \text{Equation 4-3}$$

The coefficient of determination (R^2) for Equation 4-3 was 0.996. It was observed that the thickness ($p = 2.04 \times 10^{-15}$) and height of rectangular wire ($p = 9.686 \times 10^{-15}$) had the highest impact on the stiffness of the spring.

4.3.2.2 Spiral Springs

4.3.2.2.1 Parametric study

The FEA stiffness results of 26 spirals with 1 and 1.5 loops are listed in Table 4.10. Figure 4.21 shows the stress in the control spiral model (Model 1) with single and 1.5 loops. It was observed that thickness of the spiral had the greatest effect on the stiffness of the model (Figure 4.22).

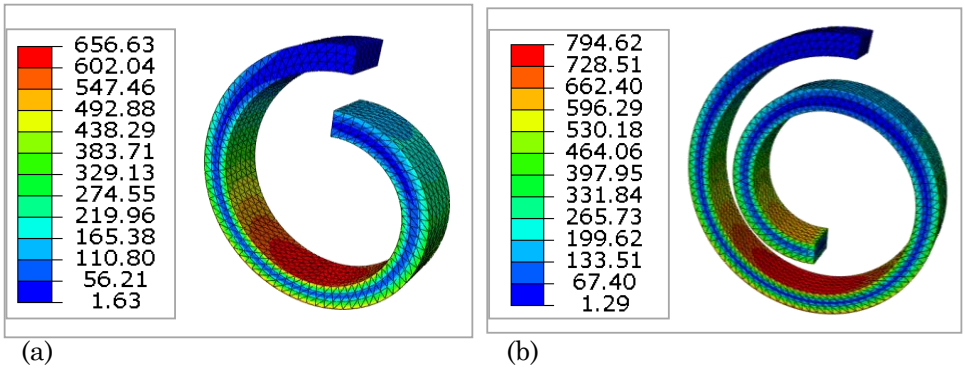


Figure 4.21: von Mises stress (MPa) distribution in the control spiral spring model (Model 1) with 1 and 1.5 loops under 80 N load.

The results of the multiple linear regression analysis showed that all the considered geometrical factors had significant effect on the stiffness of the spiral models. The thickness of the wire had the highest impact ($p < 0.001$) on the stiffness. The results of this analysis showed the following relationship

between the geometrical parameters and the stiffness of the spiral spring with a single loop:

$$\text{Stiffness} = -106 + 1212(t) - 14(r0) + 17.44(b) - 16(h) \qquad \text{Equation 4-4}$$

The coefficient of determination (R^2) for the above function is 0.993.

Equation 4-5 shows the relationship between the geometrical parameters and the stiffness of the spiral spring made of 1.5 loops:

$$\text{Stiffness} = -0.88 + 44.57(t) - 4.59(r0) + 0.67(b) - 11.8(h) \qquad \text{Equation 4-5}$$

The coefficient of determination (R^2) for the above function is 0.999.

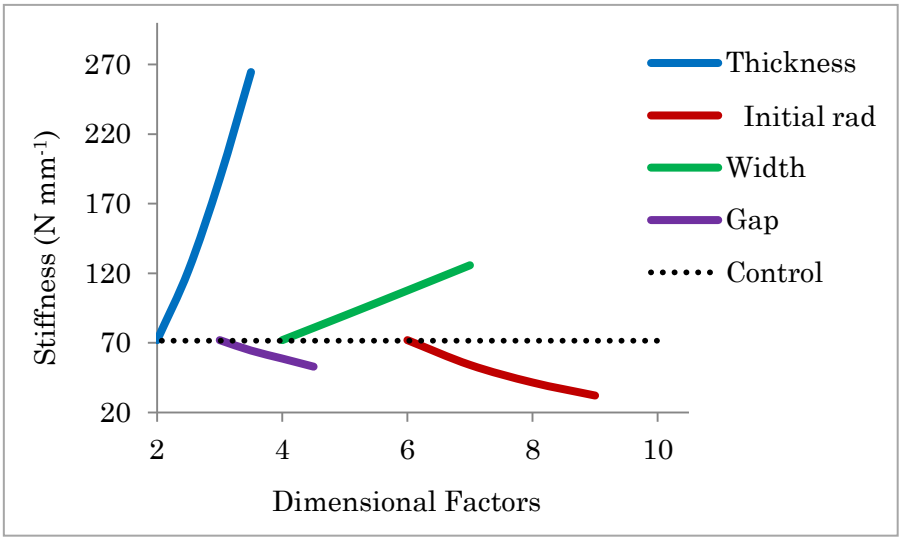


Figure 4.22: Graphical representation of the effect of different geometrical factors on the stiffness of the spiral springs.

It should be considered that Equation 4-5 only predict the stiffness of the spiral springs with the geometry defined within the values listed in Table 4.10. To predict the stiffness of the springs with geometries outside the range examined, the parametric study would need to be expanded.

Table 4.10: Results of the FEA of the spiral models with different dimensions.

Parameter	Model	Stiffness (N mm^{-1})	
		1 loop	1.5 loops
	1-Control	71.57	29.05
Thickness (t)	2	121.77	48.85
	3	187.35	72.67
	4	264.03	95.36
Initial radius (r_0)	5	54.03	23.07
	6	41.86	18.36
	7	33.11	14.76
Width (b)	8	89.29	29.49
	9	107.1	29.57
	10	125.39	29.68
Gap (h)	11	102.97	46.08
	12	91.24	39.35
	13	81.16	33.92

The estimated stiffness of the simple spiral models with thicknesses of 1.7 mm and 2.2 mm using the parametric equation were compared to those found from the FEA of the simplified and the more advanced spiral designs in Table 4.11.

Table 4.11: Stiffness of the simple and advanced designs of spiral spring obtained from parametric calculation and FEA using axial and torsional loads.

Spring	Parametric Estimation	FEA Simple spiral	FEA advanced spiral spring	
			Axial	Torsion
DD13864-1.7	27.8	35.13	18.68	18.38
DD13864-2.2	51.3	65.79	38.96	41.57

4.3.2.2.2 Probabilistic study

In this study, the variation of thickness (2 mm), initial radius (6 mm) and width (4 mm) of the simple spiral springs within the manufacturing tolerances of ± 0.1 mm on their stiffness were investigated using 60 FE models. The stiffness for each set of analysed models with variable thickness, initial radius and width were found to be 71.85 ± 5.02 N mm^{-1}, 71.74 ± 0.84 N mm^{-1} and 71.66 ± 0.74 N mm^{-1}, respectively (Figure 4.23).

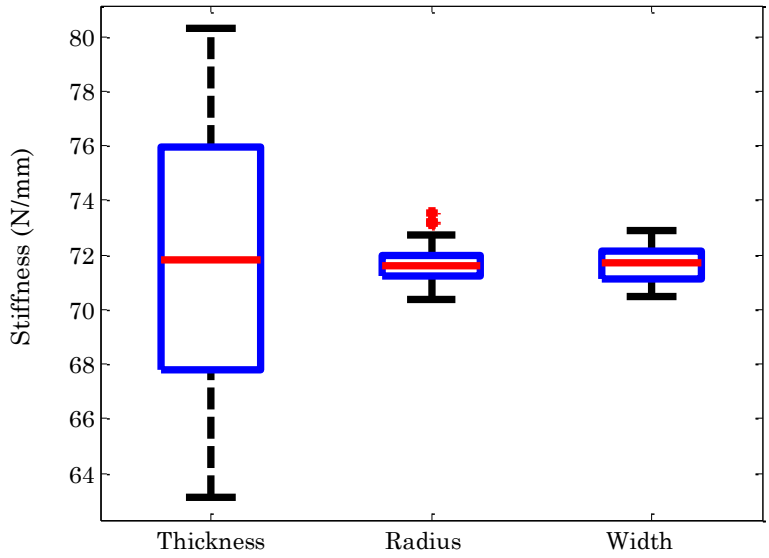


Figure 4.23: Results of the probabilistic analysis investigating the effect of varying of thickness (2 mm), initial radius (6 mm) and width (4 mm) of the spiral springs within the manufacturing tolerance of ± 0.1 mm on the spring's stiffness. Red lines show the median stiffness.

4.4 Discussion

A 3 % difference was observed between the results of the mechanical tests of the helical compression springs to those found from the FEA, which indicated consistency between the mechanical and the FEA test set-up including the boundary conditions and material properties to create an accurate model. The

von Mises stress of the springs when tested under the safe compression load suggested by the manufacturing company, experienced a stress below both the yield, and fatigue strength of the Co-Cr-Mo alloy, confirming the information provided by the manufacturer.

It was observed that the load-elongation curve of the helical spring was linear, as originally identified by Robert Hooke [204]; so to obtain a non-linear stiffness, more than one spring with constant stiffness would be necessary. For a multi-spring design, stop mechanisms would also be necessary to prevent over-loading the springs and to achieve a non-linear stiffness; yet may increase the risk of fretting.

During the torsional mechanical tests on the spiral spring, the metal cord connecting the actuator to the test rig slipped, influencing the displacement results. The torsional rig can be improved for future studies by securing the attachment with a larger clamp between the metal cord and the actuator in order to avoid slippage of the cord.

Due to the limited availability of the metal prototypes of the spiral springs due to time and cost of manufacturing; it was unfortunately not possible to repeat the mechanical tests and measure the stiffness of the springs under torsional load. Nevertheless, the test indicated that the use of a laser weld to connect the headpin to the main body of the spring was ill-advised and created a weak spot in the design, as 50 % of the springs failed in the head-pin weld region. The FEA simulations were unable to reproduce this failure mechanism as

material homogeneity had been assumed. Based on this result it is important to consider a different manufacturing technique to make this section.

The difference observed between the stiffness of the spiral springs found from the mechanical test to those found from the FEA was likely to be due to limitations of the mechanical test outlined above. The stiffness of the tested spiral spring up to 5 mm elongation, before the coils came into contact, was linear; therefore, for a non-linear stiffness artificial ACL, more than one spring would be required. It was observed that spiral spring responded differently to the axial and rotational loading; it is therefore necessary for this component to simulate the *in vivo* loading condition for more accurate assessment of the load-elongation behaviour of the designed spiral spring. The *in vivo* loading scenario would involve a combination of both torsional and axial loading; this loading scenario will be examined in Chapter 6.

The results of the parametric study on helical compression springs showed that the dimensions of the rectangular wire had the greatest effect on the stiffness of the elastic system. Therefore, by altering the height and thickness of the wire, the stiffness can be modified. As the range of each parameter examined was limited by the size constraints for this study, it is possible that the true effect of some of the analysed geometrical parameters (e.g. pitch angle) on the stiffness of the helical spring could not be highlighted. Therefore, a wider range of parameters should be considered for a more accurate estimation of the mechanical springs if different size constraints are to be used.

Results of the parametric analysis on the spiral springs showed that the thickness, initial radius and width of the spiral had the highest impact on the stiffness. These parameters were selected as inputs for the probabilistic analysis. The parametric estimations for the stiffness of two simple spiral models were approximately 21 % smaller than those found from the FEA. The reason for this difference may be due to the limited variables considered in the parametric study. Also some of the dimensions of the spirals tested in this study were smaller than the minimum inputted thickness (2 mm) and width (6 mm) used for the parametric study. Therefore, to get a better prediction for the stiffness of the spirals, a more extensive parametric study with wider range of input parameters would be required.

The flexural stiffness of a beam similar to the rectangular wire used in the helical and spiral springs is equal to E × I, where 'E' is the Young's modulus and 'I' is the second moment of area calculated by $\frac{bt^3}{12}$ [204]. Therefore, thickness (t) and width (b) of the wire have high impacts on the flexural stiffness of both helical and spiral springs; this was in agreement with the results of the parametric studies.

Results of the probabilistic study showed that manufacturing accuracy is particularly important when creating the thickness of the spring as this caused a standard deviation of 5 N mm^{-1}, whereas the initial radius and width only caused a deviation of with 0.84 N mm^{-1} and 0.74 N mm^{-1}, respectively.

The von Mises stress of all of the springs tested was lower than the fatigue strength of CoCrMo (Section 2.5.2.2), which indicated the springs have a low

risk of fatigue failure, when loaded within the loading range tested in this study.

4.5 Optimised Spring Designs

The results of the finite element analyses have shown that the desired non-linear stiffness of the ACL cannot be achieved using a single helical or a single spiral spring within the given size constraints. Therefore, the artificial ACL design must consist of more than one spring with stop mechanisms to reproduce the non-linear load-elongation behaviour of the ACL with a multi-linear stiffness. The stop mechanism should prevent overloading the springs and limit the amount of deformation, but must also be carefully designed to minimise the risk of fatigue, corrosion and wear.

As was mentioned in Section 2.5.3.2, the stiffness of the toe and linear regions of the load-elongation curve of the ACL in middle aged people are approximately 38 N mm^{-1} and 100 N mm^{-1} respectively [88]. The artificial ACL should be able to reproduce the stiffness of the toe and linear region of the ACL's load-elongation curve. Therefore, the stiffness of femoral spring, tibial springs and cord in series should reproduce the stiffness of the toe region, and the stiffness of the tibial spring and cord should reproduce the stiffness of the linear region (Figure 4.24).

The stiffness and elastic modulus of the tested Dyneema loop at a steady state was found to be about 2000 N mm^{-1} and 20000 MPa, respectively (Section 3.2.2.3). Although it would be possible to increase the stiffness and modulus of

the cord further by adding more yarns to its construct or by cross-linking. However, for the purposes of this thesis, it will be assumed that the maximum stiffness of the cord is approximately 2000 N mm^{-1}.

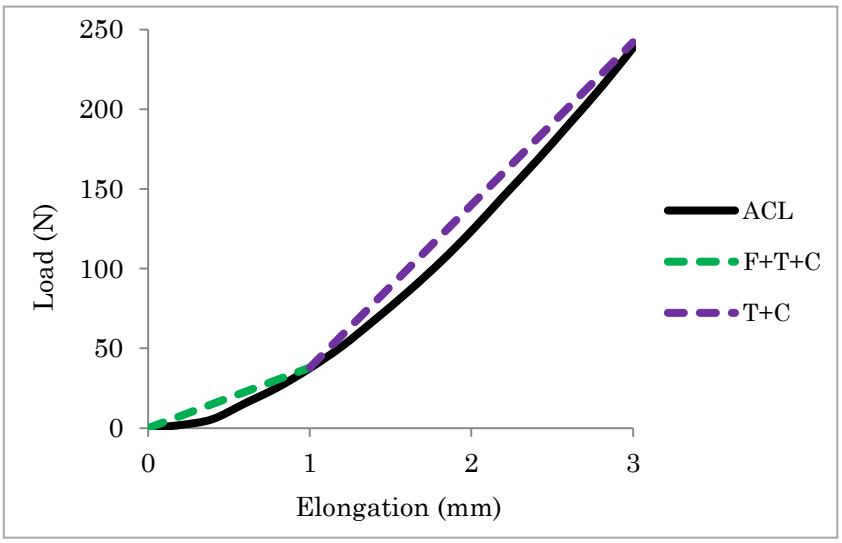


Figure 4.24: Schematic diagram of the multilinear stiffness values required to reproduce the non-linear stiffness of the native ACL [88] with an artificial ACL consisting of a femoral spring (F), tibial spring (T) and cord (C).

Using Hooke's law for the linear springs in series, the stiffness of the tibial and femoral spring can be calculated. In order to achieve the stiffness of the linear region (100 N mm^{-1}) by having the Dyneema cord in series with a tibial spring, the tibial spring should have a stiffness of roughly 104 N mm^{-1}. To reproduce the stiffness of the toe region (38 N mm^{-1}), the stiffness of the femoral spring in series with the tibial spring and cord was found to be 60 N mm^{-1}. To reproduce the toe region of the non-linear load-elongation curve of the ACL, the femoral and tibial stops should come into action at 0.63 mm and 0.37 mm respectively.

Considering the size constraints in the tibia and the results of the parametric studies, the maximum stiffness of the tibial spring in the form of helical and spiral springs was 102 N mm^{-1} and 108 N mm^{-1}. A helical compression spring with a stiffness of 61 N mm^{-1} was designed to be implanted in the femoral side for both stand-alone ACLR and ACLR-TKR devices. The dimensions of the final femoral and tibial springs designed for the ACLR and ACLR-TKR devices are shown in Figure 4.25.

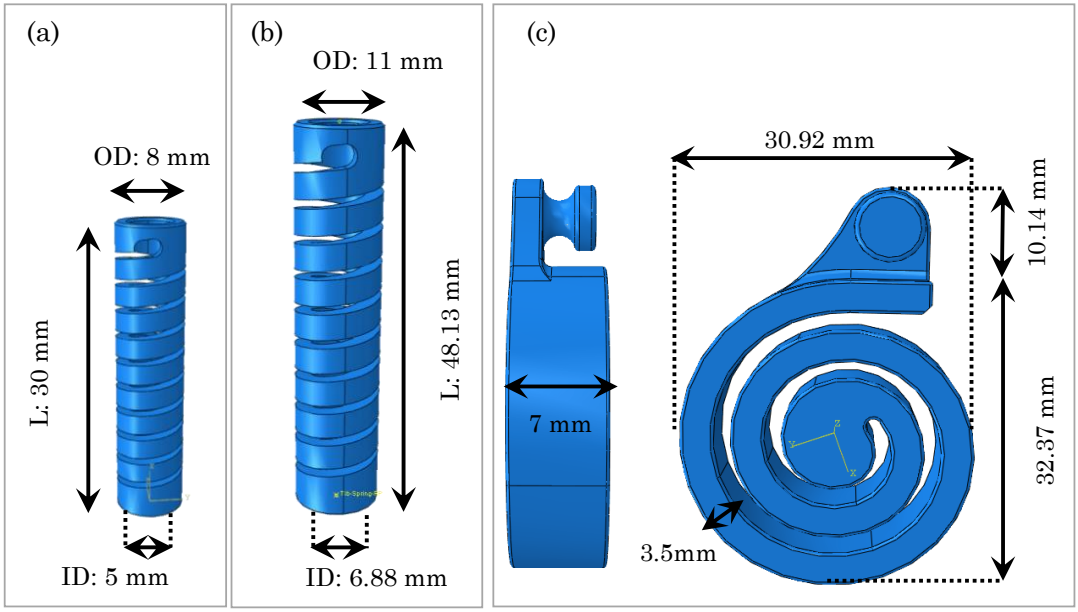


Figure 4.25: Dimensions of the final designs of the (a) femoral helical spring (61 N mm^{-1}) and (b) tibial helical spring (102 N mm^{-1}) for ACLR device. (c) Tibial spiral spring for ACLR-TKR.

The results of the FEA on the optimised designs of helical and spiral springs are presented in Table 4.12.

Table 4.12: Results of the FEA on final designs of femoral and tibial springs.

Spring	Force	Deformation	Von Mises	Stiffness
	(N)	(mm)	(MPa)	(N mm^{-1})
Femoral- Helical	54	0.9	434	61
Tibial- Helical	150	1.35	450	102
Tibial- Spiral	240	2.2	454	108

4.6 Conclusions

This chapter presented the results of the mechanical tests and the FEA performed on the elastic systems for the ACLR devices. The spiral and helical springs have a linear stiffness; therefore, to reproduce the non-linear stiffness of the ACL, two or more linear springs must be used in series with mechanical stops. It can be concluded that FE models of the helical and spiral springs can give an accurate prediction of the spring's mechanical behaviour under axial and torsional loading conditions. The rig used for torsional testing the spiral spring requires further improvements in order to reliably measure the torsional stiffness of the springs. The thickness of the spiral spring, and the thickness and height of the rectangular wire used in the helical compression spring have the highest influence on the stiffness of the springs. The variation of the thickness of the spiral spring within the manufacturing tolerances can have the highest impact on the stiffness of the spring; therefore the manufacturing tolerance may need to be reduced. In the last section of this chapter, the designs of the helical and spiral springs were finalised to meet the required non-linear stiffness of the design for both the ACLR-device and the ACLR-TKR device.

Chapter 5: ACL Attachments

5.1 Introduction

Understanding the anatomical attachments of the ACL on the femur and the tibia, particularly the location of the isometric ACL fibre, are essential for reconstructing the ACL so it can restore the normal kinematics and mechanics of the knee [205,206]. There is a considerable controversy regarding the ideal placement of the reconstruction graft [138,206]. It is very common for surgeons to misjudge the position of the ACL tunnels on the femur and tibia[207]; therefore, it is very important to understand the effect of misplacing the ACL attachments on the behaviour of the reconstructed ACL.

This chapter begins with a review of the conventional techniques used to find the ACL attachment sites. Then a MRI study on human knees is described with the aim of understanding the behaviour of the reconstructed ACL during passive and loaded knee motions. The impact of surgical error in positioning of the ACL tunnels on the behaviour of the reconstructed ACL is also investigated.

5.2 Conventional Arthroscopic Methods

5.2.1 Femoral Attachment

ACL attachments have a variety of different sizes and shapes. Due to difficulties in finding the accurate ACL attachment sites on the femur and tibia for tunnel positioning in arthroscopic ACL reconstruction, different techniques have been developed to help surgeons judge where to drill the bony

tunnels [149,208–211]. Several authors have used their own original methods to describe the position of the ACL insertions sites; these methods of finding the femoral attachment sites include the o'clock, Mochizuki, Takahashi, Watanabe, and Quadrant methods.

In the traditional o'clock method, the femoral notch is considered to be the dial of a clock. The position of the femoral AMB and PLB attachments are described to be between 9:30 and 11 o'clock in the right knee [209] (Figure 5.1). This method has been reported to be inaccurate and subjective as the position of the ACL attachment is not clearly defined on the femoral notch wall and in other planes [212].

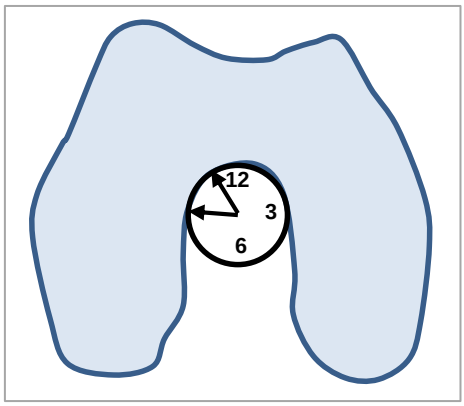


Figure 5.1: Schematic illustration of the o'clock method. AMB is inserted at 11:00 and PLB is inserted at 9:30 o'clock. Adapted from Giron *et al.*, 2006 [213].

Takahashi *et al.* [214] described the position of the centre of the AMB and PLB from the deep margins of the articular surface of the lateral femoral condyle in 32 Mongolian cadavers (18 male and 14 female) (Figure 5.2). The centre of the AMB was reported to have a distance of 7.6 mm (24.5 % ± 4.7 %) from the posterior margin of the lateral femoral condyle and 4.1 mm from the intercondylar roof. The centre of the PLB was located 7 mm (22.9 % ± 4.7 %)

from the posterior margin of the lateral condyle and 11.3 mm from the intercondylar roof. Mochizuki *et al.* [215] described the central points of the ACL bundles on the femur relative to the posterior bone, articular surface border and Blumensaat's line (Figure 5.2). The centres of the AMB and PLB were found to be located 28.3 % ± 2.1 % and 59.8 % ± 4.1 %, respectively, from the deep border between the bony wall and the articular surface. Blumensaat's line is located on the roof of intercondylar notch in the sagittal plane [140].

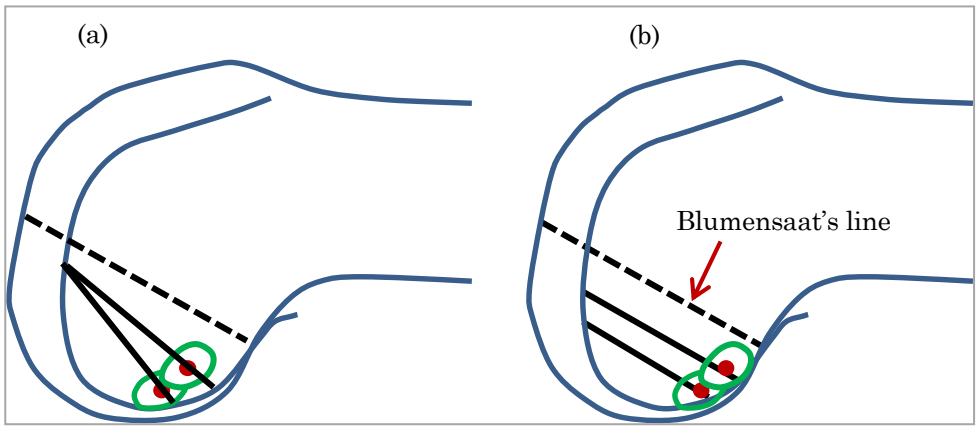


Figure 5.2: (a) Schematic illustration of the Takahashi method: The location of the centres of the AMB and PLB are expressed as their distances to the deep border of the articular surface. (b) Mochizuki method: Distances between the centre of the AMB and PLB to the deep and shallow borders of the articular surface are measured. Adapted from Tsukada *et al.*, 2008 [149].

It has been reported that Mochizuki and Takahashi methods are difficult to utilise during arthroscopic surgery due to complications in finding the reference points [149].

In the Watanabe method, the position of the centre of the AMB and PLB were expressed in terms of their distances to reference points; the over the top position (O), the anterior notch outlet (A), and the most inferior point (I) (Figure 5.3a) [149]. The central point of the AMB was reported to be at 23.7 % ±

3.1 % from point O in the sagittal plane, and at 21.9 % ± 5.1 % from point A in the axial plane.

One of the most common techniques in finding the centres of the ACL bundles is the Quadrant method [209,216,217]; in which a measurement mesh is drawn on the sagittal radiograph of the lateral femoral condyle. The location of the centres of the ACL bundles are expressed in terms of their distance to the sagittal diameter of the lateral femoral condyle along the Blumensaat's line (t), and the height of intercondylar notch (h) (Figure 5.3b) [149,218,219]. Tsukada *et al.* [149] reported that the central point of the AMB was located at 25.9 % ± 2.0 % from the deep margin of the articular surface (in a deep-shallow direction), and at 17.8 % ± 2.9 % from Blumensaat's line (in a high-low direction).

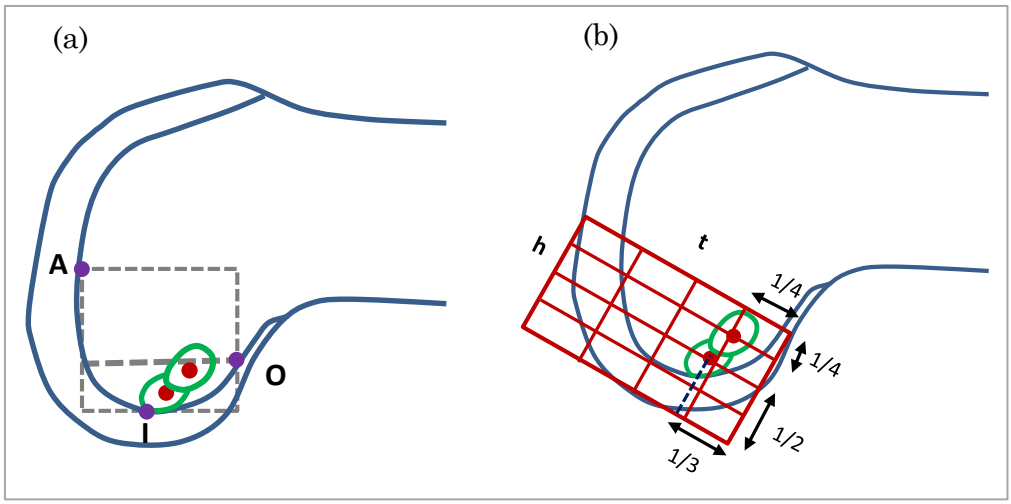


Figure 5.3: (a) Schematic diagram of the Watanabe's method: The centres of AM and PL bundles are found relative to the position of the reference points O, A, and I. (b) Quadrant method: 't' is the sagittal diameter of the femoral condyle along Blumensaat's line, and 'h' is the height of the intercondylar notch. Adapted from Tsukada *et al.*, 2008 [149] and Colombet et al., 2006; [218].

Computer-assisted navigation systems have been used to locate the position of the femoral and tibial bone tunnel placements. Kawakami *et al.* [206]

investigated the position of the ACL's bone tunnels using a fluoroscopic-based navigation system. These authors reported that the femoral ACL bone tunnel was located 74.9 % ± 3.0 % (from anterior to posterior) along Blumensaat's line. The tibial tunnel was located 42.3 % ± 1.4% along the tibial plateau (from anterior to posterior). The navigation system was reported to increase the accuracy and reproducibility of the placement procedure [206].

Surgical navigation systems could be used to assist implantation of the designed artificial ACLR device based on the isometric ACL attachment points. The locations of the ACL attachments could be planned pre-operatively using 2D templates or intra-operatively using 3D templates [220,221]. 2D templates could be overlaid on the lateral radiographs [219], CT scans, or fluoroscopic images [206,222] to provide real-time feedback of anatomical information. Quadrant method [219] for the femoral attachment and the method described earlier by Tsukada *et al.* [149] for the tibial attachment could be used for creating 2D templates.

Intra-operative digitisation of some osseous anatomical landmarks such as Blumensaat's line, resident's ridge and lateral bifurcate ridge on the femoral side, and the tibial eminence and medial and lateral intercondylar tubercles on the tibial side can help to provide guidelines for planning the ACL attachment tunnel positions [208,223,224].

5.2.2 Tibial Attachment

The tibial plateau has an average medio-lateral (ML) width of 80 ± 6 mm (range: 66 mm to 90 mm) and AP depth of 52 ± 5 mm (range: 39 mm to 64 mm)

[162]. Excessive anterior placement of the tibial graft can lead to impingement of the graft on the roof of the femoral notch during knee extension [216]. The locations of the centres of AMB and PLB on the tibia are most commonly expressed in terms of percentages of the AP and ML lengths of the tibial plateau. The distance between the centre of the AMB to the anterior (A) and medial edges (B) of the tibial plateau are 37.6 ± 3.6 %, and 46.5 ± 3.2 %, respectively (Figure 5.4). The distance between the centre of the PLB to the anterior (C) and medial (D) edges of the tibial plateau are 50.1 ± 5 % and 51.2 ± 2.4 %, respectively [149].

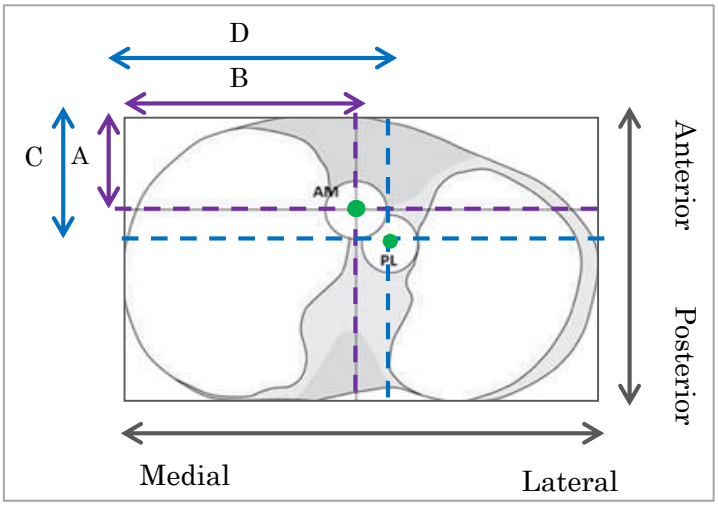


Figure 5.4: Locations of the centers of the AMB and PLB on the tibial plateau relative to the anterior and medial edges. Adapted from Tsukada *et al.*, 2008 [149].

5.3 Reconstructed ACL

It is essential to study the movements of the reconstructed ACL *in vivo* throughout flexion, so that the artificial ACL is designed and positioned in such a way to function as desired, and its functionality and the mechanical properties can be assessed.

The purpose of this study was: (1) to investigate the 3D movements of the ACL attachment sites for 18 patient knee geometries throughout passive and loaded flexion, and find the load and deformation the reconstructed ACL would undergo during both passive and loaded knee flexion; and (2) to evaluate the effect of misplacing the location of the ACL attachment sites on the behaviour of the reconstructed ligament and restoration of knee mobility and stability.

5.3.1 Methodology

5.3.1.1 Behaviour of the Reconstructed ACL

5.3.1.1.1 Input Data

The input data for tibiofemoral movements during passive and loaded flexion utilised in this study was based on the published results of an experimental study performed by Johal *et al.* [225]. These authors reported 3D movements of the femur relative to the tibia for ten healthy Caucasian patients during passive and weight bearing flexion (deep squatting) [26,225]. The study used an open MRI scanner throughout each exercise to record the position of the bones.

As the posterior femoral condyles have a circular profile in the sagittal plane, the study used the centres of these circles, called the flexion facet centre (FFC), to indicate the position of the femur relative to the posterior cortex of the tibia (Figure 5.5) [26,226].

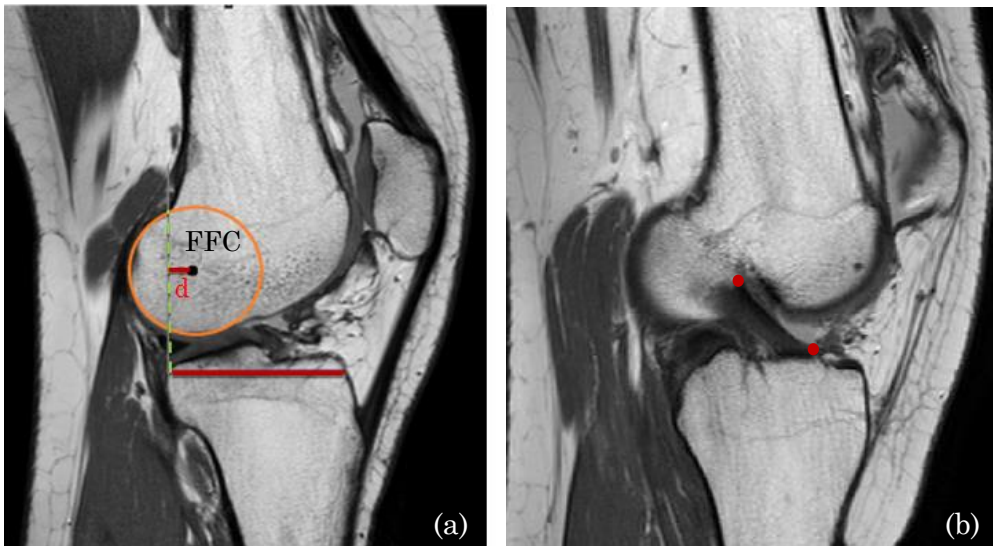


Figure 5.5: One of the MRI scans used in the current study showing a sagittal view of the knee. (a) 'd' is the distance between FFC (flexion facet centre) of the femoral condyle and the most posterior point of the tibial cortex. (b) Locations of the isometric ACL fibre attachment points on the femur (most proximal and anterior) and tibia (most anterior).

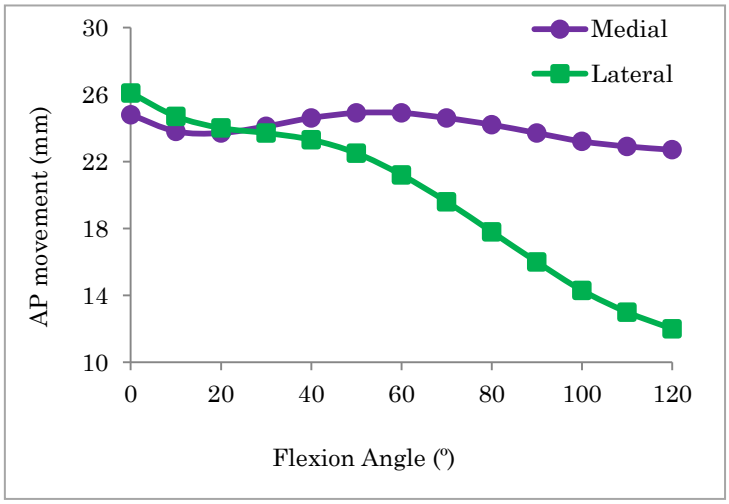


Figure 5.6: Antero-posterior (AP) translation of the centres of the medial and lateral femoral condyles during passive tibio-femoral knee motion found from the open MRI study. Adapted from Johal *et al.*, 2005 [225].

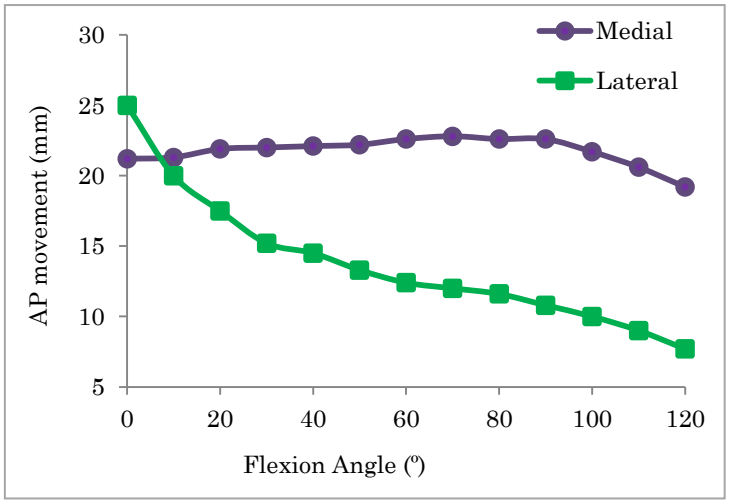


Figure 5.7: Antero-posterior (AP) translation of the centres of the medial and lateral femoral condyles during weight bearing tibio-femoral knee motion found from the open MRI study. Adapted from Johal *et al.*, 2005 [225].

5.3.1.1.2 Analysis

The input data from the open MRI study (Section 5.3.1.1.1) was used to analyse the behaviour of the reconstructed ACL in 3D knee models. The geometry of the knee models were based on the segmented MRI models described in Section 2.4.2.1. The 3D meshed models were created using Mimics software (version 14.12, Materialise, Leuven, Belgium) and then converted to ABAQUS input files (.inp).

The 3D co-ordinates of a number of landmarks on the 18 MRI models were manually measured in the sagittal plane of the centre of each condyle, these landmarks included:

- The flexion facet centre (FFC) of each femoral condyle
- The isometric ACL fibre attachment points on the femur and tibia. It has been reported that the isometric fibre originates anteriorly and proximally on the femur and inserts anteriorly on the tibia [20]

- The most posterior point on the tibial cortex

The anteroposterior movements of the medial and lateral femoral condyles (Figure 5.6 and Figure 5.7) were converted to a percentage distance relative to the AP length of the respective condyle, enabling the results to be used on different knee geometries. The AP length of the condyle of each of the 18 knee geometries used in this study was then measured, and the femoral condyle position for each flexion angle was found.

A Python code (version 2.7.3, Python Software Foundation, OR, USA) was developed by Dr. Elise Pegg (Botnar Research Centre, University of Oxford, UK) to automate this process, and convert the input values of tibiofemoral movements into one 3D rigid body transformation matrix which represented the femoral position on the tibia at each flexion angle for both passive and weight bearing (deep squatting) flexion. This transformation matrix was then applied to the ACL attachment site co-ordinates to determine their positions throughout passive and weight bearing knee motions. The ACL femoral attachment site was recorded relative to the ACL tibial attachment. This data was then used to calculate the ACL elongation, the twist angle and the predicted load as the knee flexed from 0° to 120°.

The elongation of the reconstructed ACL was found by calculating the change in distance between the femoral and tibial attachment points in space. The load in the reconstructed ACL was calculated by multiplying elongation by the stiffness of 97 N mm^{-1} (Section 2.2). The strain in the reconstructed ACL

during squatting at each flexion angle was calculated by using the original length of the unloaded ACL at 30 º of flexion angle.

The twist angle of the reconstructed ACL was found by measuring the angle between one axis on the femoral attachment area and the corresponding axis on the tibial attachment area using the method described by Zavatsky and O'Connor [136] (Figure 5.8).

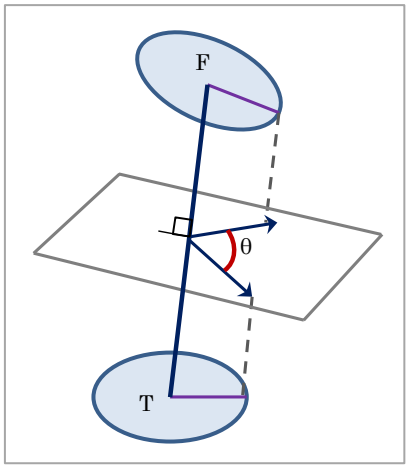


Figure 5.8: Schematic illustation of the measured twist angle (θ) of the long axis of the ACL connecting the femoral attachment centre (F) to the tibial attachment centre (T). Adapted from Zavatsky and O'Connor., 1994 [136].

Some of the additional assumptions of this code were:

- The bones and articulating surfaces were rigid and could not deform under load.
- The distance between the lowest point on the surface of the femur and tibia was kept constant, therefore, assuming a flat tibial plateau.
- The reconstructed ACL was assumed to be surgically fixed to the femoral and tibial attachments at 30 º of passive flexion [227], therefore,

the load, elongation and twist angle were calculated relative to this and were consequently zero at this passive flexion angle.

- The reconstructed ACL had a diameter of 6 mm and a linear elastic stiffness of 97 N mm^{-1}.
- Bending of the reconstructed ACL was not considered in this study.
-

5.3.1.2 ACL Placement Sensitivity

The smallest 3D knee model out of the eighteen available models described in Section 2.4.2.1 was used for this study to represent the most severe case of the ACL placement error. It was assumed that a surgeon could insert the ACL attachment to accuracy of ± 5 mm antero-posterior or ± 5 mm superior-inferior to the femoral isometric fibre attachment point (Figure 5.9). Similarly on the tibial side ± 5 mm antero-posteriorly or ± 5 mm medio-laterally relative to the isometric ACL fibre attachment point on the tibial plateau was considered (Figure 5.10). A plane was defined tangent to the bony surface on the medial wall of the lateral condyle, where the isometric ACL attachment is normally located. The four new attachment points with 5 mm distance from the isometric attachment points were found and then projected on the bony surface plane.

Combinations of five femoral and five tibial attachment points (Table 5.1) were assessed in this study, resulting in a total of 25 combinations (Table A.2 in Appendix 4). Using the method described in Section 5.3.1.1, the movements of

the different combinations of attachment sites and the corresponding ACL load, elongation and twist were calculated.

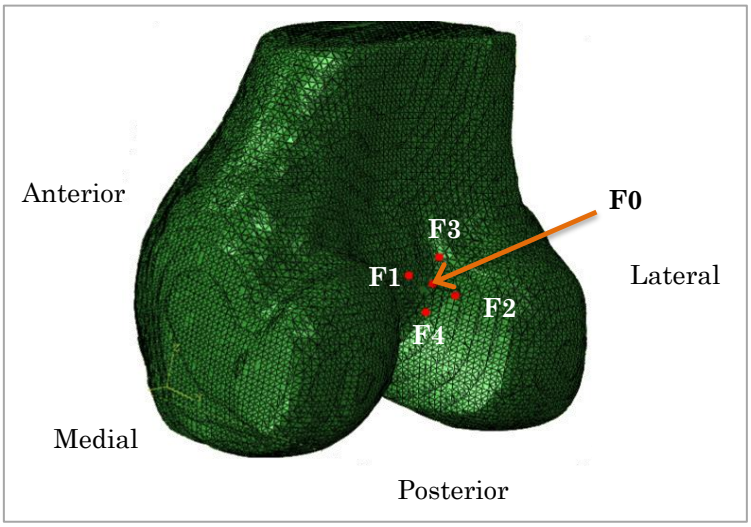


Figure 5.9: Femoral attachment points considered in this study. F0 is isometric fibre attachment point, F1, F2, F3 and F4 are located 5 mm anterior, posterior, superior and inferior to the F0, respectively.

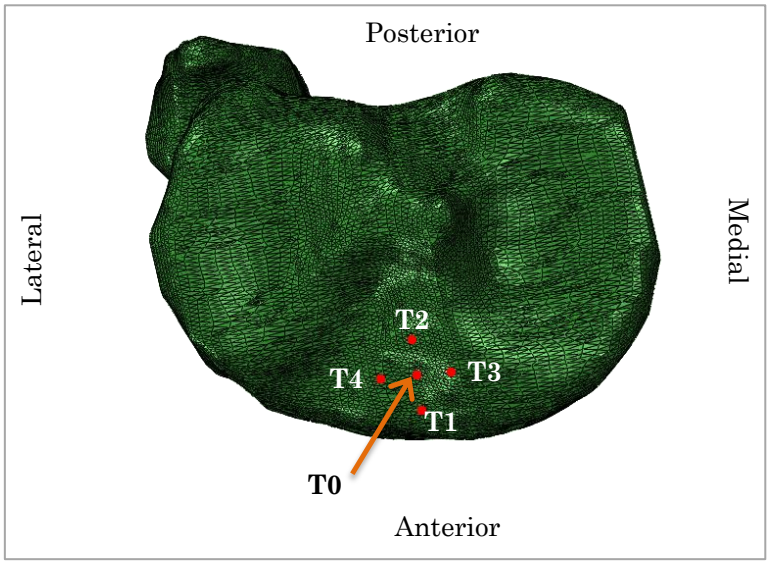


Figure 5.10: Tibial attachment points considered in this study. T0 is the isometric fibre attachment. T1, T2, T3, and T4 are located 5 mm anterior, posterior, medial and lateral to the T0, respectively.

Table 5.1: The coordinates of the femoral and tibial attachment points.

Femoral Attachment				Tibia Attachment			
	X	Y	Z		X	Y	Z
Isometric	-20.76	0.87	79.60	Isometric	-41.13	35.38	74.99
Anterior (+5)	-25.65	1.39	79.27	Anterior (+5)	-45.06	38.08	74.27
Posterior (-5)	-16.45	1.54	81.98	Posterior (-5)	-36.13	35.38	74.99
Superior (+5)	-21.13	-3.52	80.88	Medial (+5)	-42.14	33.80	70.28
Inferior (-5)	-20.98	6.45	80.36	Lateral (-5)	-40.27	37.56	79.41

5.3.1.3 Statistical Analysis

One-way analysis of variance (ANOVA) test was performed on the results of the elongation and load during passive and weight bearing motions. A Student t-test was performed to compare the reconstructed ACL's twist angle at each knee flexion angle during passive and weightbearing motions. To analyse the placement sensitivity results, a multiple regression analysis was carried out to find the effect of independent variables (e.g. femoral placement, tibial placement) on the dependent variables of load, strain, and twist angle of the reconstructed ACL.

Each input variable had five different levels representing the location of the ACL attachment (e.g. isometric, anterior, posterior, superior and inferior on the femur, and isometric, anterior, posterior, medial, and lateral on the tibia). Given that the femoral and tibial placements were categorical variables (e.g. anterior, posterior, etc.); in the regression model they were transformed to numerical equivalents using dummy variables (e.g. 0 and 1).

All the placement levels were compared to the isometric position. Looking at the coefficients in the multiple regressions and their significance, it is possible to interpret whether or not the independent variables had significant effects on the dependent variables. Also, the positive or negative correlation between these variables was found.

5.3.2 Results

5.3.2.1 Behaviour of the Reconstructed ACL

It was assumed that the artificial ACL was secured at the attachment sites during surgery at 30 º of passive flexion with no applied pretension, therefore, elongation, load and twist angle were zero at this passive flexion angle. Load, strain and twist angle of the reconstructed ACL corresponding to various flexion angles during passive motion and squatting are shown in Figure 5.11, Figure 5.12 and Figure 5.13.

During passive motion and squatting, maximum strain and corresponding load occurred at 10 º (strain of 0.54 % ± 1.65 %, load of 22.15 N ± 59.19 N) and 50 º (strain of 10.56 % ± 3.23 %, load of 372.11 N ± 67.93 N) of flexion, respectively (Figure 5.11). The average length of the most anterior fibre of the AMB during passive motion in 18 models was found to be 37.43 ± 5.17 mm. The value of strain and load remained approximately constant during passive motion.

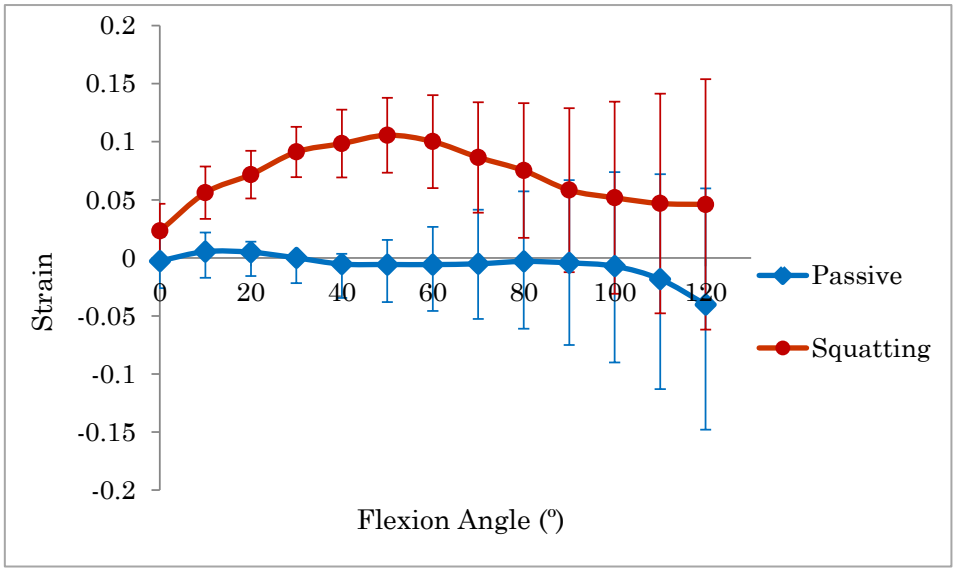


Figure 5.11: Mean strain in the reconstructed ACL predicted by the knee model for eighteen knee geometries during passive flexion and squatting. Error bars represent the standard deviation.

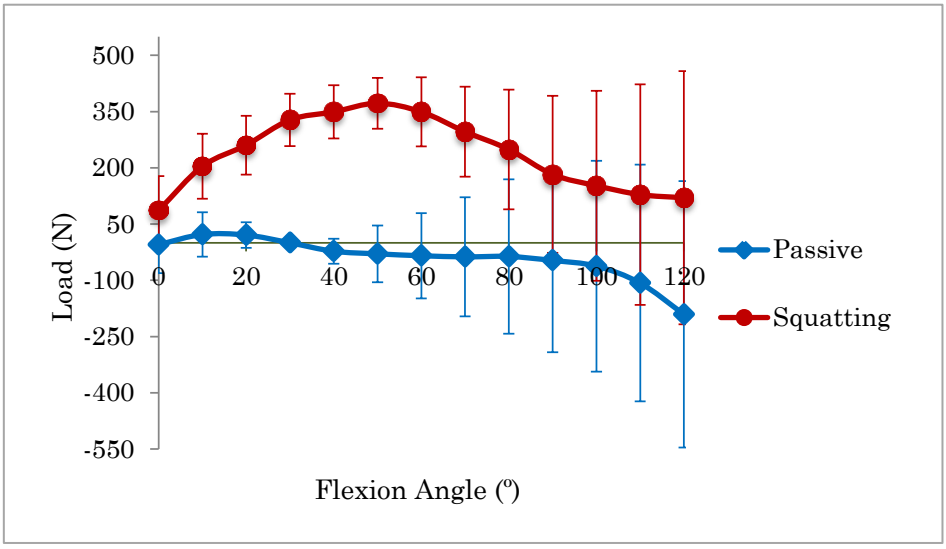


Figure 5.12: Mean load in the reconstructed ACL predicted by the knee model for eighteen knee geometries during passive flexion and squating. Error bars represent the standard deviation.

The twist angle of the reconstructed ACL at various degrees of flexion had a similar trend for both passive and weight bearing motions. The twist angle ascended non-linearly with increasing flexion angle. The maximum twist angle

during passive (61.04 ° ± 5.84 °) and loaded motions (64.17 ° ± 7.81 °) occurred at 120 ° of flexion (Figure 5.13). A significant difference was found between the twist angles during passive and weight bearing motion when the flexion angles were 10 ° (p <0.001), 20° (p <0.001), 110° (p = 0.031), and 120 ° (p = 0.016). No significant difference was seen at other flexion angles.

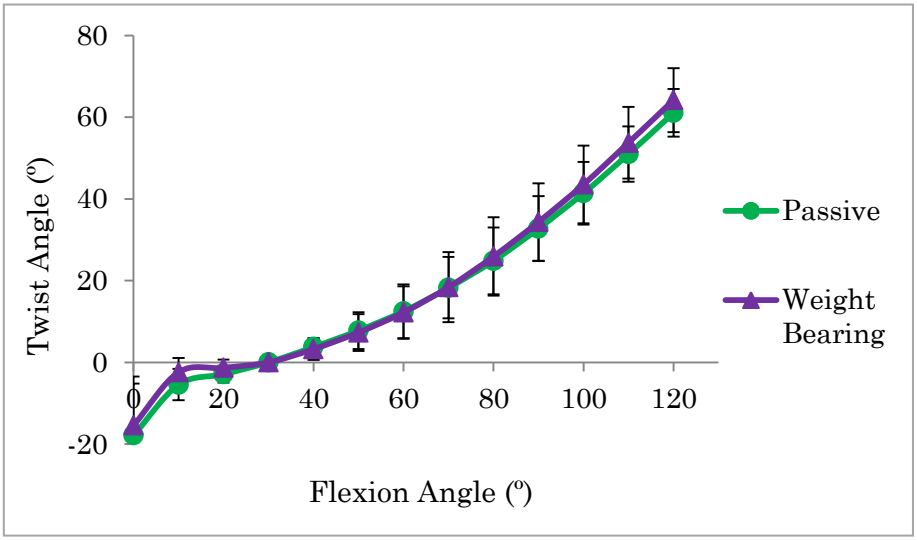


Figure 5.13: Mean and standard deviation of the reconstructed ACL twist angle predicted by the knee model for eighteen knee geometries during passive flexion and squatting.

5.3.2.2 ACL Placement Sensitivity

5.3.2.2.1 Passive Motion

Anterior and inferior placements of the femoral attachment significantly (p<0.001) increased the ACL load and strain, whereas posterior placement of the femoral attachment significantly (p<0.001) reduced the load and strain (Table 5.2 , Figure 5.14 and Figure 5.15).

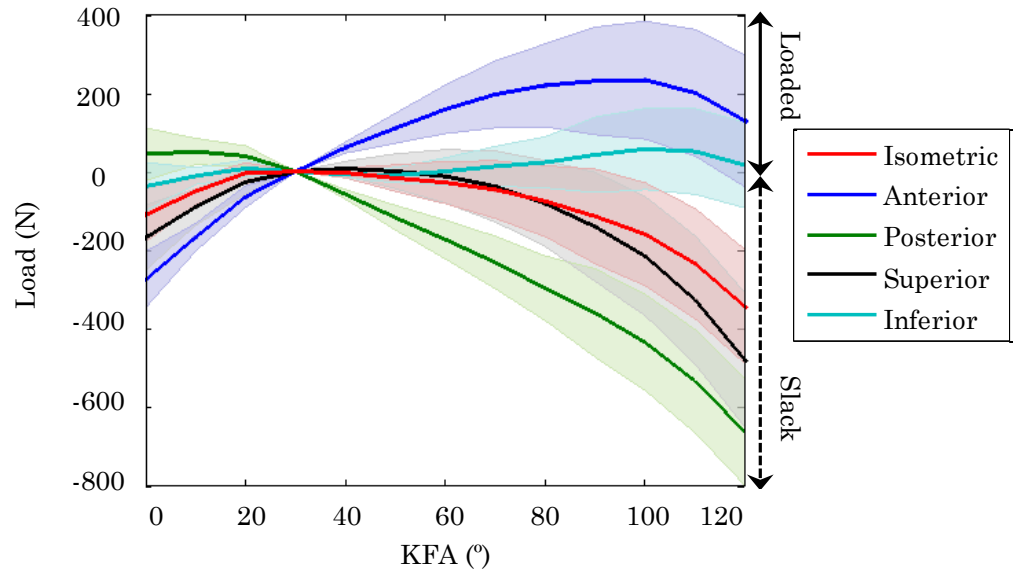


Figure 5.14: Effect of different femoral placements on the load of the reconstructed ACL during passive knee flexion. Positive and negative values imply the ACL is loaded or slack, respectively.

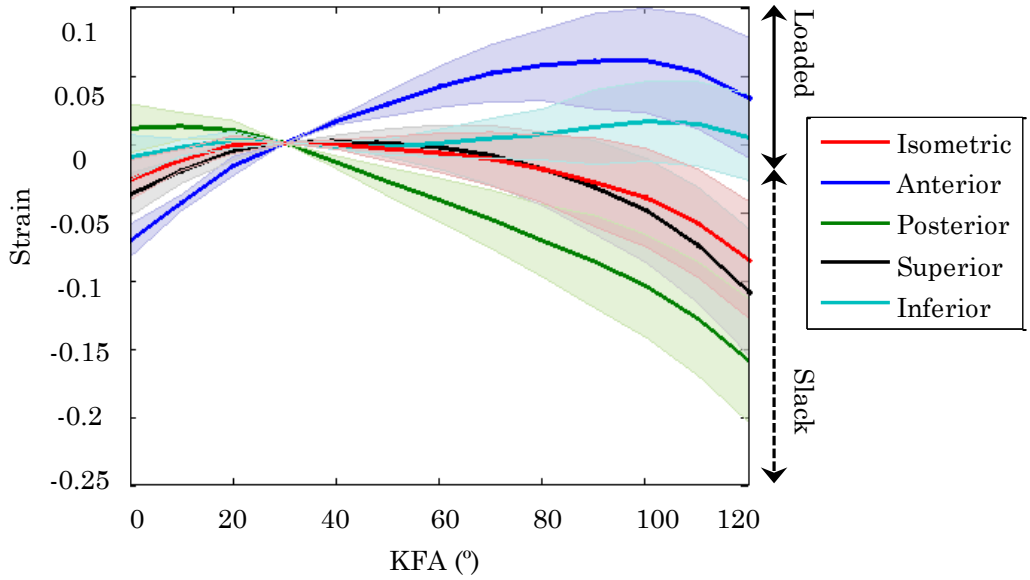


Figure 5.15: Effect of different femoral placements on the strain of the reconstructed ACL during passive knee flexion. Positive and negative values imply the ACL is loaded or slack, respectively.

The positive values of load and strain imply that the ligament is loaded/ stretched, whereas the negative values imply that the ligament is unloaded/ slack. None of the tibial placements had a significant effect on the load and

strain experienced by the reconstructed ACL; however, lateral tibial placement significantly (p<0.001) reduced the twist angle. Inferior (p<0.001) and superior (p<0.05) placements of the femoral attachment significantly increased the twist angle (Figure 5.16).

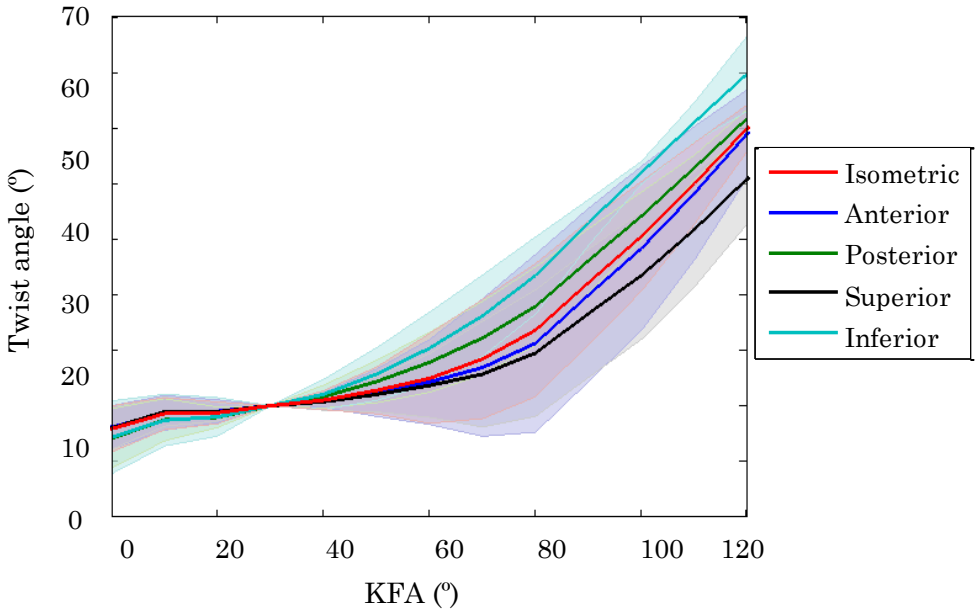


Figure 5.16: Effect of different femoral placements on the twist angle of the reconstructed ACL during passive knee flexion.

Table 5.2: The significance of the femoral and tibial placement on the load, strain, and twist angle of the reconstructed ACL during passive motion. *: p<0.05, ** p<0.01, ***p<0.001

Placement		Strain	Load	Twist angle
Femur	Anterior	*** (+)	*** (+)	-
	Posterior	*** (-)	*** (-)	-
	Superior	-	-	* (-)
	Inferior	*** (+)	*** (+)	*** (+)
Tibia	Anterior	-	-	-
	Posterior	-	-	-
	Medial	-	-	-
	Lateral	-	-	* (-)

5.3.2.2.2 Squatting

As was observed with the passive motion results, during deep squatting activity, anterior (p<0.001) and inferior (p<0.01) femoral placement significantly increased the load and strain of the reconstructed ACL, and posterior placement of the femoral tunnel significantly (p<0.01) decreased the load and strain (Table 5.3). Again, tibial placement did not have a significant impact on the load and strain of the reconstructed ACL. However, in the twist results for weight bearing motion, the tibial position was shown to have a much greater impact. A more medially or anteriorly located tibial tunnel led to an increase in the twist angle, whereas a more laterally or posteriorly located tibial tunnel placement caused a reduction in the twist angle. Femoral placement also had an effect on the twist angle. Superior placement of the femur reduced the twist angle, whereas the posterior and inferior femoral placements significantly increased the twist angle (Table 5.3).

In all of the groups where the femoral placement was located posteriorly, regardless of the tibial placement; the load and strain of the reconstructed ACL was below zero. This would mean that a reconstructed ACL with a posteriorly located attachment on the femur is lax during loaded knee flexion and is unable to restrain anterior tibial translation. In all the groups where femoral placement was either 5 mm posterior or inferior; the twist angle was higher than the control group (isometric).

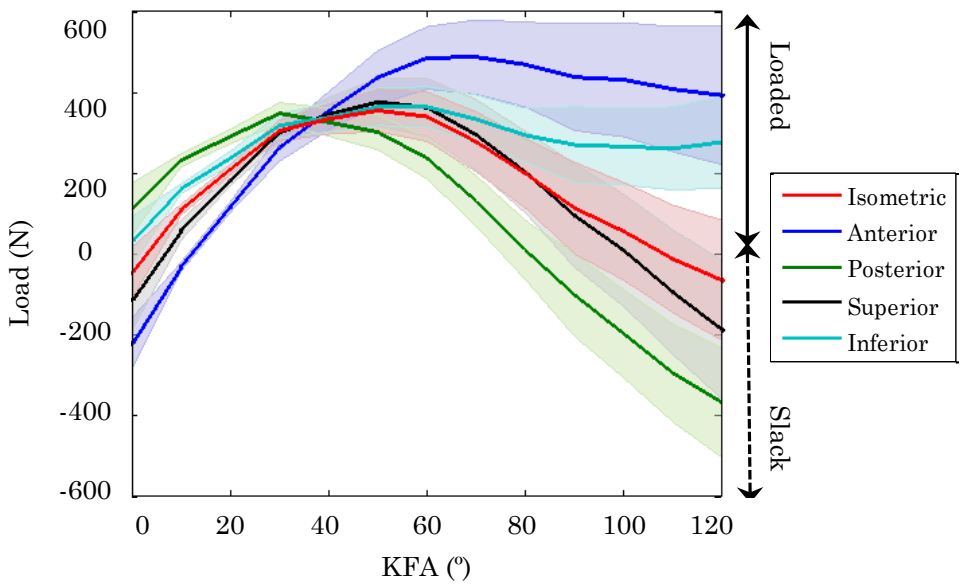


Figure 5.17: Effect of different femoral placements on the load of the reconstructed ACL during squatting. Positive and negative values imply the ACL is loaded or slack, respectively.

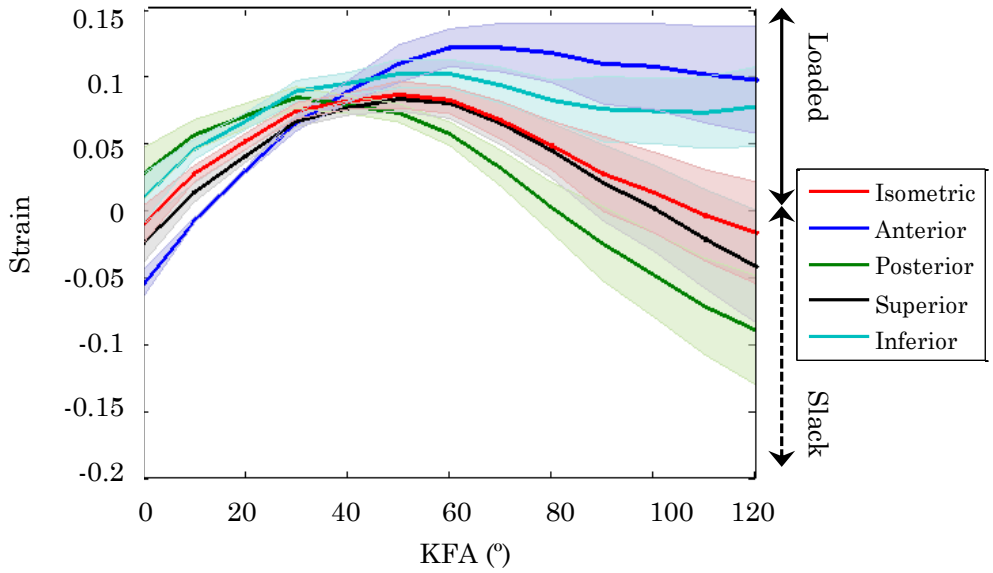


Figure 5.18: Effect of different femoral placements on the strain of the reconstructed ACL during squatting. Positive and negative values imply the ACL is loaded or slack, respectively.

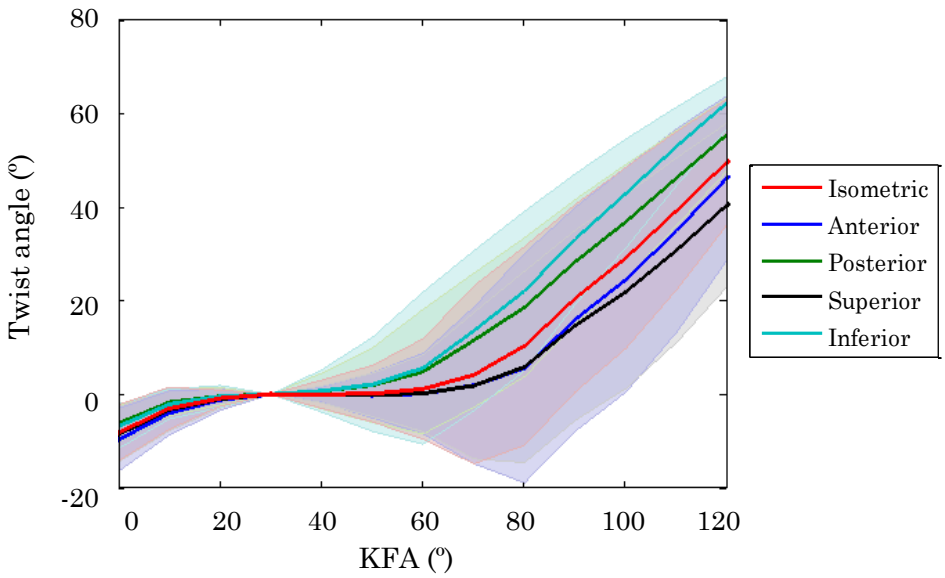


Figure 5.19: Effect of different femoral placements on the twist angle of the reconstructed ACL during squatting.

Table 5.3: The significance of the femoral and tibial placement on the load, strain, and twist angle of the reconstructed ACL during squatting. *: $p<0.05$, ** $p<0.01$, ***$p<0.001$

Placement		Strain	Load	Twist angle
Femur	Anterior	*** (+)	*** (+)	-
	Posterior	** (-)	** (-)	** (+)
	Superior	-	-	* (-)
	Inferior	*** (+)	** (+)	*** (+)
Tibia	Anterior	-	-	* (+)
	Posterior	-	-	* (-)
	Medial	-	-	*** (+)
	Lateral	-	-	*** (-)

5.4 Discussion

As was mentioned in Chapter 1, the tensile behaviour of the ACL is highly dependent on the flexion angle and the loading condition (type of exercise).

Since the attachment site positions measured from the MRI images were the theoretical isometric points, there should be no tension in the ACL and therefore the ACL fibres would be expected to remain just tight throughout the passive flexion, to guide joint motion. The constant load and elongation of the reconstructed ACL during passive motion (Figure 5.11 and Figure 5.12) of the knee found in this study agrees with the isometricity concept [71,72,110] and indicates the isometric attachment sites of the ACL were correctly selected. The non-zero values of the ACL load and strain at higher flexion angles could be the result of measurement errors from the open MRI test data that was input into the current knee models, or may relate to the flat tibia assumption.

The results of the present study showed that the reconstructed ACL had maximum strain and load of 10.56 % ± 3.23 % and 372.11 N ± 67.93 N at 50 º of flexion during weight bearing flexion. Hosseini *et al.* [77] reported 4.4 % ± 3.4 % strain of the AM bundle at 30 ° of flexion under full body weight during a lunge activity.

The maximum load in the reconstructed ACL is comparable to the maximum ACL load of 360 N under maximum quadriceps muscle force at full extension reported by Huss and co-workers [67]. Hosseini *et al.*[88] estimated 242 N ACL load at 15 º of flexion under full body weight. O'Connor *et al.* [228] reported a similar pattern of the reconstructed ACL force versus KFA during squatting; the ACL force was zero at full extension and 90 º of flexion, whereas, the maximum ACL force occurred at 40 º of KFA.

The differences between the strain and load of the reconstructed ACL measured in the present study to those of the native ACL reported in the literature may be a result of the constant stiffness of the modelled synthetic ACL as oppose to the varying stiffness of the native ACL through fibre recruitment. Alternatively, the difference may be due to variations in the loading condition, the patient geometries examined, or may be a result of the assumptions made in the knee model mentioned in Section 5.3.1.1.

The twist angle of the ACL has been reported to increase with increasing knee flexion angle [135,229]. The increased twist angle with flexion has been reported to be because the femoral attachment is oriented predominantly in the longitudinal axis of the femur, whereas, the tibial attachment is in the antero-posterior axis of the tibia [6]. Jordan *et al.* [135] measured the *in vivo* twist angle of the ACL in seven healthy patients during weight bearing knee flexion (quasi-static lunge) and reported an average twist angle of 62.2 ° at 120 º; this corresponds well with the results of the present study (Figure 5.20). Similarly, Zavatsky and O'Connor [136] reported 100 º changes in the twist angle of the ACL over 120 º of passive flexion; which was slightly greater than the 90 º observed in this study. These authors reported that tibial rotation was not considered in their 3D knee model, therefore, the calculated angle of twist would be greater than the actual ACL twist angle [136].

Normally surgeons apply pretension to the ACL graft at the time of fixation. In this study no pretension was considered because the magnitude of pretension will vary depending on surgical technique, however, if pretension

were added it would simply add a constant load to each flexion angle, effectively raising the weight-bearing curve up the y-axis (Figure 5.12). In single bundle ACL reconstruction it is also common to apply pre-torsion to synthetic grafts before fixing the ends of the artificial ACL [136]. Li *et al.* [229] suggested a 20 º internal twist of the tibial end of the graft prior to fixing the artificial ACL at 30 º of flexion.

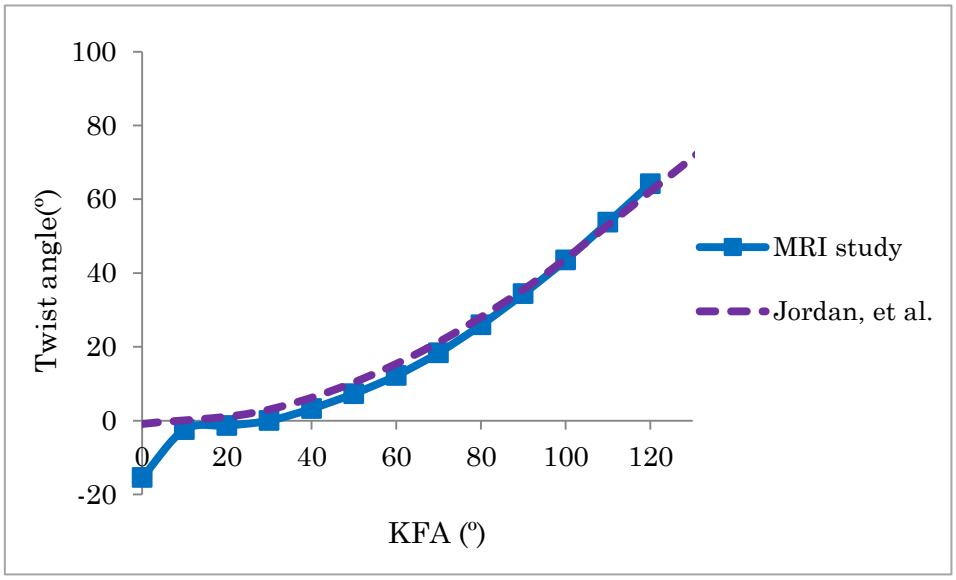


Figure 5.20: The ACL twist angle at different knee flexion angles (KFA) found in the current MRI study compared to a study by Jordan *et al.* [135].

This study highlights the importance of considering both twist as well as ligament elongation when testing designed artificial ligaments for ACL reconstruction. Guidoin *et al.* [117] reported abrasion caused by flexural and torsional fatigue as the main failure mechanism in textile fibres of the artificial ligaments; it is possible that cyclic torsional loading tests could have predicted these problems.

The results of the placement sensitivity study showed that incorrect tibial tunnel placement can be better tolerated than femoral misplacement, which agrees with a number of radiological and clinical studies [138,140,230]. The present study found the load-elongation behaviour of the reconstructed ACL was significantly dependent on the femoral tunnel location, and that anterior placement of the femoral attachment site significantly increased load and strain. Studies have shown that patients with an excessively anterior femoral tunnel placement had abnormal knee stability and range of motion [230]. In addition, anterior placement of the femoral tunnel in the sagittal plane has been reported to shorten the graft length and cause high strain in the graft as the knee flexes [140], which corresponds well with the results of this study which found maximal strain at high flexion angles in models with excessively anterior femoral placement. Conversely, posterior placement of the femoral tunnel has been reported to cause excessive tightening of the graft as the knee extends [140], this effect was only observed in the present study for the passive motion results; posteriorly placed femoral tunnels for weight bearing motion were slack at all flexion angles.

The knee model used in this study has significant limitations. It should be noted that the reconstructed ACL was assumed to have a linear stiffness (97 N mm^{-1}), whereas as outlined in Chapter 1, the native ACL behaves non-linearly, and the stiffness of the UHMWPE cord has been shown to vary with strain rate. It was also assumed that the tibial plateau was flat and the heights of the menisci were constant, whereas in reality, depending on the position of the femur, the height would vary across the tibial condyle. Another limitation of

this study was that it used only one resource to define the tibio-femoral motion of the knee. It was also assumed that the movements of the knee after the ACL reconstruction, using either isometric or misplaced attachment points, were the same as those in the healthy patients with normal ACL.

5.5 Conclusion

It can be concluded that the load-elongation behaviour of the reconstructed isometric fibre of the ACL highly depends on the KFA, type of activity (e.g. passive flexion or squatting), amount of pre-tension in the artificial ligament, and the flexion angle at which the ACL attachments are surgically fixed. When the artificial ACL with a linear stiffness is implanted at 30 º KFA angle, the maximum load and strain occurs at 50 º KFA during squatting, whereas, the artificial ACL experiences a constant change of load and strain during passive motion.

Also the surgical placement of the femoral ACL attachment has a significant impact on the mechanical behaviour of the reconstructed ACL. Therefore, a more forgiving artificial ACL with lower stiffness than the native ACL might be required to prevent over-constraining the joint

Chapter 6: FE Modelling of the Artificial ACL

6.1 Introduction

The preliminary designs of the elastic systems and connecting cord for both the stand-alone artificial ACLR and the artificial ACLR-TKR devices in medium size patients have now been described. As was reported in Chapter 4, the helical and spiral springs designed to reproduce the non-linear stiffness of the native ACL had a linear stiffness, therefore, stop mechanisms would be required in the femoral and tibial springs in order to achieve a design with a multi-linear stiffness. To reproduce the stiffness of the toe (38 N mm^{-1}) and linear (100 N mm^{-1}) regions of the load-elongation curve of the native ACL, it was decided to use a femoral spring with stiffness of 61 N mm^{-1} and a tibial helical and spiral spring with stiffness of 102 and 108 N mm^{-1}, respectively. The springs in series were connected to each other by a Dyneema cord with a stiffness of 2000 N mm^{-1}.

This chapter aims to study the load-elongation behaviour of the designed artificial ACLR devices and see whether they can replicate the behaviour of the native ACL and to highlight any potential weaknesses in the designs. The ACLR devices were examined when subjected to the simulated axial loading, weight bearing flexion (squatting) and the Lachman test using FEA (ABAQUS, version 6.11, Simulia, RI, USA). The results of the tibiofemoral movements during deep squatting from Chapter 5 were used to represent the kinematic movements of the reconstructed ACL throughout weight bearing flexion.

6.2 Methodology

In order to investigate the behaviour of the artificial ACLR devices under the simulated axial loading, squatting and the Lachman test, following steps were taken:

- All of the components were aligned in a way to either represent the axial loading test set-up (Figure 6.1), or the position at the reconstructed isometric fibre sites of the ACL for the simulations of squatting and the Lachman test (Figure 6.2).
- Material properties were applied to the different components.
- Interactions between different parts (e.g. friction and stop mechanisms for the springs) were defined.
- Relevant boundary conditions for each FE model were defined. In the axial loading study, the ACLR device was displaced 5 mm axially, whereas in the FE simulations of squatting and the Lachman test, tibiofemoral movements were applied based on the tibiofemoral movements of the segmented MRI knee model used in Section 5.3.1.2 during passive knee flexion and squatting.
- Meshed FE models of the ACLR devices were solved and the behaviour of the artificial ACLR system in each study was analysed. The elongation of the reconstructed ACL was calculated from the distance between the isometric attachments points on the femur and tibia. The load of the reconstructed ACL was calculated from the elongation and the assigned constant stiffness of the reconstructed ACL.

6.2.1 Component Positioning

6.2.1.1 Axial Loading

In the axial loading study, the femoral and tibial springs were aligned axially (Figure 6.1). The distance between the inner heads of the springs was equal to the distance between the isometric ACL attachments on the femur and tibia at full extension (43.88 mm) found in the 3D knee model created in Section 2.4.

A simplified model of the braided Dyneema loop consisting of a cylindrical cord with a diameter of 3.6 mm was used to connect the femoral spring to the tibial spring. As the diameter and length of the cord model affects its stiffness, in order to reproduce the stiffness of the Dyneema loop tested in Section 3.2.1.3, a diameter of 3.6 mm was used.

A rigid shell component with curved surfaces (femoral / tibial head in Figure 6.1) was added to the helical compression springs to guide the cord, provide smooth surfaces for the cord to articulate against, and subsequently reduce the potential for wear and abrasion.

6.2.1.2 Squatting & Lachman test

In the squatting and the Lachman test studies, the femoral and tibial compression springs were positioned at their respective isometric ACL attachment sites on the femur and tibia and a cylindrical Dyneema cord was modelled between them (Figure 6.2).

As the ACL is shortest at full extension and all the fibres are parallel to each other, the cord connecting the femoral and tibial attachments should be straight at 0 ° flexion. The coordinates of the isometric ACL femoral and tibial attachment points found from the 3D knee model were used (Table 6.1).

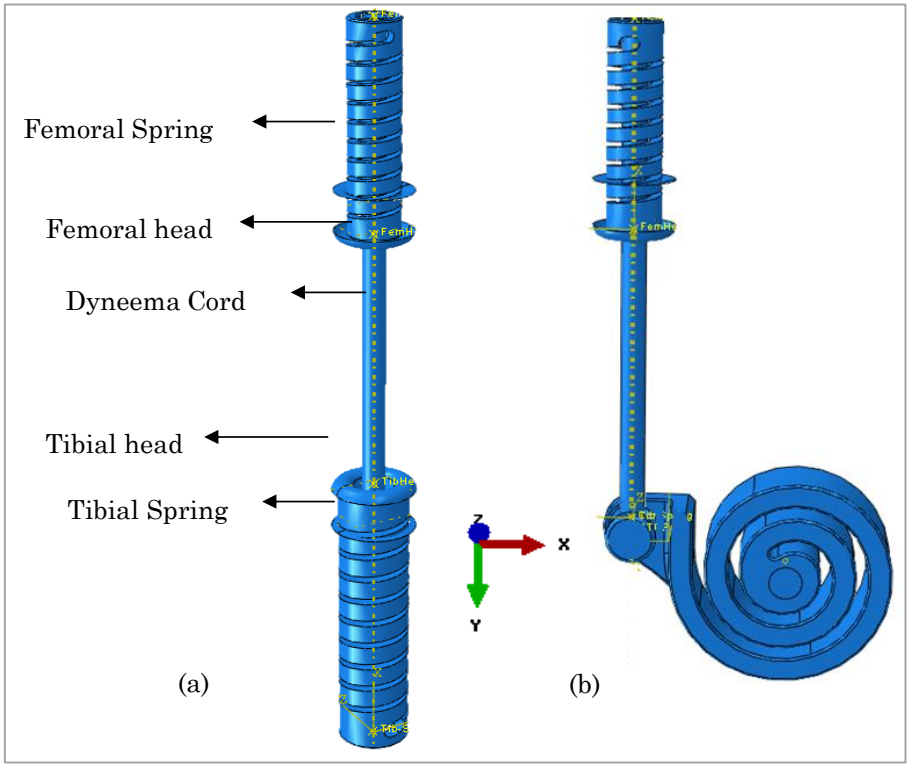


Figure 6.1: Illustration of the component positioning for (a) the artificial ACLR and (b) the ACLR-TKR models used in the axial loading study.

Table 6.1: Coordinates of the isometric ACL femoral and tibial attachment points of a 3D knee model used to position the springs in the FE models.

Attachment	X	Y	Z
Femoral	21.91	-31.612	-3.97
Tibial	0	0	0

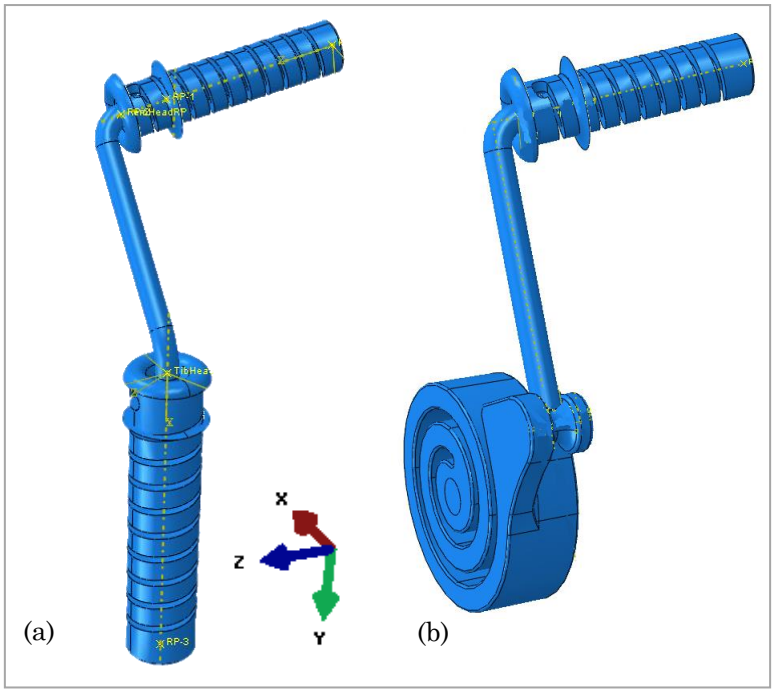


Figure 6.2: Illustration of the component positioning for (a) the artificial ACLR and (b) the ACLR-TKR models used in the FE simulations of squatting and the Lachman test.

6.2.2 Properties

Linear elastic mechanical properties were used for the springs made of CoCrMo (BioDur CCM+) alloy and consisted of elastic modulus of 241,316 MPa and Poisson's ratio of 0.3. Non-linear properties were not modelled because the stress was not expected to exceed the yield stress of the material due to the stop mechanisms.

Dyneema (UHMWPE fibre) was considered an orthotropic material which is commonly used to represent textile structures (both woven and braided material) [231]. An orthotropic material is anisotropic and its properties depend on the direction of loading; greater strength and stiffness is modelled axially than transversely, this gives textiles structure their flexibility. The modulus of

elasticity (E1 = 20000 MPa) along longitudinal fibres of the cord was found from the results of the cyclic fatigue test (Section 3.2.2.3) on Dyneema sample at the stabilised 3000th cycle. It was assumed that the modulus of elasticity in the longitudinal axis of the cord was at least 100 times higher than those in the other transverse directions (E2 = E3 = 200 MPa) to ensure flexibility of the cord. The shear stiffness of the braided loop was also considered to be a 100th of the axial modulus in all directions (G12 = G12 = G23 = 200 MPa). A Poisson's ratio (v) of 0.46 [232] in all directions was applied to the cord model (Table 6.2).

Table 6.2: Material properties of the Dyneema cord used in the FEA model. 'E' represents the elastic modulus in MPa, 'v' the Poisson's ratio and 'G' the shear modulus in MPa, in the x (1), y (2), and z (3) directions.

E1	E2	E3	v1	v2	v3	G12	G13	G23
20000	200	200	0.46	0.46	0.46	200	200	200

6.2.3 Interactions

A frictionless contact definition was used for regions where the cord articulated with the helical spring containers. To model the action of the spring end-plate on the helical springs, kinematic coupling was used to link the movement of the cord with the ends of the helical springs. This meant that any displacement of the cord was transferred to the end of springs and caused compression of the springs as the knee was flexing, without the need to include the geometry of the end-plate into the model.

In order to add a stop mechanism to the springs, the amount of spring deformation was limited by assigning a connector stop wire to each spring. Each spring was permitted to deform up to its safe deformation limit determined in Chapter 4; this was 0.9 mm for the femoral helical spring, 1.35 mm for the tibial helical spring, and 2.2 mm for the tibial spiral spring.

6.2.4 Boundary Conditions

6.2.4.1 Axial Loading

During axial loading, the upper end of the tibial spring container was fully constrained and the femoral head was displaced 5 mm axially away from the tibial spring. All parts were prevented from rotating around the axial axis. A mesh size of 0.7 mm was used for all the parts in this study with quadratic tetrahedral elements (C3D10).

6.2.4.2 Squatting

The movement of the ACL attachment site on the femur relative to the fixed tibial attachment site was defined based on the results of the open MRI study (Chapter 5). The translations in X, Y and Z directions (U1, U2, and U3) and rotations about X, Y and Z directions (UR1, UR2, UR3) of the femur in a 3D knee model relative to the tibia at different flexion angles during weight bearing flexion (squatting) are listed in Table 6.3.

All the translations and rotations (Table 6.3) were applied to the femoral attachment point (Table 6.4) which was kinematically coupled to the femoral spring. The head of the tibial helical spring was constrained in X, Y and Z

directions and the centre of the tibial spiral spring was constrained in all degrees of freedom. Apart from the constrained areas of the tibial springs, their remaining parts were allowed to deform freely. The total deformation of the ACLR device was found by calculating the distance between the femoral and tibial attachment points in space. The load in each individual component of the ACLR device was calculated by multiplying the deformation of each part by its stiffness.

A mesh size of 0.7 mm was used for all the parts in this study with quadratic tetrahedral elements (C3D10).

Table 6.3: Translations (in mm) and rotations (in radians) of the femoral attachment point relative to the fixed tibial attachment point during squatting.

Flexion Angle (º)	U1	U2	U3	UR1	UR2	UR3
0	0	0	0	0	0	0
10	3.979	1.116	-3.956	0.014	0.115	0.176
20	6.312	2.200	-5.316	0.047	0.178	0.356
30	8.469	3.408	-6.065	0.101	0.215	0.541
40	9.655	4.604	-6.134	0.139	0.218	0.721
50	10.772	5.854	-6.189	0.179	0.225	0.901
60	11.364	7.299	-6.786	0.232	0.205	1.082
70	11.523	8.906	-6.257	0.273	0.159	1.258
80	11.562	10.665	-6.231	0.294	0.109	1.429
90	11.406	12.199	-4.207	0.314	0.053	1.597
100	11.461	13.638	-4.513	0.306	-0.001	1.763
110	11.357	15.022	-4.255	0.288	-0.052	1.930
120	11.399	16.323	-3.284	0.260	-0.096	2.097

6.2.4.3 Lachman Test

The Lachman test was simulated by flexing the femoral attachment point relative to the tibia up to 20 º, and then applying 4 mm posterior translation to the femur. The translations along the X, Y and Z directions (U1, U2, and U3) and rotations about X, Y and Z directions (UR1, UR2, UR3) of the femur in the 3D knee model (from Section 5.3.1.1) relative to the tibia during passive knee flexion were used to flex the model up to 20 º (Table 6.4). The femur was then displaced by 4 mm posteriorly while the tibia was fixed in place. The deformations and forces within the model were calculated using the method described in Section 6.2.4.2.

Table 6.4: Translations (in mm) and rotations (in radians) of the femur relative to the tibia used to simulate the Lachman test at 20 º of flexion.

	U1	U2	U3	UR1	UR2	UR3
Up to 20 º passive flexion	0	0	0	0	0	0
	2.535	1.118	-2.947	0.016	0.013	0.175
	4.246	2.203	-4.753	0.033	0.027	0.350
Lachman test, 4 mm posterior translation	4.646	2.203	-4.753	0.033	0.027	0.350
	5.046	2.203	-4.753	0.033	0.027	0.350
	5.446	2.203	-4.753	0.033	0.027	0.350
	5.846	2.203	-4.753	0.033	0.027	0.350
	6.246	2.203	-4.753	0.033	0.027	0.350
	6.646	2.203	-4.753	0.033	0.027	0.350
	7.046	2.203	-4.753	0.033	0.027	0.350
	7.446	2.203	-4.753	0.033	0.027	0.350
	7.846	2.203	-4.753	0.033	0.027	0.350
	8.246	2.203	-4.753	0.033	0.027	0.350

6.3 Results

6.3.1 Axial Loading

6.3.1.1 ACLR

It was observed that the artificial ACLR device elongated by 2.5 mm under 160 N. Beyond 160 N the springs were fully deformed and further deformation was accommodated by the cord. The maximum stress (492 MPa) after 5 mm of displacement was found in the cord where it was connected to the end of the tibial spring (Figure 6.3).

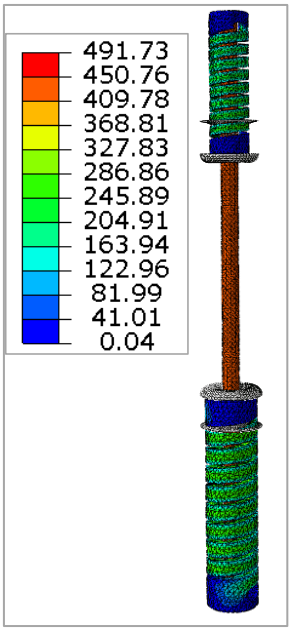


Figure 6.3: von Mises stress (MPa) in the artificial ACLR system after 5 mm axial deformation.

The multi-linear load-elongation behaviour of the ACLR system under simulated axial load was compared to that of the native ACL (Figure 6.4).

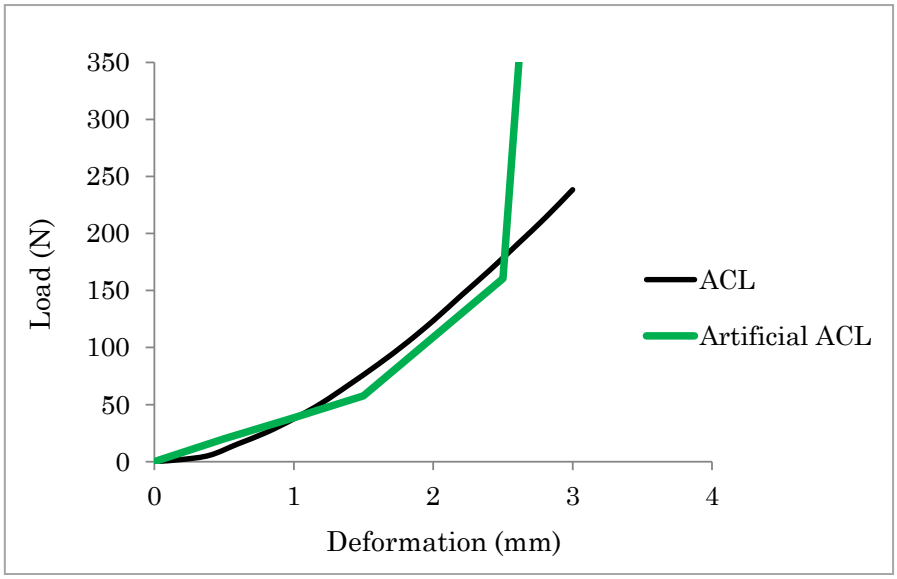


Figure 6.4: Comparision of the load-elongation results of the artificial ACLR device made of the two helical springs to those of the native ACL [88].

6.3.1.2 ACLR-TKR

It was observed that the ACLR-TKR device elongated by 3 mm at a load of 262 N, and the springs were fully deformed, after which the further deformation was accommodated by the cord. The maximum stress (900 MPa) after 5 mm of displacement was found in the cord where it was connected to the tibial spring (Figure 6.5).

The load-elongation behaviour of the ACLR device for TKR under simulated axial load matched that of the native ACL even more closely than for the ACLR device alone (Figure 6.6).

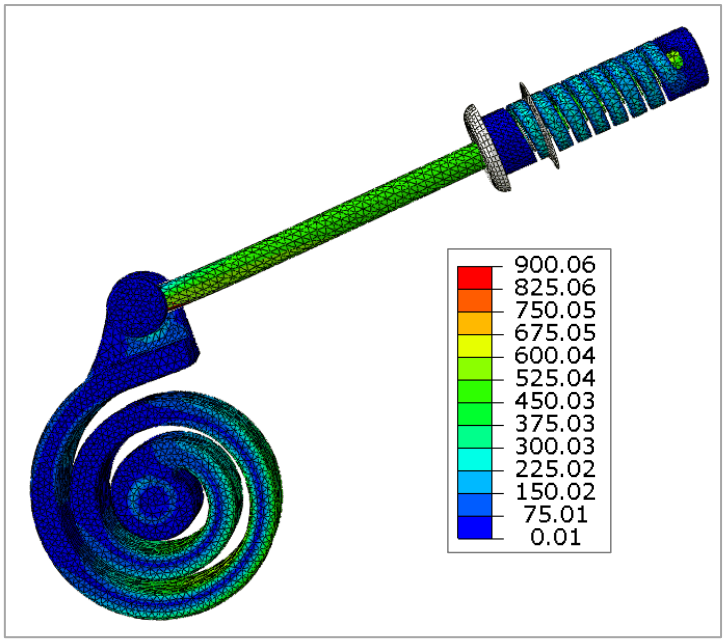


Figure 6.5: von Mises stress (MPa) within the artificial ACLR-TKR device after 5 mm axial defomation.

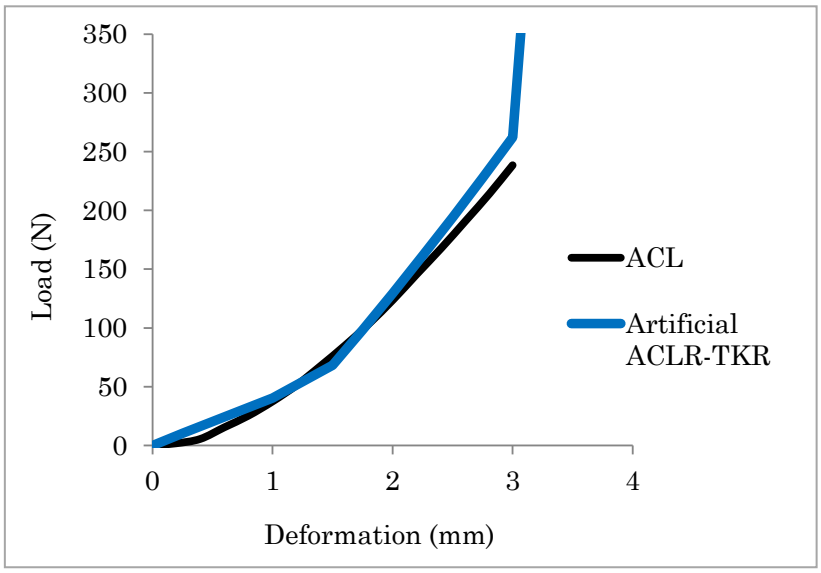


Figure 6.6: Comparision of the load-elongation results of the artificial ACLR-TKR device made of a helical and a spiral spring to the mechanical beaviour of the native ACL [88].

6.3.2 Squatting

6.3.2.1 ACLR

Results of the squatting simulated on the ACLR system showed that the femoral helical spring reached its maximum deformation limit of 0.9 mm between 25 ° and 84 ° of flexion and the tibial helical spring was maximally deformed by 1.35 mm between 16 ° and 74 ° of flexion (Figure 6.7). As the femoral and tibial springs were not able to provide the necessary deformation required in this simulation, the cord was maximally elongated to 1.22 mm at 50 ° of flexion. The ACLR device was loaded up to 2447 N at 50 ° of flexion (Figure 6.8).

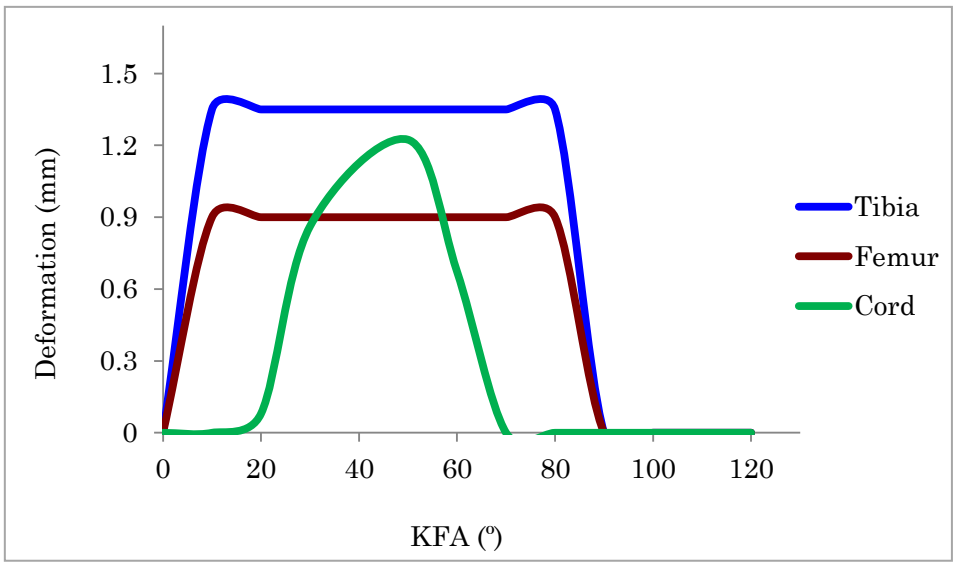


Figure 6.7: Deformation of the stand-alone ACLR device including the helical femoral and tibial springs and Dyneema cord during squatting.

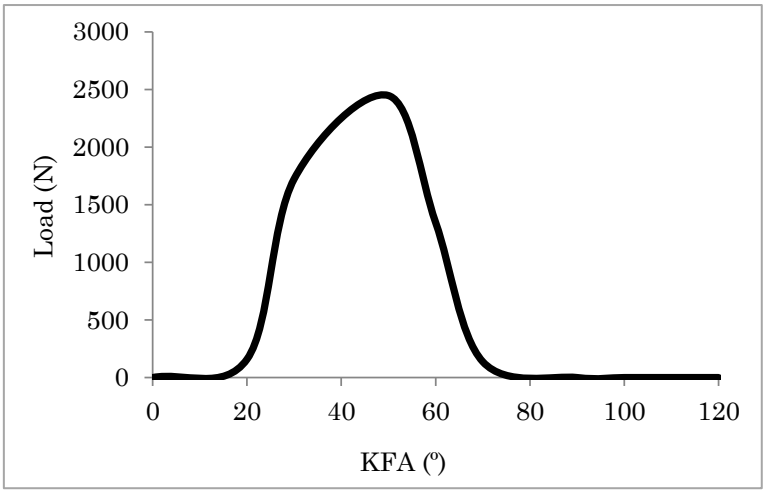


Figure 6.8: Load in the artificial ACLR device during squatting.

The maximum stress in both the femoral and tibial helical springs was observed on their internal surface, at the middle of the last coil close to the end of the spring. The maximum stress in the entire system occurred in the Dyneema cord where it was articulating against the tibial head (Figure 6.9). Maximum stress in the femoral spring, tibial spring and cord were found to be 468.74 MPa, 474.46 MPa and 1624.94 MPa, respectively (Figure 6.10).

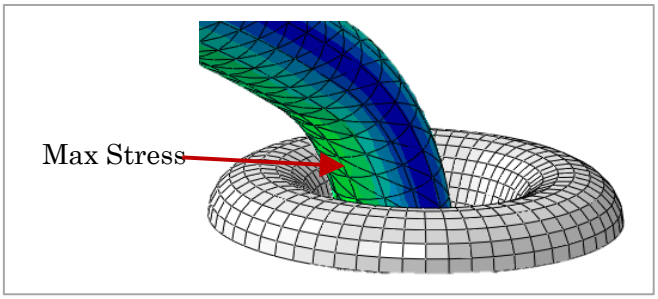


Figure 6.9: Maximum stress of 1625 MPa in the artificial ACLR device during squatting occurred in the cord where it was articulating with the tibial head.

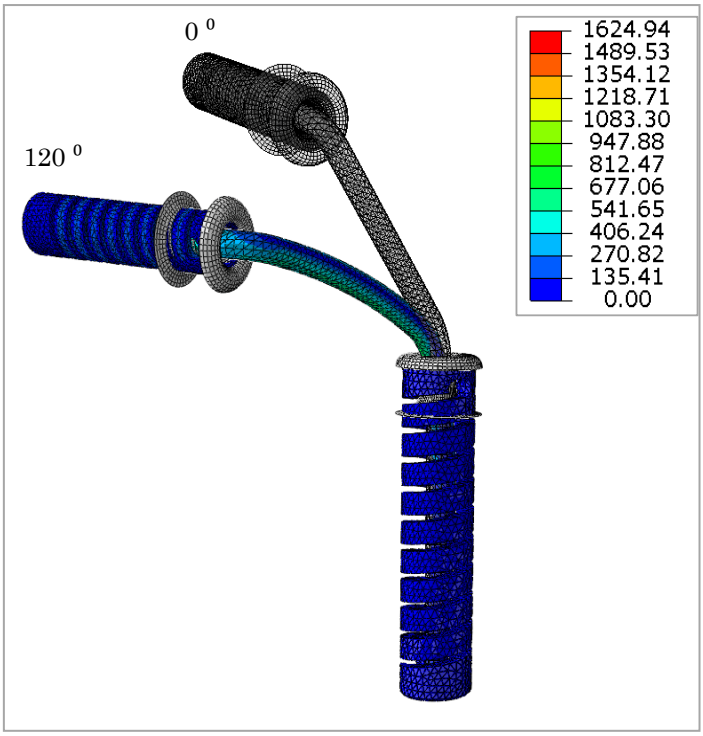


Figure 6.10: Stress (MPa) in the artificial ACLR device at 120 ° of KFA when the knee is squatting from 0 ° to 120 ° of KFA.

6.3.2.2 ACLR-TKR

Results of the squatting simulation on the artificial ACLR system showed that both femoral helical spring and tibial spiral spring reached their maximum deformation limit at 20 ° of flexion. The femoral and tibial springs remained compressed up to 60 ° and 80 ° of flexion, respectively, and then started to unload. Load in the ACLR-TKR device reached zero at 90 ° of flexion (Figure 6.11). Maximum load of 238 N occurred between 20 ° and 70 ° of flexion (Figure 6.12). The maximum stress in the femoral helical spring, tibial spiral spring and cord were 469.40 MPa, 397.63 MPa and 1172.75 MPa, respectively.

The maximum stress in the entire system occurred in the Dyneema cord where it connects with the tibial spring. The maximum stress in the femoral

spring occurred on the internal surface of its last coil, and the maximum stress in the spiral spring was close to the bollard end where it was connected with the Dyneema cord (Figure 6.14). Another high stress region found in the spiral spring was at the small curvature close to the centre of the spring which had been fully constrained.

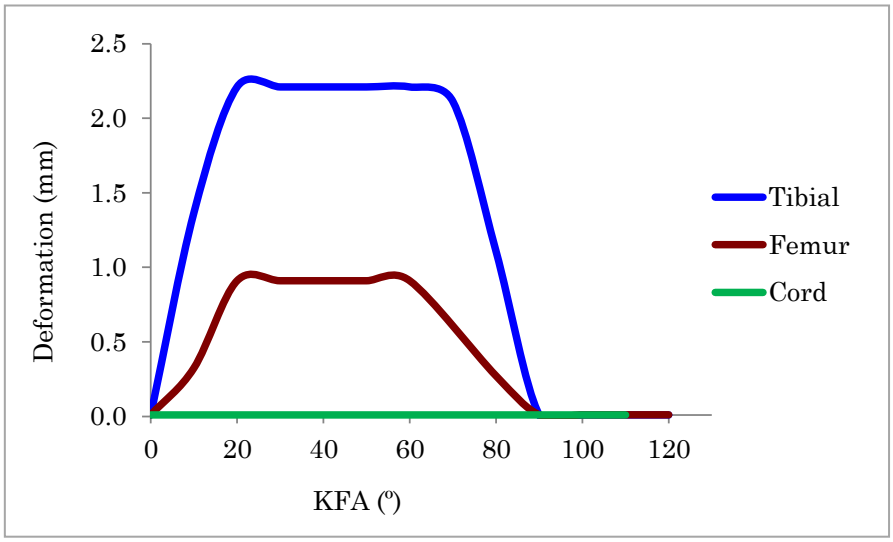


Figure 6.11: Deformation of the femoral helical spring, tibial spiral spring and Dyneema cord during squatting.

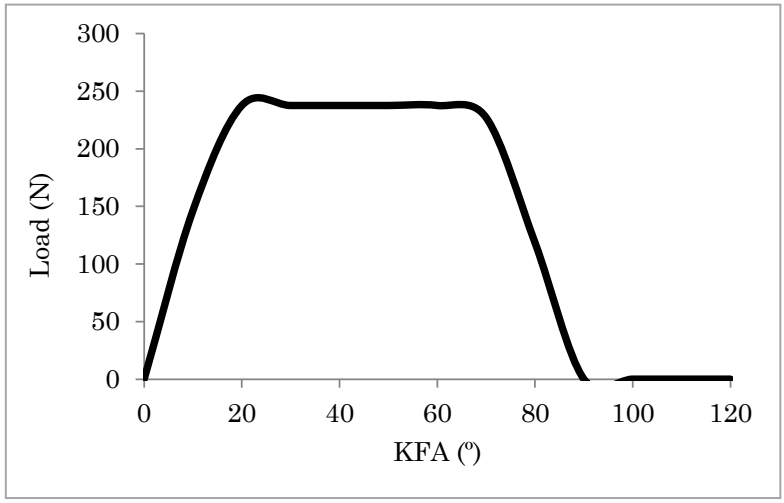


Figure 6.12: Load in the ACLR-TKR device during squatting.

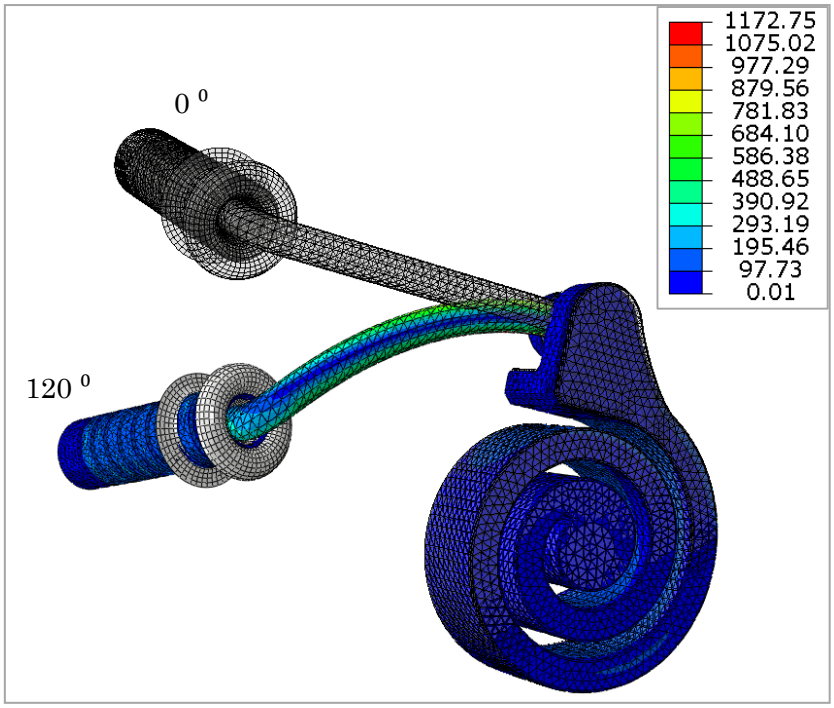


Figure 6.13: Stress (MPa) in the artificial ACLR-TKR device during squatting from 0 ° to 120 ° of flexion.

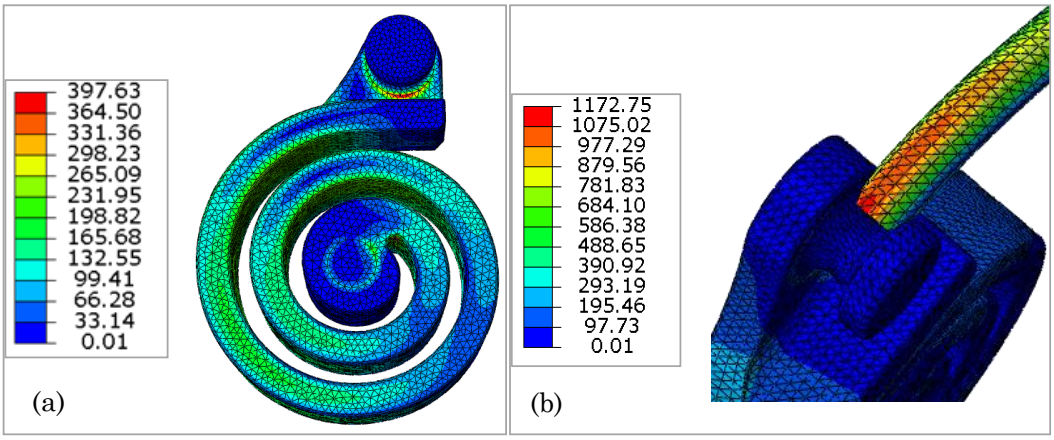


Figure 6.14: Illustration of maximum stress (MPa) in (a) the spiral spring at 20 ° of KFA and (b) in the Dyneema cord at 120 ° of KFA.

6.3.3 Lachman Test

6.3.3.1 ACLR

The load-elongation results of the Lachman test performed on the ACLR system is shown in Figure 6.15. The maximum load in the ACLR device was 4241 N after 4 mm AP translation of the femur. The cord was elongated by 2.12 mm to provide the necessary laxity in the ACLR system. The maximum stress in the system occurred in the cord where it was articulating against the femoral head.

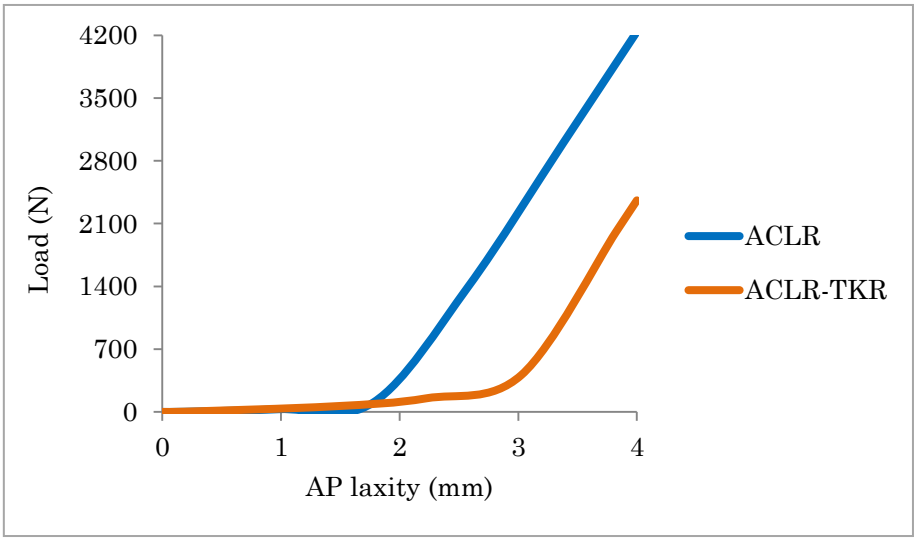


Figure 6.15: Load in the artificial ACLR and ACLR-TKR devices during the Lachman test.

6.3.3.2 ACLR-TKR

The maximum load in the ACLR- TKR device after 4 mm AP translation was 2360 N (Figure 6.15). The cord was elongated by 1.14 mm to provide the necessary laxity in the ACLR-TKR system. The maximum stress in the system occurred in the cord where it was articulating against the femoral head.

6.4 Discussion

6.4.1 Axial Loading

The results of the simulated axial loading on both the ACLR and ACLR-TKR devices showed that the non-linear stiffness of the native ACL could be reproduced using a multi-linear reconstruction system; however, there were some issues with the amount of deformation taken up by the tibial helical spring. It was only possible to design tibial and femoral springs with a combined deformation limit of 2.25 mm for the ACLR device and 3.1 mm for the ACLR-TKR device within the size constraints defined in Section 2.4. In Chapter 2, the design criteria for both devices had a desired elongation of between 3 and 5 mm; the ACLR device design did not meet this requirement as the spring systems in ACLR and ACLR-TKR devices only provided 2.25 mm and 3.1 mm, respectively. As a result, the extra elongation was provided by the Dyneema cord during deep squatting.

As the helical compression springs need to be housed in a metal pot before implantation in the bone, the overall diameter of the system could be decreased by reducing the thickness of the metal pot; however the pot must retain sufficient strength. Another option to obtain more deformation from the springs would be to use Titanium alloy instead of CoCrMo alloy as it has a lower elastic modulus; however, as was mentioned in Section 2.5.2, Titanium has a lower fatigue strength compared to CoCrMo alloy. Also, wear between the Titanium and the UHMWPE cord could be problematic, however, wear might be minimised by using a ceramic coating on the articulating areas

between the cord and the spring. All these factors would need to be considered in order to create an ACLR design able to elongate sufficiently to function safely.

As was determined in Section 5.3.2.2, the position of the ACL attachment site on the femur has a significant impact on the load-elongation behaviour of the reconstructed ACL. As the risk of misplacing the ACL attachment during surgical implantation is high, implanting a more forgiving design with lower stiffness would reduce the risk of over-constraining the joint. Over constraining the joint can be more problematic than under-constraining the joint as it can affect the mobility, cause damage to the artificial ACL and the surrounding tissues. Therefore, these results indicate a more compromised spring design with lower stiffness will be required to provide the necessary deformation for both artificial ACLR devices.

6.4.2 Squatting

As the elongation needed from both artificial ligament devices during weight-bearing flexion was greater than the overall permitted deformation from the femoral and tibial springs, the cord was subjected to high level of stress. As was mentioned in Section 5.3.2 the average required elongation in a reconstructed ACL during squatting is 2.95 mm, which was the difference between the minimum elongation at 0 º and maximum elongation at 50 º of flexion. However, this elongation result was based on the average results of the 18 knee models, whereas the parameters used for the knee flexion simulations reported in this study were based on the behaviour of just one

knee model in which the maximum elongation required from the artificial ACL was 4.17 mm. This model was chosen because it was the smallest tibia and represented a worst-case scenario, but the extra elongation required during squatting resulted in excessive stress in both artificial ACL devices and over stretching the Dyneema cord; therefore these results may not represent the majority of patient geometries.

The excessive stress observed could cause long term creep and possibly failure of the cord. Both the femoral and tibial springs reached their maximum deformation limits at about 20 º of flexion and remained fully deformed throughout the majority of knee flexion angles. In the artificial ACLR, the Dyneema cord was stretched by 1.22 mm which significantly increased the load experienced in the device.

The maximum stress in the ACLR devices occurred in the Dyneema cord where it was articulating against the tibial spring. This is in agreement with the most common failure mechanisms of the polymeric grafts used in the past for reconstruction [117]. It also indicates on the importance of careful design of the spring's head to minimise abrasion, stress and wear of the cord. The design could be improved by enlarging the radius of this component, manufacturing this part out of low friction material (such as ceramic or CoCrMo alloy) and ensuring a highly polished surface finish.

It should be noted that the motion data used to simulate flexion of the knee were derived from data reported from an open MRI study [26]. Any inaccuracy in their measured tibiofemoral motions could affect the behaviour of the designed

ACLR devices in this project. Therefore, in addition to the studies outlined in this thesis, it will be necessary to validate the behaviour of the artificial ACL with experimental kinematic studies to assess the efficacy and safety of using the devices designed in this project.

6.4.3 Lachman Test

The results of the Lachman test on the designed ACLR devices can be compared to the results of the same test on cadaver knees with healthy intact ACL (Figure 6.16). Amis [233] studied the anteroposterior stability of 28 cadaver knees and reported a wide range of normal laxity. The author found that a small pretension error on the artificial ACLR graft can highly affect the stability of the joint. The stability of the knee specimens were measured after reconstructing the ACL with three different ACLR grafts made of carbon fibre and polyester. It was stated that despite the four times difference in the stiffness of the grafts, the behaviour of the knee remained the same. A preliminary cadaver study (Appendix 2) using the stand-alone ACLR and ACLR-TKR devices also showed no significant difference between the anterior tibial laxity of the healthy knee with intact ACL to the ACLR and ACLR-TKR knees.

When the results of the simulated Lachman test on the artificial ACLR devices presented in this study are compared with those reported by Amis [233] it could be concluded that the artificial ACLR devices resulted in a greater constraint of the joint. The high level of load observed in both devices was due to the

elongation of the cord. As the stiffness of the cord was about 2000 N mm^{-1}, at least 2000 N was required in order to provide 1 mm elongation of the cord.

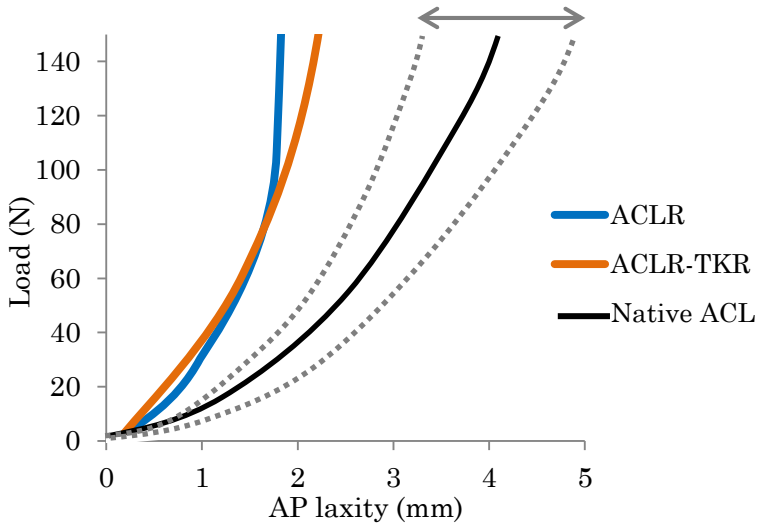


Figure 6.16: Results of the simulated Lachman test on the artificial ACLR devices compared to the result of the same test on the native ACL in cadaver knees (n=20) [233]. Dashed lines indicate the range of normal laxity.

One limitation of this study was that the Lachman test was performed only on the artificial ACL devices whereas those reported in the literature tested the entire human knee. As was mentioned previously, inextensible grafts of Carbon fibre and polyester could reproduce the non-linear anteroposterior movements of the knee in response to the anterior tibial load [233], therefore, it is likely that the presence of other soft tissues within the knee (particularly the muscles and tendons) effect the behaviour of the artificial ACLR device and balance the stability of the joint. Despite these limitations, based on the results of this study it can be concluded that the ACLR devices constrained the joint more than a standard ACL-reconstruction, and although this would restore stability in the short term, greater laxity may be necessary to ensure the long-term durability of the device.

6.5 Conclusion

This chapter described the FEA performed on the designed artificial ACLR devices by simulating the axial loading, weight bearing flexion (squatting) and Lachman tests. The load-elongation behaviour of the designed ligaments was compared to those of the native ACL. Although the designed devices both could accurately produce the non-linear stiffness of the natural ACL, the elastic components of the stand-alone ACLR device were unable to reach sufficient elongation required to function throughout the whole range of flexion. The difficulty in designing mechanical springs that can reproduce the elongation of the native ACL within the limited size constraints defined in this project was discussed. Also, due to the common surgical error in misplacing the ACL attachment sites that changes the mechanical behaviour of the reconstructed ACL, it was concluded that a more forgiving design with lower stiffness would be required to reduce the risk of over-constraining the knee joint and some possible ways by which this could be achieved were suggested.

Chapter 7: Conclusions & Future Work

7.1 Conclusions

The review of literature highlighted the importance of reproducing the functions of the ACL; the abnormal kinematics and accelerated osteoarthritic disease progression observed in ACL-deficient patients were discussed. However, the current methods for reconstructing the ACL using biological grafts, as well as the synthetic grafts, were shown to be prone to premature failure and unable to replicate the mechanical behaviour of the native ACL and therefore cannot restore the normal kinematics and mechanics of the knee and prevent degenerative disease progression. For these reasons, the clinical need for a novel durable synthetic ACL reconstruction device which could reproduce the functions of the ACL was demonstrated.

The design criteria for an artificial ACLR alone and ACLR-TKR devices were defined based on the mechanical properties of the native ACL, the manufacturing and biological considerations, and the size constraints in the knee joint. The specified criteria were:

- A total elongation of 3-5 mm
- A multi-linear stiffness of ~38 N mm^{-1} for the toe region and ~100 N mm^{-1} for the linear region
- Be able to withstand a load of 2000 N or higher without permanent deformation
- Be able to withstand cyclic loading up to at least 6 million cycles
- Resistant to creep, fatigue and wear, and biocompatible
- Easy to manufacture, sterilise, assemble and implant
- Fit within a tunnel of up to 12 mm diameter and 39 mm length within the femur

- The tibial elastic system to fit within a tibial boney tunnel with a maximum 12 mm diameter and 50 mm length for the stand-alone ACLR device
- The upper section of the tibial elastic system for the ACLR-TKR to fit within a rectangular space no more than 13 mm wide and an average height of 5.3 mm higher than the centre of the medial meniscus
- The lower section of the tibial elastic system for the ACLR-TKR to fit within a TKR tibial stem with dimensions defined in Section 2.4.3.2

A connecting cord with an elastic system comprising of two springs was chosen to reproduce the non-linear stiffness of the native ACL. Dyneema (UHMWPE fibre) was selected to be used in the connecting cord. The results of the mechanical tests on the braided Dyneema loops indicated it had sufficient tensile strength and nominal creep after a 3000 cycle running in period, which would be reached at a relatively early time point clinically. Body temperature had no significant effect on the tensile strength and strain of the Dyneema loops; however, humidity significantly reduced the tensile strength. In order to increase the UTS to reduce the impact of humidity on the durability of the connecting cord, it is recommended that more fibres be added to the braided structure.

Material hardening models were considered to describe the cyclic behaviour of the Dyneema loops. The classical isotropic plasticity model over-predicted the residual plastic strain of the Dyneema loops [202] whereas the non-linear isotropic kinematic model could be used to predict the early cyclic behaviour of the Dyneema loop. The long-term behaviour of the Dyneema could not be

predicted, although as the material stabilised after 3000 cycles, the stabilised model was chosen to represent the Dyneema.

Two CoCrMo alloy helical compression springs, and a CoCrMo spiral spring combined with a CoCrMo helical compression spring, were chosen for the ACLR and ACLR-TKR devices, respectively. Both helical and spiral springs have linear stiffness; stop mechanisms were proposed to create an ACLR system with a multi-linear system, close to the non-linear stiffness of the native ACL. The main disadvantage of using a mechanical stop was identified as accelerated fatigue and wear at the articulating surfaces, use of a wear resistant surface would minimise this risk.

The height and thickness of the rectangular wire in the helical compression spring and also thickness, central radius and width of the spirals spring had the highest impact on the stiffness of the elastic system. Therefore by altering these dimensions, the stiffness of the helical and spirals springs were optimised. The stiffness of the spiral spring was more influenced by varying the thickness of its wire within the estimated manufacturing tolerances (± 0.1 mm) compared to other geometrical factors; therefore manufacturing this dimension would need to be carefully controlled.

During passive flexion of the knee, the reconstructed isometric fibres represent a constant load and strain, however, during weight bearing flexion, the maximum load and elongation of the reconstructed ACL was seen at 50 º of flexion. The twist angle of the ACL ascended with increasing flexion angle;

therefore it was concluded that the artificial ACLR device must be able to reproduce the twist angle as well as the attachment points of the native ACL.

Incorrect tibial placement of the artificial ACL was shown to be better tolerated than femoral misplacement. Excessive anterior or inferior placement of the femoral tunnel significantly increased the load and strain of the reconstructed ACL, whereas excessive posterior placement of the femoral attachment had a reverse effect.

The native ACL can extend more than 10 mm at failure (Figure 1.9) and up to 3 mm under full body weight (Figure 1.11), however, the FEA modelling of the artificial ACLR devices illustrated that it is not possible to design a CoCrMo spring that could provide a similar amount of elongation while meeting the stiffness criteria and the size constraints in the knee joint. The designed artificial ACLR devices could provide less than 3 mm deformation under the defined safe stress level of 465 MPa. Both the designed devices successfully reproduced the stiffness of the native ACL under axial loading, but the Lachman test revealed the devices over-constrained the joint when exposed to anterior laxity compared with more conventional ACL-reconstruction methods.

This thesis has described the novel design of two ACL reconstruction devices which behave non-linearly in response to load and flexion. Further work is required to optimise these designs to ensure sufficient joint laxity to account for surgical error, and to ensure design durability. Nevertheless, the essential

design criteria have been defined, prototype components tested and validated, and the design processes outlined.

7.2 Future work

7.2.1 Design Modification

7.2.1.1 Spring

As was reported in Chapter 4 and Chapter 6, it is difficult to design a mechanical spring that can meet the defined stiffness requirements, provide enough elongation under the safe fatigue stress limit and also meet the size constraint requirements. Also, the results of the attachment sensitivity study showed that the ACL placement has a significant impact on the load, elongation, and twist angle of the reconstructed ACL. As it is common for surgeons to misplace the ACL isometric attachment sites, the artificial ACLR should be designed in a way to reduce the risk of over constraining the knee joint.

A compromised design of the artificial ACL with lower stiffness and higher deformation limit will be designed to help overcome these problems. The size constraints will be reviewed for a wider selection of patients to determine if the use of larger springs might be possible. Using Titanium alloy will be considered in the future spring design; as the elastic modulus of the titanium is lower than the CoCrMo alloy, more deformation can be achieved with a same size spring.

7.2.1.2 Connections

As the connection between the mechanical springs and the Dyneema cord was not extensively covered in this project, it is essential to consider designing connection mechanisms that safely connect the Dyneema cord to the femoral and tibial springs, prevent cord dislocations during high demanding activities, and have smooth surfaces that reduce abrasion and wear of the cord. As was mentioned earlier, abrasion was reported to be the main failure mechanism for the polymeric reconstruction grafts [117]; indicating the importance of optimal connector design.

7.2.1.3 Stop Mechanism

The design of the stop mechanism was not extensively investigated in this project; therefore, as future work a stop mechanism will be designed for both helical and spiral springs. One possible mechanical stop design for the helical spring might consist of a plate positioned at the end of the spring (Figure 7.1).

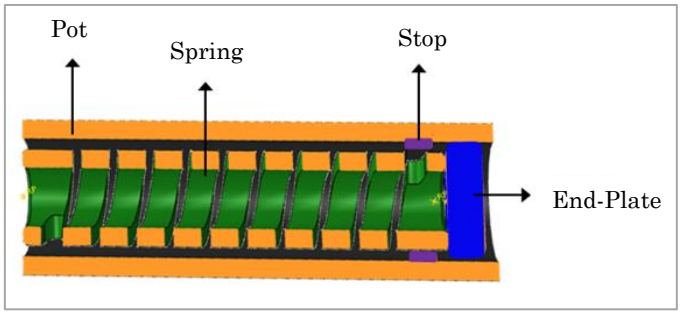


Figure 7.1: A potential stop mechanism design for the helical compression spring.

Tension of the Dyneema cord would cause the end-plate to compress the helical spring housed in a closed pot until the plate reaches its travel limit.

7.2.2 Knee Model

The knee model used in this project to simulate the passive and loaded knee motions on the segmented MRI assumed that the femur is articulating against a flat tibia, whereas the human tibia is not flat. In order to improve the results of this study, the simulations will be repeated while accounting for the geometry of the relative segmented tibial models. A non-linear stiffness for the ACL will also be used to assess load.

Figure 7.2 demonstrated the positions of the artificial ACLR devices developed in this project, relative to the femoral and tibial bones.

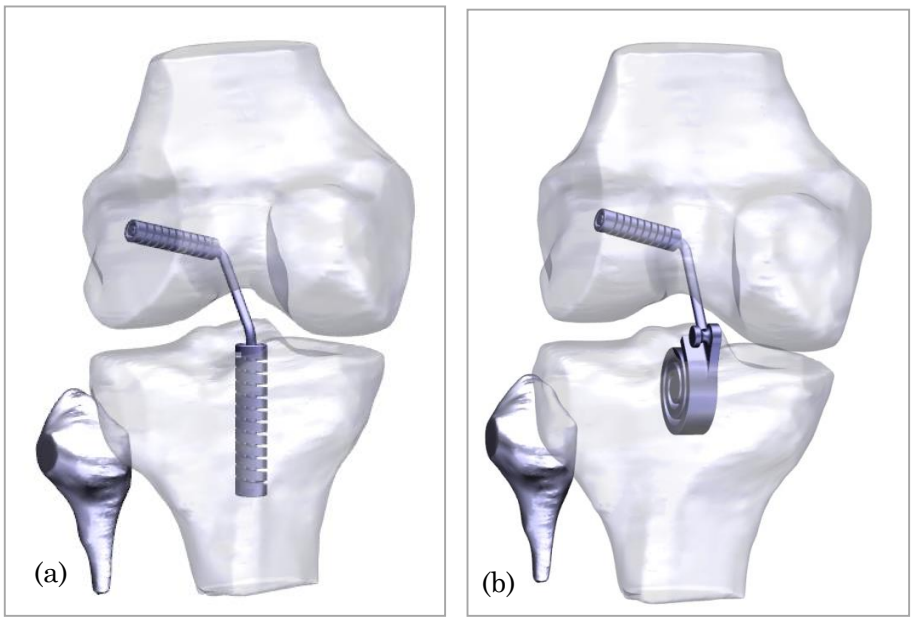


Figure 7.2: (a) The artificial ACLR device comprised of femoral and tibial helical springs and (b) ACLR-TKR device comprised of a helical femoral spring and a tibial spiral spring. The TKR components and the spring containers are removed for clarity.

7.2.3 Mechanical Tests

As the artificial ACLR devices are designed to be implanted into the human body, and will be commercially launched by Biomet UK Healthcare Ltd., the necessary regulatory approval should be obtained. Some of the mechanical tests that need to be performed in order to meet the BSI and FDA approvals are; wear testing of all articulating surfaces, fatigue testing in excess of 10 million loading cycles and mechanical test of the implant fixation within the bone or to the TKR.

Some of the mechanical tests that should be considered for the final design of the connecting cord are:

- A combination of tensile, torsional and bending fatigue test
- The abrasion of the cord at the attachment areas as well as yarn on yarn abrasion
- The effect of the tissue ingrowth (if any) on the mechanical properties of the cord

7.2.4 Kinematic Study

In order to validate the functionality of the designed artificial ACLR devices in reproducing the normal kinematics and restoring stability of the knee joint, a cadaveric kinematic study will be performed using a 3D motion tracking system (Vicon, Oxford Metrics, Oxford, UK) during both passive and loaded knee flexion [234].

Bibliography

1. Duthon, V., Barea, C., Abrassart, S., Fasel, J., Fritschy, D., Ménétrey, J. Anatomy of the anterior cruciate ligament. *J Knee Surg.* 14 (3), 204–13 (2006).

2. Vieira, A., Guedes, R., Marques, A. Development of ligament tissue biodegradable devices: a review. *J Biomech.* 42 (15), 2421–30 (2009).

3. Calmbach, W., Hutchens, M. Evaluation of Patients Presenting with Knee Pain: Part I. History, physical examination, radiographs, and laboratory tests. *J Am Fam Physician.* 68 (5), 917–922 (2003).

4. Butler, D. Anterior cruciate ligament: Its normal response and replacement. *J Orthop Res.* 7 (6), 910–921 (1989).

5. Mommersteeg, T., Kooloos, J., Blankevoort, L., Kauer, J., Huiskes, R., Roeling, F. The fibre bundle anatomy of human cruciate ligaments. *J Anat.* 187, 461–71 (1995).

6. Zantop, T., Petersen, W., Fu, F. Anatomy of the anterior cruciate ligament. *Oper Techn Orthop.* 15 (1), 20–28 (2005).

7. Woo, S., Abramowitch, S., Kilger, R., Liang, R. Biomechanics of knee ligaments: injury, healing, and repair. *J Biomech.* 39 (1), 1–20 (2006).

8. Steiner, M., Murray, M., Rodeo, S. Strategies to improve anterior cruciate ligament healing and graft placement. *Am J Sports Med.* 36 (1), 176–89 (2008).

9. Tandeter, H., Shvartzman, P. Acute Knee Injuries: Use of Decision Rules for Selective Radiograph Ordering. *J Am Fam Physician.* 60 (9), 2599–2608 (1999).

10. Wilson, S., Vigorita, V. J., Scott, W. Anatomy. In Scott, W., editor, *The Knee,* Chapter 2. Mosby Ltd., St. Louis, 15-54, (2006).

11. Odensten, M., Gillquist, J. Functional anatomy of the anterior cruciate ligament and a rationale for reconstruction. *JBJS (Am).* 67 (2), 257–62 (1985).

12. Amis, A., Dawkins, G. Functional anatomy of the anterior cruciate ligament. Fibre bundle actions related to ligament replacements and injuries. *JBJS (Br).* 73, 260–267 (1991).

13. Anderson, A., Dome, D., Gautam, S., Awh, M., Rennir, G. Correlation of anthropometric measurements, strength, anterior cruciate ligament size, and intercondylar notch characteristics to sex differences in anterior cruciate ligament tear rates. *Am J Sports Med.* 29 (1), 58–66 (2001).

14. Kastelic, J., Galeski, A., Baer, E. The multicomposite structure of tendon. *J Connect Tissue Res.* 6 (1), 11–23 (1978).

15. Fuss, F. Anatomy of the cruciate ligaments and their function in extension and flexion of the human knee joint. *Am J Anat.* 184 (2), 165–76 (1989).

16. Zantop, T., Herbort, M., Raschke, M., Fu, F., Petersen, W. The Role of the Anteromedial and Posterolateral Bundles of the Anterior Cruciate Ligament in Anterior Tibial. *Am J Sports Med.* 35 (2), 223–227 (2007).

17. Bessette, G., Hunter, R. The anterior cruciate ligament. *J Orthop.* 17 (5), 369–377 (1990).

18. Kopf, S., Musahl, V., Tashman, S., Szczodry, M., Shen, W., Fu, F. A systematic review of the femoral origin and tibial insertion morphology of the ACL. *J knee Surg.* 17 (3), 213–9 (2009).

19. Robinson, J., Stanford, F., Kendoff, D., Stüber, V., Pearle, A. Replication of the range of native anterior cruciate ligament fiber length change behavior achieved by different grafts: measurement using computer-assisted navigation. *Am J Sports Med.* 37 (7), 1406–11 (2009).

20. Feikes, J. The Mobility and Stability of the Human Knee Joint. DPhil thesis, University of Oxford, 76–101 (1999).

21. O'Connor, J., Zavatsky, A. ACL function in the normal knee. *J Biomech.* 3 (5), 121–132 (1995).

22. Belvedere, C. Ensini, A. Feliciangeli, A. Cenni, F. D'Angeli, V. Giannini, S. Leardini, A. Geometrical changes of knee ligaments and patellar tendon during passive flexion. *J Biomech.* 45, 1886–92 (2012).

23. Cohen, S., VanBeek, C., Starman, J., Armfield, D., Irrgang, J., Fu, F. MRI measurement of the 2 bundles of the normal anterior cruciate ligament. *Orthop.* 32 (9), (2009).

24. Boone, D. & Azen, S. Normal range of motion of joints in male subjects. *JBJS (Am).* 61, 756–9 (1979).

25. Collins, J. & O'Connor, J. Muscle–ligament interactions at the knee during walking. *Proc Insn Mech Eng.* 205 (1), 11–18 (1991).

26. Williams, A., Logan, M. Understanding tibio-femoral motion. *Knee.* 11 (2), 81–8 (2004).

27. Belvedere, C. Leardini, A. Giannini, S. Ensini, A. Bianchi, L. Catani, F. Does medio-lateral motion occur in the normal knee? An in-vitro study in passive motion. *J Biomech.* 44, 877–84 (2011).

28. Karmani, S., Ember, T. The anterior cruciate ligament-I. *J Curr Orthop.* 17 (5), 369–377 (2003).

29. Moglo, K., Shirazi-Adl, A. Cruciate coupling and screw-home mechanism in passive knee joint during extension-flexion. *J Biomech.* 38 (5), 1075–83 (2005).

30. Andriacchi, T. & Dyrby, C. Interactions between kinematics and loading during walking for the normal and ACL deficient knee. *J Biomech.* 38 (2), 293–8 (2005).

31. Nicholson, J., Sutherland, A., Smith, F., Kawasaki, T. Upright MRI in kinematic assessment of the ACL-deficient knee. *Knee.* 19 (1), 41–8 (2012).

32. Tashman, S., Kopf, S., Fu, F. The Kinematic Basis of ACL Reconstruction. *Oper Techn Sports Med.* 16 (3), 116–118 (2008).

33. Hogervorst, T., Brand, R. Current Concepts Review-Mechanoreceptors in Joint Function. *JBJS (Am).* 80A, 1365–1378 (1998).

34. Andriacchi, T. Dynamics of pathological motion: applied to the anterior cruciate deficient knee. *J Biomech.* 23, 99–105 (1990).

35. Li, G., Rudy, T., Sakane, M., Kanamori, A., Ma, C., Woo, S. L. Y. The importance of quadriceps and hamstring muscle loading on knee kinematics and in-situ forces in the ACL. *J Biomech,* 32 (4), 395–400 (1999).

36. Wu, J., Herzog, W., Epstein, M. Joint contact mechanics in the early stages of osteoarthritis. *Med Eng Phys.* 22 (1), 1–12 (2000).

37. Isaac, D., Beard, D., Price, A., Rees, J., Murray, D., Dodd, C. In-vivo sagittal plane knee kinematics: ACL intact, deficient and reconstructed knees. *Knee.* 12 (1), 25–31 (2005).

38. Pandit, H, Van Duren, B, Gallagher, J, Beard, D, Dodd, C, Gill, H, Murray, D. Combined anterior cruciate reconstruction and Oxford unicompartmental knee arthroplasty: in vivo kinematics. *Knee.* 15 (2), 101–6 (2008).

39. Price, A, Rees, J, Beard, D, Gill, R, Dodd, C, Murray, D. Sagittal plane kinematics of a mobile-bearing unicompartmental knee arthroplasty at 10 years. *J Arthroplasty.* 19 (5), 590–597 (2004).

40. Goodfellow, J. & O'Connor, J. The anterior cruciate ligament in knee arthroplasty: A risk-factor with unconstrained meniscal prostheses. *J Clin Orthop.* 276, 245–252 (1992).

41. Murray, D., Goodfellow, J., O'Connor, J. The Oxford medial unicompartmental arthroplasty; A ten-year survival study. *JBJS (Br).* 80 (6), 983–989 (1998).

42. Price, A., Dodd, C., Svard, U., Murray, D. Oxford medial unicompartmental knee arthroplasty in patients younger and older than 60 years of age. *JBJS (Br).* 87 (11), 1488–92 (2005).

43. Banks, S., Markovich, G., Hodge, W. In vivo kinematics of cruciate-retaining and -substituting knee arthroplasties. *J Arthroplasty.* 12 (3), 297–304 (1997).

44. Miller, R., Goodfellow, J., Murray, D., O'Connor, J. In vitro measurement of patellofemoral force after three types of knee replacement. *JBJS (Br).* 80 (5), 900–6 (1998).

45. Catani, F., Benedetti, M., Felice, R., Buzzi, R., Giannini, S., Aglietti, P. Mobile and fixed bearing total knee prosthesis functional comparison during stair climbing. *J Clin Biomech.* 18 (5), 410–418 (2003).

46. Pandit, H., Ward, T., Hollinghurst, D., Beard, D., Gill, H., Thomas, N., Murray, D. Influence of surface geometry and the cam-post mechanism on the kinematics of total knee replacement. *JBJS (Br).* 87 (7), 940–5 (2005).

47. Cloutier, J., Sabouret, P., Deghrar, A. Total knee arthroplasty with retention of both cruciate ligaments. A nine to eleven-year follow-up study. *JBJS (Am).* 81 A, 697 (1999).

48. van Duren, B., Pandit, H., Beard, D., Zavatsky, A., Gallagher, J., Thomas, N., Shakespeare, D., Murray, D., Gill, H. How effective are added constraints in improving TKR kinematics? *J Biomech.* 40, 31–7 (2007).

49. Ritter, M. & Meneghini, R. Twenty-year survivorship of cementless anatomic graduated component total knee arthroplasty. *J Arthroplasty.* 25 (4), 507–13 (2010).

50. Murray, D., Frost, S. Pain in the assessment of total knee replacement. *JBJS (Br).* 80 (3), 426–431 (1998).

51. Baker, P., Van der Meulen, J., Lewsey, J., Gregg, P. The role of pain and function in determining patient satisfaction after total knee replacement. Data from the National Joint Registry for England and Wales. *JBJS (Br).* 89 (7), 893–900 (2007).

52. Scott, C., Howie, C., MacDonald, D., Biant, L. Predicting dissatisfaction following total knee replacement: a prospective study of 1217 patients. *JBJS (Br).* 92 (9), 1253–8 (2010).

53. Bourne, R., Chesworth, B., Davis, A., Mahomed, N., Charron, K. Patient satisfaction after total knee arthroplasty: who is satisfied and who is not? *Clin Orthop.* 468 (1), 57–63 (2010).

54. Wylde, V., Learmonth, I., Potter, A., Bettinson, K., Lingard, E. Patient-reported outcomes after fixed- versus mobile-bearing total knee replacement: a multi-centre randomised controlled trial using the Kinemax total knee replacement. *JBJS (Br).* 90 (9), 1172–9 (2008).

55. Frank, C., Jackson, D. Current concepts review-the science of reconstruction of the anterior cruciate ligament. *JBJS (Am).* 79 A, 1556–76 (1997).

56. Adachi, N., Ochi, M., Uchio, Y. Mechanoreceptors in the anterior cruciate ligament contribute to the joint position sense. *Acta Orthop Scand.* 73 (3), 330–334 (2002).

57. Dodds, J. & Arnoczky, S. Anatomy of the anterior cruciate ligament: a blueprint for repair and reconstruction. *Arthroscopy.* 10 (2), 132-9 (1994).

58. Beard, D., Murray, D., Gill, H., Price, A., Rees, J., Alfaro-Adrián, J., Dodd, C. Reconstruction does not reduce tibial translation in the cruciate-deficient knee an in vivo study. *JBJS (Br).* 83, 1098–103 (2001).

59. Butler, D., Noyes, F., Grood, E. Ligamentous restraints to anterior-posterior drawer in the human knee. *JBJS (Am).* 62 (2), 259–270 (1980).

60. Gollehon, D., Torzilli, P., Warren, R. The role of the posterolateral and cruciate ligaments in the stability of the human knee. A biomechanical study. *JBJS (Am).* 69 (2), 233–242 (1987).

61. Markolf, K., Graff-Radford, A., Amstutz, H. In Vivo Knee Stability- A quantitative assessment using an instrumented clinical testing apparatus. *JBJS (Am).* 60 (5), 664 (1978).

62. Shoemaker, S. & Markolf, K. In Vivo Rotatory Knee Stability. ligamentous and muscular contributions. *JBJS (Am).* 64A, 208–216 (1982).

63. Woo, S., Smith, B., Livesay, G., Blomstrom, G. Why do ligaments fail?. *J Curr. Orthop.* 7 (2), 73–84 (1993).

64. Noyes, F., Butler, D., Grood, E., Zernicke, R., Hefzy, M. Biomechanical analysis of human ligament grafts used in knee-ligament repairs and reconstructions. *JBJS (Am).* 66 (3), 344–352 (1984).

65. Kwan, M., Lin, T., Woo, S. On the viscoelastic properties of the anteromedial bundle of the anterior cruciate ligament. *J Biomech.* 26, 447–52 (1993).

66. Woo, S., Wu, C ., Dede, O., Vercillo, F., Noorani, S. Biomechanics and anterior cruciate ligament reconstruction. *J Orthop. Surg. Res.* 1, 1–10 (2006).

67. Huss, R. A., Holstein, H., O'Connor, J. J. A mathematical model of forces in the knee under isometric quadriceps contractions. *J Clin Biomech.* 15 (2), 112–22 (2000).

68. Zavatsky, A. B., O'Connor, J. J. Ligament forces at the knee during isometric quadriceps contractions. *J Eng Med.* 207 (1), 7–18 (1993).

69. Zavatsky, A., Beard, D., O'Connor, J. Cruciate Ligament Loading During Isometric Muscle Contractions: A Theoretical Basis for Rehabilitation. *Am J Sports Med.* 22 (3), 418–423 (1994).

70. Lu, T., O'Connor, J., Taylor, S., Walker, P. Validation of a lower limb model with in vivo femoral forces telemetered from two subjects. *J Biomech.* 31 (1), 63–9 (1998).

71. Zavatsky, A., O'Connor, J. A model of human knee ligaments in the sagittal plane. Part 1: Response to passive flexion. *J Eng Med.* 206 (3), 125–34 (1992).

72. Zavatsky, A., O'Connor, J. A model of human knee ligaments in the sagittal plane. Part 2: Fibre recruitment under load. *Proc Inst Mech Eng.* 206 (3), 135–45 (1992).

73. Wilson, D., Feikes, J. & O'Connor, J. Ligaments and articular contact guide passive knee flexion. *J Biomech*. 31, 1127–36 (1998).

74. Parenti-Castelli, V., Leardini, A., Gregorio, R. & O'Connor, J. On the modeling of passive motion of the human knee joint by means of equivalent planar and spatial parallel mechanisms. *Auton. Robot.* 16, 219–232 (2004).

75. Sakane, M., Fox, R., Woo, S., Livesay, G., Li, G., Fu, F. In situ forces in the anterior cruciate ligament and its bundles in response to anterior tibial loads. *J Orthop Res.* 15 (2), 285–93 (1997).

76. Imran, A., Huss, R. A., Holsten, H., O'Connor, J. J. The variation in the orientations and moment arms of the knee extensor and flexor muscle tendons with increasing muscle force : a mathematical analysis. *Proc Inst Mech Eng.* 214 (3), 277–286 (2000).

77. Hosseini, A., Gill, T. J., Li, G. In vivo anterior cruciate ligament elongation in response to axial tibial loads. *J Orthop Sci.* 14 (3), 298–306 (2009).

78. Li, G., DeFrate, L. E., Sun, H., Gill, T. J. In vivo elongation of the anterior cruciate ligament and posterior cruciate ligament during knee flexion. *J Sports Med.* 32 (6), 1415–20 (2004).

79. Noyes, F., Grood, E. The strength of the anterior cruciate ligament in humans and Rhesus monkeys. *JBJS (Am).* 58 (8), 1074–1082 (1976).

80. Woo, S., Hollis, J., Adams, D., Lyon, R., Takai, S. Tensile properties of the human femur-anterior cruciate ligament-tibia complex: The effects of specimen age and orientation. *JBJS (Am).* 19 (3), 217–225 (1991).

81. Chandrashekar, N., Mansouri, H., Slauterbeck, J., Hashemi, J. Sex-based differences in the tensile properties of the human anterior cruciate ligament. *J Biomech.* 39 (16), 2943–50 (2006).

82. Butler, D., Guan, Y., Kay, M., Cummings, J., Feder, S., Levy, M. Location-dependent variations in the material properties of the anterior cruciate ligament. *J Biomech.* 25 (5), 511–518 (1992).

83. Mommersteeg, T. J. A., Blankevoort, L., Huiskes, R., Kooloost, J. G. M. Characterization of the mechanical behavior of human knee ligaments: A numerical-experimental approach. *J Biomech.* 29 (2), 151–160 (1996).

84. Karmani, S., Ember, T. The anterior cruciate ligament—II. *J Curr Orthop.* 18 (1), 49–57 (2004).

85. Henning, C., Lynch, M., Glick, K. An in vivo strain gage study of the anterior cruciate ligament elongation of. *J Sports Med.* 13 (1), 22–26 (1985).

86. Vahey, J., Draganich, L. Tensions in the anterior and posterior cruciate ligaments of the knee during passive loading: predicting ligament loads from in situ measurements. *J Orthop Res.* 9 (4), 529–38 (1991).

87. Shelburne, K., Pandy, M. A musculoskeletal model of the knee for evaluating ligament forces during isometric contractions. *J Biomech.* 30 (2), 163–76 (1997).

88. Hosseini, A., Gill, T., Van de Velde, S., Li, G. Estimation of in vivo ACL force changes in response to increased weightbearing. *J Biomech Eng.* 133 (5), 1–9 (2011).

89. Shelburne, K., Pandy, M., Anderson, F., Torry, M. Pattern of anterior cruciate ligament force in normal walking. *J Biomech.* 37 (6), 797–805 (2004).

90. Morrison, J. The mechanics of the knee joint in relation to normal walking. *J Biomech.* 3 (1), 51–61 (1970).

91. Toutoungi, D., Lu, T., Leardini, A., Catani, F., O'Connor, J. Cruciate ligament forces in the human knee during rehabilitation exercises. *J Clin Biomech.* 15 (3), 176–87 (2000).

92. O'Connor, J., Shercli, T., Fitzpatrick, D., Biden, E. & Goodfellow, J. The Muscle-Stablized Knee. In Daniel, D., O'Connor, J. J., editors. *Knee Ligaments, Structructure, Function, Injury and Repair*. Raven Press, NY, 239–256 (1990).

93. Gill, H. & O'Connor, J. Biarticulating two-dimensional computer model of the human patellofemoral joint. *J Clin Biomech.* 11 (2), 11–81 (1996).

94. Lu, T. & O'Connor, J. Lines of action and moment arms of the major force-bearing structures crossing the human knee joint: comparison between theory and experiment. *J Anat.* 189 (3), 575–85 (1996).

95. Shelburne, K., Torry, M., Pandy, M. Muscle, Ligament, and Joint-Contact Forces at the Knee during Walking. *J Med Sci Sports Exerc,* 37 (11), 1948–1956 (2005).

96. Woo, S., Debski, R., Vangura, J., Withrow, J., Wong, E., Fu, F., Debski, R., Vangura, A., Vogrin, T. Use of robotic technology to study the biomechanics of ligaments and their replacements. *Oper Techn Orthop.* 10 (1), 87–91 (2000).

97. Woo, S. & Fisher, M. Evaluation of knee stability with use of a robotic system. *JBJS (Am).* 91, 78–84 (2009).

98. Rudy, T., Livesay, G., Woo, S., Fu, F., Livesay, G. A combined robotic/universal force sensor approach to determine in situ forces of knee ligaments. *J Biomech.* 29 (10), 1357–1360 (1996).

99. Collins, J,. The redundant nature of locomotor optimization laws. *J Biomech* 28 (3), 251-67, (1994).

100. Gabriel, M., Wong, E., Woo, S., Yagi, M., Debski, R. Distribution of in situ forces in the anterior cruciate ligament in response to rotatory loads. *J Orthop Res.* 22 (1), 85–89 (2004).

101. Meisterling, S., Schoderbek, R., Andrews, A. Anterior Cruciate Ligament Reconstruction. *Oper Techn Sports Med.* 17 (1), 2–10 (2009).

102. Miyasaka, K., Daniel, D., Stone, M., Hirshman, P. The incident of knee ligament injuries in the general population. *Am J Knee Surg.* 4 (1), 3–8 (1991).

103. Hewett, T., Ford, K., Myer, G. Anterior cruciate ligament injuries in female athletes: Part 2, a meta-analysis of neuromuscular interventions aimed at injury prevention. *Am J Sports Med.* 34 (2), 490–8 (2006).

104. Allen, C., Livesay, G., Wong, E., Woo, S. Injury and reconstruction of the anterior cruciate ligament and knee osteoarthritis. *Osteoarthr Carti.* 7 (1), 110–21 (1999).

105. Spindler, K. & Wright, R. Anterior cruciate ligament tear. *N Engl J Med.* 359, 2135–42 (2008).

106. Hewett, T., Myer, G., Ford, K. Anterior cruciate ligament injuries in female athletes: Part 1, mechanisms and risk factors. *Am J Sports Med.* 34 (2), 299–311 (2006).

107. Jonsson, T., Althoff, B., Peterson, L., Renström, P. Clinical diagnosis of ruptures of the anterior cruciate ligament: a comparative study of the Lachman test and the anterior drawer sign. *Am J Sports Med.* 10 (2), 100–2 (1982).

108. Wiertsema, S., van Hooff, H., Migchelsen, L., Steultjens, M. Reliability of the KT1000 arthrometer and the Lachman test in patients with an ACL rupture. *Knee.* 15 (2), 107–10 (2008).

109. Fu, F., Christel, P., Miller, M., Johnson, D. Graft selection for anterior cruciate ligament reconstruction. *Instr Course Lect.* 5 (3), 251–265 (1995).

110. Amis, A., Zavras, T. Isometricity and graft placement during anterior cruciate ligament reconstruction. *Knee.* 2 (1), 12 (1995).

111. Bartlett, R., Clatworthy, M., Nguyen, T. Graft Selection in Reconstruction of the Anterior Cruciate Ligament. *JBJS (Br).* 83 (5), 625–634 (2001).

112. Mascarenhas, R. & Macdonald, P. B. Anterior cruciate ligament reconstruction: a look at prosthetics- past, present and possible future. *McGill J Med.* 11 (1), 29–37 (2008).

113. Lidén, M., Ejerhed, L., Sernert, N., Laxdal, G., Kartus, J. Patellar tendon or semitendinosus tendon autografts for anterior cruciate ligament reconstruction: a prospective, randomized study with a 7-Year follow-up. *Am J Sports Med.* 35 (5), 740–8 (2007).

114. Biau, D., Katsahian, S., Kartus, J., Harilainen, A., Feller, J., Sajovic, M., Ejerhed, L., Zaffagnini, S., Röpke, M., Nizard, R. Patellar tendon versus hamstring tendon autografts for reconstructing the anterior cruciate ligament: a meta-analysis based on individual patient data. *Am J Sports Med.* 37 (12), 2470–8 (2009).

115. Mody, B., Howard, L., Harding, M. The ABC carbon and polyester prosthetic ligament for ACL deficient knees. *JBJS (Br).* 75 (B), 818 (1993).

116. Gao, K., Chen, S., Wang, L., Zhang, W., Kang, Y., Dong, Q., Zhou, H., Li, L. Anterior cruciate ligament reconstruction with LARS artificial ligament: a multicenter study with 3- to 5-year follow-up. *Arthroscopy*. 26 (4), 515–23 (2010).

117. Guidoin, M., Marois, Y., Bejui, J., Poddevin, N., King, M., Guidoin, R. Analysis of retrieved polymer fiber based replacements for the ACL. *Biomaterials,* 21 (23), 2461–74 (2000).

118. Ventura, A., Terzaghi, C., Legnani, C., Borgo, E., Albisetti, W. Synthetic grafts for anterior cruciate ligament rupture: 19-year outcome study. *Knee.* 17 (2), 108–13 (2010).

119. Legnani, C., Ventura, A., Terzaghi, C., Borgo, E., Albisetti, W. Anterior cruciate ligament reconstruction with synthetic grafts. A review of literature. *Int Orthop.* 34 (4), 465–71 (2010).

120. Seon, J., Song, E., Park, S. Osteoarthritis after anterior cruciate ligament reconstruction using a patellar tendon autograft. *Int Orthop.* 30 (2), 94–98 (2006).

121. Jomha, N., Borton, D., Clingeleffer, A., Pinczewski, L. Long-term osteoarthritic changes in anterior cruciate ligament reconstructed knees. *Clin Orthop.* 358, 188–93 (1999).

122. Shelbourne, K., Lawrance, S., Kerr, B. Patellar Tendon Rupture After Anterior Cruciate Ligament Surgery. *Oper Techn Sports Med.* 14 (1), 6 (2006).

123. Shelbourne, K. & Gray, T. Anterior cruciate ligament reconstruction with autogenous patellar tendon graft followed by accelerated rehabilitation. A two- to nine-year followup. *Am J Sports Med.* 25 (6), 786–95 (1997).

124. Keays, S., Newcombe, P., Bullock-Saxton, J., Bullock, M., Keays, A. Factors involved in the development of osteoarthritis after anterior cruciate ligament surgery. *Am J Sports Med.* 38 (3), 455–63 (2010).

125. Rubenstein, D., Sarin, G., Subbio, C., Miller, L. Revision of failed gore-tex anterior cruciate ligament reconstruction. *Oper Techn Sports Med.* 6 (2), 97–101 (1998).

126. Richmond, J., Manseau, C., Patz, R. Anterior cruciate reconstruction using a Dacron ligament prosthesis. *J Sports Med.* 20 (1), 24–28 (1992).

127. Kdolsky, R., Gibbons, D., Kwasny, O., Schabus, R., Plenk, H. Braided Polypropylene Augmentation Device in Reconstructive Surgery of the Anterior Cruciate Ligament. *J Orthop Res.* 15 (1), 1–10 (1997).

128. Murray, A. & Macnicol, M. 10–16 year results of Leeds-Keio anterior cruciate ligament reconstruction. *Knee.* 11 (1), 5 (2004).

129. Amis, A. & Kempson, S. Failure mechanisms of polyester fiber anterior cruciate ligament implants: A human retrieval and laboratory study. *J Biomed Mater Res.* 48 (4), 534–9 (1999).

130. Nau, T., Lavoie, P., Duval, N. A new generation of artificial ligaments in reconstruction of the anterior cruciate ligament: two-year follow-up of a randomised trial. *JBJS (Br).* 84 (3), 356 (2002).

131. Chen, E., Black, J. Materials design analysis of the prosthetic anterior cruciate ligament. *J Biomed Mater Res.* 14 (5), 567–586 (1980).

132. Grood, E. & Noyes, F. Cruciate ligament prosthesis: strength, creep, and fatigue properties. *JBJS (Am).* 58 (8), 1083–8 (1976).

133. Frank, C. & Jackson, D. The Science of Reconstruction of the Anterior Cruciate Ligament. *JBJS (Am).* 79 (10), 1556–1576 (1997).

134. Escamilla, R., Macleod, T., Wilk, K., Paulos, L., Andrews, J. Anterior cruciate ligament strain and tensile forces for weight-bearing and non-weight-bearing exercises: a guide to exercise selection. *J Orthop Sports Phys Ther.* 42 (3), 208–20 (2012).

135. Jordan, S., DeFrate, L., Nha, K., Papannagari, R., Gill, T., Li, G. The in vivo kinematics of the anteromedial and posterolateral bundles of the anterior

cruciate ligament during weightbearing knee flexion. *Am J Sports Med.* 35 (4), 547–54 (2007).

136. Zavatsky, A. & O'Connor, J. Three-dimensional geometrical models of human knee ligaments. *Proc Instn Mech Eng.* 208 (48), 229–240 (1994).

137. Abebe, E., Kim, J., Utturkar, G., Taylor, D., Spritzer, C., Moorman, C., Garrett, W., DeFrate, L. The effect of femoral tunnel placement on ACL graft orientation and length during in vivo knee flexion. *J Biomech.* 44 (10), 1914–20 (2011).

138. Amis, A. & Jakob, R. Anterior cruciate ligament graft positioning, tensioning and twisting. *J Knee Surg.* 6 (1), S2–12 (1998).

139. Kaseta, M., DeFrate, L., Charnock, B., Sullivan, R., Garrett, W. Reconstruction technique affects femoral tunnel placement in ACL reconstruction. *J Clin Orthop.* 466 (6), 1467–74 (2008).

140. Sommer, C., Friederich, N., Müller, W. Improperly placed anterior cruciate ligament grafts: correlation between radiological parameters and clinical results. *Knee Surg Sports Traumatol Arthrosc.* 8 (4), 207–13 (2000).

141. British Standards Institution- BS ISO 14243-1. Implants for surgery: Wear of total knee joint prostheses. Part 1: Loading and displacement parameters for wear testing machines with load control and corresponding environmental conditions for test. BSI, London (2009).

142. British Standards Institution- ISO 14879-1. Implants for surgery : Total knee joint prostheses, Part 1: Determination of endurance properties of knee tibial trays. BSI, London (2000).

143. Jacobs, J., Gilbert, J., Urban, R. Current Concepts Review-Corrosion of Metal Orthopaedic Implants. *JBJS (Am).* 80 (10), 268–82 (1998).

144. Niinomi, M. Fatigue characteristics of metallic biomaterials. *Int J Fatigue,* 29 (6), 992–1000 (2007).

145. Liu, F., Fisher, J. Wear prediction of orthopeadic implants. In Affatato, S. editor, *Wear of orthopeadic implants and artificial joints*. Chapter 15. Woodhead Publishing Ltd, Cambridge, 403-416 (2012).

146. Bhatt, H. & Goswami, T. Implant wear mechanisms-basic approach. *Biomed Mater,* 3 (4), 1-9 (2008).

147. Lee, M., Seong, S., Lee, S., Chang, C., Park, Y., Jo, H., Kim, C. Vertical femoral tunnel placement results in rotational knee laxity after anterior cruciate ligament reconstruction. *J Arthrop,* 23 (7), 771–8 (2007).

148. Illingworth, K., Hensler, D., Working, Z., Macalena, J., Tashman, S., Fu, F. A simple evaluation of anterior cruciate ligament femoral tunnel position: the inclination angle and femoral tunnel angle. *Am J Sport Med.* 39 (12), 2611–8 (2011).

149. Tsukada, H., Ishibashi, Y., Tsuda, E., Fukuda, A., Toh, S. Anatomical analysis of the anterior cruciate ligament femoral and tibial footprints. *J Orthop Sci.* 13 (2), 122–9 (2008).

150. Markolf, K. L., Park, S., Jackson, S. R., McAllister, D. R. Simulated Pivot-Shift Testing with Single and Double-Bundle Anterior Cruciate Ligament Reconstructions. *JBJS (Am).* 90 (8), 1681–9 (2008).

151. Gray, H., Taddei, F., Zavatsky, A., Cristofolini, L., Gill, H. Experimental validation of a finite element model of a human cadaveric tibia. *J Biomech Eng.* 130 (3), 1-9 (2008).

152. Schroer, W., Stormont, D. & Pietrzak, W. Seven-year survivorship and functional outcomes of the high-flexion Vanguard complete knee system. *J Arthroplasty*. 29, 61–5 (2014).

153. National Joint Registry for England, Wales and Northern Ireland: 10th Annual Report. (2013).

154. Van der Bracht, H., Verhelst, L., Stuyts, B., Page, B., Bellemans, J., Verdonk, P. Anatomic single-bundle ACL surgery: consequences of tibial tunnel diameter

and drill-guide angle on tibial footprint coverage. *Knee Surg Sports Traumatol Arthrosc.* 22 (5), 1030–1039 (2013).

155. Fahey, M. & Indelicato, P. Bone tunnel enlargement after anterior cruciate ligament replacement. *Am J Sports Med.* 22 (3), 410–4 (1992).

156. Kim, S., Jo, S., Kumar, P., Kyung-Soo, O. Comparison of Single- and Double-Bundle Anterior Cruciate Ligament Reconstruction Using Quadriceps Tendon–Bone Autografts. *Arthroscopy.* 25 (1), 7 (2009).

157. Austin, J., Phornphutkul, C., Wojtys, E. Loss of knee extension after anterior cruciate ligament reconstruction: effects of knee position and graft tensioning. *JBJS (Am).* 89 (7), 1565–74 (2007).

158. Wallace, M., Bedi, A., Lesniak, B., Farrow, L., Ajibade, D., Israel, H., Kaar, S. What Effect Does Anterior Cruciate Ligament Tibial Guide Orientation Have on Tibial Tunnel Length?. *J Arthroplast,* 27 (6), 803–808 (2011).

159. Luites, J., Wymenga, A., Blankevoort, L., Kooloos, J. Description of the attachment geometry of the anteromedial and posterolateral bundles of the ACL from arthroscopic perspective for anatomical tunnel placement. *J Knee Surg.* 15 (12), 1422–31 (2007).

160. Darling, A, Hakim, O., Horton, K., Gibbs, M., Cui, L., Berry, J., Lanham-New, S., Hart, K. Adaptations in tibial cortical thickness and total volumetric bone density in postmenopausal South Asian women with small bone size. *Bone.* 55 (1), 36–43 (2013).

161. Yoshioka, Y., Siu, D. W., Scudamore, R., Cooke, T. Tibial anatomy and functional axes. *J Orthop Res.* 7 (1), 132–7 (1989).

162. Edwards, A., Bull, A., Amis, A. The attachments of the anteromedial and posterolateral fibre bundles of the anterior cruciate ligament: Part 1: tibial attachment. *J Knee Surg.* 15 (12), 1414–21 (2007).

163. Vanguard Primary Knee: Surgical Technique. Biomet UK Ltd. (2008). Retrieved (11.03.2014) from www.biomet.se/resource/17724/FLK167 Vanguard Premier ST.pdf.

164. Liao, Y., Hoffman, E., Wimmer, M. CoCrMo metal-on-metal hip replacements. *Phys Chem Chem Phys.* 15 (3), 746–56 (2013).

165. Berger, L., Kausch, H., Plummer, C. Structure and deformation mechanisms in UHMWPE-fibres. *J Polym.* 44 (19), 5877–5884 (2003).

166. Kurtz, S. A primer on UHMWPE. In Kurtz, S., editor, *The UHMWPE Handbook: Ultra-High Molecular Weight Polyethylene in Total Joint Replacement,* Chapter 1. Elsevier Academic Press, London, 1-10, 2004.

167. Teoh, S. Fatigue of biomaterials: a review. *Int J Fatigue,* 22 (10), 825–837 (2000).

168. Vaz, C. Dyneema purity fibre- The Life Sciences and Materials Sciences Company. *DSM Ltd.* 1–29 (2010). Retrieved (19.04.2014) from http://www.kyon.ch/wp-content/uploads/2011/06/kyon_symp_2010_Becker.pdf.

169. Van Dingenen, J. Gel-spun high-performance polyethylene fibres. In Hearle, J., editor, *High-performance fibres,* Chapter 3. Woodhead Publishing Ltd, Cambridge, 62–92, (2001).

170. Long, M., Rack, H. Titanium alloys in total joint replacement-a materials science perspective. *Biomaterials.* 19 (18), 1621–39 (1998).

171. ASTM standard F75-12: Standard Specification for Cobalt-28 Chromium-6 Molybdenum Alloy Castings and Casting Alloy for Surgical Implants. ASTM international, West Conshohocken, PA (2012).

172. Christensen, E., Eriksen, S., Gillesberg, B. Evaluation of biocompatibility, mechcanical and chemical properties of Tantalum coated metals. In Davis, J. R., editor, *Medical Device Materials*. ASM International, CA, 116 (2003).

173. Boyer, R., Welsch, G., Collings, E., editors, in *Materials property handbook: Titanium alloys,* Ti 6Al-4V. ASM international, OH, 483-530 (1994).

174. Technical datasheet- Titanium alloy Ti 6Al-4V. Carpenter Technology Corporation, PA, (2000). Retrieved (19.04.2014) from http://cartech.ides.com/datasheet.aspx?i=101&E=269.

175. Technical datasheet- BioDur CCM Plus Alloy. Carpenter Technology Corporation, PA, (2007). Retrieved (19.04.2014) from http://cartech.ides.com/datasheet.aspx?i=101&E=9.

176. Technical datasheet- MP35N Ni-Co-Cr-Mo alloy (65% cold reduction). MatWeb LLC, VA. Retrieved (19.04.2014) from www.matweb.com/search/datasheet.aspx?matguid=64f260df11094625b18d000211deedb8

177. Technical data sheet- MP35N Ni-Co-Cr-Mo alloy (25% cold reduction). MatWeb LLC, VA. Retrieved (19.04.2014) from www.matweb.com/search/datasheet.aspx?matguid=08c265e65b114a57a458c3f561bba195

178. Avanzini, A. Mechanical characterization and finite element modelling of cyclic stress–strain behaviour of ultra high molecular weight polyethylene. *Mater Des.* 29 (2), 330–343 (2008).

179. Meyer, R., Pruitt, L. The effect of cyclic true strain on the morphology, structure, and relaxation behavior of ultra high molecular weight polyethylene. *J Polym.* 42 (12), 5293–5306 (2001).

180. Krzypow, D. & Rimnac, C. Cyclic steady state stress-strain behavior of UHMW polyethylene. *Biomaterials,* 21 (20), 2081–7 (2000).

181. ASTM standard D885: Standard Test Methods for Tire Cords, Tire Cord Fabrics, and Industrial Filament Yarns Made from Manufactured Organic-Base Fibers. ASTM international, West Conshohocken, PA (2010).

182. ASTM standard D2256: Standard Test Method for Tensile Properties of Yarns by the Single-Strand Method. ASTM international, West Conshohocken, PA (2010).

183. Geller, J, Malchau, H., Bragdon, C., Greene, M., Harris, W., Freiberg, A. Large diameter femoral heads on highly cross-linked polyethylene: minimum 3-year results. *Clin Orthop.* 447, 53–9 (2006).

184. Murray, M., Drought, A., Kory, R. Walking Patterns of Normal Men. *JBJS (Am).* 46, 335–60 (1964).

185. Winter, D. Human balance and posture control during standing and walking. *Gait Posture,* 3, 193–214 (1995).

186. Askeland, D., Fulay, P., Wright, W., editors. In *The Science and Engineering of Materials*. Chapter 6: Mechanical properties. Cengage Learning, CT, 216–218 (2011).

187. Marissen, R., Nelis, M., Janssens, M., Meeks, M., Maessen, J. A Comparison between the Mechanical Behaviour of Steel Wires and Ultra High Molecular Weight Poly Ethylene Cables for Sternum Closure. *Mater Sci Appl.* 2 (10), 1367–1374 (2011).

188. Hubel, H. Basic conditions for material and structural ratcheting. *Nucl Eng Des.* 162 (1), 55–65 (1996).

189. ABAQUS 6.11, Analysis User's Manual, Section 22.2.2: Models for metals subjected to cyclic loading. Simulia, RI (2011).

190. Arruda, E., Boyce, M. A three-dimensional constitutive model for the large strech behavior fo rubber elastic materials. *J Mech Phys Solids,* 41 (2), 389–412 (1993).

191. Broggiato, G., Campana, F., Cortese, L. The Chaboche nonlinear kinematic hardening model: calibration methodology and validation. *Meccanica,* 43 (2), 115–124 (2008).

192. Dhakal, H., Zhang, Z., Richardson, M. Effect of water absorption on the mechanical properties of hemp fibre reinforced unsaturated polyester composites. *Compos Sci Tech Res.* 67 (7-8), 1674–1683 (2007).

193. Valenzuela, L. Variability of water uptake studies of biomedical polymers. *J App. Polym Sci.* 121 (3), 1311–1320 (2011).

194. Greenbaum, E., Burroughs, B., Harris, W., Muratoglu, O. Effect of lipid absorption on wear and compressive properties of unirradiated and highly

crosslinked UHMWPE: an in vitro experimental model. *Biomaterials.* 25 (18), 4479–84 (2004).

195. Pioletti, D., Rakotomanana, L., Leyvraz, P. Strain rate effect on the mechanical behavior of the anterior cruciate ligament-bone complex. *Med Eng Phys.* 21 (2), 95–100 (1999).

196. Russell, B., Kandan, K., Deshpande, V., Fleck, N. In *The high strain rate response of UHMWPE: from fibre to laminate*. Cambridge University, 1–21 (2013).

197. Huang, W., Wang, Y., Xia, Y. Statistical dynamic tensile strength of UHMWPE-fibers. *Polym,* 45 (11), 3729–3734 (2004).

198. Kurtz, S., Villarraga, M., Herr, M., Bergström, J., Rimnac, C., Edidin, A. Thermomechanical behavior of virgin and highly crosslinked ultra-high molecular weight polyethylene used in total joint replacements. *Biomaterials,* 23, 3681–97 (2002).

199. Bergström, J., Kurtz, S., Rimnac, C., Edidin, A. Constitutive modeling of ultra-high molecular weight polyethylene under large-deformation and cyclic loading conditions. *Biomaterials,* 23 (17), 2329–43 (2002).

200. Pruitt, L. Deformation, yielding, fracture and fatigue behavior of conventional and highly cross-linked ultra high molecular weight polyethylene. *Biomaterials,* 26 (8), 905–15 (2005).

201. Ngai, V., Wimmer, M. Kinematic evaluation of cruciate-retaining total knee replacement patients during level walking: a comparison with the displacement-controlled ISO standard. *J Biomech.* 42 (14), 2363–8 (2009).

202. Kurtz, S., Pruitt, L., Jewett, C., Crawford, R., Crane, D., Edidin, A. The yielding, plastic flow, and fracture behavior of ultra-high molecular weight polyethylene used in total joint replacements. *Biomaterials.* 19 (21), 1989–2003 (1998).

203. Mahmoud, A., Wakabayashi, N., Takahashi, H. Prediction of permanent deformation in cast clasps for denture prostheses using a validated nonlinear finite element model. *Dent Mater.* 23 (3), 317–24 (2007).

204. Case, J., Chiver. A. *Strength of materials and structures- An introduction to the mechanics of solids and structures*, Chapter 19: Springs. Edward Arnold Ltd., London, 334–345, (1971).

205. Khalfayan, E., Sharkey, P., Alexander, A, Bruckner, J., Bynum, E. The relationship between tunnel placement and clinical results after anterior cruciate ligament reconstruction. *Am J Sports Med.* 24 (3), 335–41 (1994).

206. Kawakami, Y., Hiranaka, T., Matsumoto, T., Hida, Y., Fukui, T., Uemoto, H., Doita, M., Tsuji, Mi., Kurosaka, M., Kuroda, R. The accuracy of bone tunnel position using fluoroscopic-based navigation system in anterior cruciate ligament reconstruction. *J Knee Surg Sports Traumatol Arthros,* 20 (8), 1503–10 (2012).

207. Topliss, C. & Webb, J. An audit of tunnel position in anterior cruciate ligament reconstruction. *Knee.* 8 (1), 59–63 (2001).

208. Purnell, M., Larson, A., Clancy, W. Anterior cruciate ligament insertions on the tibia and femur and their relationships to critical bony landmarks using high-resolution volume-rendering computed tomography. *J Sports Med.* 36 (11), 2083–90 (2008).

209. Edwards, A., Bull, A., Amis, A. The attachments of the anteromedial and posterolateral fibre bundles of the anterior cruciate ligament. Part 2: femoral attachment. *J Knee Surg.* 16 (1), 29–36 (2008).

210. Giuliani, J., Kilcoyne, K., Rue, J. Anterior cruciate ligament anatomy: a review of the anteromedial and posterolateral bundles. *J Knee Surg.* 22 (2), 148–54 (2009).

211. Siebold, R., Ellert, T., Metz, S., Metz, J. Femoral insertions of the anteromedial and posterolateral bundles of the anterior cruciate ligament: morphometry and

arthroscopic orientation models for double-bundle bone tunnel placement-a cadaver study. *J Arthrosc,* 24 (5), 585–92 (2008).

212. Yasuda, K., Kondo, E., Ichiyama, H., Kitamura, N., Tanabe, Y., Tohyama, H., Minami, A. Anatomic reconstruction of the anteromedial and posterolateral bundles of the anterior cruciate ligament using hamstring tendon grafts. *J Arthrosc.* 20 (10), 1015–25 (2004).

213. Giron, F., Cuomo, P., Aglietti, P., Bull, A., Amis, A. Femoral attachment of the anterior cruciate ligament. *Knee Surg Sports Traumatol Arthrosc.* 14 (3), 250–6 (2006).

214. Takahashi, M., Doi, M., Abe, M., Suzuki, D., Nagano, A. Anatomical study of the femoral and tibial insertions of the anteromedial and posterolateral bundles of human anterior cruciate ligament. *Am J Sports Med.* 34 (5), 787–92 (2006).

215. Mochizuki, T., Muneta, T., Nagase, T., Shirasawa, S., Akita, K., Sekiya, I. Cadaveric Knee Observation Study for Describing Anatomic Femoral Tunnel Placement for Two-Bundle Anterior Cruciate Ligament Reconstruction. *Arthroscopy.* 22 (4), 356–361 (2006).

216. Zantop, T., Wellmann, M., Fu, F., Petersen, W. Tunnel positioning of anteromedial and posterolateral bundles in anatomic anterior cruciate ligament reconstruction: anatomic and radiographic findings. *Am J Sports Med.* 36 (1), 65–72 (2008).

217. Forsythe, B. Kopf, S., Wong, A., Martins, C., Anderst, W., Tashman, S., Fu, F. The location of femoral and tibial tunnels in anatomic double-bundle anterior cruciate ligament reconstruction analyzed by three-dimensional computed tomography models. *JBJS (Am).* 92 (6), 1418–26 (2010).

218. Colombet, P., Robinson, J., Christel, P., Franceschi, J., Djian, P., Bellier, G., Sbihi, A. Morphology of anterior cruciate ligament attachments for anatomic reconstruction: a cadaveric dissection and radiographic study. *J Arthrosc,* 22 (9), 984–92 (2006).

219. Bernard, M., Hertel, P., Hornung, H. & Cierpinski, T. Femoral insertion of the ACL. Radiographic quadrant method. *Am J Knee Surg.* 10, 14–21; discussion 21–2 (1997).

220. Musahl, V., Burkart, A., Debski, R., Van Scyoc, A., Fu, F., Woo, S. Accuracy of anterior cruciate ligament tunnel placement with an active robotic system: A cadaveric study. *Arthroscopy.* 18, 968–973 (2002).

221. Luites, J., Wymenga, A., Blankevoort, L., Eygendaal, D. & Verdonschot, N. Accuracy of a computer-assisted planning and placement system for anatomical femoral tunnel positioning in anterior cruciate ligament reconstruction. *Int J Med Robot.* (2013).

222. Shafizadeh, S., Balke, M., Wegener, S., Tjardes, T., Bouillon, B., Hoeher, J., Baethis, H. Precision of tunnel positioning in navigated anterior cruciate ligament reconstruction. *Arthroscopy*. 27, 1268–74 (2011).

223. Luites, J., Wymenga, A, Blankevoort, L., Kooloos, J. & Verdonschot, N. Development of a femoral template for computer-assisted tunnel placement in anatomical double-bundle ACL reconstruction. *Comput Aided Surg*. 16, 11–21 (2011).

224. Hoshino, Y., Kim, D. & Fu, F. Three-dimensional anatomic evaluation of the anterior cruciate ligament for planning reconstruction. *Anat Res Int*. 2012, 569704 (2012).

225. Johal, P., Williams, A, Wragg, P., Hunt, D., Gedroyc, W. Tibio-femoral movement in the living knee. A study of weight bearing and non-weight bearing knee kinematics using "interventional" MRI. *J Biomech.* 38 (2), 269–76 (2005).

226. Iwaki, H., Pinskerova, V., Freeman, M. Tibiofemoral movement. The shapes and the unloaded cadaver knee. *JBJS (Br).* 82 (8), 1189-95 (2000).

227. Koga, H., Muneta, T., Yagishita, K., Ju, Y., Sekiya, I. The effect of graft fixation angles on anteroposterior and rotational knee laxity in double-bundle anterior

cruciate ligament reconstruction: evaluation using computerized navigation. *Am J Sports Med.* 40 (3), 615–23 (2012).

228. O'Connor, J., Shercli, T., Fitzpatrick, D., Biden, E. & Goodfellow, J. The Muscle-Stablized Knee. In Daniel, D., O'Connor, J., editors. *Knee Ligaments, Structructure, Function, Injury and Repair*. Raven Press, NY, 239–256 (1990).

229. Li, G., Defrate, L., Rubash, H., Gill, T. In vivo kinematics of the ACL during weight-bearing knee flexion. *J Orthop Res.* 23 (2), 340–4 (2005).

230. Behrend, H., Stutz, G., Kessler, M., Rukavina, A., Giesinger, K., Kuster, M. Tunnel placement in anterior cruciate ligament (ACL) reconstruction: quality control in a teaching hospital. *Knee Surg Sports Traumatol Arthrosc.* 14 (11), 1159–65 (2006).

231. Quaglini, V., Corazza, C., Poggi, C. Experimental characterization of orthotropic technical textiles under uniaxial and biaxial loading. *Compos.* 39 (8), 1331–1342 (2008).

232. Edidin, A., Villarraga, M., Herr, M ., Muth, J., Yau, S., Kurtz, S. Accelerated aging studies of UHMWPE. II. Virgin UHMWPE is not immune to oxidative degradation. *J Biomed Mater Res.* 61 (2), 323–9 (2002).

233. Amis, A. Anterior cruciate ligament- Knee stability and the effects of implants. *JBJS (Br).* 71, 819–824 (1989).

234. Zavatsky, A. A kinematic freedom analysis of a flexed knee stance testing rig. *J Biomech.* 30 (3), 277–280 (1997).

235. Hearn, E. *Mechanics of Materials Volum 1: An Introduction to the Mechanics of Elastic and Plastic Deformation of Solids and Structural Materia*ls, Chapter 12: Springs. Butterworth-Heinemann Ltd., Oxford, 297–323 (1997).

Appendices

Appendix 1: Helical spring calculation

Compression springs are considered open coil springs in which the coils of a helical spring are not very close to each other so the pitch angle (α) can be treated as a small angle (Figure A.0.1). One way to calculate the stiffness of helical compression springs is by using torsional and bending stiffness [204,235].

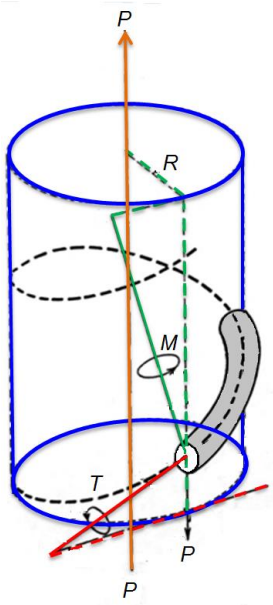


Figure A.0.1: Schematic diagram of an open coil helical spring, '*M*' is the bending moment and '*T*' is the twisting moment [204].

For the materials that follow the Hooke's law, $U = (P \times \delta)/2$ the strain energy (U) of the helical compression spring with radius of (R) under axial load (P) considering the torsional couple ($T = PRcos\alpha$) and bending couple ($M = PRsin\alpha$) is:

$$U = \frac{l.T^2}{2GJ} + \frac{l.M^2}{2EI} = \frac{l(PR\cos\alpha)^2}{2GJ} + \frac{l(PR\sin\alpha)^2}{2EI} \qquad \text{Equation A-1}$$

where length of wire(l) = $2\pi nR$, 'n' is number of coils, 'G' is shear modulus (MPa), 'E' is Young's modulus (MPa), 'J' is polar moment of inertia, and 'I' is second moment of area.

For the springs with circular wire (radius of 'r'), the second moment of area (I) and the polar moment of the inertia (J) are:

$$I = \frac{\pi r^4}{4} \text{ and } J = \frac{\pi r^4}{2}$$

For the springs with rectangular wire the second moment of area (I) and the polar moment of the inertia (J) are:

$$I = \frac{bt^3}{12} \text{ and } J = \frac{bt\,(b^2 + t^2)}{12}$$

'b' is the bigger dimension of the rectangular cross section (b>t).

Displacement (δ = 2U/P) and stiffness (K = P/δ) of the compression helical spring become:

$$\delta = lPR^2\left(\frac{\cos^2\alpha}{GJ} + \frac{\sin^2\alpha}{EI}\right) = 2\pi nPR^3\sec\alpha\,(\frac{\cos^2\alpha}{GJ} + \frac{\sin^2\alpha}{EI}) \qquad \text{Equation A-2}$$

$$K = \frac{1}{2\pi n\,R^3\sec\alpha\left(\frac{\cos^2\alpha}{GJ} + \frac{\sin^2\alpha}{EI}\right)} \qquad \text{Equation A-3}$$

Appendix 2: Spiral spring calculation

The complementary strain energy method was used to calculate the deformation of a flat spiral spring (Figure A.2) [204].

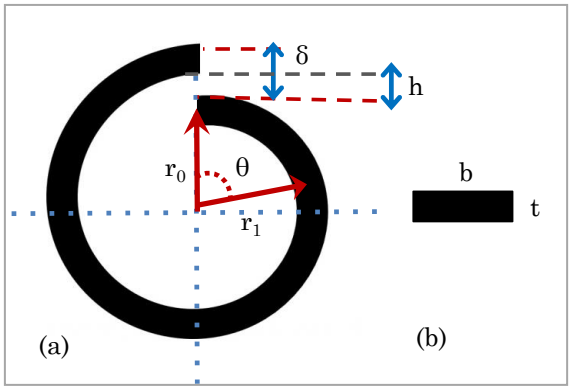


Figure A.2: (a) Schematic diagram of a flat spiral spring and (b) its cross section. Where 'b' = width of the rectangular wire (b > t), 't' = thickness of wire, 'h'=gap between coils, and 'δ'=h+t.

The following equation was derived to calculate the displacement of a single loop spring. The moment-curvature relationship for an element of a beam with a length of δs and radius of R due to a bending moment of M is:

$$\int_0^M \left(\frac{\delta s}{R}\right) dM$$

For a linear elastic beam of flexural stiffness EI:

$$\frac{1}{R} = \frac{M}{EI}$$

So the complementary energy is:

$$\int_0^M \frac{M}{EI}\, \delta s\, dM = \frac{M^2\, \delta s}{2\, EI}$$

For a length L of the beam, the complementary energy is:

$$C = \int_0^L \frac{M^2 \delta s}{2EI}$$

Moment (M) = Q. r. sin θ + P ((r_0 + δ) – (r. cos θ))

$$\text{Complementary energy (C)} = \int_0^{2\pi} \frac{\mathrm{M}^2\ \mathrm{r.d}\theta}{2\mathrm{EI}} = \frac{1}{2EI}\int_0^{2\pi} M^2(r_0 + \Delta.\theta)d\theta$$

Where 'Q' and 'P' are vertical and horizontal loads respectively applied to the end of the spiral, and 'Δ' = δ/2π

The corresponding displacements for the external loads P and Q are δ_x and δ_y:

$$\delta_x = \frac{\partial C}{\partial P} = \frac{1}{EI}\int_0^{2\pi} (M.\frac{\delta M}{\delta P}).r.d\theta \qquad \text{therefore: } \frac{\partial M}{\partial P} = (\mathrm{r}_0 + \delta) - (\mathrm{r.cos}\,\theta)$$

$$\delta_y = \frac{\partial C}{\partial Q} = \frac{1}{EI}\int_0^{2\pi} (M.\frac{\delta M}{\delta Q}).r.d\theta \qquad \text{therefore: } \frac{\partial M}{\partial Q} = \mathrm{r.sin}\,\theta$$

Substituting M into the above equation and solving it using integral by parts, the corresponding displacement becomes:

$$-2\pi\left(\frac{Q.\Delta.r_0\,(r_0+\delta)}{EI}\right) + \frac{3\pi}{2}\left(\frac{Q.\Delta.{r_0}^2}{EI}\right) + \pi\left(\frac{P.{r_0}^3}{EI}\right) + 3\pi^2\left(\frac{P.\Delta.{r_0}^2}{EI}\right) + 3\pi^2\left(\frac{Q.\Delta^2.r_0}{EI}\right)$$
$$- 8\pi\left(\frac{P.\Delta^2.(r_0+\delta)}{EI}\right) + \left(\frac{4\pi^3}{3}+\frac{\pi}{2}\right)\left(3\,\frac{P.\Delta^2.r_0}{EI}\right) + (-4\pi^2)\left(\frac{Q.\Delta^2.(r_0+\delta)}{EI}\right)$$
$$+ (-2\pi^3 + \frac{3}{4}\pi)\left(-\frac{Q.\Delta^3}{EI}\right) + (2\pi^4 + \frac{3}{2}\pi^2)\left(\frac{P.\Delta^3}{EI}\right)$$

Appendix 3: Cadaver trial

Aim: A preliminary cadaver trial was performed to investigate the efficiency of an early design of artificial ACL device consisted of 2 helical springs (20 N mm^{-1}) and a braided Dyneema loop (30480 dtex) in providing stability in the cadaveric knees, a cadaver trial was performed.

Method: A KT-1000 knee ligament Arthrometer (MEDmetric, CA, USA**)** was used to determine the magnitude of anterior tibial translation relative to the femur in one cadaver knee. The knee specimen was visually inspected before the test for the signs of surgical scars, osteophytes, valgus/varus deformities and ligament injuries. The arthrometer was placed against the knee with its arrows pointing directly at the joint line and the measurement pads secured against the tibial tubercle and patella using Velcro straps (Figure A.3). The arthrometer was calibrated by applying alternating anterior forces a few times to the handle to adjust the arthrometer to the zero point.

The tibial translation under 89 N anterior load (second load level of the KT100 arthrometer) was measured at 30 º, 60 º, and 90 º of the knee flexion angles at the following conditions:

- Healthy knee after surgical exposure
- ACLD
- ACLR
- ACLD-TKR
- ACLR-TKR: Bone to bone attachments

The artificial ACLR device used in this study consisted of a femoral helical spring (20 N mm^{-1}) and a tibial helical spring (20 N mm^{-1}) in series. No mechanical stop was used in this prototype implant.

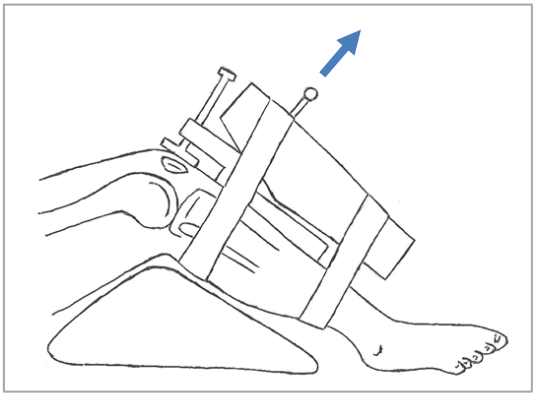


Figure A.3: Schematic diagram of the KT-1000 arthrometer positioned on a human knee.

Statistical analysis: Each measurement was repeated 5 times. The results of the measured anterior tibial laxity were compared using a 1 way ANOVA test followed by a Dunnett test in order to compare the results of all groups versus the control group (i.e. healthy knee after surgical exposure).

Results: The results of the visual examination of the cadaver specimen revealed patello-femoral arthritis. Results of the anterior draw test are summarised in Table A.1, Figure A.4, and Figure A.5. Results of the statistical analysis showed that the anterior tibial translation at all of the measured flexion angles in ACLD and ACLD TKR groups were significantly (p<0.0001) higher than the control group of the healthy knee with intact ACL.

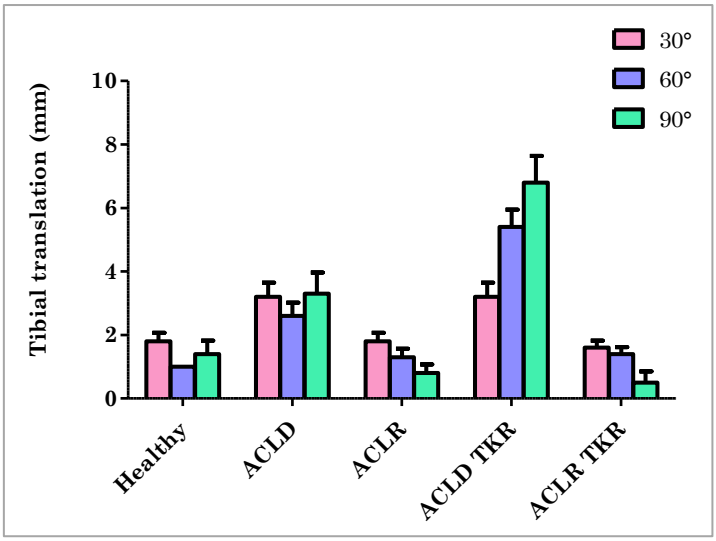


Figure A.4: Results of the anterior tibial draw test on a cadaver knee specimen after different ACL treatments perfomed at 30 °, 60 ° and 90 °.

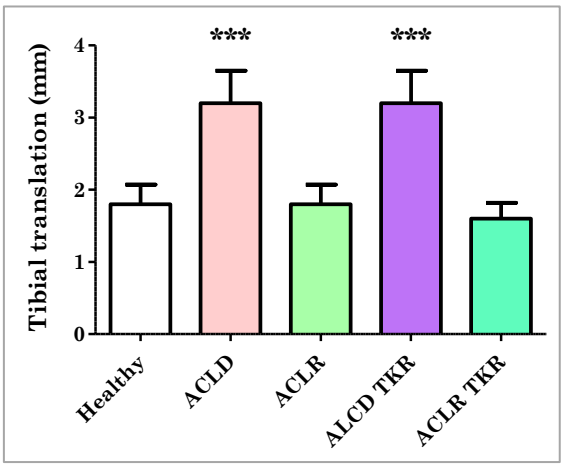


Figure A.5: Significant difference in the measured anterior tibial translation at 30 ° of flexion for the different ACL treatments compared to the healthy control group.

Table A.1: Results of the anterior tibial draw test on a cadaveric specimen using the KT-1000 knee arthrometer.

Knee condition	30 °		60 °		90 °	
	Mean	SD	Mean	SD	Mean	SD
Healthy	1.8	0.27	1	0	1.4	0.42
ACLD	3.2	0.45	2.6	0.42	3.3	0.67
ACLR	1.8	0.27	1.3	0.27	0.8	0.27
ACLD TKR	3.2	0.45	5.4	0.55	6.8	0.84
ACLR TKR	1.6	0.22	1.4	0.22	0.5	0.35

Appendix 4: Placement sensitivity study

Different combinations of the ACL placements on the femur and tibia used in the sensitivity study are listed in the Table A.2.

Table A.2: Combinations of different tunnel placements on the femur and tibia.

Combination	Femur	Tibia
1	Isometric	Anterior
2		Posterior
3		Medial
4		Lateral
5	Anterior	Isometric
6		Anterior
7		Posterior
8		Medial
9		Lateral
10	Posterior	Isometric
11		Anterior
12		Posterior
13		Medial
14		Lateral
15	Superior	Isometric
16		Anterior
17		Posterior
18		Medial
19		Lateral
20	Inferior	Isometric
21		Anterior
22		Posterior
23		Medial
24		Lateral
25 (Control)	Isometric	Isometric

The results of the ACL placement sensitivity study performed on 18 knee models are listed in the Table A.3.

Table A.3: The overall change in the load, strain, extension and twist angle of the reconstructed ACL with variable ACL placements during passive flexion.

Combination	Load (N)	Strain	Extension (mm)	Twist (º)
1	311.51	0.07	3.21	56.88
2	453.45	0.12	4.67	52.61
3	257.75	0.07	2.66	57.78
4	399.08	0.10	4.11	49.46
5	539.59	0.14	5.56	52.77
6	585.79	0.14	6.04	56.91
7	362.88	0.10	3.74	49.58
8	565.14	0.15	5.83	57.83
9	498.22	0.13	5.14	46.91
10	688.30	0.17	7.10	56.95
11	681.10	0.15	7.02	59.05
12	837.66	0.22	8.64	57.29
13	625.55	0.15	6.45	60.22
14	769.82	0.18	7.94	54.22
15	461.07	0.11	4.75	44.67
16	460.45	0.10	4.75	49.74
17	600.09	0.15	6.19	40.83
18	400.78	0.09	4.13	51.09
19	540.86	0.12	5.58	37.96
20	115.83	0.03	1.19	64.61
21	135.30	0.03	1.39	65.23
22	65.65	0.02	0.68	67.21
23	134.38	0.04	1.39	65.23
24	97.38	0.03	1.00	64.49
25	321.60	0.08	3.32	53.63